UNIVERSITY OF
BIRMINGHAM

Investigating the Mechanical Properties of Yeast Cells

By

John Douglas Stenson

A thesis submitted to

The University of Birmingham

For the degree of

Doctor of Philosophy

Department of Chemical Engineering

School of Engineering

The University of Birmingham

United Kingdom

May 2008

Abstract

To predict cell breakage in bioprocessing it is essential to have an understanding of the cell wall mechanical properties. This project involved a study of the wall mechanical properties of individual Baker's yeast cells (*Saccharomyces cerevisiae*) using compression testing by micromanipulation.

An analytical model has been developed to describe the compression of a single yeast cell between flat parallel surfaces. Such cells were considered to be thin walled, liquid filled, spheres. Because yeast cells can be compressed at high deformation rates, time dependent effects such as water loss during compression and visco-elasticity of the cell wall could be and were neglected in the model. As in previously published work, a linear elastic constitutive equation was assumed for the material of the cell walls. However, yeast compression to failure requires large deformations, leading to high wall strains, and new model equations appropriate to such high strains were developed.

It was shown that the preferred model, based on work-conjugate Kirchhoff stresses and Hencky strains, fitted Baker's yeast compression data well up to cell failure. This agreement validated the modelling approach, which might also be useful in characterising the material properties of the walls of other cells and microcapsules.

Using the analytical model, the effects of compression speed on the elastic modulus obtained by fitting numerical simulations to experimental compression data was investigated. It was found that above a compression speed of approximately 45 μms^{-1} the estimated elastic modulus was essentially unchanged. By using a compression speed of 68 μms^{-1} it could be assumed that water loss during compression was negligible. It was then possible to treat the initial stretch ratio and elastic modulus as adjustable parameters within the numerical simulation. In addition to this, as the numerical simulations fitted experimental data well up to the point of cell rupture, it was possible to extract cell wall failure criteria. This study has given mean cell wall properties for late stationary phase Baker's yeast of: elastic modulus 185 ± 15 MPa, initial stretch ratio 1.039 ± 0.006, circumferential stress at failure 115 ± 5 MPa, circumferential strain at failure of 0.46 ± 0.03, and strain energy per unit volume at failure of 30 ± 3 MPa.

Following this, the effect on the intrinsic material properties of treating Baker's yeast with dithiothreitol (DTT) was investigated. DTT has the effect on Baker's yeast cells of breaking the disulphide bonds in the cell wall releasing invertase into the suspending solution. It was found that this did not affect the intrinsic material properties or failure criteria. In addition to this, Baker's yeast cells were mechanically perturbed by sonication and the resulting intrinsic material properties investigated. The surface modulus was found to decrease with increased sonication time while the surface strain energy at failure remained constant. However, it was not possible to determine the extent of damage to each individual cell, preventing explicit conclusions from being reached.

Acknowledgements

The author would like to express his gratitude to the following people who contributed to this thesis in one way or another and without whom this would not have been possible:

Prof Colin Thomas (Department of Chemical Engineering) and Dr Peter Hartley (Mechanical and Manufacturing Engineering) for their invaluable, guidance, advice and patience.

The excellent staff of the School of Chemical Engineering and those in the Centre for Biochemical Engineering more specifically Hazel, and Elaine.

Colleagues and friends of the Micromanipulation Research Group in the past and present for their encouragement, support and hands-on help during the course of this work.

The author would also like to thank his family for their continued help and support.

Table of Contents

List of Figures

List of Tables

List of Appendices

Nomenclature

Symbol	Definition
b	non - osmotic volume of the cell
d	displacement of the probe (μm)
f_1, f_2, f_3	functions of the principal tensions
h	cell wall thickness during compression (nm)
h_0	initial (uninflated) cell wall thickness (nm)
$\underline{n}$	normal to the centre of the element
r	corrected inner cell radius in Figure A 10 (μm)
r_0	uninflated cell wall radius (μm)
r_i	inflated cell radius or measured inner cell radius in Figure A 10 (μm)
s	infinitesimal length in the meridian direction
t_o	time of initial contact between the probe and the cell. (s)
t	time (s)
v	speed of compression (μms^{-1})
x_i	i^{th} co-ordinate of a material particle in the deformed (or final) configuration
z	half the displacement of the probe (μm)
A	projected cell area (μm^2)
A_c	contact area between the probe and the cell (μm^2)

B	material constant in the STZC strain energy function
C	material constant in the STZC strain energy function
C_1, C_2	material constants in the Mooney-Rivlin (1940) strain energy function
D_i	cell diameter (μm)
E	elastic modulus (MPa)
Eh_o	surface modulus (Nm^{-1})
E_i	principal component of Green strain in direction i
F	force on cell (μN)
$\hat{F}$	dimensionless force (Lardner and Pujara, 1980)
F_{Smith}	dimensionless force (Smith *et al.*, 2000b)
$\overline{H}$	corrected cell wall thickness (nm) in Figure A 10
H_i	principal component of Hencky strain in direction i
H_{1f}, H_{2f}	Hencky strains at failure in the meridian and circumferential direction, respectively
I_1, I_2	strain invariants in the STZC and Mooney-Rivlin strain energy function
J	Jacobian determinant
K	Sensitivity of the transducer (mNV^{-1})
P	turgor pressure (MPa) or cell perimeter in equation 3.9 (μm)
$\overline{R}$	corrected cell radius (μm) in Figure A 10
S	compliance of the transducer (μm mN^{-1}) or the length of the wall element in the meridian direction in the inflated and deformed state in Appendix 10

S_i	principal component of 2nd Piola-Kirchhoff (PK2) stress in direction i
S_{ij}	2nd Piola-Kirchhoff (PK2) stress in the jth direction, on the plane normal to the ith direction
T_1, T_2	tension in the meridian and circumferential directions respectively
V	cell volume (μm^3)
V_o	uninflated cell volume (μm^3)
W	strain energy function or voltage (V)
W_o	baseline voltage (V)
W_f	strain energy per unit volume at failure (MPa)
W_{sf}	surface strain energy at failure (Nm^{-1})
X	fractional deformation
X_i	ith co-ordinate of a material particle in the undeformed (or initial) configuration
$\frac{\partial x_i}{\partial X_k}, \frac{\partial x_j}{\partial X_l}$	components of the deformation gradient tensor
γ	half the angle subtended by the edge of the centre of curvature
δ	$\delta = \lambda_2 \sin\psi$
δ_{ij}	Kronecker delta
ε_i	principal infinitesimal strain component in direction i
ε_{ij}	infinitesimal strain in the jth direction, on the plane normal to the ith direction
ε_{kk}	summation of the three strain components (equivalent to volumetric strain)
$\varepsilon_{axial}, \varepsilon_{trans}$	axial strain, transverse strain in uniaxial, infinitesimal strain

ε_v	bulk or volumetric strain
ε_{Bulk}	bulk elastic modulus
η	vertical coordinate of cell wall
$\overline{\eta}$	distance between the compression surface and the equatorial plane
η'	derivative of η with respect to ψ
θ	angle between the normal to the surface and the η axis following compression
κ_i	curvature in the direction i
λ_i	principal stretch ratio in direction i
λ_s	initial stretch ratio
μ	Lamé's constant
ν	Poisson's ratio
ξ	angle in Figure A 10
ρ	horizontal coordinate of cell wall
σ_i	Cauchy stress in direction i
σ_{ij}	Cauchy stress in the j^{th} direction, on the plane normal to the i^{th} direction
τ	Cell wall thickness to cell radius ratio (h_o/r_o)
τ_i	Kirchhoff stress in direction i
φ	angle in Figure A 10
ω	derivative of δ with respect to ψ

ψ	the angular position of a point on the cell wall from the vertical axis of symmetry prior to compression
Γ	the angle of the point on the edge of the contact region between the compression surface and the cell following compression
Δ	difference
Θ	angle of rotation in the circumferential direction
Λ	Lamé's constant
Π_i	internal osmotic pressure (MPa)
Π_e	external osmotic pressure (MPa)

Chapter One: Introduction

The disruption of cells is a key step in many bioprocesses in which the target product is not secreted by a cell into the suspending solution. The level of disruption required will depend on the mechanical strength of the organism and the mechanism of disruption being employed.

The aim of this study was to determine intrinsic cell wall mechanical properties of Baker's yeast (*Saccharomyces cerevisiae*) cells. In order to achieve this, a mathematical model was required which could be used to extract the intrinsic material properties and failure criteria of yeast cells from experimental compression data. These data are essential to help improve the optimisation and design of cell disruption equipment.

Chapter 2 contains a review of the literature covering the biological structure of the yeast cell wall. In addition, a number of methods that have been previously used to measure the mechanical properties of cells are covered. The advantages of using compression testing are described and some of the mechanical models that have been used previously are briefly covered.

Chapter 3 outlines the method of compression testing by micromanipulation which is used to determine the mechanical properties of the yeast cell wall. In addition to this, complementary experimental techniques are described that were used to determine other properties of yeast cells, such as their viability.

Experimental data extracted directly from the compression testing by micromanipulation technique are presented in Chapter 4. The relationships between the force, deformation at failure and cell size are presented and the limitations of these data discussed.

In Chapter 5 mathematical models are described for the extraction of intrinsic material properties from the compression testing data. Three different mathematical models were developed, each utilising a different strain definition, and from these, numerical simulations of compression testing data were produced. The appropriateness of each of these models is examined.

The methods necessary to obtain intrinsic material properties by fitting the numerical simulations to experimental data are then described in Chapter 6. A detailed description of the fitting process is given and the results produced by each of the models compared.

In Chapter 7 the experimental data was used in conjunction with the preferred numerical simulation to allow the intrinsic material properties of the yeast cell wall to be investigated at a range of compression speeds. In addition to this a number of different failure criteria were also investigated.

Chapter 8 describes how compression testing was employed to investigate how chemical and mechanical treatment of cells affected their intrinsic material properties and the failure criteria of the yeast cell wall. Overall conclusions are then presented in Chapter 9. Finally, recommendations for improvements to the compression testing and mathematical modelling techniques are presented in Chapter 10.

Chapter Two: Literature survey

The yeast cell wall has many functions. In the case of cell disruption the most important of these is its physical protection of the cell. While significant work has been done to increase our understanding of cell disruption efficiency only a minimal amount of work has concentrated on the intrinsic material properties of the yeast cell wall. This literature survey is intended to describe briefly the mechanisms used to cause cell disruption, the biological construction of some of the major constituents of the cell wall, and then the techniques that might be use to gain further insight into the intrinsic material properties of the cell wall.

The cell wall has a number of functions besides maintenance of cell shape and protection from physical stresses. It also plays a crucial role in the stabilisation of the internal osmotic conditions and limits the permeability of macromolecules in and out of the cell. An osmotic pressure difference between the inside and outside of the cell generates a turgor (or hydrostatic) pressure within the cell. This pressure is balanced by the mechanical strength of the cell wall. The construction of the cell wall is a tightly regulated process where the polysaccharide composition, structure and wall thickness can vary considerably depending on the environmental conditions and the period during the cell cycle (Klis *et al.*, 2006; Aguilar-Uscanga and Francois, 2003).

2.1. Importance of cell mechanical properties

The disruption of microbial cells is important in bioprocessing, as a means to release the cellular contents. Baker's yeast cells (*Saccharomyces cerevisiae*) have been widely used to

produce many biological products, such as Hepatitis B vaccine (McAleer *et al.*, 1984), hydrocortisone (anti - inflammatory steroid hormone) (Kelly and Kelly, 2003), and precursors to Artemisinin (potent anti - malaria drug) (Zeng *et al.*, 2008). If these products cannot be engineered to be secreted from the Baker's yeast cells, disruption is necessary. Cell disruption involves breaking the cell structure to release the internal contents of the cell into the suspending solution (Farkade *et al.*, 2005).

To understand and predict cell disruption, knowledge of both the effects of fluid stress on the cell and the material properties of the cell wall are required (Thomas and Zhang, 1998; Kleinig, 1997). Disruption of the cell will occur when some failure criterion within the cell wall is exceeded.

In high-pressure homogenisation, the extent of release depends on the local fluid flow fields in the processing equipment and on the mechanical properties of the cells (Kleinig and Middelberg, 1996, 1998). In other types of disruption, there may be different types of stress generation but the mechanical properties of the cells will still be important. Improvement in disruption has been the motivation of recent studies into the mechanical properties of yeast cells (Mashmoushy *et al.*, 1998; Smith *et al.*, 1998, 2000 a, b and c).

This work aimed to characterise the material properties of yeast cell walls to help improve the design and optimisation of cell disruption equipment. In order to do this it is necessary to have an understanding of the methods used in cell disruption, as described in the next Section. In addition, investigating the links between yeast cell mechanical properties and the cell wall composition and structure should improve our understanding of the mechanisms controlling the form, growth and division of cells (Harold, 2007).

2.1.1. Cell disruption in bioprocessing

There are a number of methods used in cell disruption which are based on mechanical techniques, such as homogenisation and bead mills, or non - mechanical methods such as physical techniques and chemical or enzymatic treatment (Figure 2.1).

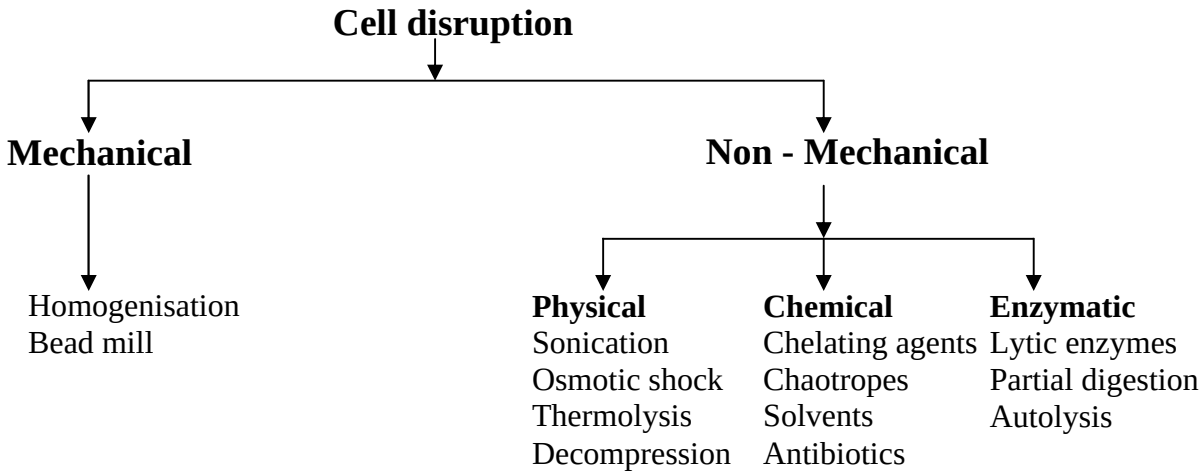

Figure 2.1: Overview of the mechanisms of cell disruption. (modified from Middelberg,1995)

Mechanical cell disruption in bioprocessing

To achieve non - specific large scale disruption of cells, mechanical techniques are often employed. While non - mechanical methods are applicable for specific microorganisms, mechanical methods can be applied to most organisms. In industrial situations, high-pressure homogenisation and bead mills are the preferred methods by which to cause cell disruption. These processes will generally cause the total indiscriminate disruption of cells with no selectivity of the products released.

High pressure homogenisation generally works by forcing a cell suspension through a small orifice under high pressure leading to a large pressure drop. Usually it is necessary to pass the suspension through the homogeniser a number of times for complete release of the intracellular product. The precise mechanism of cell disruption in homogenisers is not entirely clear, although it seems to include a large pressure drop, cavitation, and impact of the cells. There are many factors which influence how efficient the cell disruption will be. These include the operating pressure, valve design, number of passes, suspension temperature, and cell concentration. (Middelberg, 1995).

Non - mechanical - physical cell disruption in bioprocessing

Physical cell disruption operates by indirectly causing the cell wall structure to be disrupted. Examples of this method include osmotic shock, gas decompression and sonication. The osmotic shock method works by transferring cells into hypertonic solutions leading to cell swelling and breakage. The gas decompression bomb uses nitrogen decompression and has been shown to be effective in disrupting mammalian cells (Hunter and Commerford, 1961), bacterial cells (Fraser, 1951, Carpita, 1985) and plant cells (Loewus and Loewus, 1971). However, this technique is not effective at disrupting yeast cells or spores and when applied to bacteria the cells will usually require a pre-treatment before rupture from nitrogen decompression will occur.

Sonication operates by the creation of high frequency sound (ultrasound) that is produced electronically and transferred to the cell suspension. Ultrasound is any sound that is above the frequency at which human ears can hear (greater than 16 kHz). The effect of sonication on the mechanical structure of the cell wall has been attributed to the cavitation

phenomenon (Guerrero *et al.*, 2001; Ciccolini *et al.*, 1997). In this process pressure waves are generated by high frequency mechanical vibrations which lead to the formation of microscopic bubbles. Once these bubbles are formed they oscillate, grow and split in response to the continuing pressure waves. At high frequencies these micro bubbles will implode violently. The implosion of these bubbles is known as cavitation which can generate temperatures near 5000 ^{o}C and pressures of 100 MPa (Santos and Capelo, 2007). During the sonication process reactive free radicals are also generated. The extent of their production depends on the intensity of the sonication process which can be controlled by varying the operating conditions such as the initial concentration of the cell suspension, temperature (Ciccolini *et al,* 1997) and the power input (Guerrero *et al.,* 2001). Sonication has the ability to cause only the partial disruption of cells allowing selective release of products from the cell wall and periplasmic space which can make down stream processing simpler.

Non - mechanical - chemical and enzymatic cell disruption in bioprocessing

Non - mechanical methods of cell disruption can be used in conjunction with mechanical methods to improve their efficiency, or as the sole mechanism of inducing cell failure.

In addition non - mechanical methods can be used in the selective release of products from the cell wall and periplasm of cells. These methods have the ability to cause selective damage to the cell wall or cytoplasmic membrane of the microbial cell. This can be especially useful if the desired product is susceptible to damage from mechanical disruption (i.e. due to heat production or oxidation).

There are a number of chemical treatments which can selectively act on the cell, releasing cell wall associated and periplasmic products. While treatment of cells with some chemicals will lead to the complete cell disruption, there are many methods which cause selective disruption such as, solvents, chaotropic agents, and reducing agents.

Solvents act on cells by causing the extraction of the lipid component from the cell and at high concentrations completely disrupt the membrane of the cell (Balasundarum, 2004). Chaotropic agents are believed to lead to the weakening of the stabilising hydrophobic interactions within the wall promoting cell wall disruption. Reducing agents, including dithiothreitol (DTT), and β - mercaptoethanol are found to create pores within the cell wall by reducing the number of disulphide links in the cell wall (Klis *et al.*, 2007). The breaking of these bonds has the effect of expanding the cell wall and increasing its porosity. This allows cell wall associated products, such as invertase (Sommer and Lewis, 1971), to be released from the cell.

Enzymic treatments can be used to attack the cell wall of microbial organisms allowing the release of intracellular products. These enzymes can be used to selectively affect the outer surface of the cell wall allowing the release of periplasmic products and production of protoplasts. Due to the large variations in cell wall composition and structure between different microorganisms these enzymic treatments are highly specific(Balasundarum,2004).

2.1.2. Prediction of cell disruption

One of the major factors in determining the choice of the cell disruption technique is the overall aim of releasing the maximum amount of product at the minimum cost. To achieve

this aim the most efficient mechanism of cell disruption is required in both the release of product from the cell and purification of the product. This means the most preferred mechanism of failure would break open the cell, releasing the product while allowing efficient purification with the minimum number of processing steps. In order to do this it is essential to be able to predict cell disruption.

In order to understand whether treatment with chemicals and enzymes will help the disruption process it is necessary to have a detailed understanding of the contribution of different cell wall components to the mechanical strength of the cell wall.

As well as having a detailed understanding of the mechanisms that cause cell disruption it is also important to have knowledge of the cell wall structure. The structure and composition of the Baker's yeast cell wall are discussed in Section 2.2.

2.2. Structure of the yeast cell wall

In this Section the major constituents of the Baker's yeast cell wall (*Saccharomyces cerevisiae*) will be discussed. This will focus on the cell wall of Baker's yeast though many similarities are found with the cell wall of other organisms and where relevant these will be referred to. One of the reasons for choosing Baker's yeast for the present work is that the whole organism is under intense study (Klis *et al.*, 2006; Lesage and Bussey, 2006). While our knowledge of the temporal and spatial construction of the cell wall is far from being complete, significant advances have been made in recent years. For a more complete discussion of the yeast cell wall structure readers are referred to Klis *et al.* (2006) and Lesage and Bussey (2006).

2.2.1. Structural organisation and composition of the cell wall

The composition and structure of the yeast cell wall is controlled by about 1200 genes (Klis *et al.*, 2006). Electron microscopy has demonstrated that the yeast cell wall is constructed of a number of layers of different materials (Osumi, 1998).The components that make up the cell wall are covalently linked together to form macromolecular complexes that are constructed into the cell wall (Kollar *et al.,* 1997). This model has been described as a latticework rather than a solid structure as the wall components only occupy 10-20% of the cell wall volume (Lipke and Ovalle., 1998). The Baker's yeast cell wall consists of β 1,3 - glucan, β 1,6 - glucan, chitin, and mannoproteins.

The Baker's yeast cell wall makes up approximately 30% of the dry cell weight depending on the growth conditions, which is composed mainly of β 1,3 - glucan and mannoprotein (Table 2.1).

Component (Degree of polymerisation)	**Mean molecular mass (kDa)**	**Percentage of cell wall mass**
β 1,3 - glucan (1500)	240	30 – 45
β 1,6 - glucan (150)	24	5 – 10
Mannoprotein	Highly variable	30 – 50
Chitin (120)	25	1.5 – 6

Table 2.1: Major components that make up the yeast cell wall. (Data taken from Lipke and Ovalle, 1998 and Klis et al., 2006)

β 1,3 - glucan is the major constituent of the inner layer of the cell wall while mannoproteins are the major constituents of the outer layer. The moderately branched β 1,3 - glucan structure provides the support for further components to be attached. The actual protein content of the mannoprotein constituent is 4 - 5 % with the remaining mass being protein linked mannose carbohydrate side chains (Aguilar - Uscanga and Francois., 2003). β 1,6 - glucan links these inner and outer layers together. Chitin is deposited in the lateral cell wall layer late in the cell cycle following cytokinesis forming β 1,3 - glucan complexes, though the majority is found in the cell bud scars.

A yeast cell's life span is defined by the number of buds produced by a cell before cessation of cell replication. The yeast mother cell divides asymmetrically producing a daughter cell. The process of cell division is a tightly regulated process which may be lethal to both mother and daughter if incorrectly performed. Cell division leads to the production of a bud scar on the mother cell wall and a birth scar on the daughter cell wall (Smits *et al.,* 2001). Therefore, the age of the yeast mother cell can be determined simply by counting the number of bud scars on the cell wall (Sinclair *et al.,* 1998). The bud scar is composed of a thick chitin ring and a layer of chitin across the entire scar. This is in comparison to the thinner or non existent chitin ring contained in the birth scar on the daughter cell (Powell *et al.,* 2003; Smits *et al.* 2006). This chitin ring within bud scars is a rigid structure that expands little or not at all as the cell grows. This is in contrast to the birth scar which expands during the subsequent growth of the cell (Powell *et al.,* 2003; Smits *et al.* 2006).

Like Baker's yeast, the opportunistic fungal pathogen *Candida albicans* main structural component of the cell wall are β - glucans also in a complex with chitin (Iorio *et al.,* 2008).

This suggests that structural information obtained from Baker's yeast might be applied to other yeast species.

The cell wall may vary in composition, and its thickness depends on several factors, including the growth nutrients, external pH and oxygen levels (Aguilar-Uscanga and Francois, 2003). However, much less is known about how the length and branching of the β - glucan is affected by these changing factors. It is also unknown how the glycosylation of the cell wall proteins change due to growth factor differences. Although the composition of the cell wall can vary greatly (see Figure 2.2) a general model can be produced.

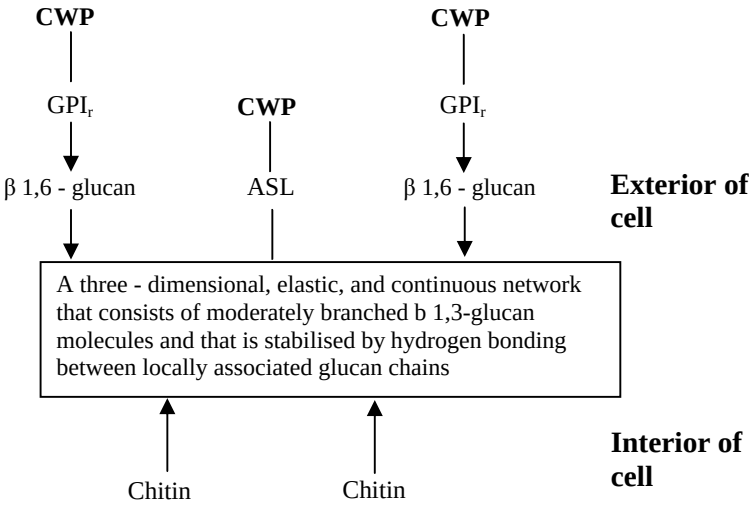

Figure 2.2: Diagrammatic representation of the Baker's yeast cell wall, (modified from Klis et al., 2002). CWP = Cell Wall Proteins (mannoprotein), GPI_r = lipidless GPI remnant connecting the carboxylterminal end of a mature GPI-modified cell wall protein to the cell wall polysaccharide network, ASL = Alkali-sensitive linkage. A sketch of this is shown in Appendix 19.

In this model, mannoprotein is attached to β1,6 - glucan through a remnant of a glycosylphosphatidylinositol (GPI) anchor. The reducing terminus of chitin is attached to β1,6 - glucan which in turn is linked to β1,3 - glucan (Kollar *et al.*,1997). Chitin is deposited

in the cell wall following cytokinesis, coupling to β1,3-glucan, which is expected to lead to a stiffening of the cell wall (Smits *et al.,* 1999). These modules are then associated by hydrogen bonding in the β1,3 -glucan-chitin layer and in the mannoprotein layer by covalent cross-links, including disulphide bonds between the mannoproteins (Klis *et al.,* 2002). This cross-linking within the cell wall contributes to the mechanical strength of the cell.

2.2.1.1. β 1,3 - glucan

β 1,3 - glucan is a structural polymer that forms a fibrous network believed to be responsible for the mechanical strength of the yeast cell wall (Zlotnik *et al.,* 1984). In stationary phase cells β 1,3 - glucan chains are approximately 1500 monomers in length though significantly higher values have been reported (Klis *et al*., 2006). The stationary phase monomer value may be lower due to the harsh acid based extraction methods used which may hydrolyse the polymer (Muller *et al.,* 1997; Williams *et al.,* 1991). The degree of polymerisation may also depend on the growth conditions, i.e. carbon source or pH, and the growth phase (Muller *et al.,* 1997).

The β 1,3 - glucan chains form coiled spring or wire like structures that can exist in various states of extension (Krainer *et al.,* 1994). These wire like structures form into a helical structure that is composed of up to three polymer chains H-bonded together (Stokke *et al.,* 1993). These structures are assumed to provide the cell wall with its observed elasticity and its ability to hold tensile forces (Klis *et al.,* 2006). The ability of the yeast cell to shrink or expand rapidly when exposed to hypo/hypertonic solutions is believed to be due to this elastic nature (Klis *et al.,* 2006). This allows the yeast cell to survive when stressed. Other species of yeast such as *Pichia, Candida,* or *Schizosaccharomyces* will also respond to high

osmotic pressures in a similar manner indicating the combination of mechanical strength and elasticity is common in yeast cells (Morris *et al.,* 1986).

There is moderate branching of the β 1,3 - glucan network within the cell wall (about 3% branch points) which covalently links to other wall components. There is no direct information available about the length of the branches though they are believed to be of significant length. The long branch points would result in a bushy polysaccharide with the reducing end at the base of the stalk. The length of these branches controls whether the β 1,3 - glucan chains form single or triple helices (Stokke *et al.,* 1993; Williams *et al.,* 1991).

β 1,3 - glucan has multiple non - reducing ends which function as a receptors for the covalent attachment of both β 1,6 - glucan and chitin (Kollar *et al.,* 1995; 1997). At the external surface of the network the β 1,3 - glucan is linked to β 1,6 - glucan by an as yet uncharacterised link. The non-reducing end of the fibre joins to the reducing end of chitin chains at the inside of the lateral wall through a β 1,4 link (Kollar *et al.,* 1995). However, it should be noted that this only happens after cytokinesis. This suggests that chitin does not play an integral role in providing structural support to the cell wall though its influence on the mechanical response may be significant. When chitin is attached to the β 1,3 - glucan layer it leads to the β 1,3 - glucan becoming insoluble to alkali leading to the presence of alkali soluble and alkali insoluble β 1,3 - glucan in the cell wall. Also, chitin may not be linked solely to β 1,3 - glucan but also to β 1,6 - glucan in a process usually stimulated by perturbation ((Klis *et al.,* 2006; Lesage and Bussey, 2006). Some cell wall proteins (CWP) are also linked to the β 1,3 - glucan network through an unidentified alkali-sensitive bond. These PIR-CWP (Proteins with Internal Repeats - Cell Wall Proteins) are uniformly distributed within the inner skeletal structure of the β 1,3 - glucan network.

2.2.1.2. β 1,6 - glucan

β 1,6 - glucan is a highly branched amorphous polysaccharide that consists of approximately 350 glucose monomers and comprises approximately 10% of the cell wall glucan (Kollar *et al.*, 1997). β 1,6 - glucan is a critical structural polysaccharide acting as a flexible glue that connects GPI-dependent cell wall proteins to the inner β 1,3 - glucan polysaccharide layer. The mechanism of synthesis is unclear. It is likely that the majority of β 1,6 - glucan synthesis takes place at the cell surface following some key intracellular processes. Genetic techniques have shown that the disruption of the synthesis of β 1,6 - glucan leads to reduced growth of *S. cerevisiae* (Shahinian and Bussey, 2000). It is also unknown whether this polymer is synthesised as a linear molecule and becomes branched following this, or if it is synthesised with branching points.

2.2.1.3. Chitin

Chitin is a linear polymer that exists within the bud scars and to a lesser in the lateral cell wall of cells following cytokinesis (Molano *et al.,* 1980; Cabib *et al.,* 2001). The cell wall is composed of relatively low levels of chitin with it contributing only 0.1 – 0.2 % to the lateral walls and 2 % in the bud scar of the total cell wall weight. Deposition of chitin within the wall is controlled in both a spatial and temporal manner. Chitin associated with the bud scar is approximately 190 N-acetylglucosamine monomers in length, though it is unknown if this length is valid for chitin found in the lateral wall (Klis *et al.,* 2002). Approximately 40% of the chitin located in the lateral cell wall is linked to the non-reducing end of β 1,3-glucan via a β 1,4 bond to the reducing end of the chitin chain. The chitin chains anneal together to form crystalline α-chitin whose structure is similar to that of α-cellulose, with

hydrogen bonded anti-parallel chitin units. This crystalline structure of the deposited chitin in the lateral wall is assumed to provide stretching resistance to the cell wall (Lesage and Bussey, 2006). The increased deposition of chitin in the lateral wall is essential in increasing the resistance of β 1,3 - glucan to alkali solubility (Hartland *et al.,* 1994). Also chitin may become linked to the non - reducing ends of β 1,6 - glucan chains in response to cell wall perturbation. When cells are exposed to perturbation the levels of chitin can increase dramatically up to 20% in the lateral wall by weight (Dallies *et al.,* 1998; Klis *et al.,* 2002).

2.2.1.4. Mannoproteins

Mannoproteins form the outer layer of the yeast cell wall and are highly glycosylated polypeptides whose carbohydrate content can be up to 90% (w/w). Glycosylation is the process where saccharides are added to proteins and lipids. This process is an essential part of post - translational modification and disabling this results in misfolded unstable proteins. The outer layer of mannoproteins is significantly less permeable than the inner β - glucan fibre layer (Klis *et al.,* 2006). The reduced permeability is due to the presence of long branched carbohydrate side chains and to the presence of disulphide bridges. Also there are phosphodiester bridges located within the N and O-linked mannosyl side chains on the cell surface which leads to negative charge regions. Finally serine and threonine residues, often carrying short oligomannosyl side chains, are clustered together leading to a rod-like region within the polypeptide backbone that is relatively rigid. This increased rigidity occurs due to the effect of O-glycosylation which leads primarily to steric interactions between amino acids in the peptide core (Jentoft, 1990).

There are two main methods by which proteins are covalently linked to the cell wall polysaccharides, glycosylphosphatidylinositol dependent cell wall proteins (GPI-CWP) and proteins with internal repeats cell wall proteins (PIR-CWP). These modified CWP can be linked directly or indirectly to the structural polymers of the yeast cell wall. The GPI-CWP complex is believed to play an important role in the cell wall response to perturbation. Cells grown in a rich medium will contain mostly GPI-CWPs.

PIR-CWP are linked directly to the β 1,3 - glucan structure via an alkali sensitive linkage (Castillo *et al.,* 2003) and are uniformly distributed within the inner skeletal structure. These PIR-CWP are able to interconnect with a number of β 1,3-glucan fibres and this process is expected to considerably strengthen the cell wall (Castillo *et al.,* 2003). In addition PIR-CWPs have been found to be highly expressed during the G1 phase of the cell cycle and during periods of cell perturbation which is believed to both increase the strength of the cell wall and limit the cell wall permeability.

2.2.1.5. Cell wall summary

The Baker's yeast cell wall is a very complex organelle and while significant advances have been made in improving our understanding of its construction, our knowledge is still incomplete. For instance while it is believed that only the inner β - glucan and chitin layers provide the cell with mechanical strength, there is still no direct evidence of this. Also as has just been mentioned, during times of stress PIR - CWP production is increased which might lead to increasing the strength of the wall. From this it does not seem reasonable to assume that the mannoproteins layer does not contribute to cell wall strength at least in times of

stress. However, without any direct mechanical evidence it is not possible to reach a definitive conclusion.

2.3. Investigating the mechanical properties of cells

In order to determine the mechanical properties of a material it is necessary to measure initial geometric parameters and perform some stress/strain experiment on the sample. These parameters can then be combined with an appropriate mathematical model to determine the intrinsic material properties of the sample.

The choice of experimental technique will depend on the type, size, mechanical properties of the material and the property of interest. When investigating large samples of materials such as metals, it is relatively easy to obtain the initial geometric parameters. Also the methods used to measure the stress/strain relationships have been widely used and are well established, such as impact, tension, stress - relaxation, and indentation tests.

When investigating the mechanical properties of individual biological cells a number of difficulties arise and the traditional methods used for other materials cannot be employed. Due to the small size of the samples, measuring the initial geometry is difficult. In addition, the traditional techniques used to measure the stresses and strains imposed on the sample are not usually applicable to small biological materials. For example, tensile tests require sections of the cell boundary to be isolated from the cell, which is technically very difficult.

As described later in Chapter 3, compression testing by micromanipulation is a large deformation method (large in comparison to the cell size) that can be applied to single cells

and is the technique of choice for this work. The techniques discussed in the following sections have previously been used to measure the mechanical properties of a range of cells. The appropriateness of their use with yeast cells will be discussed as well as prior art with other biological materials. Some techniques, such as the gas decompression bomb and micro penetration, have been used to measure the mechanical properties of plant tissues or cell populations rather than single cells and are not considered here. In addition, techniques which are not appropriate but have been used to extract information about the mechanical properties of other cells are considered, but only briefly. The compression testing technique is discussed in detail and the methods used to extract intrinsic material properties described.

2.3.1. Pressure probe and micropipette aspiration

Pressure probe

The pressure probe is used to study the hydraulic structure of tissues and individual cells, water movement in plant structures and the response of tissues to water stress. In this technique a capillary probe penetrates the cell and allows the cell turgor pressure to be measured. By manipulating the pressure within the cell it is possible to derive the volumetric elastic modulus of the cell (Tomos, 2000; Tomos and Leigh, 1999). However, the volumetric modulus (defined in Appendix 12) has been previously described as a meaningless parameter suggesting that the results obtained by this process cannot be used to increase our understanding of cell disruption (Wu *et al.*, 1985).

Wang *et al.,* (2006b) used the pressure probe to determine the internal turgor pressure of suspension tomato cells. This technique was combined with compression testing (Section 2.3.5) to obtain independent turgor pressure measurements. To be able to use this technique

it is necessary to be able to visualise the probe which generally limits this method to cells over 20 μm in diameter. Due to the small size of yeast cells (approximately 5 μm) obtaining a probe sufficiently small would be extremely challenging, and it would probably become blocked when it penetrated the cell.

Micropipette aspiration

The mechanical behaviour of living cells has been studied widely using the micropipette aspiration technique. In the most common application a cell suspended in solution is partially or wholly aspirated into the mouth of a pipette, the initial diameter of which may range from less than 1 μm to 10 μm (Lim *et al*, 2006). The elongation of the cell into the pipette is measured using video microscopy to record the change in shape of the cell. Measuring this elongation and suction pressure allows the mechanical properties of the cell to be determined (Hochmuth, 2000).

Micropipette aspiration has been widely used to measure the mechanical properties of many types of cells including red blood cells, leukocytes and chondrocytes (Lim *et al.*, 2006). When compared to AFM (Section 2.3.3) or optical tweezers (Section 2.3.4) the micropipette aspiration technique appears to be simpler. One of the main disadvantages of this method is the friction that occurs between the cell membrane and the glass pipette which is difficult to account for. Also the pipette aspiration technique produces stress concentrations at the edge of the pipette and the cell membrane. Recent advances in the use of finite element techniques have allowed these stress concentrations to be accounted for, though direct measurement of these forces is impossible (Boudou *et al.*, 2006). Also the curvature in the cell membrane as it is drawn into the pipette can easily cause damage to the cell. In addition to this the process of micropipette aspiration does not allow failure criteria to be determined,

essential for improving our understanding of cell disruption. As well as this, micropipette aspiration has only been used on cells that are large and easily deformable.

2.3.2. Osmotic pressure variations

In the osmotic experiment cells are suspended in a hypotonic solution. This solution is gradually changed for a hypertonic solution causing the cell volume to decrease as water flows out of the cell. The volume changes of the cell are then measured using image analysis (Berner and Gervais, 1994), Coulter Counter (Meikle *et al.*, 1988, Srinorakutara, 1997) or a Malvern Mastersizer (Smith *et al*., 2000a). From this the Boyle van't Hoff relationship (discussed in detail in Sections 3.3 and 7.2.6.2) can be used to calculate the internal pressure (turgor pressure) of the cell or (for some cells) it can be measured directly using the pressure probe (Tomos, 2000). The turgor-volume relationship can then be analysed using a mathematical model which allows the determination of the cell membrane or cell wall mechanical properties. Meikle *et al.* (1988) used this method to calculate the bulk elastic modulus of exponentially growing yeast cells to be 3.25 MPa which is similar to values produced by Levin *et al.* (1979) using the same method.

The main disadvantage of this method is that the mechanical properties can only be inferred from cell volume changes and are not measured directly. In addition, generally only the bulk elastic modulus is calculated using this technique, which has been described by Wu *et al.* (1985) as being a meaningless parameter because it treats the cell as a homogeneous sphere, and does not give direct information about the cell wall. Although this technique might provide useful information from the response of yeast cells to osmotic pressure changes, it is

not appropriate to be the main technique for analysing the mechanical strength of yeast cells in this work.

2.3.3. Atomic force microscopy (AFM)

Atomic force microscopy can be used to produce an image of a target sample and also locally measure the material properties by nanoindentation.

Figure 2.3 shows a schematic of a typical AFM set up.

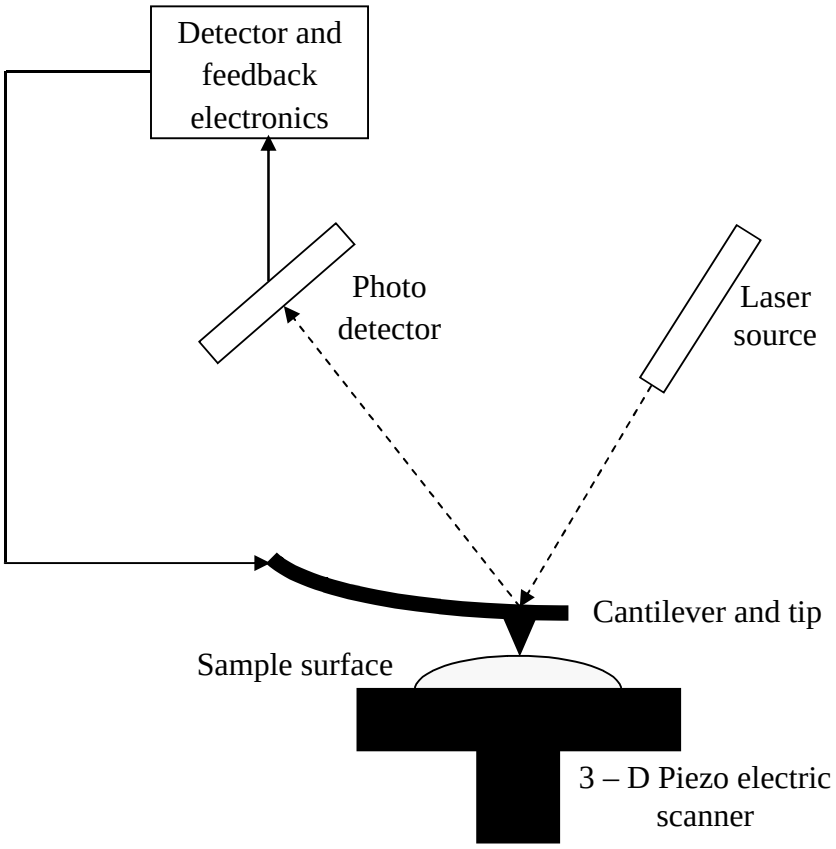

Figure 2.3: Schematic of an AFM set up.

The AFM instrument consists of a cantilever-mounted tip, a Piezoelectric scanner, four position - sensitive photo detectors, a laser diode and a control unit (Figure 2.3). The process of operation of an AFM is relatively simple. The beam from the laser is directed against the back of the cantilever beam onto the quadrants of the photo detector. As the tip is moved across a sample this causes the cantilever beam to bend or be twisted in manner that is proportional to the interaction force. This bending or twisting of the cantilever causes the position of the laser on the photo detector to be altered. The deflection of the cantilever beam can then be converted into a 3D topographical image of the sample surface (Kuznetsova *et al.,* 2007; Gaboriaud *et al.,* 2007; Lim *et al.,* 2006).

Initially this technique was intended purely as a high resolution imaging device, down to the sub-nanometre level (Alessandrini and Facci, 2005). However, it was soon adapted for measuring the interactive forces in a process known as force spectroscopy. In this process the sample is moved towards the tip and retracted with the vertical displacement of the Piezoelectric scanner being recorded. This produces voltage data recorded by the photodetector as a function of the displacement of the Piezoelectric scanner. A force curve can be produced from this which provides information about the interactions between the tip of the probe and the sample. This force data can be interpreted to allow information about the mechanical properties of the sample to be obtained.

One of the simplest and most widely used methods to extract mechanical information from the AFM force curves is the Hertz model. The Hertz model describes the contact between an elastic sample and a rigid indenter assuming negligible adhesion between the tip and the sample (Kuznetsova *et al.,* 2007). This technique was employed by Touhami *et al.* (2003) to determine the Young's modulus of different areas of the Brewer's yeast cell wall

(*Saccharomyces cerevisiae*). In this work Touhami *et al.* (2003) found that the chitin bud scar had a Young's modulus value of 6.1 ± 2.4 MPa, which is 10 times higher than the value for surrounding cell wall area of 0.6 ± 0.4 MPa. This demonstrates that AFM can be used to investigate the effects of different cell materials on the mechanics of the cell wall.

Using simple Hertz theory leads to material properties that are significantly lower than previously reported Young's modulus values, obtained using compression testing (Section 2.3.5) for *S. cerevisiae* of 150 ± 15 MPa by Smith *et al.* (2000b). In addition to this the elastic modulus of the cell wall of *Aspergillus nidulans* has been found from AFM testing to be 110 – 200 MPa (Zhao *et al.*, 2005). Both of these investigations used finite element analysis (FEA) employing elastic shell theories with the sample considered as a liquid filled shell. The significant difference in the results obtained when using FEA and Hertz theory has been confirmed by Ohashi *et al.* (2002) by the exposure of endothelial cells to shear. Ohashi *et al.* (2002) attributed these differences to approximation functions used to determine the elastic modulus whereby nonlinearity would affect the Hertz theory leading to a poor fit between the model and experimental data. While Hertz theory can be used as a comparative measurement, it might not produce accurate estimates of the elastic modulus when used with biological materials.

In addition to the force curve data obtained from AFM, other properties can also be measured. Another technique has been used to determine the adhesive forces of *S. cerevisiae*, as well as many other organisms, to surfaces in biofilm formation (Bowen *et al.*, 2001). An additional method has used AFM to detect local nanomechanical motion of the cell wall of *S. cerevisiae* caused by the active metabolic processes of a cell (Pelling *et al.*, 2004).

AFM has become an indispensable tool when investigating the forces associated with cellular and molecular biomechanical events. However, AFM techniques do not currently have the ability to produce cell wall failure data. As the aim of this project is to help improve the design and optimisation of cell disruption equipment it is essential that some failure parameters are produced.

2.3.4. Optical trap method (also known as laser tweezers)

The optical trap method uses a highly focused laser to trap and manipulate particles of interest in a medium (illustrated in Figure 2.4). The laser is focused on a dielectric particle (e.g. silica micro bead) whose refractive index is higher than the suspension medium. This produces a light pressure (or gradient force) which moves the particle towards the focal point of the beam (i.e. beam waist) (Lim *et al.,* 2006).

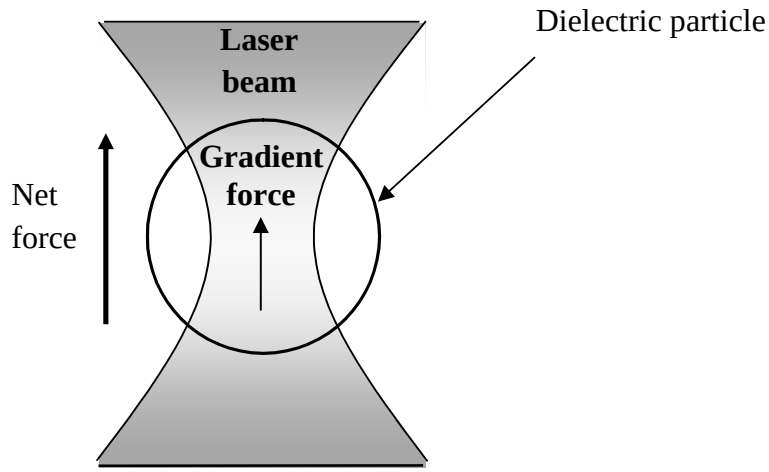

Figure 2.4: Optical trap of a dielectric particle (Simplified from Lim et al., 2006)

The optical trap is a very sensitive method that is capable of the manipulation of sub micron particles such as individual viruses and bacteria. Currently no studies into the mechanical

properties of the yeast cell wall have been performed using the optical trap method, though other biological systems have been investigated. Figure 2.5 is an example of the use of the optical trap method to measure the elastic properties of cells such as red blood cells (Mills *et al.,* 2004).

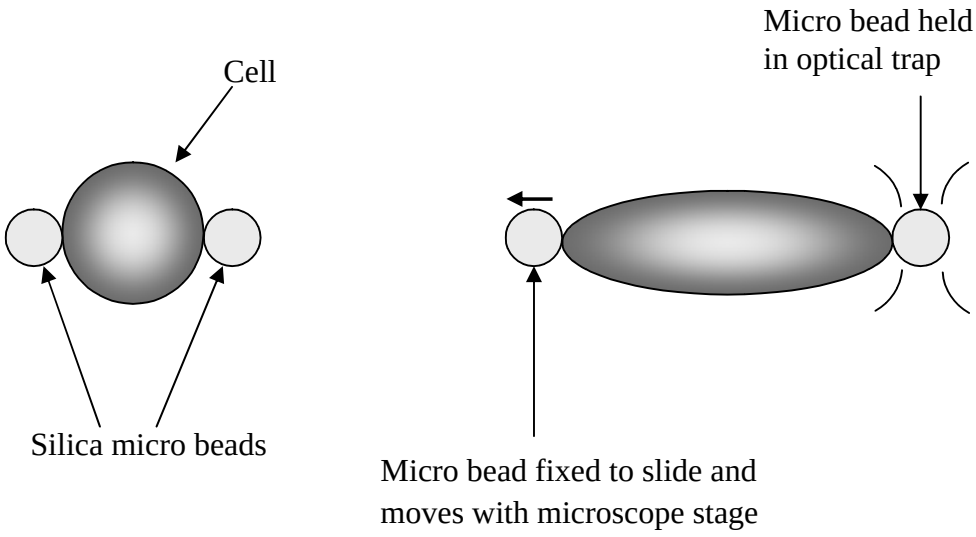

Figure 2.5: Stretch of a particle (e.g. red blood cell) using the optical trap method.

(modified from Mills et al., 2004).

Initially silica micro beads were attached to geometrically opposite sides of the cell with the bead on the left hand side being attached to the surface of a glass slide and the right hand bead held in the optical trap. The trapped bead remained stationary as the glass slide was moved to the left causing the cell to stretch. From this measurements of the stretching force of the cell could be determined. As well as measuring, the mechanical properties of red blood cells, the stretching of DNA molecules has also been investigated (Smith *et al.,* 1996; Bryant *et al.,* 2003) in addition to measurements of the Young's modulus of the bacterial macrofibers of *Bacillus subtilis* (Mendelson *et al.,* 2000).

One of the advantages of the optical trap method is that there is a limited physical contact with the cell although it is possible that the cell will be damaged by the laser (Lim *et al*, 2006). In addition, it is also possible to measure forces in the sub picoNewton range, which is extremely difficult to do by other methods. However, due to this it may not be appropriate for use when investigating the response of samples to large deformations, especially if the sample has a cell wall.

While the optical trap technique has been shown to be able to produce valuable information on the mechanical response of cells, like AFM and micropipette aspiration it is unable to produce information on the failure of cells. In addition, yeast cells have been shown to fail by compression testing at approximately 100 μN due to the presence of a cell wall (Smith *et al.*, 2000a; Mashmoushy *et al.*, 1998). As optical traps are only able to measure forces in the picoNewton range this technique would be inappropriate for use on cells with cell walls.

2.3.5. Compression testing techniques

Compression testing can be applied on a large scale when sections of a tissue are compressed, or to individual cells or particles. As it is necessary to have the material properties of individual cells to model their disruption in bioprocessing only this will be discussed here. In this technique an individual cell is compressed between two flat parallel surfaces, usually until it fails. By measuring the force being applied to the cell and the displacement of the surfaces, force - deformation data can be found. From this the force at cell failure is recorded which can be used as a comparative measurement between cell populations.

Initial experiments using this method involved the compression of relatively large sea urchin eggs and visual measuring the surface displacement to determine the forces being imposed (Cole, 1932; Hiramoto, 1963; Yoneda, 1964; 1973). Recently compression testing by micromanipulation was developed, which is capable of determining the mechanical properties of small cells or particles with sizes down to about 1 μm and forces 1 μN or greater (Zhang *et al.*, 1992). A review of this technique can be found in Thomas *et al.* (2000). The compression testing by micromanipulation technique and its development is discussed further in Section 3.2.1. It has been used to study many experimental systems including single tomato cells from suspension cultures (Blewett *et al.*, 2000; Wang *et al.*, 2004), animal cells (Zhang *et al*., 1992; Peeters *et al.*, 2005), microcapsules (Liu *et al.*, 1996), yeast cells (Mashmoushy *et al.*, 1998; Smith *et al.*, 1998, 2000a, 2000b, 2000c), bacteria (Shiu *et al.*, 1999), microspheres (Wang *et al.*, 2005) and pollen grains (Liu and Zhang, 2004).

The forces measured by compression testing are dependent on many factors including cell size, cell wall thickness and the speed of compression. In order to extract useful information about the cell wall material properties it is essential to obtain intrinsic material properties that allow cells of different sizes and composition, and with different histories, to be compared. By linking the compression technique to a cell mechanical model it is possible to obtain such properties e.g. the cell wall elastic modulus, and the stresses and strains, and strain energy within the wall at failure.

Initial attempts to extract elastic modulus data from the compression testing experiments were based on measuring the contact area between the surface and the cell, the applied force and the principal radii of curvature at the point of contact (Cole, 1932; Hiramoto, 1963).

From this it was possible to obtain elastic modulus and surface tension data. The major difficulty with this method was obtaining accurate measurements of the contact area.

Following on from this work two types of mathematical model have been developed which do not rely on measuring the contact area. These models are the ‘liquid - drop’ model (Yoneda, 1973) and the elastic membrane model (Feng and Yang, 1973; Lardner and Pujara, 1980; Cheng, 1987a).

The liquid - drop model has been used to model the deformation of sea urchin eggs (Yoneda, 1973), animal cells (Zhang *et al.*, 1992) and yeast cells (Kleinig, 1997; Zhang *et al.*, 1999). This theory assumes that the tensions in the wall during the compression are uniform and isotropic as is stated by Cole (1932) and Yoneda (1964). However, Hiramoto (1963) suggested that the circumferential tensions are up to two times greater than the tensions in the meridian direction. This result suggests that the use of the liquid - drop model is not appropriate to determine material properties of the cells being compressed.

The elastic membrane model was developed by Feng and Yang (1973) to model the compression of an inflated, nonlinear elastic, spherical membrane between two parallel surfaces where the internal contents of the cell was taken to be gas. This model was extended by Lardner and Pujara (1980) to represent the contents of the cell as an incompressible liquid. This assumption would obviously make the model more representative of biological cells. Importantly this model also does not assume that the cell wall tensions are isotropic, which as described previously is more appropriate for a cell during compression. The model is based on a choice of constitutive relationships (e.g. linear-elastic, Mooney-Rivlin) which describe the material of the cell wall and governing

equations which link the constitutive equations to the geometry of the cell during compression. In the case of Feng and Yang (1973) the constitutive equations were based on a Mooney – Rivlin model initially used to describe rubber. Other constitutive relationships can also be used, for example Lardner and Pujara (1980) employed a Skalak-Tozeren-Zarda-Chien (STZC) material. These relationships have been used to represent the material properties of red blood cells and sea urchin eggs. In addition to this Cheng (1987a) gives a generalised Hookes law strain energy function which has been used to model the data of Yoneda (1964) and the deformation of suspension tomato cells (Wang *et al.*, 2004). The constitutive relationships found within the elastic membrane model are discussed further in Chapter 5.

The elastic membrane model has been solved by both analytical (Wang *et al.*, 2004) and finite element methods (Cheng, 1987a). The finite element approach has the advantage of being able to take into account irregularities such as non-spherical cells, local and geometric material differences (e.g. bud scars) assuming that detailed information is available about such irregularities. However, it is advisable to validate any finite element model with an appropriate analytical solution. As well as this, all but the most expert of users treats the finite element model as a 'black box' without fully understanding how the model results are generated. In Chapter 5 a number of analytical solutions are fully developed and the effects of different strain definitions examined.

2.4. Concluding remarks

In this Chapter the reasons for investigating the mechanical properties of Baker's yeast cells have been described. The biological construction of the cell wall has been briefly described and some of the major changes that occur during the cell cycle outlined. Much of the literature concerning the yeast cell wall details the structure and composition with only limited attention paid to the mechanical strength. Following this a number of techniques that have been used to measure the material properties of individual cells have been described. The compression testing technique has been described in detail and the models that have been used to extract material properties from force - deformation data outlined. In Chapter 3 the methods that are necessary to investigate the intrinsic material properties of Baker's yeast cells are described.

Chapter Three: Materials and methods

The micromanipulation apparatus and experimental methods are outlined and the methods of data analysis are described.

3.1. Cell suspensions

In order to determine the mechanical properties of yeast cells it was necessary for stable reliable and consistent suspensions of cells to be produced. Furthermore, to perform compression testing by micromanipulation, single spherical cells were required. Previous work has shown that dried Baker's yeast was able to fulfil these criteria (Smith *et al.*, 2000a, Kleinig, 1997).

Dried Baker's yeast (*Saccharomyces cerevisiae*) (Fermipan Red, DSM Bakery Ingredients, Dordrecht, Holland) was suspended in Isoton II solution (Coulter Electronics Ltd, Hertfordshire, UK; details in Table 3.1) at 2 g/l for 24 hrs at 4 ^{o}C to give a reproducible suspension of late stationary phase cells (Kleinig, 1997). Prior to use the suspension of cells was warmed to room temperature and a 1:100 dilution made using the Isoton II solution (Table 3.1) to allow individual cells to be selected for compression experiments.

Components	Concentrations (g/l)
Sodium chloride	7.93
Disodium hydrogen orthophosphate	1.95
EDTA, disodium salt	0.38
Potassium chloride	0.4
Sodium dihydrogen orthophosphate	0.19
Sodium fluoride	0.3

Table 3.1: Components of the Isoton II solution.

3.1.1. Methylene blue viability test

The methylene blue test is a simple cell stain that is used to determine the percentage of a population that is viable. 0.1 ml of the diluted yeast solution was added to 0.9 ml of methylene blue staining solution and agitated for 1 minute. A sample drop of this mixture was viewed under an optical microscope (Leica Microsystems Ltd, Milton Keynes, UK). Non-viable cells were stained dark blue while viable cells remained clear (Figure 3.1).

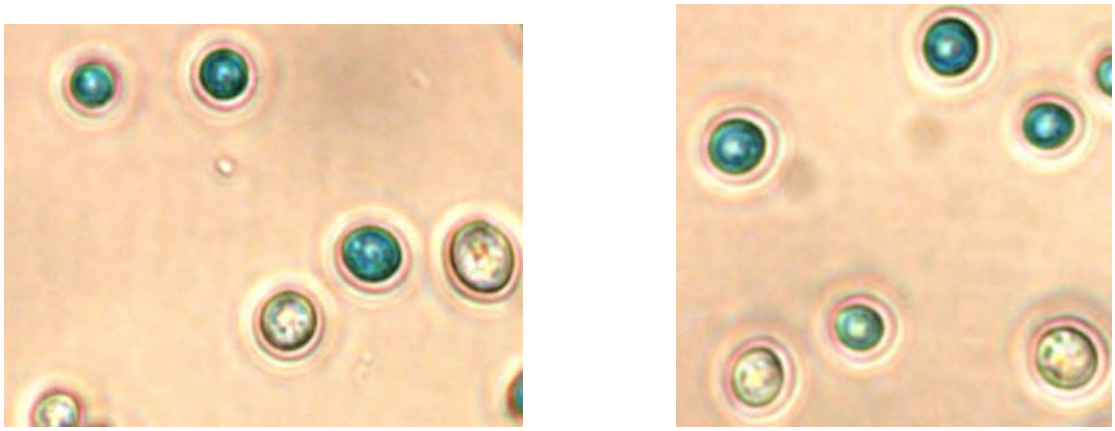

Figure 3.1: Example of yeast cells stained with methylene blue. × 40 magnification

3.2. Introduction to micromanipulation

Micromanipulation has been used to measure the mechanical properties of biological materials with the aim of being able to predict their responses to hydrodynamic stresses and so improve understanding of bioprocesses (Thomas and Zhang, 1998). Since the first practical rig was used in the early 1990's (Zhang *et al.*, 1991), the technique has been under continual evolution. There are three main configurations that have been used to measure the mechanical properties of biological materials, i.e. 'pulling', 'squeezing' and 'stamping'.

The 'pulling' test was designed to test the tensile strength of microorganisms. Filamentous bacteria were attached between two probes (Stocks and Thomas, 2001), one of which was bound to a force transducer (Figure 3.2). A uniaxial strain was then applied to the filamentous bacteria at a fixed rate and the force recorded. From this it was possible to determine the force required to cause breakage.

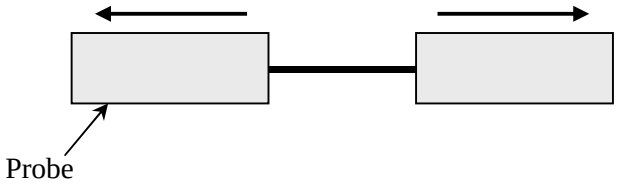

Figure 3.2: Uni-axial strain applied to fungal Hyphae.

The 'squeezing' technique was first used by Zhang *et al.* (1991) to measure the mechanical properties of mammalian cells. In this work a mouse hybridoma TB/C3 cell was captured between two parallel probes which were driven together at 3.9 μms^{-1} to deform the cell (Figure 3.3). One of the probes was attached to a transducer (Section 3.2.1) which was able to measure the force being imposed on the cell and the distance between the two probes

during compression. This allowed the force at which cell failure occurred and the cell diameter to be measured. By modelling the compression data it was possible to extract the membrane tension data, internal pressure and the compressibility modulus of the cell (Zhang *et al.*, 1991; Yoneda, 1964).

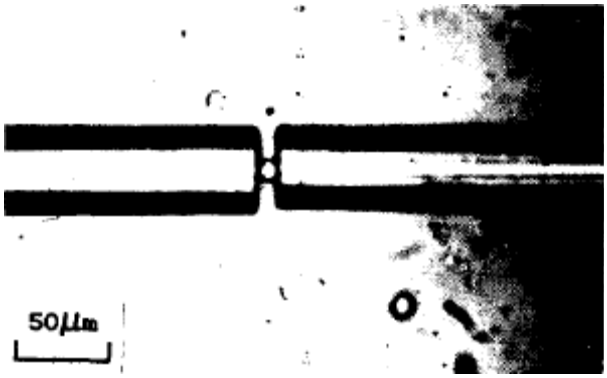

Figure 3.3: Two probes (optic fibres) positioned for squeezing a mouse hybridoma cell (Image taken from Zhang et al., 1991)

The current technique has been described previously as the 'stamping' technique (Mashmoushy *et al.*, 1998; Blewett, 2000) but will be referred to here as compression testing by micromanipulation. In this method an individual cell or particle was compressed between a large flat probe and a glass base usually until rupture (Figure 3.4).

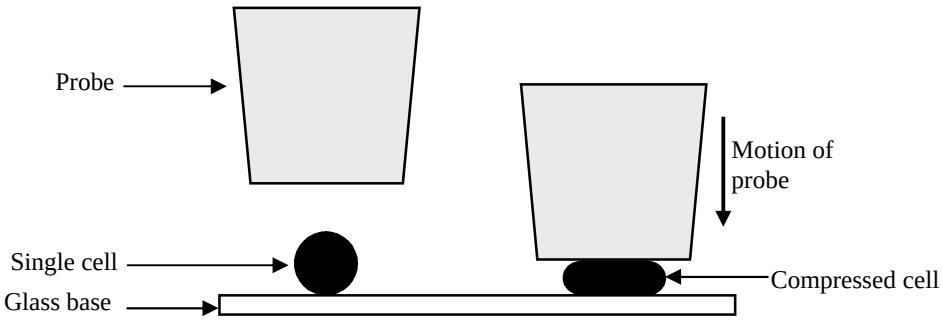

Figure 3.4: Schematic diagram of the compression of an individual cell between a large flat probe and a glass slide (Not to scale).

In the compression testing method a sample was placed on a slide or in a chamber and allowed to settle on the glass base. A flat probe attached to a force transducer was then positioned over the sample and moved down compressing the cell against the glass base. This again leads to force - displacement data being measured from which material properties are calculated. This compression testing method is faster and allows easier manipulation of the cells being compressed than the 'squeezing' technique.

3.2.1. Compression testing by micromanipulation – general description

Many biological systems have been tested using compression testing by micromanipulation. The apparatus in Figure 3.5 has been used to investigate the mechanical properties of tomato cells (Blewett *et al.*, 2000; Wang *et al.*, 2004), bacterial cells (Shui *et al.*, 1999), and yeast cells (Mashmoushy *et al.*, 1998; Smith *et al.*, 2000a).

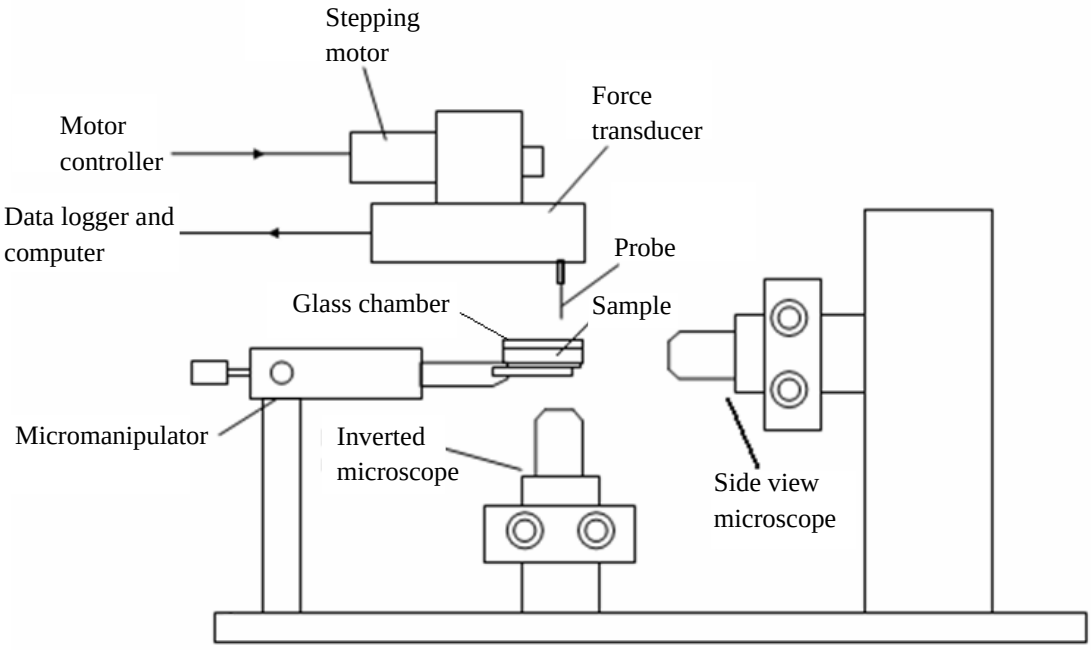

Figure 3.5: Schematic of the Low strain rate compression testing apparatus (LSRT). Modified from Shui (2000).

A sample of the experimental material was placed in the glass chamber or on a glass slide depending on the sample size. The glass chamber was held firmly on a metal stage that was temperature controlled. The inverted microscope with ×20 objective (Leica Imaging Systems Ltd, Cambridge, UK) was used to focus on the cells resting on the base of the slide. This stage was attached to a micromanipulator that allowed fine adjustment in the horizontal plane. The side view microscope with a long working distance objective was then used to focus on the side of an individual cell. This microscope was attached to a micromanipulator which allows fine adjustment in the vertical and the horizontal direction. The images were transmitted by high performance CCD camera (4910 Series, COHU Inc., San Diego, USA) to separate monitors and recorded. This allowed the stage to be manipulated while still observing the target cell from two perpendicular directions. The sample stage was illuminated using fibre optic light sources (MFO – 90, Mircotec fibre optics) to allow the sample to be visualised clearly. An individual cell to be compressed was selected using the inverted microscope and a flat probe (Section 3.2.2) attached to a force transducer (described later) positioned over the cell. This probe was significantly larger than the cell being compressed so that it was in effect of infinite size. For example with yeast cells the probe was about 50 μm in diameter, significantly larger than the approximately 5 μm cell (Mashmoushy *et al.*, 1998; Smith *et al.*, 2000). This was necessary as when the cell was compressed it will extend horizontally and it was important that this expansion did not reach the edge of the probe as this would invalidate any mathematical model that was used to analyse the results.

The probe was attached to the output tube of the force transducer using commercial superglue or paraffin wax. This gave a firm attachment while allowing easy removal and adjustment of the probe position. The probe was lowered until it was close to the cell using

the side view microscope. The inverted microscope was then used to ensure that the cell was positioned in the centre of the probe.

For work with yeast cells and bacteria (Smith *et al.* 2000a; Shui 2000) an optic fibre probe was attached to a series 406A force transducer (Aurora Scientific Inc., Ontario, Canada) which was capable of measuring forces up to 0.5 mN. In contrast, for work with plant cells, a 400A force transducer was used which was able to measure forces up to 50 mN. The choice of transducer depends on the strength of the cells under test.

The force transducer contains two silica cantilever beams, a reference cantilever and a measurement cantilever with an output tube attached to the latter (Appendix 1). The cantilever beams, of identical construction, size and mounting within the transducer, act as capacitors. If no force was applied to the measurement beam then the capacitance of the beams was equal and the output voltage was zero. When a force was applied to the measurement beam it was deflected and the capacitance changed. This new capacitance was compared to that of the reference beam leading to a non-zero result, proportional to the beam deflection and hence the force being applied. The resultant voltage verses time data was recorded by an Amplicon PCI 120 card (Amplicon Liveline Ltd., Brighton, UK). The frequency of voltage measurement and sampling time could be adjusted. Any thermal effects, mechanical vibration or electrostatic interference would affect both cantilever beams and should be cancelled out. However, as the output tube increased the weight of the measurement cantilever this was not exactly the case and mechanical noise was still a problem. Precautions needed to be taken which included performing all experiments on solid air cushioned benches to eliminate unnecessary vibrations.

To convert the raw voltage - time data to force - displacement data (Section 3.2.4) it was necessary to calculate the sensitivity and compliance of the transducer. The Aurora force transducers were able to measure a limited force over the ±10 volt range of the transducer. The bending of the measurement beam was directly correlated to the applied force. The sensitivity of the transducer is the measure of force that is represented by each volt of change in the output. This parameter was checked before every experiment as with increased usage and age of the transducer this value may have changed. The compliance of the transducer is the bending that occurs in the silicon beam during the compression experiment. It was essential to determine the compliance prior to any experimental work. The methods used to calculate these parameters are outlined in Appendix 2 and 3.

The force transducer was attached to a stepping motor (Prior-Martock Ltd, Cambridge, UK) to control the compression of the cell by the probe. The stepping motor worked in conjunction with a control box that was able to specify the distance and speed of compression. The speed of compression was set from the control box in the range of 1 μms^{-1} to 54 μms^{-1} and the distance moved was also set, up to 300000 steps (3600 μm).

When the probe was positioned over the target cell the motor was initiated to move down at a pre-determined speed and for an assigned distance. The downwards movement of the probe compressed the cell, resulting in a voltage time trace being recorded by the force transducer, this was used for further analysis, as described later (Section 3.2.4).

3.2.2. Production of glass probes

One of the major assumptions of the compression testing technique is that the cell is compressed between two parallel and rigid platens of infinite size. There are a number of sources of error that can lead to the bottom surface of the probe not being parallel with the base of the chamber. Firstly the probe may not be mounted vertically on the output tube and also its flat surface may not be perpendicular to the vertical axis of the probe. With large experimental materials, such as animal or plant cells, slight deviations will not have an adverse effect on the results. However, with small particles such as yeast, if the probe surface was not sufficiently parallel with the base, attempts to compress cells would cause them to move from under the probe.

The probe was made from solid borosilicate glass fibre that had initially been heated and stretched until it was approximately 2 mm in diameter. A probe with a flat surface approximately 50 μm in diameter had to be produced from this stretched fibre. Initially the 2 mm glass fibre was placed within a PC-10 Narishige dual stage micropipette puller (Narishige Co Ltd., London, UK), which tapered the glass fibre to a sharp point. This fibre was then placed vertically in a Narishige EG-40 micropipette grinder (Narishige Co Ltd., London, UK) and ground at high speed on successively finer lapping film (3.0 mm, 1 mm and 0.3 μm). The probe was rotated by 90^{o} every hour to prevent any permanent bending of the end of the probe. It took approximately two hours per lapping film to produce a probe that was flat and smooth. While changing lapping films the end of the probe was cleaned with acetone and checked for cracks, other imperfections or permanent bending. Following this process the uniformity and size of the probe was assessed from a number of directions using an optical microscope. Figure 3.6 shows typical examples of probes produced in this

way, both of which are approximately 50 μm in diameter. Probe A is suitably flat and uniform for use with yeast cells. Probe B is sloped upwards on the right side and has debris from grinding attached, making this unacceptable.

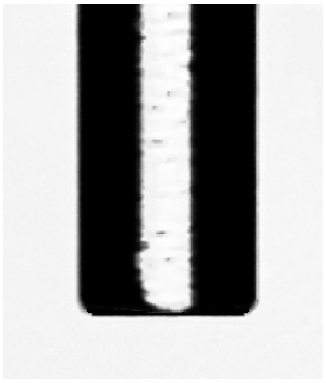

A)

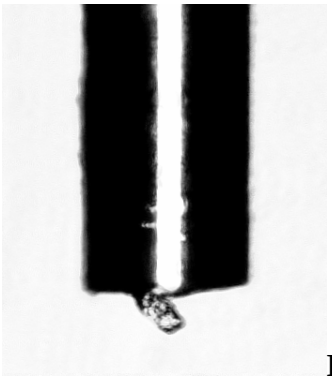

B)

Figure 3.6: Comparison of two different flat ended probes. A) Acceptable flat surface, B) unacceptable end with debris attached.

3.2.3. *Current techniques for use with yeast cells*

This research involved the use of two different micromanipulation rigs, a low strain rate micro-compression tester (LSRT) and a high strain rate micro-compression tester (HSRT) recently described by Wang *et al.* (2005). Both of these were designed and built in conjunction with Micro Instruments Ltd (Oxon, UK) and used compression testing to produce force - deformation data. The principles of the two sets of equipment were very similar to that already described but some important differences are discussed below.

3.2.3.1. Low strain rate micro-compression tester (LSRT)

The compression testing apparatus has undergone significant modification since the initial experiments with yeast cells of Mashmoushy *et al.* (1998), Shrinokutara (2000) and Smith *et al.* (2000a). The inverted microscope has been modified to allow movement in two dimensions in the horizontal plane. This enabled individual cells for compression to be identified more easily.

The most significant changes have been made to the stepping motor and system used to control the motion. The stepping motor and control box (Prior-Martok Ltd., Cambridge, UK) work in conjunction with each other to allow the distance and the speed of compression to be controlled through a PC. The motion of the stepping motor is controlled through HyperTerminal (Hilgrave Inc. Monroe, MI, USA). A full list of control commands is given in Appendix 4. The distance of each step within the motor was initially calculated (Appendix 5) and found to be 0.012 μm. Using this, the maximum reliable speed of compression was found to be 68 μms^{-1}. A detailed method for calculating the speed and results are given in Appendix 6.

About 200 μl of the diluted yeast cell suspension (Section 3.1) was placed within the glass sample chamber (Figure 3.5). A glass probe was attached to a series 403A force transducer (Aurora Scientific Inc., Ontario, Canada) which was capable of measuring forces up to 5mN. For work with yeast cells the voltage output was amplified 10 fold to allow easier data analysis. Approximately 100 cells could be compressed over a period of three hours during which time the temperature of the suspending solution and viability of the cells remained

nearly constant. As before the inverted and side view microscope was used to position the probe over the cell.

Figure 3.7 is an example of the images obtained from the LSRT. The yeast cell in the image was approximately 17 pixels in diameter making accurate measurement of the cell size from this impossible.

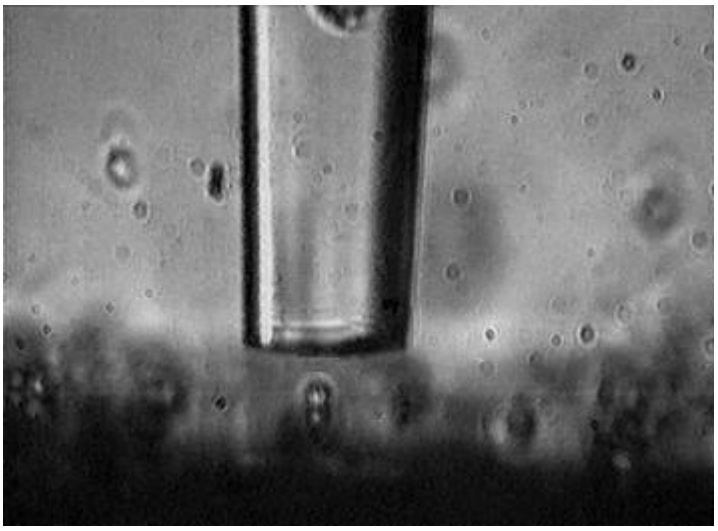

Figure 3.7: Example image of a yeast cell being compressed on the LSRT. In this image the probe is 30 μm in diameter and the yeast cell approximately 5 μm in diameter. (× 350 magnification)

Prior to compression the probe was at least 15 μm above the base of the chamber to prevent problems introduced by motor lag and backlash. Motor lag occurs when the motor is initiated to move and does not respond immediately at the assigned speed. Although the time taken to reach the desired speed was short it could still have had a significant effect on the calculated displacement of the probe. Backlash occurs from looseness within the gearing apparatus of the motor which prevents the motor from returning accurately to the initial position. This leads to errors in the movement of the motor which would have had an effect on the calculated displacement of the probe.

Although the initial gap was necessary to prevent these errors it did in itself lead to a problem with identification of the point at which the probe came into contact with the cell. This could lead to errors in the calculated force-displacement results which will be discussed in Section 3.2.4.

3.2.3.2. High strain rate micro-compression tester (HSRT)

The recently developed HSRT has a very similar operation to the LSRT though is capable of significantly higher compression speeds (Wang *et al.*, 2005). A schematic of the HSRT is shown in Figure 3.8.

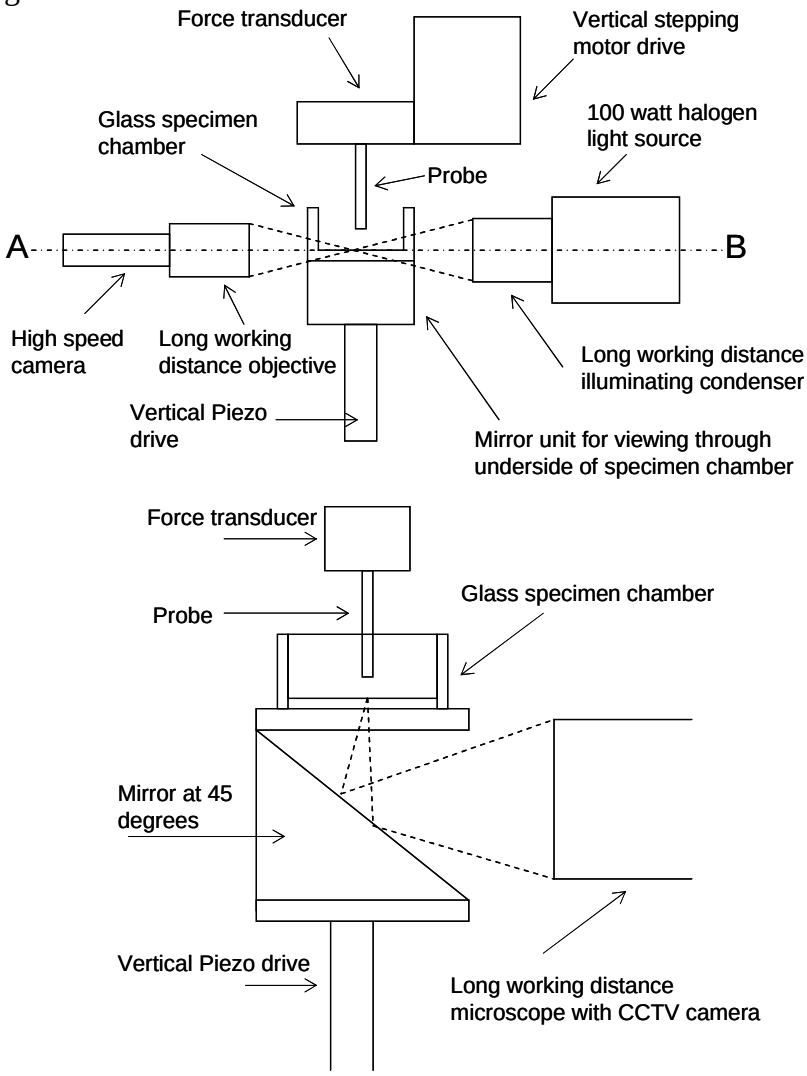

Figure 3.8: Schematic of the high strain rate micro compression tester, (taken from Wang et al. (2005)).

The HSRT was capable of compressing particles using either a stepping motor (Prior-Martok Ltd) or a Piezo-stack (Model P-841.60, Physik Instrumente (PI) GmbH & Co. KG, Germany). The Piezo-stack has been used for compression speeds up to 1000 μms^{-1} although the maximum speed has not yet been determined. The stepping motor in the HSRT is capable of compression speeds up to about 300 μms^{-1}, significantly higher than the LSRT (Appendix 6). The speed of compression could be altered using a Prior control box (Prior-Martok Ltd., Cambridge, UK). The motion of the motor was controlled using Hyperterminal (Hilgrave Inc. Monroe, MI, USA) in a similar manner to the LSRT. All calibrations where performed using the same methods as described for the LSRT (Appendix 5).

Although not shown in the schematic, in a similar manner to the LSRT it is possible to observe the particle using a side view and inverted microscope, both of which can be manipulated in the vertical and horizontal direction. The side view microscope uses a high speed camera (MEMRECAM ci/RX-2, NAC Image Technology Incorporated, Japan) and the inverted microscope uses a Norbain Vista CCTV camera (Norbain SD Ltd, UK) to record the compression images and display them on separate monitors. The side view microscope is mounted and operates in the same way as on the LSRT. The Piezo-stack is fixed to the base of the rig holding the sample chamber in the space occupied by the inverted microscope in the LSRT. This meant a 45^{o} mirror had to be positioned between the sample chamber and the Piezo-stack to allow the sample to be observed from the base using another horizontally mounted microscope. This is described more fully in Wang *et al.* (2005). Illumination is provided by a long working distance illuminating condenser and fibre optic light source. The probes and transducer used with the HSRT are the same as those used with the LSRT.

The HSRT had previously been used only with particles approximately 60 μm in diameter, significantly larger than the 5 μm yeast cells. It proved extremely difficult to visualise the yeast cells. The visualisation problems occurred with the inverted microscope due to the position of the Piezo-stack which restricted the maximum objective to × 4.5 due to a lack of space for a larger lens.

Using the high speed camera with the side view also meant that a lower magnification had to be used. This is because the use of a high speed camera also means that the time to collect light for an image is reduced. In addition, as with any camera, increasing the magnification also requires the light levels to be increased to produce a clear image. However, above magnifications of × 140 it proved impossible for a clear image to be obtained.

All compression testing of yeast cells with the HSRT was performed using the stepping motor at speeds between 61.6 and 308 μms^{-1}.

3.2.4. Interpreting experimental data

Figure 3.9 shows an example of the raw data obtained directly from the compression of a yeast cell using the LSRT. Similar data was obtained using the HSRT.

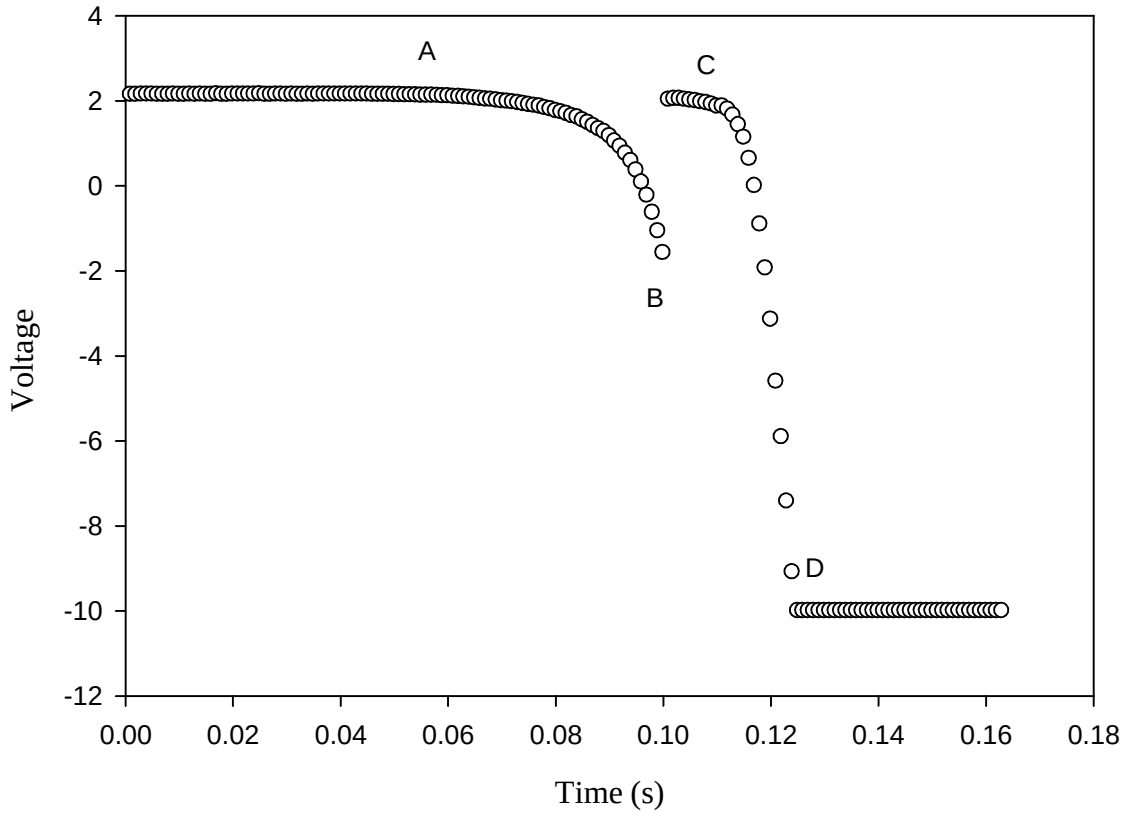

F*igure 3.9: Voltage time output for a typical yeast cell compression using the LSRT at a speed of 68 µms^{-1}. Point A shows the initial contact between the cell and the probe. Cell rupture occurred at point B. The probe contacted the cell debris at point C and compression continued until only the base of the chamber was resisting the probe, point D.*

As previously mentioned it was necessary to calculate the compliance and sensitivity of the transducer being used. For the 403A force transducer used in this work the manufacturer gave a value for sensitivity of 0.5 mNV^{-1}. This value was expected to change with increasing age of the transducer due to permanent deformation of the cantilever beam. As described in Appendix 2 if the relationship between the voltage and the weight deflecting the cantilever beam was not linear then the transducer was not used.

For the 403A force transducer used in this work the manufacturer gave a compliance value of 1 µm mN^{-1}. As the sensitivity changes with increasing transducer age it would be

expected that the compliance would also change. However, it was found that the probe positioning (i.e. vertical on the output tube and flat end parallel with the glass base) had the greatest influence over the compliance and so probably masked this effect.

The point at which the probe contacted with the cell, point A in Figure 3.9, was chosen manually and defined the time of initial contact (t_o) and the baseline voltage (W_o). To find this point, the minimum point before the continued increase in the voltage is chosen as the start of the compression, point A in Figure 3.10.

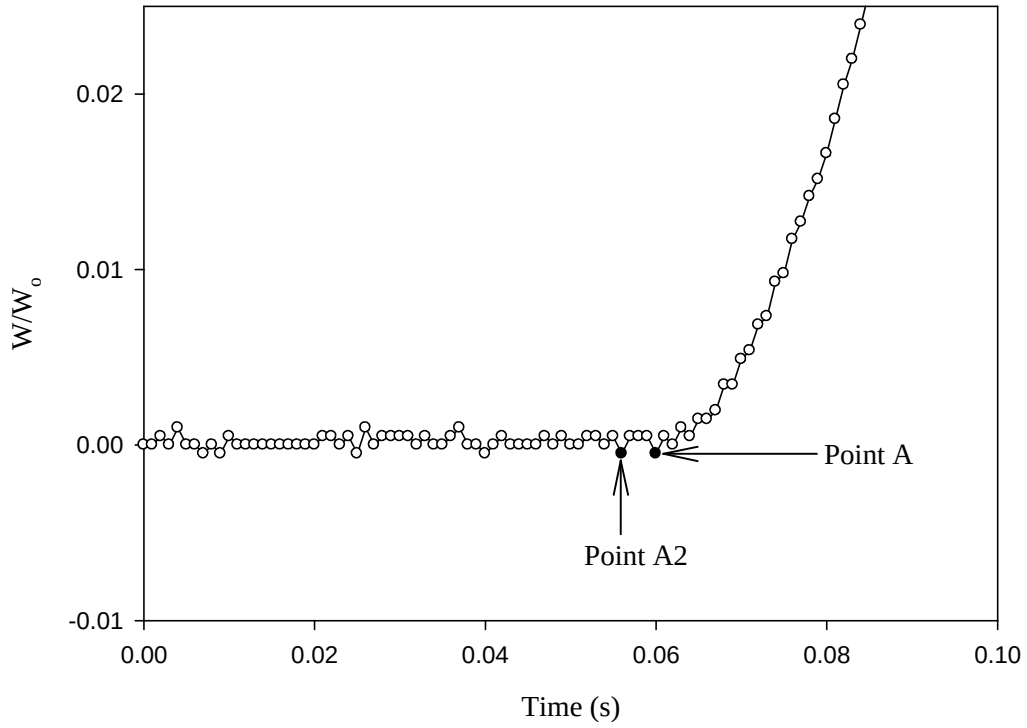

Figure 3.10: Data from Figure 3.9 with voltage converted to W/W_o. Point A is taken from Figure 3.9.

In Figure 3.10 instead of choosing point A as the point of initial contact it was plausible that point A2 might have been chosen. The error in cell size that occurred from choosing this different point will be shown later in this section.

The compressive force acting on the cell at any time was determined from the difference between the output voltage (W) and the baseline voltage (W_o) (equation 3.1).

$$F = K(W_o - W) \quad \ldots (3.1)$$

where K represents the sensitivity of the transducer (mNV^{-1}).

The displacement of the probe was also determined using the voltage time trace. The displacement depended on the speed of compression and the compliance of the silicon transducer beam. The distance the probe moved was calculated from:

$$d = v(t - t_0) - SK(W_o - W) \quad \ldots (3.2)$$

where S is the compliance of the force transducer beam ($\mu m\ mN^{-1}$), v is the speed of compression (μms^{-1}), and t is the sampling time (s^{-1}).

Figure 3.11 shows a typical force - displacement trace obtained from voltage - time compression testing data.

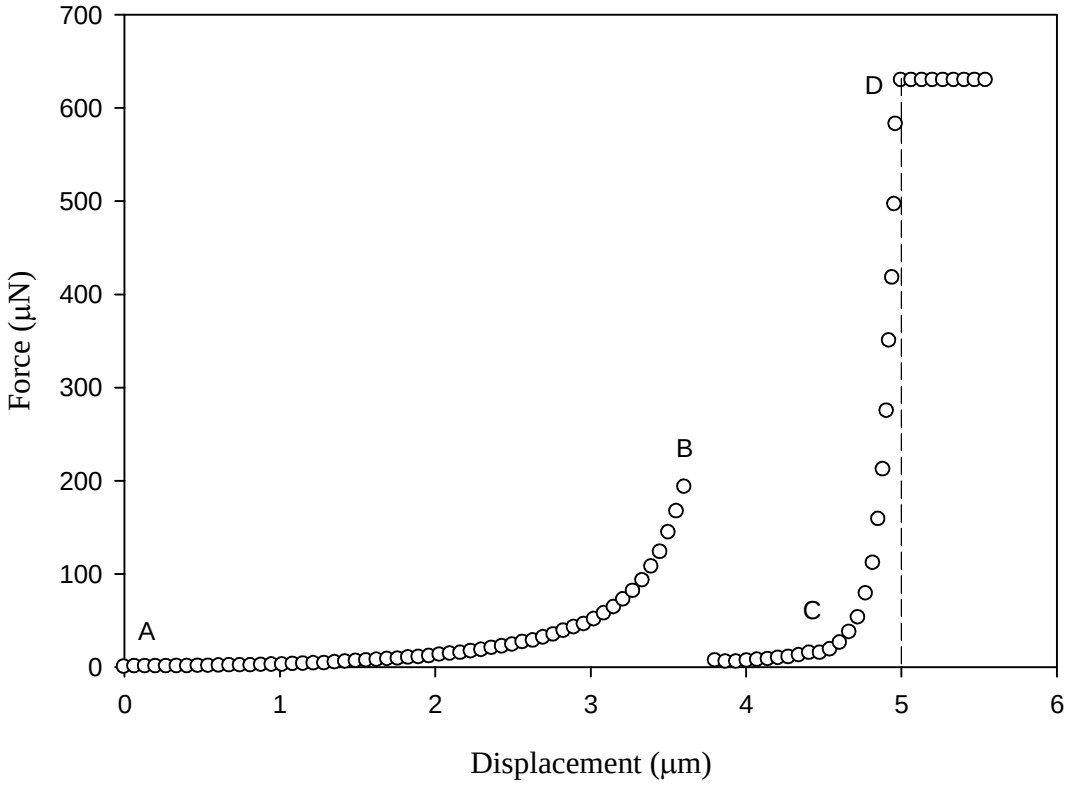

Figure 3.11: Force verses displacement data obtained from the voltage - time trace shown in Figure 3.9 with the same data labels as before. The diameter of the cell was 5 μm, as shown by the dashed line.

The cell diameter (D_i) was calculated as the distance travelled by the probe from the point of initial contact between the probe and the cell (point A) and the contact between the probe and the base of the chamber (Point D). In the example shown in Figure 3.11 the bursting force was at point B, and this distance was found to be 5 μm using point A as the initial contact. If point A2 (Figure 3.10) was taken instead as the point of initial contact then the cell diameter changed by approximately 2 % for this example. In general this change could be up to 3 %. The error associated with cell diameter calculations on the output from

mathematical modelling are discussed later (Section 6.1.3). Once the cell diameter had been found, the force - (fractional) deformation data could be obtained (Figure 3.12). The fractional deformation is a measure of the displacement of the probe (*d*) divided by the cell diameter (D_i). These data show the cell deformation at which cell rupture occurred, here shown to be at a fractional deformation of 0.72, equivalent to 72 % deformation.

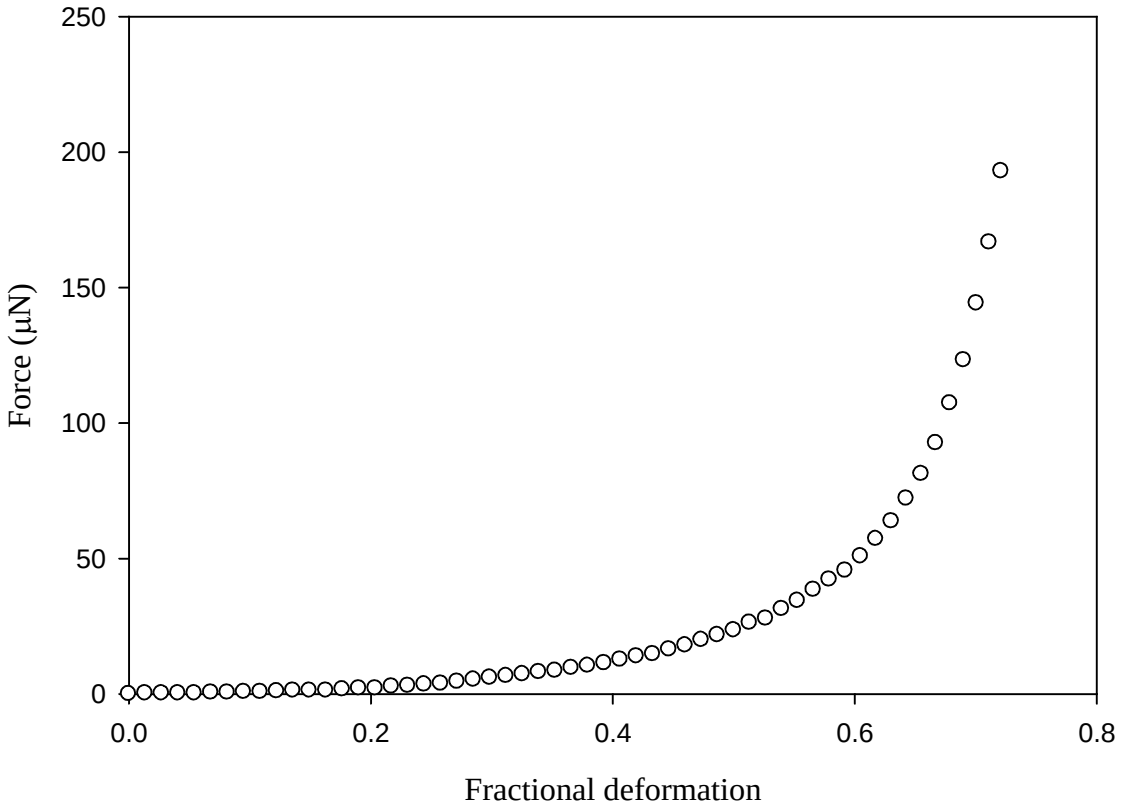

Figure 3.12: Force verses fractional deformation data produced from the voltage time data in Figure 3.9 and using the cell diameter found in Figure 3.11.

Further analysis of the force - deformation data to allow intrinsic material properties of the yeast cell wall to be determined is discussed in detail in Chapter 6.

3.3. Calculation of the initial stretch ratio using osmotic shift methods.

The initial stretch ratio (λ_s) is the difference in the cell radius at some positive turgor pressure to the radius at zero turgor pressure. During growth the internal osmotic pressure of a cell will be higher than the external osmotic pressure. This will have the effect of water flowing into the cell increasing the cell volume. This will cause a stretch in the wall leading to the generation of an internal turgor or hydrostatic pressure. The positive osmotic pressure difference that occurs across the cell boundary controls the turgor pressure and is therefore a function of the osmotic pressure of the suspending medium. If the external osmotic pressure is increased water flows out of the cell decreasing the cell volume and turgor until a new equilibrium is reached. In this work the initial stretch ratio is treated as an adjustable parameter within the mathematical modelling (Section 5.7.3). However, it was still considered desirable to obtain independent measurement of this parameter to ensure any modelling results were reasonable.

3.3.1. Osmotic theory

Many authors have studied the effect of altering the external osmotic pressure on the volume of yeast cells (Martínez de Marañón *et al.*, 1997; Marechal *et al.*, 1995; Berner and Gerbais, 1994; Meikle *et al.*, 1988; Levin, 1979). In addition to this, significant advances have been made in recent years in the understanding of the osmoregulation of yeast cells during changes in the external osmotic pressure (Klipp *et al.*, 2005; D'Haeseleer, 2005; Kapteyn *et al.*, 2001).

The theory outlined here was used by Smith *et al.* (2000a) to obtain information about the initial stretch ratio of yeast cells. Osmotic theory states that at equilibrium the internal and external osmotic pressure differences will balance across the membrane.

$$\Delta P = \Delta \Pi = \left(\Pi_i - \Pi_e \right) \quad \ldots (3.3)$$

where ΔP is the turgor pressure (measured against atmospheric pressure), Π_e is the external osmotic pressure and Π_i is the internal osmotic pressure.

In order to determine the initial stretch ratio of the yeast cell it is necessary to find the point of incipient plasmolysis which occurs when the turgor pressure within the cell is zero. At this point the cell membrane will no longer push against the cell wall causing it to stretch. When the external osmotic pressure is increased further water will flow out of the cell establishing a new equilibrium, lowering the turgor pressure and decreasing the cell diameter. At incipient plasmolysis the internal osmotic pressure will be equal to the external osmotic pressure:

$$\Pi_{e,\Delta P=0} = \Pi_{i,\Delta P=0} \quad \ldots (3.4)$$

When the external pressure is increased further the cell volume (V) will decrease below the volume at which the turgor pressure is abolished (V_o). At external osmotic pressures higher than the point of zero turgor pressure the cell will behave as an ideal osmometer and obey the Boyle van't Hoff relationship (Nobel, 1991 and 1969; Gervais *et al.*, 1996). This means that the cell will shrink in proportion to the increase in the osmotic pressure of the suspending solution.

From this at constant temperature we have:

$$\Pi_i(V-b)=\Pi_{i,\Delta P=0}(V_{\Delta P=0}-b) \quad \ldots (3.5)$$

where *b* is the non - osmotic volume of the cell and *V* is the volume of the cell. The non - osmotic volume includes the total volume of the internal solutes that are not water. Due to this it is sometimes referred to as the non - water volume of the cell. The cell volume (*V*) minus the non - osmotic volume (*b*) gives the volume of internal cell water.

Combining equations 3.3, 3.4 and 3.5 gives:

$$V=\frac{\Pi_{e,\Delta P=0}(V_{\Delta P=0}-b)}{\Delta P+\Pi_e}+b \quad \ldots (3.6)$$

From this relation, the convention in the literature is to plot the volume against the reciprocal of the external osmotic pressure (Smith *et al.*, 2000a; Marechal *et al.*, 1995). It is assumed that a straight-line relationship exists between the cell volume and high external osmotic pressures (Figure 3.13). This is followed by a curved region which presumably asymptotes or at least tends towards a value for Π_e at zero (i.e. the osmotic pressure of water). It is assumed that the transition point between these two regions can be used to determine the volume of the cell at zero turgor pressure (Figure 3.13). The non - osmotic volume (b) is assumed to be at the volume where the straight line relationship intercepts with the volume axis. This relationship is discussed in more detail in Section 7.2.6.2.

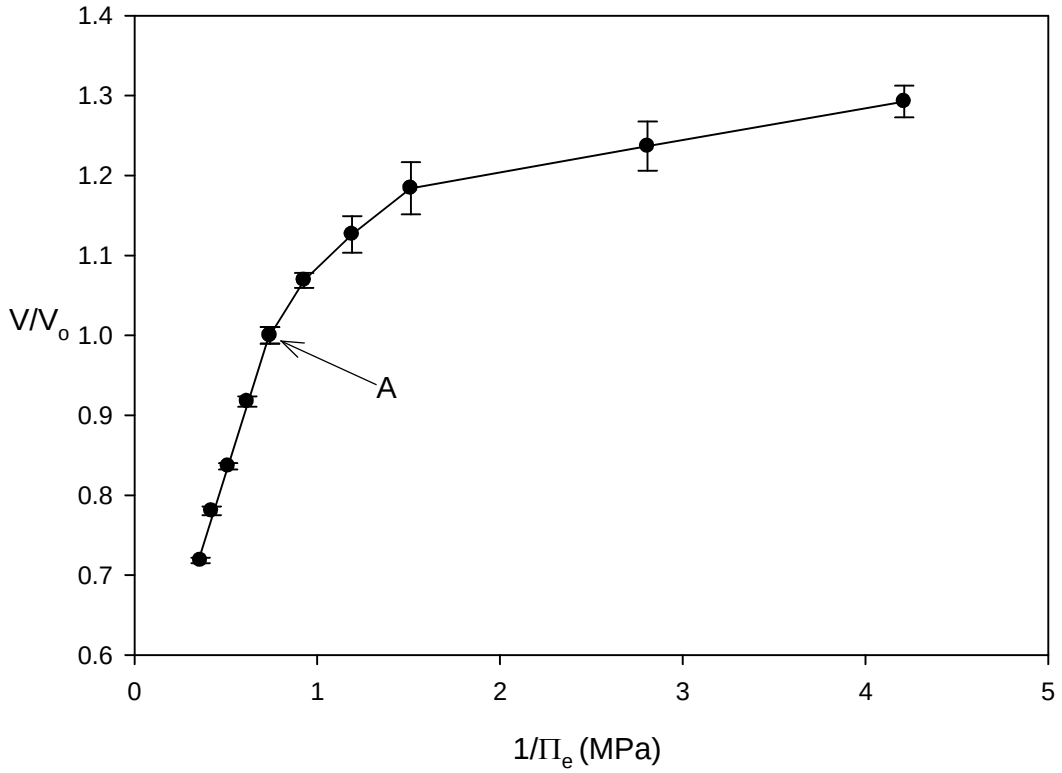

Figure 3.13: Typical plot of the volume verses the reciprocal of the external osmotic pressure. Point A indicates incipient plasmolysis. Error bars are standard deviations.

Figure 3.13 shows a typical plot of the volume against the reciprocal of the external osmotic pressure. This data was produced using the Malvern Mastersizer for a cell population (Section 3.3.3). As can be seen the point of zero turgor pressure, is assumed to be at point A. Having identified the assumed point of zero turgor pressure it is possible to derive a plot of the initial stretch ratio against the external osmotic pressure. This allows an approximation of the mean initial stretch ratio of the cell population to be determined.

The initial stretch ratio of the cell can then be calculated using equation 3.7:

$$\lambda_s = \left(\frac{V}{V_o}\right)^{\frac{1}{3}} \qquad \ldots (3.7)$$

A plot of λ_s against the external osmotic pressure is then produced allowing the λ_s of cells suspended in solutions of known osmotic pressure to be determined. In this work the osmotic pressure of the suspending solution, Isoton II, is 0.8 MPa.

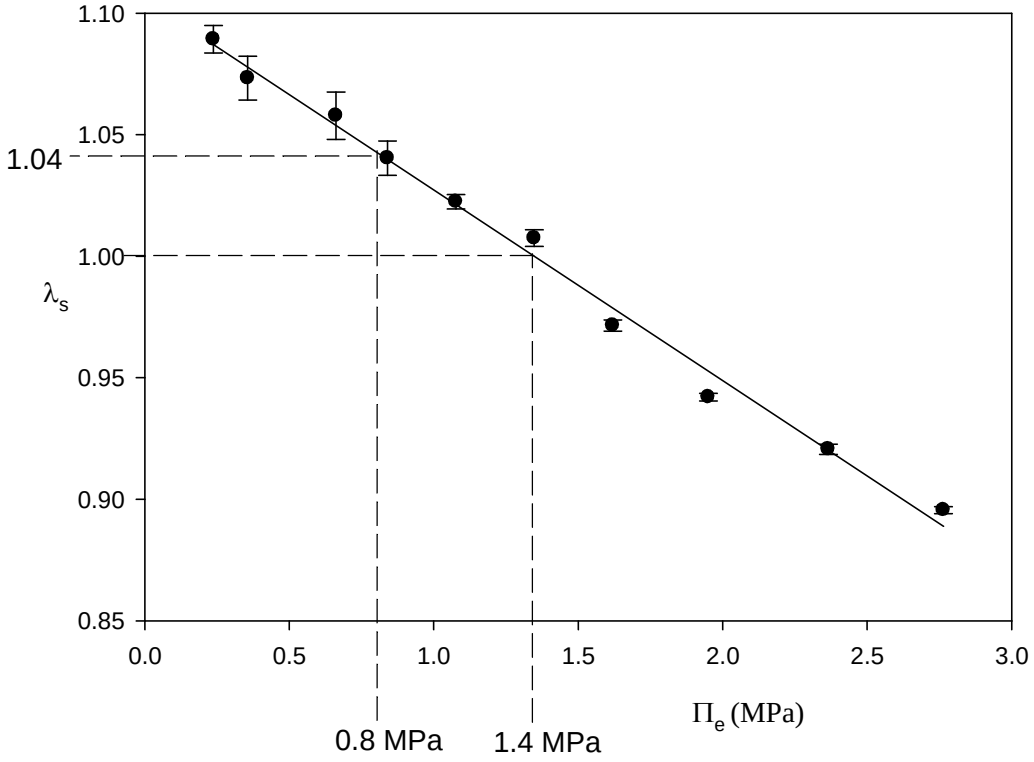

Figure 3.14: Example of the external osmotic pressure against the corresponding initial stretch ratio. As can be seen here at a pressure of 0.8 MPa, that of Isoton II, the initial stretch ratio of the cell population is found to be 1.04 ± 0.007. Zero turgor pressure occurred at 1.4 MPa, point A. Error bars are standard deviations

From Figure 3.14 at an external pressure of 0.8 MPa the initial stretch ratio of the cell population is shown to be 1.040 ± 0.007 and the point of zero turgor pressure occurs at 1.4 MPa. The data shown in Figure 3.14 was produced using the Malvern Mastersizer (Section 3.3.3).

3.3.2. Visualisation chamber – measurement of the initial stretch ratio for individual cells

A visualisation chamber has been developed to analyse the effects of osmotic step increases on yeast cells and the resultant changes in cell volume (Berner and Gervais, 1994). This method involves changing a surrounding isotonic solution for a hypertonic solution, resulting in water loss and cell shrinkage.

Figure 3.15 shows a cross section of the visualisation chamber comprised of an outer Perspex Petri dish and an inner disk made of PVC. The lower petri dish is 90 mm in diameter and 10 mm deep onto which the cells were adhered as described later. The PVC disk is 85 mm in diameter and 15 mm deep with a rectangular chamber milled in the bottom. This chamber is 45 mm in length, 32 mm wide and 0.5 mm deep. Two holes were drilled at the ends of the chamber to allow the inlet and outlet of varying osmotic solutions. Also a large central cavity was milled out that does not fully penetrate the PVC block to allow visualisation of the cells. The thin layer of PVC through which the yeast cells are observed is highly polished using Brasso™.

The yeast cells were observed using a top down Leica Q500 optical imaging microscope with a × 40 objective. The images were recorded by CCD camera and sent directly to a PC where analysis was performed using QWin software (Leica Microsystems Ltd, Milton Keynes, UK).

To determine if the PVC disk was distorting the view of the yeast cells, size calibrations were performed. Firstly the microscope scale was calibrated using a 100 μm graticule. To do

this the number of pixels was measured that corresponded to 1 μm on the image. This graticule was then placed within the chamber and the size calibration performed again. No difference was found in these two techniques indicating that the chamber was not distorting the cell profile.

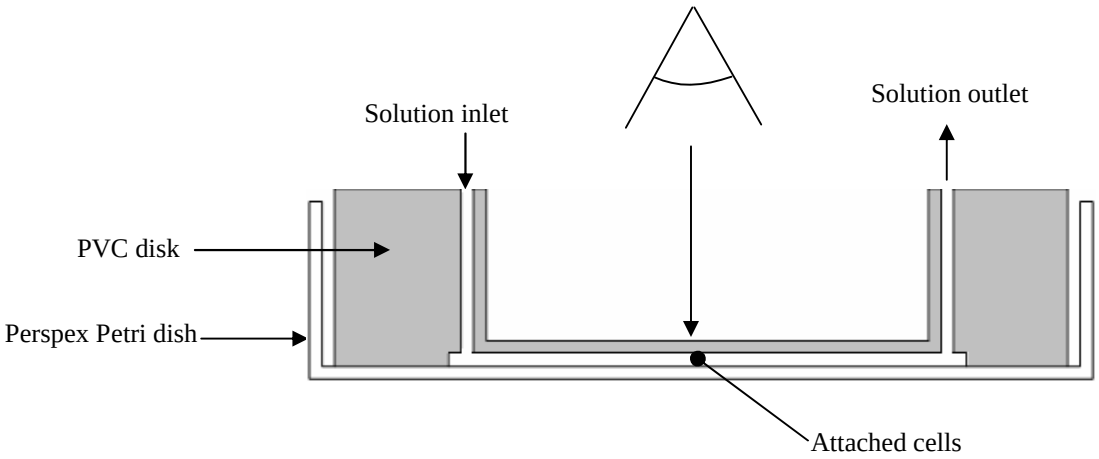

Figure 3.15: Cross section of visualisation chamber (not to scale)

Dried Baker's yeast (Fermipan Red, DSM Bakery Ingredients, Dordrecht, Holland) was suspended for 24 hrs in water at 4^{o}C. Prior to experimentation the suspension was warmed to room temperature.

Cells were fixed to the Petri dish via electrostatic interactions using a solution of chitosan (Sigma-Aldrich, ref: 448869) at 1 g of chitosan per 1 L of water (Champluvier, 1988). Although chitosan can be toxic to yeast cells it has been shown that at this low concentration it does not have a detrimental effect on cells (Berner and Gervais, 1994). The chitosan solution was left in the dish for one hour before being removed and the dish allowed to dry. 60 μl of cell suspension at a concentration of 2 g/litre was then placed in the centre of the chitosan covered Petri dish and left for 45 minutes. Following this the PVC disk was placed in the Petri dish using silicone grease in the contact regions to hold the disk tightly in place. It was possible to focus on approximately 40 cells at any one time using a × 40 objective.

Only this number of cells could be observed at any one time due to the high level of magnification that was required for an accurate measurement of the cell size.

Solutions with osmotic pressures ranging from 0.24 - 9.6 MPa were produced using sodium chloride (Sigma-Aldrich, ref: S5629). The osmotic pressures of the experimental solutions were calculated using osmotic tables (Wolf *et al.*, 1980) and checked directly during experimentation using a vapour pressure osmometer (Wescor 5500 vapour pressure osmometer, Chemlab Scientific Products Ltd, Hornchurch, UK, Appendix 7).

The chamber was firstly filled with the solution of lowest osmotic pressure and an image taken to allow the initial size of the cells to be determined. The solution in the chamber was then changed by injecting a hypertonic solution through the inlet hole and removing the previous solution via the outlet hole. The volume of solution was 10 times that of the chamber. These solutions were left for 1 minute to allow cell volume changes to occur (Berner and Gervais, 1994). An image of the cells was then taken and the process repeated until all of the solutions had been used from low to high osmotic pressure. In total it took approximately 10 minutes to pass a full series of osmotic solutions across the adhered cells. Once this had been done the final salt solution was replaced with the initial solution of lowest osmotic pressure to check if the cell would return to the initial size.

Images obtained using the visualisation chamber were analysed (Qwin Image analyser, Leica Ltd, UK) to obtain the projected area of the yeast cell. Cells which were in contact with each other or moved when the solutions were changed were not measured. From this, assuming the cell was spherical the volume of each cell was calculated using the formula:

$$V = \frac{4\pi}{3}\left(\frac{A}{\pi}\right)^{\frac{3}{2}} \qquad \ldots (3.8)$$

where V is the volume of the cell and A is the projected area of the cell. As well as measuring the volume changes that occurred, the circularity of each cell was measured at different external osmotic pressures using:

$$C = \frac{P^2}{4\pi A \times 1.064} \quad \ldots (3.9)$$

where C is the circularity, P is the cell perimeter, A is the area and 1.064 is a factor used to correct for digitisation of the image (Qwin Image analyser, Leica Ltd, UK). As long as the circularity was lower than 1.08 the cell was considered sufficiently spherical to calculate the volume using the sphericity assumption.

3.3.3. Whole population measurement of initial stretch ratio (λ_s)

A suspension of Baker's yeast cells (Fermipan Red, DSM Bakery Ingredients, Dordrecht, Holland) was produced as before at 2 g/l for 24 hours at 6 ^{o}C in water. This suspension was warmed to room temperature before use.

To measure the change in cell size 1.5 ml of suspension was added into the mixing chamber of a Malvern Mastersizer S particle-sizer (20 % obscurance) with 50 ml of water. Mild stirring conditions were used within the chamber and it was important to ensure that no bubbles were present as these would disrupt the measurements. To this suspension known amounts of sodium chloride solution were added to increase the osmotic pressure of the suspending solution. 1 minute was allowed for changes in cell volume to occur before measurements were taken (4-6 repeats). After the addition of each volume of sodium chloride a sample of the suspending solution was analysed with a vapour pressure

osmometer and the osmotic pressure of the suspending solution determined as before (Section 3.3.2). The results presented in Figure 3.13 and 3.14 were produced using this method.

3.4. Sonication and dithiothreitol (DTT) treatment

This section describes the methods used to disrupt cells via mechanical and chemical methods. Also the techniques that were necessary to determine the level of disruption are described.

3.4.1. Sonication of yeast cells

To mechanically damage cells without causing full cell rupture the method of sonication was chosen. Sonication was able to cause cell damage and disruption mainly by the process of cavitation. It has previously been shown that by adjusting the intensity of the sonication and treatment times the level of cell damage or disruption can be controlled and measured (Ruiz *et al.*, 1999).

0.5 % dry cell weight Baker's yeast (Fermipan Red) was suspended in 40 ml of phosphate buffer (pH 7.0). This suspension was placed in an ice bath to control any temperature increases caused by sonication. The sonication probe (Status US70, Philip Harris scientific, UK) was initiated and suspensions were treated for 75 minutes with 1 ml samples being taken at regular intervals for analysis. Samples were separated by micro centrifuge (Sanyo, Micro centaur) with the supernatant being kept for analysis and the cell pellet being suspended in Isoton II for compression testing.

3.4.2. *Dithiothreitol (DTT) treatment*

DTT ($C_4H_{10}O_2S_2$) is a strong reducing agent that is able to quantitatively disrupt the disulphide bonds of proteins.

0.5 % dry cell weight Baker's yeast (Fermipan Red) was suspended in phosphate buffer (pH 7.0). 20 mM DTT stock solution was produced by addition of 0.03 grams of DTT to 10 ml of phosphate buffer (pH 7.0). 0.75 ml of the DTT stock solution was added to 0.75 ml of the yeast suspension and agitated gently for 1 hour. Following this the suspension was separated by micro centrifugation at 5,000 g for 10 minutes and the supernatant kept for enzymic analysis (Section 3.4.3). The yeast cell pellet was washed 5 times with Isoton II and kept at 4 ^{o}C for approximately 2 hours before compression testing was performed.

3.4.3. Determination of the extent of cell disruption by enzyme/protein release from cells

In order to determine the extent of the disruption of the cells by mechanical and chemical methods the release of enzymes from different locations within the cell was examined. These locations include the periplasm of the cell wall, indicating partial cell disruption and the cytoplasm indicating total cell disruption. The comprehensive methods for each of these analysis techniques is outlined in detail in Appendix 8. The enzyme methods used in this work have been used previously to analyse the disruption of yeast cells by cavitation and high pressure homogenisation (Balasundaram and Harrison, 2006).

3.4.3.1. α - Glucosidase (periplasmic space)

α - Glucosidases are debranching enzymes that are capable of breaking down complex carbohydrates, such as starch and glycogen. This enzyme is located in the periplasmic space of the yeast cell.

α-Glucosidase is capable of catalysing the hydrolysis of terminal non reducing 1,4-linked α-D-glucosides to form α-D-glucose. The activity of this enzyme is measured by the release of p-nitrophenol from p-nitrophenol-α-D-glucoside (Balasundaram and Harrison, 2006). The enzyme activity is defined as the amount of enzyme that produces 1 mole of p-nitrophenol in one minute. To measure the level of enzyme activity the spectrophotometer changes at 410 nm were measured. A calibration curve was produced using different known concentrations of p-nitrophenol (Appendix 8).

3.4.3.2. Alcohol dehydrogenase (ADH, cytoplasmic)

In yeast cells alcohol dehydrogenase catalyses the reduction of acetaldehyde to ethanol *in vivo* in yeast. ADH is located in the cytoplasm of the cell. During alcoholic fermentations pyruvate, resulting from glycolysis, is converted into ethanol using pyruvate decarboxylase and alcohol dehydrogenase. The estimation of the levels of ADH released from cells is based on the principle of conversion of ethanol to acetaldehyde by using the stoichiometric consumption of NAD^+.

$$\text{Ethanol} + NAD^+ \longleftrightarrow \text{Acetaldehyde} + NADH + H^+$$

The rate of formation of NADH is used as a measure of enzyme activity. One unit of enzyme activity is defined as the amount that causes a change in the optical density of 0.001 per minute in 0.06 M sodium pyrophosphate at pH 8.5. The amount of enzyme present is measured using a spectrophotometer at an absorbance of 340 nm.

3.4.3.3. Invertase (cell wall associated)

Invertase is a sucrase enzyme that hydrolyses sucrose to glucose and fructose. Invertase is associated with the yeast cell wall. The amount of invertase can be estimated from the level of sucrose that is converted to fructose and glucose.

A dinitrosalicylic acid reagent (DNSA) is used to determine the reducing properties of the sugars produced by this process (Gascon *et al.*, 1968). DNSA reacts with the free carbonyl groups of reducing sugars which reduces 3,5-dinitrosalicyclic acid to 3-amino 5-nitrosalicylci acid. This reaction produces an orange/red colour that adsorbs light strongly at 540 nm using a spectrophotometer.

One mole of sucrose leads to the formation of one mole of fructose and one mole of glucose. From this two moles of DNSA are required to react with one mole of sucrose. A calibration curve was produced using a glucose standard. The calibration curve (Appendix 8) was used to estimate the number of moles of sucrose that are hydrolysed and so the activity of the Invertase. One unit of invertase is defined as the amount of enzyme, which hydrolyses 1 micromole of sucrose in one minute at 55 ^{o}C in sodium acetate buffer of pH 5.5.

3.4.3.4. Protein release (Bradford method)

The Bradford Protein Assay is a spectroscopic analytical procedure used to measure the concentration of proteins in a solution. The assay is based on the absorbance of the dye Commassie which exists in two forms, unbound red which shifts to blue when binding with proteins occurs. When in the presence of proteins the red Coomassie dye will donate its free proton to an ionisable group located on the protein. This will cause the hydrophobic regions of the protein to be exposed due to the changes in shape of the protein. These regions are then able to bind to the non polar region on the dye via van der Waals forces and ionic interactions. The binding of the protein stabilises the blue form of the Coomassie dye and the greater the level of protein in the solution the greater the level of binding that will occur. The bound dye has a maximum adsorption spectrum at 595 nm and the increased levels of absorption are proportional to the amount of protein that is present in solution. This protein analysis method usually requires a suitable dilution of the protein sample as the result is only linear at low concentrations of protein. To determine the levels of protein a bovine serum albumin (BSA) standard is used.

3.5. Cell wall thickness determination using TEM

The transmission electron microscope (TEM) used in this work is located in the Centre for Electron Microscopy (University of Birmingham). The preparation work was carried out by Paul Stanley (electron microscopy technician).

This technique has previously been used by Smith *et al.* (2000a) and Srinorakutara (1997) to measure the cell size and cell wall thickness. A sample of yeast was suspended in 500 µl of

2.5 % glutaraldehyde primary fixative solution and this was briefly vortexed and allowed to stand at room temperature for 2 hours. Following this, secondary fixation with 1 % osmium tetroxide was carried out followed by multiple dehydration steps with ethanol and then propylene oxide and resin embedding under vacuum. The embedded cells were then sectioned and stained to allow visualisation of the cells using a Jeol 1200 EX TEMSCAN (Jeol UK Ltd, Welwyn Garden City, UK). Images were taken at magnifications ranging from ×6,000 to ×50,000. The images were analysed using Qwin (Leica Microsystems Ltd, Milton Keynes, UK). An example of the images obtained is shown in Figure 3.16. The dark layer on the outside of the cell wall occurs due to the staining process used in the preparation of the samples. TEM sectioning cuts the cells at a random distance from their equator. This means that the radii and thickness of the wall measured from TEM images will be functions of this random distance. To correct for the random angle at which cells are cut a mathematical analysis is required (Appendix 9).

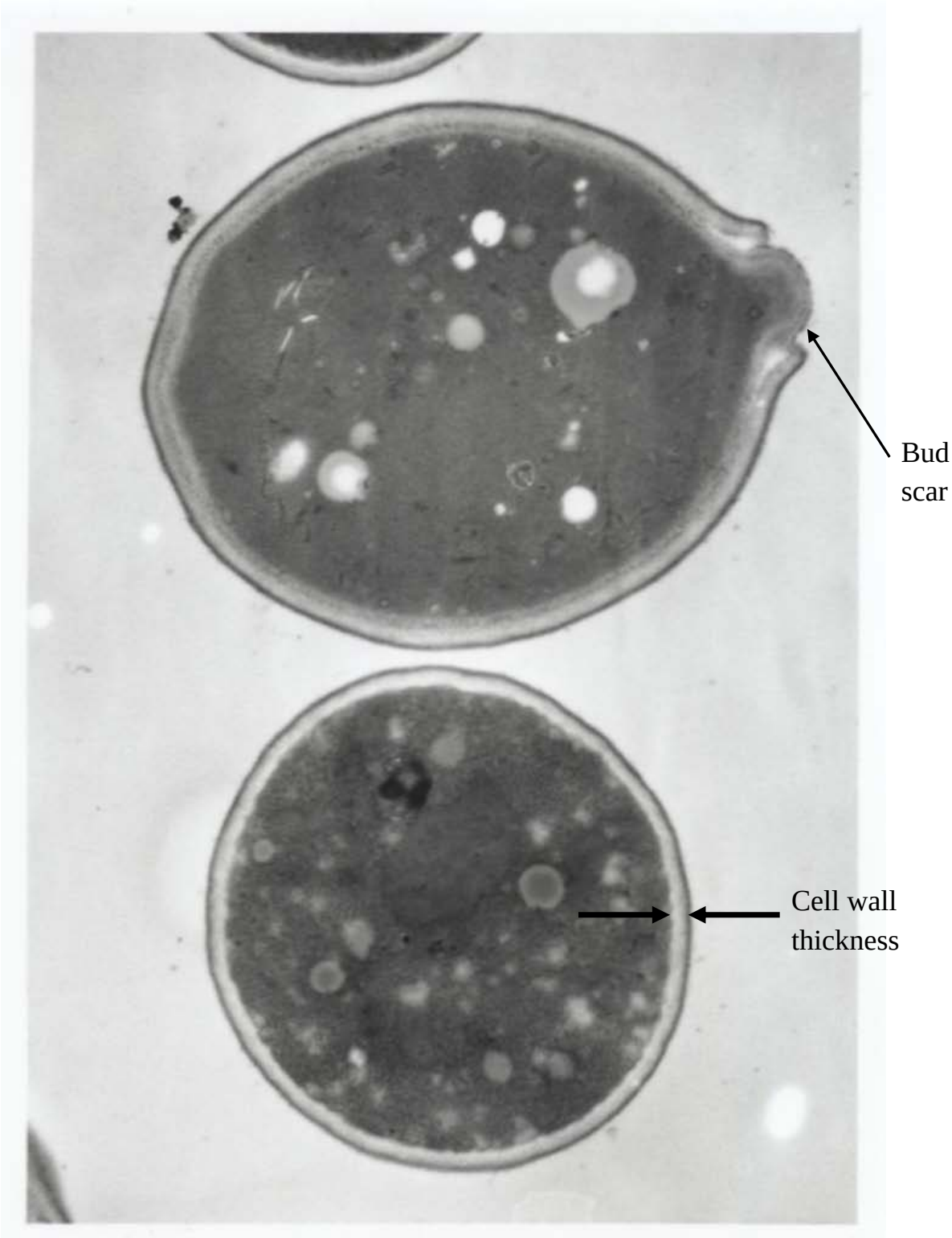

Figure 3.16: Example of the images from TEM. × 10000 magnification

3.6. Concluding remarks

In this Chapter the methodologies necessary to investigate the mechanical properties of yeast cells have been described. The compression testing by micromanipulation technique performed with yeast cells has been detailed. The techniques independent of micromanipulation used to verify the data produced have been outlined and the methods of analysis described.

In Chapter 4 force - deformation data produced from Baker's yeast cells at a range of compression speeds using the compression testing by micromanipulation technique are presented. From this the force at failure and deformation at failure were determined.

Chapter Four: Compression testing data

In Chapter 3 the methods necessary to compress yeast cells and obtain cell force - displacement measurements were described. The results presented in this section relate to the data obtained directly from the compression data (i.e. the cell diameter, the force and deformation at cell failure) and were not derived using a mathematical model (the latter is described later in Chapter 5). To obtain this data the yeast cells were compressed with either the low strain rate (LSRT) or the high strain rate (HSRT) compression testers (Section 3.2.3).

4.1. Control experiments

4.1.1. Cell population viability

It was found that more than 95 % of the cells being compressed burst (point B in Section 3.2.4, Figure 3.11). It was assumed that cells which did not show such a burst were non viable. Confirmation of the bursting process could be observed by the spilling out of the cell contents in to the surrounding medium. Unfortunately due to the poor visualisation of the cells in the compression testers it is not possible to produce a clear image of this. The viability of the cell population was also determined by methylene blue staining (Section 3.1.1). By this method the viability of the population was also found to be more than 95 % (see Figure 3.1 for examples of stained non viable cells and, un-stained, viable cells). This

result confirmed that a bursting event on a force - displacement curve can be considered an indication of the viability of the cell under test.

4.1.2. Stability of dried Baker's yeast

It was important to investigate the stability of the dried Baker's yeast stock. A test was performed on the stability of a re - suspended yeast sample over a few hours, the time of an individual experiment. Tests were also performed on the stability of the dried Baker's yeast stock when re - suspended and tested over a number of months.

One of the major drawbacks of compression testing by micromanipulation is the time it takes for the required number of cells to be compressed. In this work cells were compressed over a large range of speeds between 8 μms^{-1} and 308 μms^{-1}. For speeds higher than 68 μms^{-1} it was necessary to use the HSRT. It took approximately 3 hours to compress 100 cells at 308 μms^{-1}, with this time increasing to about 4 hours for a compression at 8 μms^{-1}. This occurred due to an increase in the time it took for the data acquisition program (Amplicon Liveline Ltd, Section 3.2.1) to output the voltage - time data into Microsoft Excel at the slower speed. No change was observed in the frequency of non - bursting events (Section 4.1.5) at the slower speeds. In all cases no relationship was found between the order in which the cells were compressed and the force measurements. This suggests that the mechanical properties of the cells were not significantly altering over the course of an individual experiment. Typical examples of the data by order of compression are shown in Figures 4.1 a) to 4.1 c) for cells which were compressed at 68 μms^{-1}. Similar results were obtained at other speeds (data not shown).

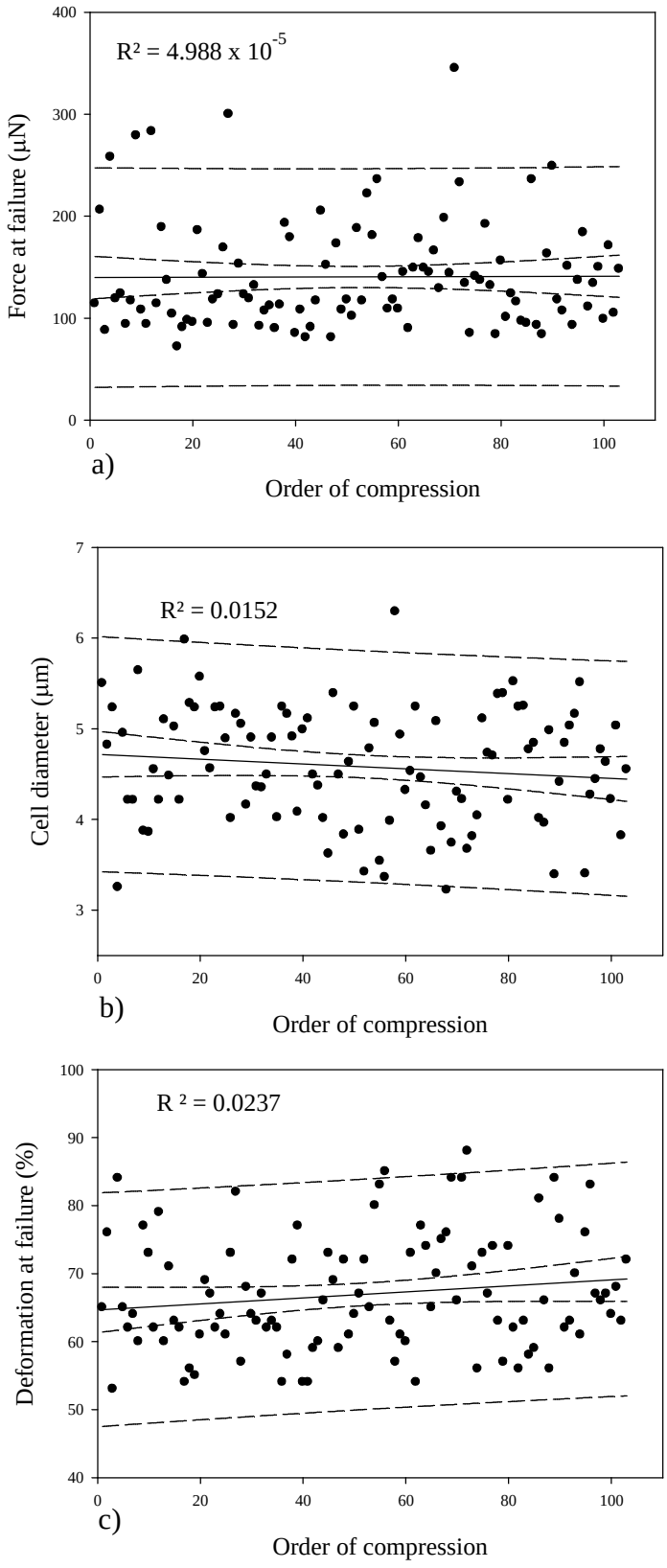

Figure 4.1a), b), and c): Effect of order of compression on the cell diameter, force and deformation at failure. Data shown here for cells compressed at 68 µms^{-1}, but these are typical results for all compression speeds.

The stability of the dry stock over a long period of time was also determined. Suspensions of Baker's yeast were produced from the same dry stock over a period of 18 months and were compressed at 68 μms^{-1}. It was found that the mean force and mean deformation at failure did not significantly change over this time period (Table 4.1).

	Mean force at failure (μN)	Mean deformation at failure (%)
Results at 0 months	138 ± 11	67 ± 2
Results at 18 months	131 ± 9	66 ± 2

Table 4.1: Comparison of the mean force at failure and mean deformation at failure when cells were compressed after an interval of 18 months. Errors are 95 % confidence limits.

As well as determining the effect of the order of compression it was also important to determine if the temperature of the suspending solution had an effect. This was important as significant levels of illumination were required to see the cells in the compression testing equipment. This high level of illumination could have led to an increase in the temperature of the suspending solution in the chamber over prolonged periods of time. The temperature in the chamber was found to be 25 ^{o}C and changed by a maximum of 1 ^{o}C between experiments. To ensure that these minor temperature changes did not influence the results a population of cells were compressed at a high temperature of 35 ^{o}C.

The effect of a change of temperature from 25 ^{o}C to 35 ^{o}C on the mean force and mean deformation at failure obtained was not significant (Table 4.2).

	Mean force at failure (μN)	Mean deformation at failure (%)
Cells compressed at 25 ^{o}C	138 ± 11	67 ± 2
Cells compressed at 35 ^{o}C	133 ± 10	68 ± 2

Table 4.2: Comparison of the mean force at failure and mean deformation at failure when cells were compressed at 25 ^{o}C and 35 ^{o}C. Errors are 95 % confidence limits.

4.1.3. Effect of speed on force - deformation data

The sizes of individual cells were measured from the compression testing experiment (Section 3.2.4) and were essential for fitting the numerical simulations (Chapter 6). It was found that there was no significant difference in the mean cell size obtained at different compression speeds. The collated mean of the cell diameter from all compression speeds was found to be 4.8 ± 0.05 μm. In order to confirm that the cell diameter measured by compression testing was reasonable the cell size was measured using a different technique. Figure 4.2 is a comparison of the cell sizes measured using a Malvern Mastersizer (Section 3.3.3) and the collated data from all compression speeds.

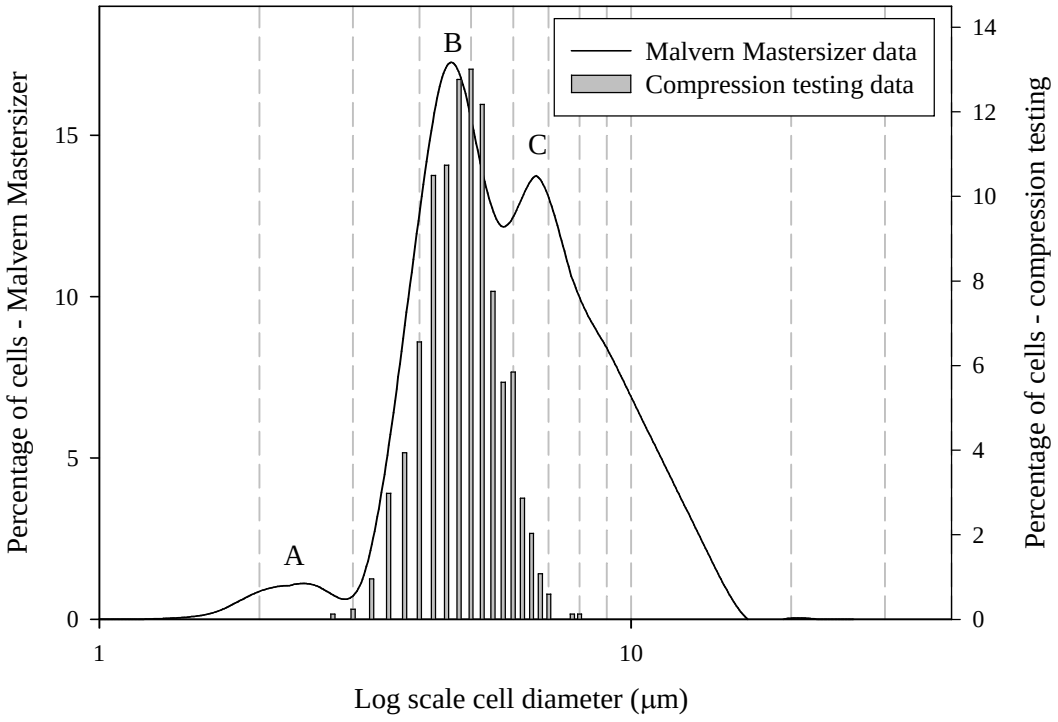

Figure 4.2: Cell size comparison of cell diameters measured using the Malvern Mastersizer (10000 measurements) and the collated compression testing data at all speeds (total of 1000 measurements). Cell diameter presented on a log scale.

From the Malvern mastersizer three distinct peaks in cell diameter were found, shown in Figure 4.2. Cell debris is believed to be represented by peak A. Individual cells are assumed to produce peak B with aggregates of cells producing peak C and the tail up to a diameter of about 18 μm. These assumptions are supported by the collated cell size data from compression testing which is normally distributed and positioned only under peak B.

Using compression testing the collated mean cell diameter was found to be 4.8 ± 0.05 μm. This is in comparison to the Malvern Mastersizer where peak B was also found to be at 4.8 μm. Assuming peak B does represent individual cells, the Mastersizer data confirm that the method used in compression testing to determine the cell size led to reasonable values.

In later work it was assumed that the cell sizes from compression testing were appropriate sizes for data analysis.

As well as this, the mean force and deformation at cell wall failure were obtained directly from experimental data for each compression speed. A collated mean deformation at failure of 68 ± 1 % and a mean force at failure of 138 ± 5 μN was found (errors are 95 % confidence limits). No trends in the mean force or mean deformation at failure over the compression speeds were found as shown in Figure 4.3 a) and 4.3 b).

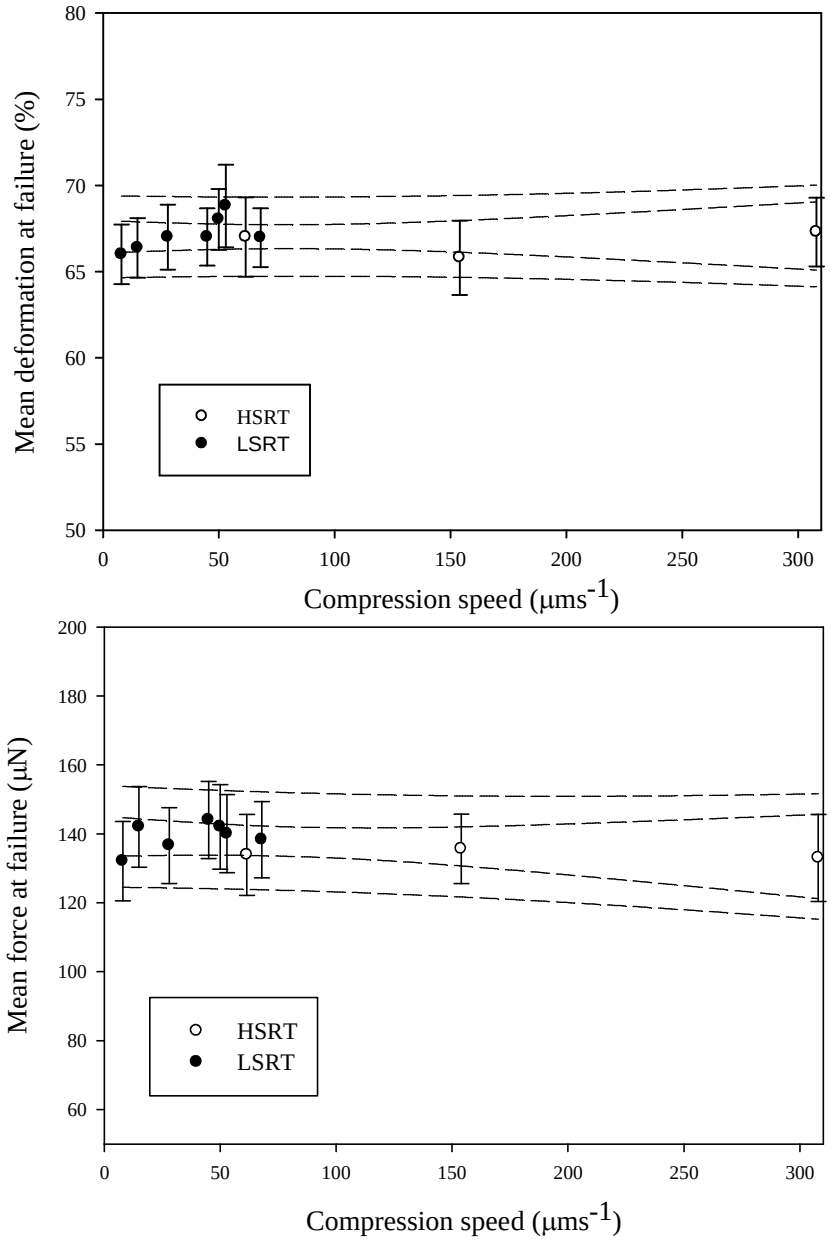

Figure 4.3 a) and 4.3 b): Relationships between compression speed and the mean deformation and mean force at failure respectively. Dashed lines represent the 95 % confidence levels for the mean and individual observations. Approximately 100 cells were measured at each compression speed.

4.1.4. Repeat compression

In order to determine whether an elastic cell wall model (developed in Chapter 5) was appropriate for use with yeast cells it was important to investigate the behaviour of the cell during compression. Previously it has been shown that it is possible to fit a model based on a linear elastic cell wall to yeast compression testing data (Smith *et al.,* 2000b). However, at the very high deformations used in this work it is possible that there was some plastic behaviour (i.e. irreversible deformation) within the wall. For example, tomato cell walls are believed to be elastic- plastic because above a deformation of 15% permanent deformation occurred (Wang *et al.,* 2006). Therefore, it was desirable to have some additional information, independent of the numerical simulations, confirming the linear elastic behaviour of the cell wall.

Ideally, a hysteresis trial would have been done, i.e. a compression - release experiment tracking the force in both directions. However, there was a significant time delay of approximately half a second whilst the compression tester reversed direction. As described later, this delay allowed sufficient water loss to occur to render the experiment invalid.

To show this an example of the data from a hysteresis experiment is shown in Figure 4.4. These data were obtained at a compression speed of 68 μms^{-1}, a speed at which it was assumed water loss during compression can be considered negligible. The reasons for this choice of compression speed and justification for the water loss assumption is described in detail later (Section 7.1).

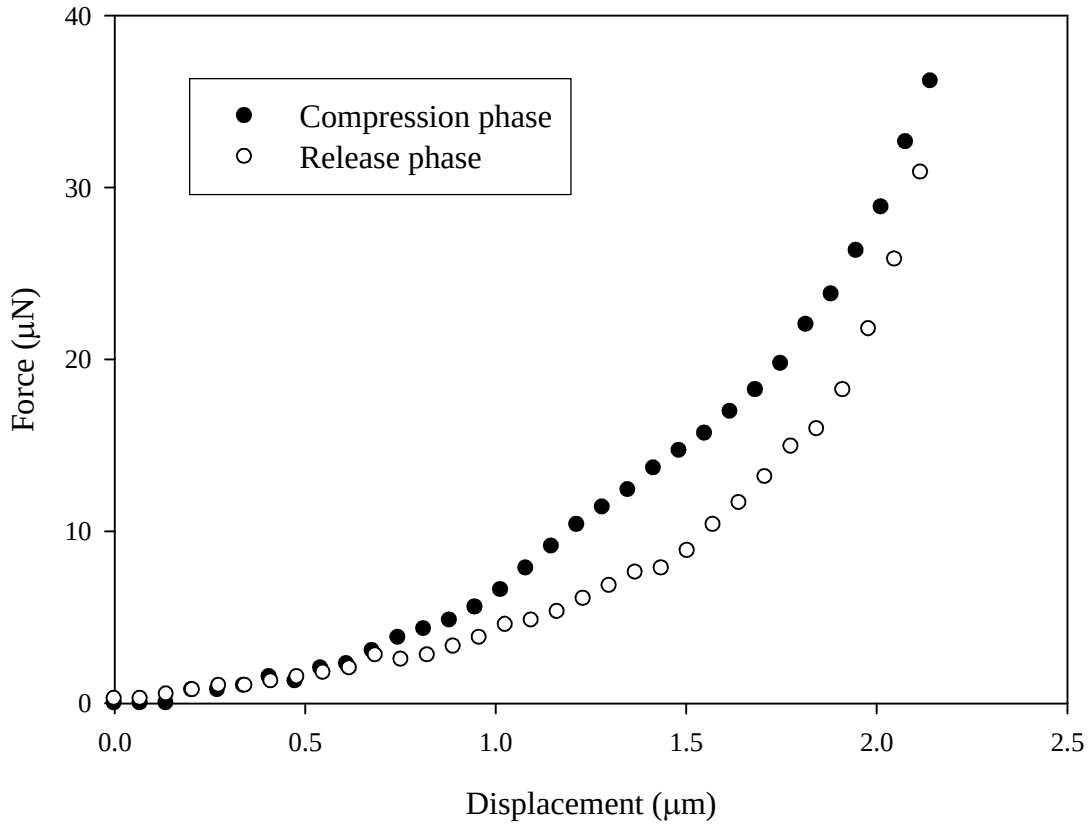

Figure 4.4: Example of data obtained from a hysteresis experiment. Data obtained using the LSRT at a compression speed of 68 μms^{-1}. Data recorded whilst the motor reversed direction has been omitted. Cell size = 4.1 μm, maximum deformation = 53 %, maximum force = 37 μN

The data recorded whilst the motor changed direction is not presented for clarity. It can be seen that the force decreased significantly from the value at the end of the compression phase to the value at the start of the release phase. As the internal contents of the yeast cell might be considered incompressible, even a small release of internal contents would lead to a significant decrease in the force. As yeast cells are small it was not possible to confirm this volume loss visually.

Due to the problems found with the hysteresis trial it was decided to compress and release a cell repeatedly (to a high deformation not causing failure i.e. 60%). Signs of hysteresis and\or permanent deformation were sought.

Figure 4.5 shows experimental data for the repeated compression and release of a typical cell. The "first compression" data are the same as those for the compression shown in Figure 4.4.

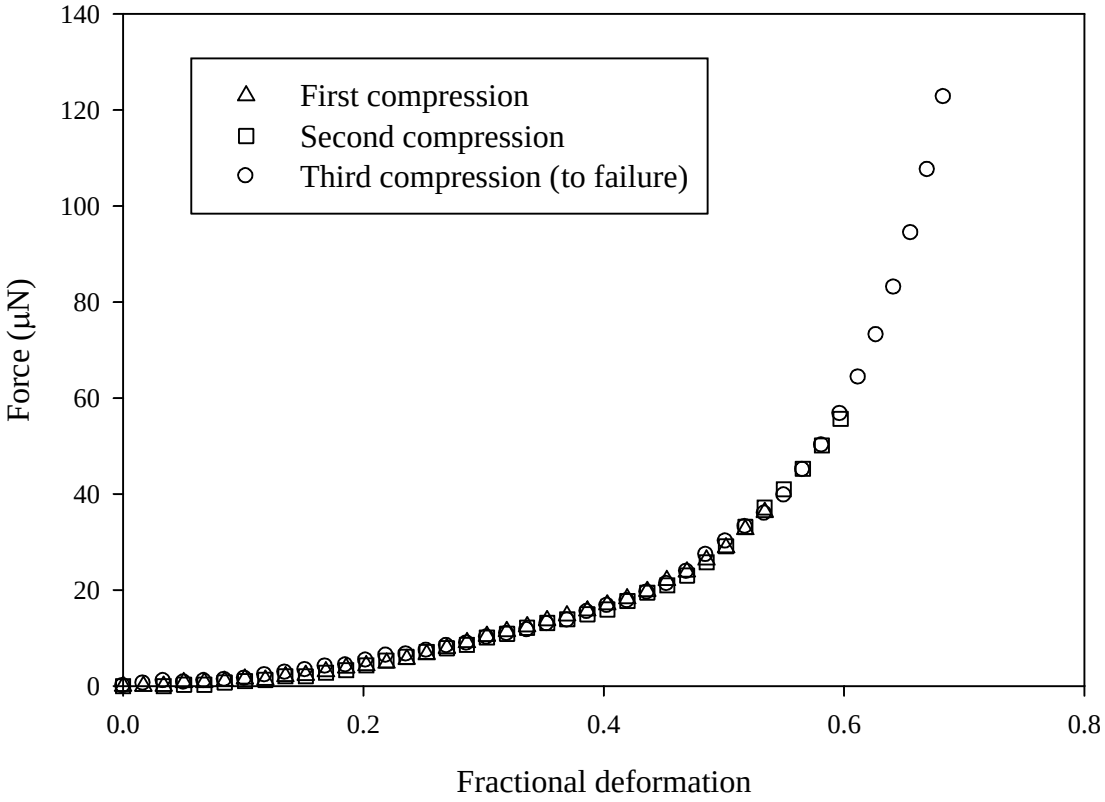

Figure 4.5: Force deformation data for the repeated compression of a cell.

Cell size = 4.1 µm, deformation at failure = 68 %, force at failure = 123 µN

The force - deformation data are very close, at least up to 60 % (second compression). As can be seen in Figure 4.5 there were no signs of permanent deformation between compressions. It is believed that if the cell wall was elastic - plastic then the high level of

deformation would have permanently deformed the cell leading to a different force - deformation curve being generated by any subsequent compressions. It remains possible that there were localised plastic effects at deformations close to failure, but model fitting (Section 6.1.4) suggested this was not the case.

As shown in Figure 4.4 a hysteresis test could not be used to determine the behaviour of yeast cells. However, when an individual cell was compressed repeatedly to high deformation it was shown that the force - deformation curve was very similar for all compressions. The appropriateness of using linear elastic constitutive equations is discussed further in Chapter 6.

4.1.5. Non - bursting / multiple bursting cells

During the compression experiments it was found that approximately 5 % of the cells either did not burst or produced two bursting peaks. An example of these data is shown in Figure 4.6.

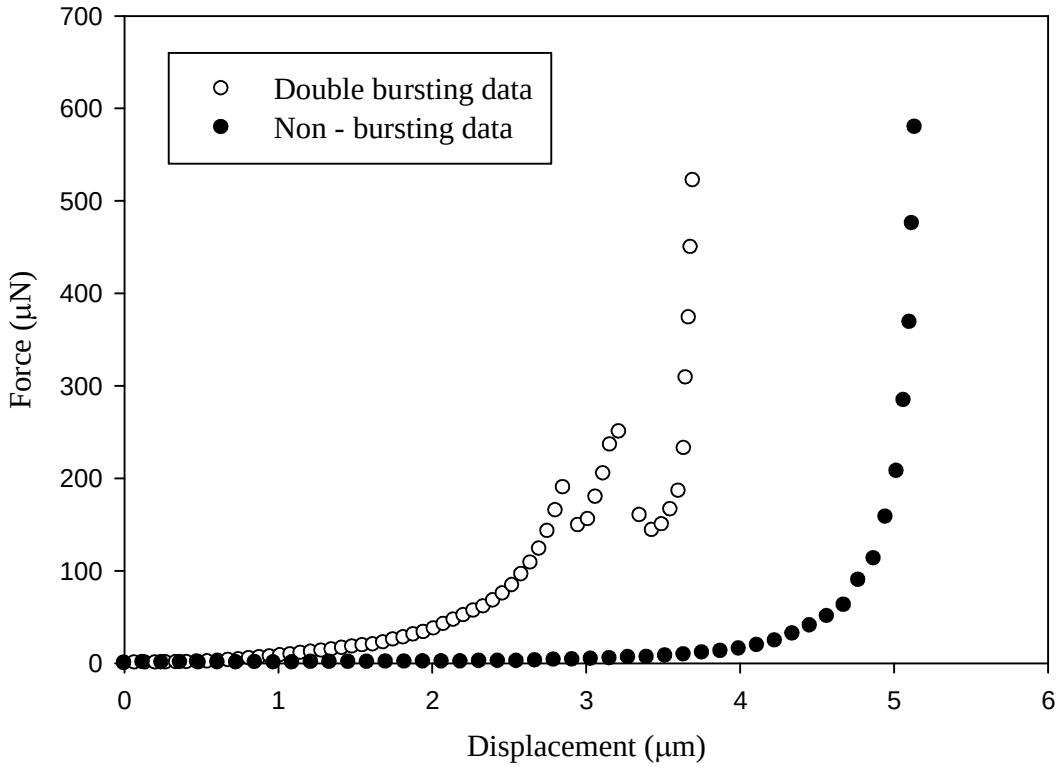

Figure 4.6: Example of non - bursting and multiple bursting cell compression data.

For the cells that did not burst the force remained low until a very high deformation after which it increased rapidly, probably as the probe contacted the base of the chamber, or cell debris on the base. It is believed that the cells that did not burst were nonviable cells which did not have intact cell membranes able to resist the flow of water out of the cells during compression. This would mean that it was only the cell wall that was resisting the compression. With no intact membrane there was no significant rise in force until the

remaining internal contents of the cell and the cell wall material were being compressed. Numerical simulations (Section 6.1.4) were not fitted to the non - bursting data.

It is unknown why compression sometimes produced double bursts (Figure 4.6). It is possible that this occurred as a doublet was being compressed rather than an individual cell. Due to the poor images that were obtained using the side view and inverted microscopes (Section 3.2.3.1) it might not have been possible in all cases to see that two cells, especially a mother and a significantly smaller bud cell, were being compressed. As the reason for the double burst was unknown these compression data were also not fitted by numerical simulations.

4.2. Population measurements of mechanical properties

The results in this section cover population measurements which were obtained directly from the compression testing experiments using the manipulation techniques outlined in Chapter 3. The parameters measured were the cell diameter, force and deformation at cell wall failure at compression speeds ranging from 8 to 308 μms^{-1}.

4.2.1. Relationships between cell size, force and deformation at failure

Figures 4.7, 4.8 and 4.9 show typical trends for parameters measured by compression testing. These data were recorded at a compression speed of 68 μms^{-1} when water loss is assumed to be negligible (an investigation of this assumption is described in Section 7.1). Relationships similar to those shown here were found for all compression speeds regardless of temperature and age of the cell stock.

Figure 4.7 shows the relationship between the force at failure and the cell diameter.

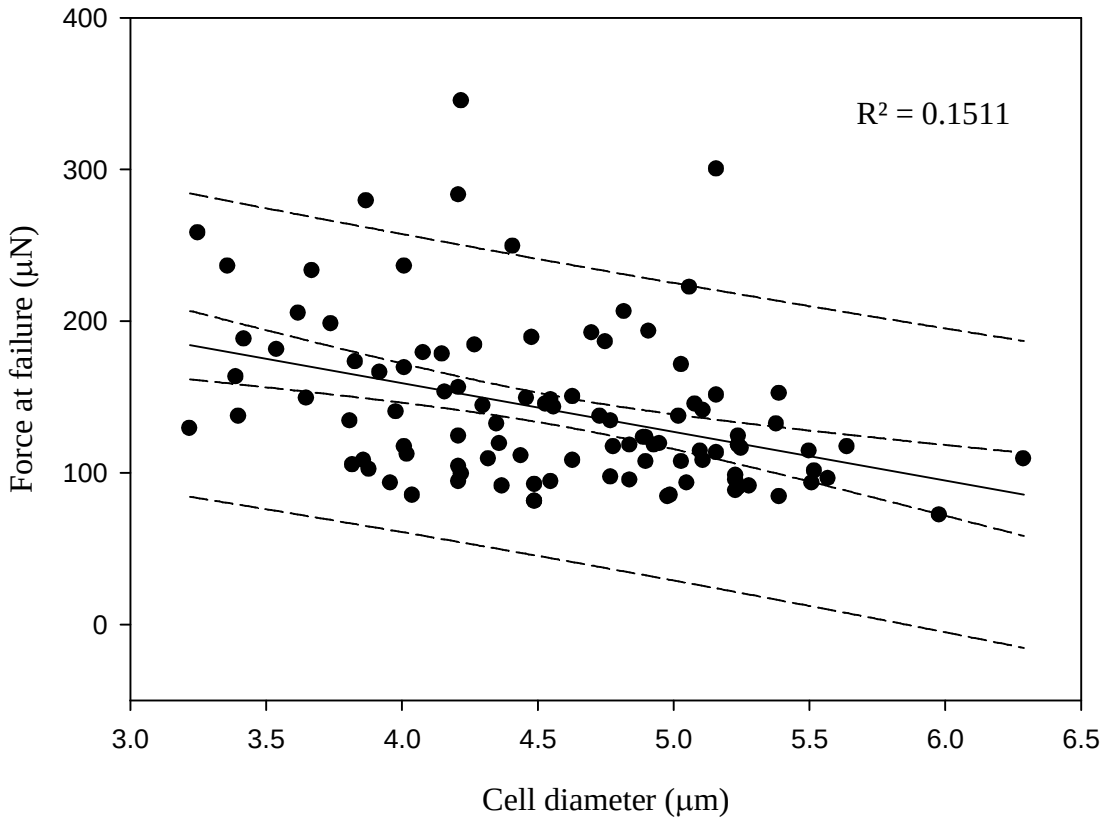

Figure 4.7: Relationship between the force at failure and the cell diameter for cells compressed at 68 μms^{-1}. Approximately 100 measurements. Dashed lines represent the 95 % confidence limits for the mean and the individual measurements.

From the data in Figure 4.7 the mean force at failure was found to be 138 ± 11 μN. This is in comparison to 97 μN (Smith *et al.*, 2000a), 101 μN (Mashmoushy *et al.*, 1997) and 113 μN (Kleinig, 1997) also for Fermipan dried Baker's yeast. As can be seen from the correlation coefficient in Figure 4.7, the force at failure is weakly negatively correlated with the cell diameter. This relationship was observed at all compression speeds and between samples in this work. This was in contrast to previous reports which showed the force at failure to be size independent (Mashmoushy *et al.*, 1997; Smith *et al.*, 2000a).

Figure 4.8 shows the relationship between the force and the deformation at failure.

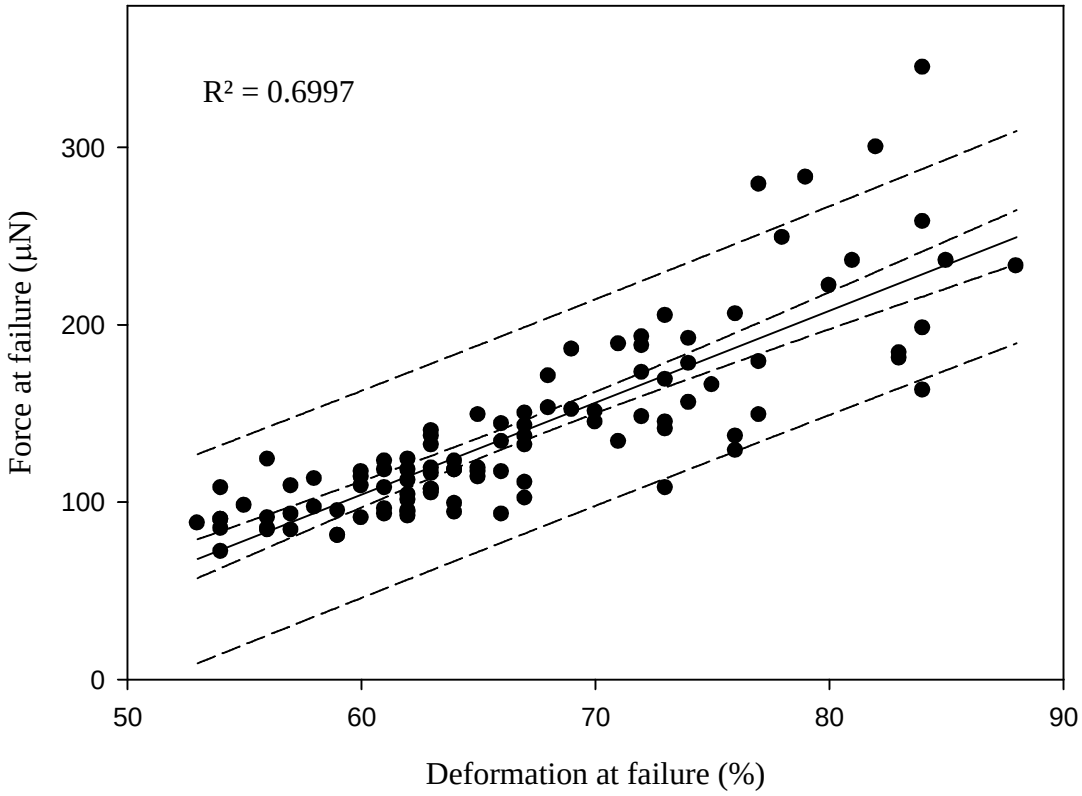

Figure 4.8: Relationship between the force and the deformation at failure for cells compressed at 68 µms^{-1}. Approximately 100 measurements. Dashed lines represent the 95 % confidence limits for the mean and the individual measurements.

Clearly these measurements are strongly correlated; this result compares well to the results of Smith *et al.* (1999) and Mashmoushy *et al.* (1998). The mean deformation at failure was 67 ± 2 % for the data in Figure 4.8 and the collated mean over all compression speeds was 68 ± 1 % (data not shown). This compares to Smith *et al.* (2000a) who gave a value of 67 % for similar cells and conditions, even though using a significantly lower compression speed. The relationship shown in Figure 4.8 was found to be similar for all compression speeds.

Figure 4.9 shows the relationship between the deformation at failure and the cell diameter.

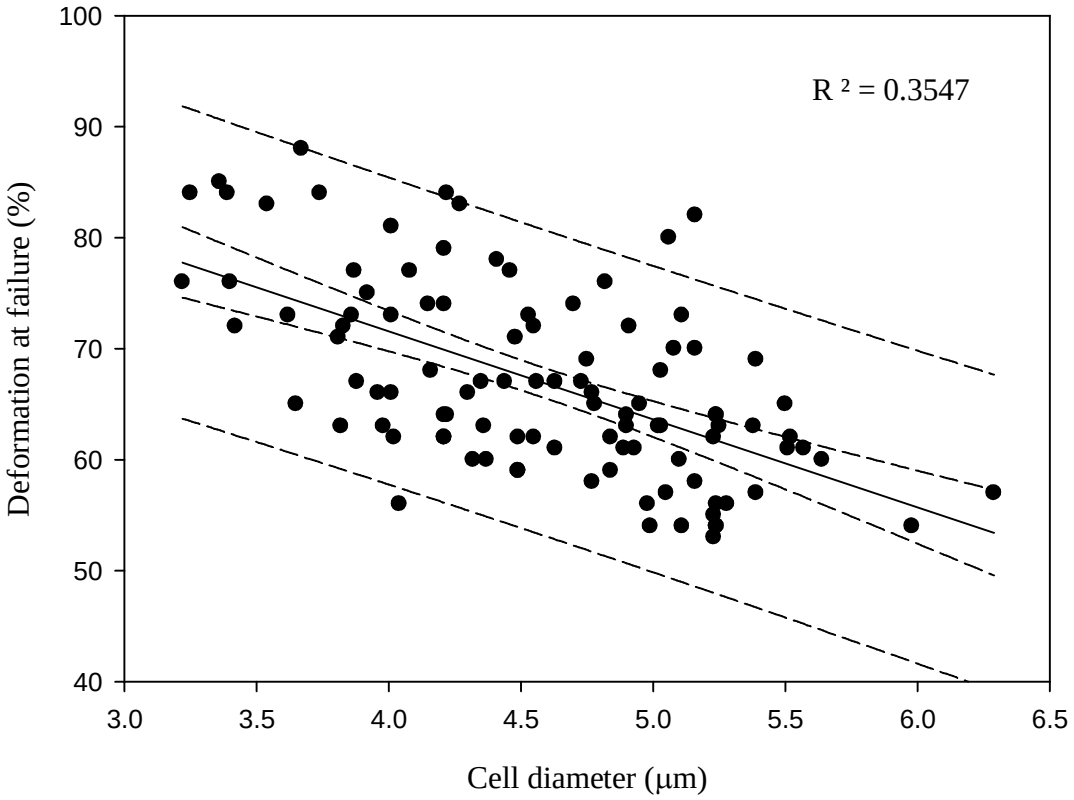

Figure 4.9: Relationship between the deformation at failure and cell diameter for cells compressed at 68 μms^{-1}. Approximately 100 measurements. Dashed lines represent the 95 % confidence limits for the mean and the individual measurements.

Figure 4.9 shows that the deformation at failure is weakly correlated with the cell diameter, decreasing with increasing cell diameter. This result compares well with that presented by Smith *et al.* (2000a). If cells had equal intrinsic material properties (i.e. elastic modulus and failure criteria) then it might be expected the cells would be deformed to the same level of deformation before failure. This relationship is discussed further in Section 7.2.6.1.

4.2.2. Discussion

It appears that the mean force and deformation at cell wall failure was not controlled by compression speed (Figure 4.3 a) and b)). It had been expected that at faster compression speeds the force at cell wall failure would be higher due to some force relaxation during slower compressions due to the flow of water out of cells (or possibly cell wall viscoelastic effects). At the higher compression speeds this time for relaxation was reduced so a correspondingly higher force (Wang *et al.*, 2005) and lower deformation at failure was expected. This effect was not observed with yeast cells suggesting that time dependent behaviour was not significant or that the measurement technique was not sensitive enough for these differences to be observed.

The data in Figure 4.7 showed that the force at failure was weakly negatively correlated with the cell size. It is known that significant changes will be made to the cell wall composition, structure and thickness during the cell cycle so some significant relationship may have been expected however only a weak correlation was found.

The force at failure is not a reliable measurement and cannot be used to compare the material properties between cell populations. For example the work of Srinorakutara (1997) found that the force at failure increased with cell diameter using a *Saccharomyces cerevisiae Y9* yeast strain. This is in contrast to Smith (1999) who showed that the force at failure of *Saccharomyces cerevisiae Y9* yeast strain decreased with cell diameter. There are a number of possible reasons for these relationships including biological variability in the cell wall thickness, turgor pressure, permeability and cell wall mechanical properties. However, what

this does show is that the relationships obtained for the force at failure are not consistent between samples.

Although the mean force and deformation at failure are not dependent on the compression speed, they are not a reliable measurement. In order to predict the disruption of the cells force and deformation data are not suitable, instead intrinsic material properties such as the elastic modulus and some failure criterion are required.

4.3. Concluding remarks

The micromanipulation technique has been successfully applied to Baker's yeast cells to produce force - deformation data. The data presented confirms that the compression speed does not have a significant effect on the results obtained.

All of the data presented a significant amount of scatter that is believed to be due to biological variability. It is possible that this biological scatter prevented compression testing from distinguishing between different behaviours of cells at the range of compression speeds. To be able to observe small changes in the results significantly more cells would need to be tested. Currently the micromanipulation equipment requires manual operation which limits the total number of cells which can be tested.

The mean force at failure obtained in compression testing by micromanipulation is useful as a comparative measurement, but is dependent on factors such as the wall properties, cell size and permeability. In order to have a proper understanding of the behaviour of the cell wall during compression it is essential to have intrinsic material properties. This knowledge is

required to improve our fundamental understanding and prediction of the cell wall behaviour. To obtain this information a numerical model is developed in Chapter 5 which allows intrinsic material properties to be derived from the force - deformation data. In addition to this it is hoped that some failure criteria can be extracted to be used in the prediction of cell disruption.

Chapter Five: Mathematical modelling

As described in Chapter 2 the experimental method of choice for measuring the mechanical properties of yeast cells is compression testing by micromanipulation. The disruption of microbial cells is important in bioprocessing, as a means to release the cellular contents. In order to understand more fully the response of yeast cells to bioprocessing it is essential to have information on the intrinsic material properties of yeast cells. Of especial interest is the behaviour of the cells at cell wall failure. This chapter will develop analytical models with different derivations of the strain energy function for large deformation and large strain compression testing. The results obtained from this model can be used to help improve the efficiency of cell disruption in bioprocessing and improve our understanding of the mechanisms of form and growth of cells.

5.1. Development of a membrane mechanical model

In high-pressure homogenisation, the extent of cell disruption depends on the local fluid flow fields in the processing equipment and on the mechanical properties of the cells (Kleinig and Middelberg, 1996, 1998). In other types of disruption, there may be different types of stress generation but the mechanical properties of the cells will still be important. Improvement in disruption has been the motivation of recent studies into the mechanical properties of yeast cells (Mashmoushy *et al.*, 1998; Smith *et al.*, 1998, 2000 a, b and c).

The development of an analytical model of cell compression provides a means of quantifying the elastic behaviour and failure of the cell wall. Combining the technique of compression testing with mathematical modelling has been applied to plant cells (Wang *et al.*, 2004; Blewett *et al.*, 2000), mammalian cells (Peeters *et al.*, 2005), sea urchins (Cheng 1987a), red blood cells (Skalak *et al.*, 1973) and yeast cells (Smith *et al.*, 2000b). By using this technique, estimates of the wall elastic modulus and stresses and strains at failure may be obtained.

Approaches to modelling the compression of hollow spheres are often based on analyses of Feng and Yang (1973), and Lardner and Pujara (1980). Both assumed the wall is thin enough to be treated as a (mechanical) membrane, and while the former concerned gas-filled spherical shells, Lardner and Pujara (1980) considered such shells filled with incompressible liquid, an assumption more appropriate when using a biological experimental system. The liquid volume was assumed to be constant, which implied impermeability of the wall material. Because the wall was treated as a mechanical membrane, the stresses were expressed as wall tensions, and it was presumed that the wall could not support out-of-plane shear stresses or bending moments. This situation is described as plane stress, as the only non-zero stresses are in the plane of the cell wall.

Feng and Yang (1973) and Lardner and Pujara (1980) solved their analytical equations numerically. Cheng *et al.* (1987a) described the alternative computational approach of finite element analysis, and applied this to previously published data on sea urchin eggs (Cheng *et al.*, 1987b). Smith *et al.* (1998) also used a finite element approach, but introduced the possibility of permeable cell walls, i.e. a changing liquid volume inside the shell. The

equations governing the deformation of a liquid-filled spherical membrane derived by Lardner and Pujara (1980) follow.

Figure 5.1 illustrates the spherical cell prior to compression where η and ρ are the vertical and horizontal axes respectively. The deformation of the surface of the cell wall may be defined in terms of stretch ratios, λ_1 and λ_2, which correspond to the meridian and circumferential directions respectively.

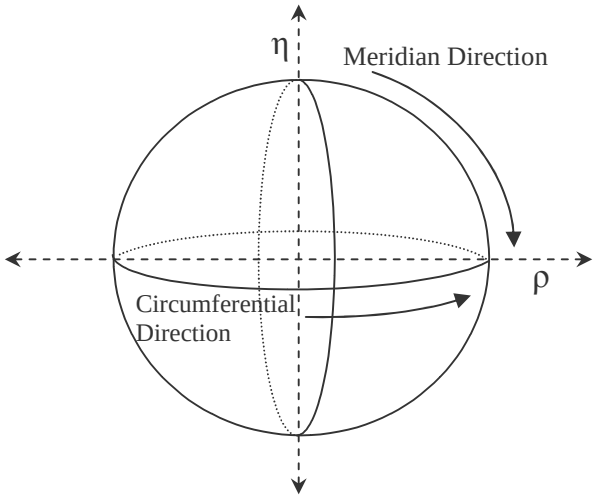

Figure 5.1: Meridian and circumferential directions of the cell prior to compression.

Figure 5.2 shows the geometry on a meridian plane during the compression phase, and it can be seen that there are parts of the cell wall that contact the compressing surfaces, and parts that do not (non-contact regions).

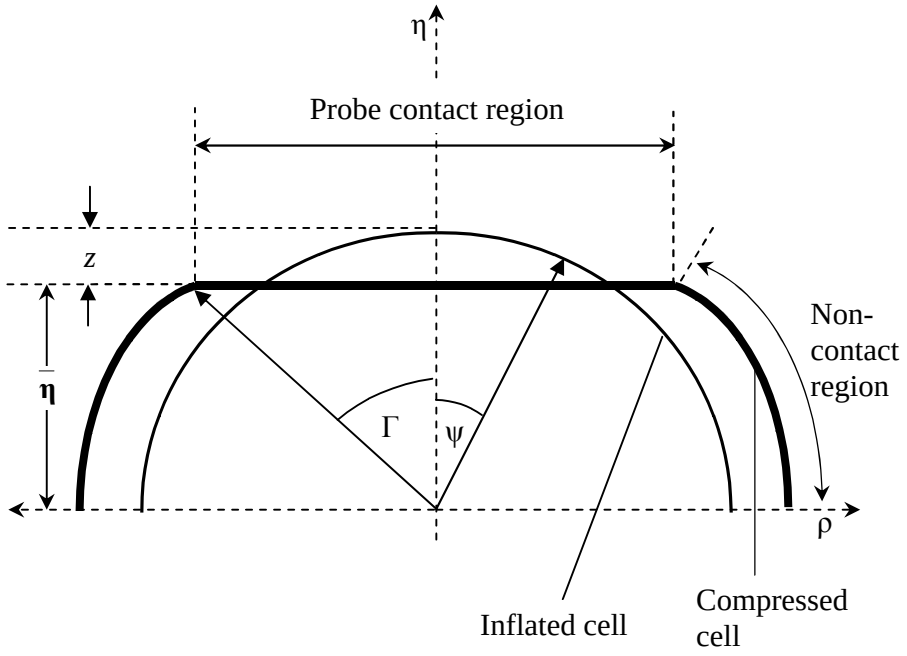

Figure 5.2: Schematic diagram of the geometry of the cell where ψ is the angular position of a point on cell wall from the vertical axis of symmetry prior to compression. ψ = Γ at the edge of the contact region between the compression surface and the cell during compression. η and ρ are the vertical and horizontal coordinates respectively. $\overline{\eta}$ is the distance between the compression surface and the equatorial plane, and z is half the distance that the cell has been compressed.

There are separate groups of governing equations for contact and non-contact regions. The independent variable in these equations is ψ, which relates the position of any point on the boundary of the cell back to the original position of that point in the inflated but uncompressed cell. ψ is the angular position of the point measured from the vertical axis of symmetry.

The governing equations are (Lardner and Pujara, 1980):

Contact region:

$$\frac{d\lambda_1}{d\psi} = -\frac{\lambda_1}{\lambda_2 \sin\psi}\left(\frac{f_3}{f_1}\right) - \left(\frac{\lambda_1 - \lambda_2 \cos\psi}{\sin\psi}\right)\left(\frac{f_2}{f_1}\right) \quad \ldots (5.1)$$

$$\frac{d\lambda_2}{d\psi} = \frac{\lambda_1 - \lambda_2 \cos\psi}{\sin\psi} \quad \ldots (5.2)$$

where f_1, f_2 and f_3 are functions of the principal tensions and are defined later.

Non-contact region:

$$\frac{d\lambda_1}{d\psi} = \left(\frac{\delta\cos\psi - \omega\sin\psi}{\sin^2\psi}\right)\left(\frac{f_2}{f_1}\right) - \left(\frac{\omega}{\delta}\right)\left(\frac{f_3}{f_1}\right) \quad \ldots (5.3)$$

where $\delta = \lambda_2 \sin\psi$ $\ldots (5.4)$

and $\omega = \frac{d\delta}{d\psi}$ $\ldots (5.5)$

$$\frac{d\lambda_2}{d\psi} = \left(\frac{\omega \sin\psi - \delta \cos\psi}{\sin^2\psi}\right) \quad \ldots (5.6)$$

The turgor pressure (P) inside the cell can be related to ω using:

$$\frac{d\omega}{d\psi} = \frac{d\lambda_1}{d\psi}\frac{\omega}{\lambda_1} + \frac{\left(\lambda_1{}^2 - \omega^2\right)}{\delta}\left(\frac{T_2}{T_1}\right) - \frac{\lambda_1\left(\lambda_1{}^2 - \omega^2\right)^{1/2} Pr_0}{T_1} \qquad \ldots (5.7)$$

where r_o is the uninflated radius of the cell.

The functions of the principal tensions are defined as:

$$f_1 = \frac{\partial T_1}{\partial \lambda_1};\ f_2 = \frac{\partial T_1}{\partial \lambda_2} \text{ and } f_3 = T_1 - T_2 \qquad \ldots (5.8a, 5.8b, 5.8c)$$

where T_1, T_2 are the tensions in the meridian and circumferential directions respectively. The full derivations of these equations are given in Appendix 10. The tensions link the geometry (equations 5.1 to 5.7) to the cell wall constitutive equation. Since the compression of the cell consists of axi-symmetric deformation, T_1 and T_2 are principal tensions, which are defined with respect to the current deformed shape of the cell.

The composition and structure of the yeast cell wall is recognised to be a complex assembly of different macromolecules. However, in the absence of better information it is generally assumed that the material is homogeneous and isotropic.

For the analysis of force - deformation data from compression experiments it is also necessary to use an appropriate constitutive equation, relating the stresses and strains that are generated in the cell wall. Suitable constitutive equations can be obtained by assuming

that the cell wall is hyperelastic, in which case the stress components are derived from a strain energy function, usually presented as depending on strain invariants. Strain energy is the energy stored in a body that results from an elastic deformation, and is equal to the work required to produce the strain in the body (assuming that any temperature changes and other losses can be ignored). Strain invariants depend on the principal strains and have values independent of the choice of coordinate system

For work on biological cells, the assumption of a suitable cell wall constitutive equation or a strain energy function is necessary because the constitutive equation is not usually or ever known, *a priori*. There are many choices of strain energy function that might be appropriate to cell walls, and a summary of those that have been used to interpret data from compression testing (of cells) is provided in Table 5.1. This table excludes models where the tension in the wall was assumed to be uniform (Zhang *et al.*,1992; Kleinig 1997). In some cases (Skalak *et al.*, 1973; Lardner and Pujara, 1980; Liu, 1995) the wall was assumed to be incompressible, whereas other workers have proposed strain energy functions incorporating Poisson's ratio v to allow for compressibility (Cheng, 1987a; Smith, 1999; Wang *et al.*, 2004). Even in the latter cases it is common to assume incompressibility i.e. $v = 0.5$, in fitting the model to experimental data, because it is very difficult to determine a value for this parameter or find a value by fitting a model to experimental data.

Source	Cell type	Strain energy function
Skalak et al. (1973)	Red blood cells	$\overline{W} = \frac{B}{4}\left(\frac{1}{2}I_1^2 + I_1 - I_2\right) + \frac{C}{8}I_2^2$ where $I_1 = 2(E_1 + E_2)$ and $I_2 = 4E_1E_2 + 2(E_1 + E_2)$, and B and C are material constants. This is the STZC strain energy function.
Skalak et al. (1973)	Red blood cells	$W = C_1(I_1 - 3) + C_2(I_2 - 3)$ where $I_1 = \lambda_1^2 + \lambda_2^2 + \lambda_3^2$ and $I_2 = \lambda_1^{\,2} + \lambda_2^{\,2} + \lambda_3^{\,2}$, and C_1 and C_2 are material constants. This is the Mooney-Rivlin (1940) strain energy function.
Lardner and Pujara (1980)	Sea-urchin eggs	Mooney-Rivlin and STZC functions
Cheng (1987a)	Sea-urchin eggs	$W = \frac{Eh_0}{2\left(1-\nu^2\right)}\left(\varepsilon_1^2 + \varepsilon_2^2 + 2\nu\varepsilon_1\varepsilon_2\right)$ where ν is Poisson's ratio.
Liu (1995)	Tomato cells	Mooney-Rivlin function
Smith (1999)	Yeast cells	Cheng (1987a) function
Wang et al. 2004	Tomato cells	Cheng (1987a) function

Table 5.1: Constitutive equations used to interpret compression testing data

[W: strain energy per unit initial volume; $\overline{W}$: strain energy per unit initial area, for (mechanical) membranes; I principal stretch ratios; E_i Green strain; ε infinitesimal strain, subscript $_1$ meridian direction, $_2$ hoop direction; E elastic modulus*; h_0 initial wall thickness]*

* *NB: Care should be taken not to confuse the use of E_i for the Green strain and E for the Elastic modulus.*

Once a constitutive equation or strain energy function has been assumed, fitting experimental data should allow the determination of parameters describing the cell wall material properties. However, Smith *et al.* (1998) showed that unique determination of these material parameters from compression testing still requires accurate and precise measurements of some geometrical parameters. Firstly, cells are usually already inflated at the start of the compression (because of a difference between internal and external pressures) and the initial stretch ratio is therefore important, as are the uninflated cell wall thickness and the volume loss caused by any liquid permeating through the cell wall during compression. Even with an assumed linear elastic constitutive equation, at least two of these geometrical parameters should be known to obtain unique values for the material parameters. However, if the constitutive equation is unknown, all three measurements are necessary, because two different constitutive relationships can give the same force - displacement curves. Even then, the resulting constitutive equation should ideally be evaluated by tests involving different types of mechanical testing.

For yeast cells, the subject of this thesis, alternatives to compression testing are not readily available, mainly because yeasts cells are microscopic and generally strong. It was decided therefore that a generalised form of Hooke's Law should be assumed, various ways of deriving a strain energy function should be considered, and simulations based on the resulting strain energy functions should be compared to each other. Hooke's Law implies a linear relation between stress and strain, i.e. a constant elastic modulus, and it is believed be the best practical choice here because,

(a) there is only one material parameter, the elastic modulus;

(b) it might in any case be difficult to identify more material parameters from limited experimental data; and

(c) the material model is simple and readily understood by workers in other fields.

Smith et al. (1998) suggested a linear constitutive equation of this form be adopted, and data from Smith et al. (2000b) suggest it may be appropriate for yeast cells. It should be noted that simulated force deformation-curves would be non-linear even if a constant elastic modulus is assumed, because of changes in the geometry of the cell as it is deformed.

Although the use of a constant (or average) elastic modulus has been assumed before (it underlies the choice of the strain energy function of Cheng (1987a), see Table 5.1), it is still important that the equations used to derive the strain energy function are properly formulated. Strain energy functions may be written as explicit functions of strain, the approach adopted here for simplicity, but this requires that careful attention is paid to how strain is defined. Alternative definitions of strain are in common use, and each has an appropriate and corresponding stress definition. The linear constitutive equations resulting from these alternative definitions are different. Furthermore, the equations of Feng and Yang (1973) and Lardner and Pujara (1980) are expressed in terms of stretch ratios, which are an alternative to strains as a measure of deformation, and are often used for materials that can support high deformations before failure. A stretch ratio in a given direction is the length of the deformed material divided by its original length. Each strain has a different relationship to the stretch ratio.

5.2. Strain, stress and energy functions

For material deformation that is very small, as in the case of elastic deformation of most metals, the infinitesimal strain approach is a valid approximation. In this case principal strain components (ε_i) may be related to the principal stretch ratios (λ_i) by the equation:

$$\varepsilon_i = (\lambda_i - 1) \qquad \ldots (5.9)$$

where the subscript *i* indicates a principal direction. Principal stretch ratios are defined and measured in directions along which there is no shear, only stretching or compression.

When loading conditions lead to greater material deformation, alternative measures of strain must be considered. For the case of non-infinitesimal strain (i.e. finite strain), the most common definition is Green (or Lagrangian) strain. The principal components of Green strain (E_i) are related to the principal stretch ratios by the equation:

$$E_i = \frac{1}{2}(\lambda_i^2 - 1) \qquad \ldots (5.10)$$

This provides a measure of strain that is rotationally invariant, and therefore avoids the errors introduced by the infinitesimal strain model when the deformation involves large rotations. There are however limitations to its use. When large deformation is accompanied by large strain, a more appropriate measure to use is Hencky strain (H_i) (often referred to as true, logarithmic or natural strain). This is related to the principal stretch ratios by the equation:

$$H_i = ln\lambda_i \qquad \ldots (5.11)$$

The immediate question this raises concerns the appropriate measure of strain for a particular deformation. There are no absolute measures and the choice of strain model may be guided by the level of accuracy deemed acceptable, or by the ease of its inclusion in an analytical model. In very broad terms, infinitesimal strain is suitable for very small deformations where the strain may be of the order of 0.1%; for larger strains of the order of 1 – 5%, especially where material rotation is involved, then Green strain should be used, and for any magnitude of strain (in particular even larger strains) the most accurate model is that defined by Hencky strain. However, these are merely approximate guidelines and in some circumstances (for example where the principal stress axes do not rotate during deformation) infinitesimal strain may provide a reasonable first approximation even where the strain reaches 5%, and Green strain will give results very close to Hencky strain if the analysis is performed in small increments of deformation. For this reason, Green strain has proved popular in computational finite-element models of material deformation.

The analytical model developed here uses a single step from the inflated un-deformed state to the compressed state (i.e. large increments of deformation). Figure 5.3 shows a simple comparison of the three strain measurements when a uni-axial strain is applied over large increments of deformation.

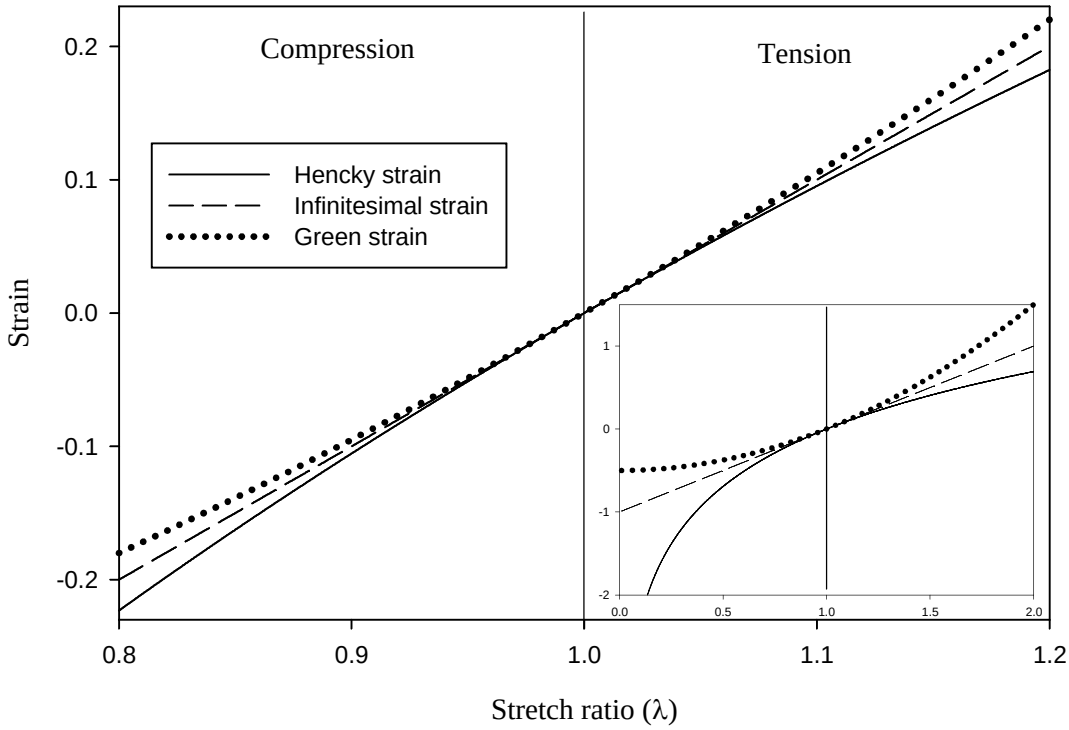

Figure 5.3: Comparison of uni-axial strain using Hencky, Green and Infinitesimal strain definitions over large increments of deformation. Inset is uni-axial strain over a larger range of stretch ratios.

The effect of the choice of strain is shown clearly in Figure 5.3 for the simple example of uni-axial strain. As can be seen up to a stretch ratio of 1.05 the strain values are almost indistinguishable. Above this value they begin to diverge and the inset shows this same comparison over a wider range of stretch ratios. For all negative strain measurements ($\lambda < 1$) the material will be considered to be in compression and in tension for all positive values ($\lambda > 1$). The inset in Figure 5.3 shows that as λ approaches zero (100% compression) the infinitesimal and Green strain models lead to a finite strain limit. This implies that in a linear elastic model a finite load would be required to compress the material down to nothing which is a physical impossibility. As can be seen in the inset the Hencky strain

definition avoids this problem. However, in the case of cell compression testing the wall is usually in tension and this limiting behaviour of the strains is not critical.

As previously mentioned if small increments in the deformation are used (as in finite element software) the results using the Green and infinitesimal strains will be closer to the Hencky strain model. Using incremental steps means that at each point the strain is calculated using the change in length from the length at the previous point (rather than the original length), and the accumulated strain is then calculated. Again a simple uni-axial strain comparison is made to demonstrate this in Figure 5.4 with increments in stretch of 0.01.

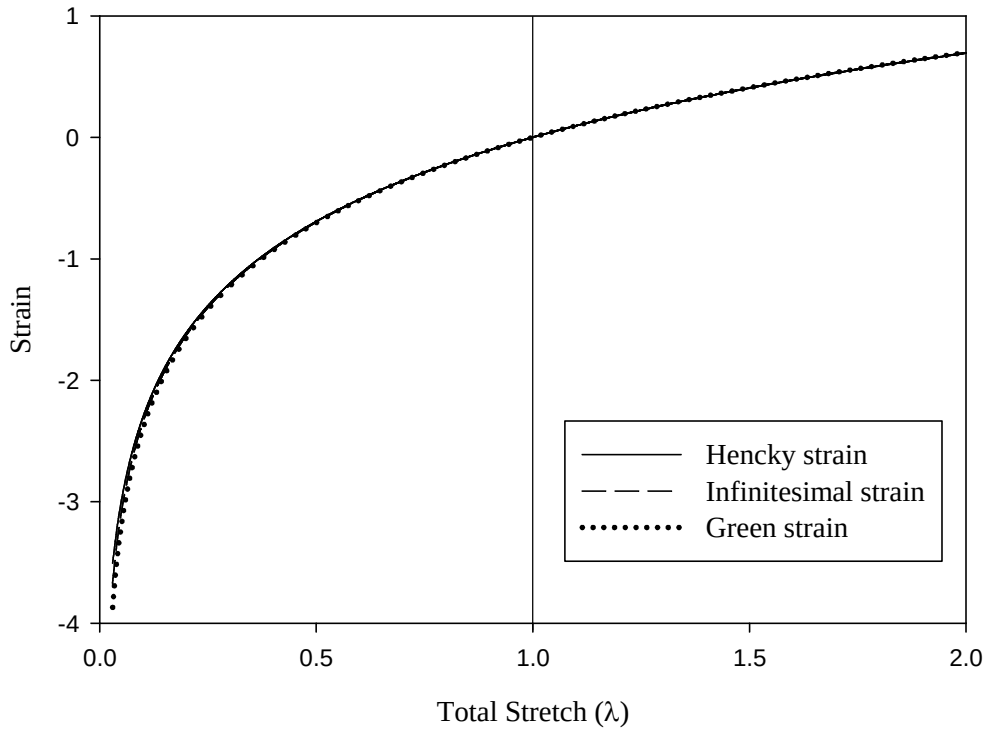

Figure 5.4: Comparison of uni-axial strain using Hencky, Green and Infinitesimal strain definitions using incremental stretches of 0.01.

As can be seen in Figure 5.4 the strains over a large range of incremental stretches are very similar. The stretch axis is total stretch, but the strain is evaluated at that stretch using incremental values. This demonstrates that if incremental deformation is used for this simple uni-axial example the results obtained using the three different strain definitions will be similar. Many finite element models will use Green strain for large strain situations as this is computationally simpler. However, when using the analytical model proposed for cell compression it is not possible to use incremental deformation in the simulations so the choice of strain definition is very important. This paper will use all three strain models to demonstrate and compare their effectiveness in the analytical approach adopted here.

For each strain, it is necessary to use an appropriate, corresponding, measure of stress. If it is assumed that the material of the cell wall is hyperelastic, then a linear constitutive equation may be applied across any magnitude of deformation (Xiao and Chen, 2002; Malvern, 1969), subject to the stress and strain being work conjugate. This implies that the stresses may be determined by differentiation of an appropriate strain energy function with respect to the chosen strain component.

The relevant work-conjugate stress-strain pairs for the measures of strain mentioned above, written in terms of the principal components, are:

Cauchy stress σ_i – infinitesimal strain ε_i, so $\sigma_i = \dfrac{\partial W}{\partial \varepsilon_i}$ … (5.12)

2nd Piola-Kirchhoff (PK2) stress S_i – Green strain E_i, so $S_i = \dfrac{\partial W}{\partial E_i}$ … (5.13)

Kirchhoff stress τ_i – Hencky strain H_i, so $\tau_i = \dfrac{\partial W}{\partial H_i}$ … (5.14)

where W is an appropriate strain energy function.

If the modelling was based only on the limiting case of infinitesimal strain, then the constitutive equation could be written using indicial notation in the form of Malvern (1969):

$$\sigma_{ij} = \Lambda \delta_{ij} \varepsilon_{kk} + 2\mu \varepsilon_{ij} \quad \ldots (5.15)$$

σ_{ij} is the stress in the jth direction, on the plane normal to the ith direction, and ε_{ij} is the corresponding strain. A repeated subscript implies a summation over all its values (1 to 3 for stress and strain tensors). Λ and μ are Lamé's constants and δ is the Kronecker delta (= 1 if $i = j$ and 0 if $i \neq j$). Lamé's constants are defined as (Lemaitre and Chaboche,1994)

$$\Lambda = \frac{E\nu}{(1+\nu)(1-2\nu)} \quad \text{and} \quad 2\mu = \frac{E}{1+\nu} \quad \ldots (5.16a, 5.16b)$$

E is the elastic modulus and v is Poisson's ratio.

The axi-symmetric deformation of the yeast cell (see Figure 5.2 Section 5.1), together with the assumption of plane stress conditions (i.e. the only non-zero stresses are in the plane of the cell wall, Appendix 10), means that the meridian and longitudinal stresses and strains are the principal components, in which case equation 5.15 may be written specifically for these components as

$$\sigma_i = \Lambda \varepsilon_v + 2\mu \varepsilon_i \quad \ldots (5.17)$$

where i indicates the principal component, and ε_v is the bulk or volumetric strain (i.e. the sum of the three principal strain components).

For each definition of strain, a strain energy function is needed that can be differentiated in accordance with equation 5.12, 5.13, or 5.14 to give an expression that is consistent with that obtained from equation 5.15 or its equivalents for the other stress-strain pairs. Using the infinitesimal strain case as an example, the σ_1 component from equation 5.17 is

$$\sigma_1 = \frac{E\nu}{(1+\nu)(1-2\nu)}(\varepsilon_1+\varepsilon_2+\varepsilon_3)+\frac{E}{(1+\nu)}\varepsilon_1 \qquad \ldots (5.18)$$

Although the cell wall is approximated here as a two-dimensional plane stress problem, there will exist a strain in the normal direction, given by (Lemaitre and Chaboche 1994)

$$\varepsilon_3 = -\frac{\nu}{1-\nu}(\varepsilon_1+\varepsilon_2) \qquad \ldots (5.19)$$

This allows equation 5.18 to be reduced to

$$\sigma_1 = \frac{E}{(1-\nu^2)}[\varepsilon_1+\nu\varepsilon_2] \qquad \ldots (5.20)$$

For this infinitesimal strain case, a suitable strain energy function that can be differentiated with respect to both ε_1 and ε_2 is

$$W = \frac{1}{2}\sigma_i\varepsilon_i = \frac{1}{2}(\sigma_1\varepsilon_1+\sigma_2\varepsilon_2) = \frac{1}{2}\left[\frac{E}{(1-\nu^2)}\varepsilon_1(\varepsilon_1+\nu\varepsilon_2)+\frac{E}{(1-\nu^2)}\varepsilon_2(\varepsilon_2+\nu\varepsilon_1)\right]$$

$$= \frac{E}{2(1-\nu^2)}(\varepsilon_1^2+\varepsilon_2^2+2\nu\varepsilon_1\varepsilon_2) \qquad \ldots (5.21)$$

This is the strain energy function derived by Cheng (1987a); see Table 5.1. A similar analysis can be followed for the other stress-strain pairs (equations 5.13 and 5.14). To do this, it is of course necessary to assume that Hooke's Law (equations 5.15 and 5.17 in the infinitesimal case) can be generalised to any work-conjugate stress-strain pair, and that Poisson's ratio υ is constant for all strains, or at least that some average value is a good approximation across the deformation range. For the uniaxial, infinitesimal strain case, Poisson's ratio is defined by

$$\nu = -\frac{\varepsilon_{trans}}{\varepsilon_{axial}} \qquad \ldots \quad (5.22)$$

where ε_{trans} is the transverse strain caused by an imposition of an axial strain ε_{axial}. It is presumed here that this is an infinitesimal strain limit of a general large strain equivalent, which is presumed to apply for all deformations. With this additional assumption, it is possible to extend equation 5.21 to large strains by replacing infinitesimal strain directly by Green strain

$$W = \frac{E}{2\left(1-\nu^2\right)}\left(E_1^2 + E_2^2 + 2\nu E_1 E_2\right) \qquad \ldots (5.23)$$

and for Hencky strain,

$$W = \frac{E}{2\left(1-\nu^2\right)}\left(H_1^2 + H_2^2 + 2\nu H_1 H_2\right) \qquad \ldots (5.24)$$

Regardless of the measure of stress used in modelling the compression of yeast cells, the final outcome of the model must be the true or Cauchy stress, defined as the ratio of the current force and current area. For infinitesimal strain, any change in area is normally assumed to be negligible and Cauchy stress is equated with the nominal stress (current force divided by initial area). For other definitions of strain the differences between the original and final dimensions cannot be ignored. In the case of Kirchhoff stress, the Cauchy stress is equal to this stress divided by the ratio of the final volume divided by the initial volume, so that

$$\tau_i = J\sigma_i \qquad \ldots (5.25)$$

where

$$J = \lambda_1\lambda_2\lambda_3 \qquad \ldots (5.26)$$

Note that $J = 1$ for an incompressible material. The PK2 stress is often interpreted as the initial force divided by the initial area. In this case, the true (Cauchy) stress may be obtained through a mapping between the original and deformed configurations. This is the basis of the general relationship between the Cauchy stress (σ_{ij}) and the PK2 stress (S_{kl}), i.e.

$$\sigma_{ij} = \frac{1}{J} S_{kl} \frac{\partial x_i}{\partial X_k} \frac{\partial x_j}{\partial X_l} \qquad \ldots (5.27)$$

in which $\frac{\partial x}{\partial X}$ are the components of the deformation gradient tensor (Malvern, 1969). Since the deformation here involves only plane stresses, the deformation gradients are equivalent to the principal stretch ratios, and therefore

$$\sigma_1 = \frac{1}{J} S_1 \lambda_1^2 \quad \text{and} \quad \sigma_2 = \frac{1}{J} S_2 \lambda_2^2 \qquad \ldots (5.28a, 5.28b)$$

For yeast cells, because the deformations required to burst yeast cells are large (Mashmoushy *et al.,* 1998), large strain assumptions may well be essential, and this has never been done in an analytical model. For example, Smith (1999), Wang *et al.* (2004) and (for analysis of the compression of pollen grains) Liu and Zhang (2004) used mixed low and high assumptions, by introducing an infinitesimal definition of strain (equation 5.9) into the large strain relations, resulting in a mixed strain approach. Smith *et al.* (1998) validated their finite element code against the analytical equations found in Smith (1999). There were discrepancies, which were attributed by Smith et al. (1998) to the inability of the analytical model to account for wall thinning, but may have been caused (at least in part) by using the mixed strain approach in the analytical model. In the present work the equations are reformulated, to allow typical yeast compression data to be fitted.

Whether or not the cell wall is assumed to be incompressible ($J = 1$), the cell wall thickness may decrease during stretching of the cell wall in the compression experiment. Several models ignore this change, and in some circumstances it may indeed be negligible. Nevertheless, cell wall thinning will be incorporated here for completeness.

5.3. Model of the compression

The equations governing the deformation of the cell have been given in Section 5.1. In using these equations, 5.8a to 5.8c, the stretch ratios must be related to an appropriate choice of strain measure (equations 5.9 to 5.11), and in each case the corresponding definition of stress (equations 5.12 to 5.14) must be used. The final stage of the modelling is to use the strain energy functions of equations 5.21, 5.23 and 5.24 to derive stresses from which tensions can be derived for use in equations 5.8a to 5.8c. Here the relations for infinitesimal strain will be derived first, followed by those for Green strain and finally Hencky strain.

Infinitesimal Strain

For the limiting case of infinitesimal strain, the strain energy function for the cell wall is that given in equation 5.20. This gives rise to the familiar plane-stress equations.

$$\sigma_1 = \frac{E}{\left(1-\nu^2\right)}\left(\varepsilon_1 + \nu\varepsilon_2\right) \qquad \text{and} \qquad \sigma_2 = \frac{E}{\left(1-\nu^2\right)}\left(\varepsilon_2 + \nu\varepsilon_1\right) \qquad \ldots (5.29a, 5.29b)$$

The principal Cauchy tensions in the wall may be defined as

$$T_1 = \sigma_1 h \qquad \text{and} \qquad T_2 = \sigma_2 h \qquad \ldots (5.30a, 5.30b)$$

where h is the (current) wall thickness. Since an infinitesimal strain approach is adopted, any change in the initial uninflated cell wall thickness (h_o) and final (h) cell wall thickness is assumed to be negligible, so $h \approx h_o$. Then, from equations 5.29 and 5.30:

$$T_1 = \frac{Eh_0}{1-\nu^2}\{(\lambda_1 - 1) + \nu(\lambda_2 - 1)\} \quad \ldots (5.31a)$$

$$T_2 = \frac{Eh_0}{1-\nu^2}\{(\lambda_2 - 1) + \nu(\lambda_1 - 1)\} \quad \ldots (5.31b)$$

respectively. This approach was adopted by Wang *et al.* (2006) as a simplification of an earlier model published by Wang *et al.* (2004).

Because a constant Poisson's ratio has been assumed, these expressions for the tensions may be used in equations 5.8a to 5.8c, to give

$$f_1 = \frac{\partial T_1}{\partial \lambda_1} = \frac{Eh_o}{(1-\nu^2)} \quad \ldots (5.32a)$$

$$f_2 = \frac{\partial T_1}{\partial \lambda_2} = \frac{\nu Eh_o}{(1-\nu^2)} \quad \ldots (5.32b)$$

$$f_3 = T_1 - T_2 = \frac{Eh_o(\lambda_1 - \lambda_2)(1-\nu)}{(1-\nu^2)} = \frac{Eh_o(\lambda_1 - \lambda_2)}{(1+\nu)} \quad \ldots (5.32c)$$

For incompressible deformation these simplify to

$$f_1 = \frac{\partial T_1}{\partial \lambda_1} = \frac{4}{3} Eh_o \quad \ldots (5.33a)$$

$$f_2 = \frac{\partial T_1}{\partial \lambda_2} = \frac{2}{3} Eh_o \quad \ldots (5.33b)$$

$$f_3 = T_1 - T_2 = \frac{2}{3} E h_o \left(\lambda_1 - \lambda_2\right) \quad \ldots (5.33c)$$

Finite (Green) Strain

Since in this model, large deformation, and hence finite (Green) strains are assumed, any strain energy functions must be formulated in terms of the 2nd Piola-Kirchhoff (PK2) stresses (Malvern, 1969). The true (Cauchy) stress may be obtained through a mapping between the original and deformed configurations using equations 5.28a and b. The principal PK2 stresses may be determined from the strain energy function given in equation 5.23, and using the definition of Green strain given in equation 5.10, these may be written in terms of the principal stretch ratios as

$$S_1 = \frac{1}{\lambda_1}\frac{\partial W}{\partial \lambda_1} \quad \text{and} \quad S_2 = \frac{1}{\lambda_2}\frac{\partial W}{\partial \lambda_2} \quad \ldots (5.34a, 5.34b)$$

The Cauchy stresses are then

$$\sigma_1 = \frac{\lambda_1}{J}\frac{\partial W}{\partial \lambda_1} \quad \text{and} \quad \sigma_2 = \frac{\lambda_2}{J}\frac{\partial W}{\partial \lambda_2} \quad \ldots (5.35a, 5.35b)$$

As earlier, the principal Cauchy tensions in the wall are defined as

$$T_1 = \sigma_1 h \quad \text{and} \quad T_2 = \sigma_2 h \quad \ldots (5.30a, 5.30b)$$

where h must be the current membrane wall thickness, for consistency with the use of Cauchy stresses in a finite strain model.

Since finite strains are assumed here, the change in cell wall thickness might be important and the true stresses (or tensions) must be defined in terms of the current dimensions. From equation 5.26, noting that

$$\lambda_3 = \frac{h}{h_o} \qquad \ldots (5.36)$$

and

$$h = \frac{Jh_o}{\lambda_1 \lambda_2} \qquad \ldots (5.37)$$

From equations 5.30, 5.35 and 5.37, expressions or T_1 and T_2 may be found.

$$T_1 = \frac{h_o}{\lambda_2}\frac{\partial W}{\partial \lambda_1} \qquad \text{and} \qquad T_2 = \frac{h_o}{\lambda_1}\frac{\partial W}{\partial \lambda_2} \qquad \ldots (5.38a, 5.38b)$$

The appropriate expression for W can be found from equation 5.23, including the definition of Green strain from equation 5.10,

$$W = \frac{E}{8\left(1-\nu^2\right)}\left(\left(\lambda_1^2-1\right)^2 + \left(\lambda_2^2-1\right)^2 + 2\nu\left(\lambda_1^2-1\right)\left(\lambda_2^2-1\right)\right) \qquad \ldots (5.39)$$

Differentiating with respect to each principal stretch ratio,

$$\frac{\partial W}{\partial \lambda_1} = \frac{E\lambda_1}{2\left(1-\nu^2\right)}\left(\left(\lambda_1^2-1\right)+\nu\left(\lambda_2^2-1\right)\right) \quad \ldots (5.40a)$$

$$\frac{\partial W}{\partial \lambda_2} = \frac{E\lambda_2}{2\left(1-\nu^2\right)}\left(\left(\lambda_2^2-1\right)+\nu\left(\lambda_1^2-1\right)\right) \quad \ldots (5.40b)$$

Substituting into equations 5.38a and 5.38b gives

$$T_1 = \frac{Eh_0}{2\left(1-\nu^2\right)}\frac{\lambda_1}{\lambda_2}\left(\left(\lambda_1^2-1\right)+\nu\left(\lambda_2^2-1\right)\right) \quad \ldots (5.41a)$$

$$T_2 = \frac{Eh_0}{2\left(1-\nu^2\right)}\frac{\lambda_2}{\lambda_1}\left(\left(\lambda_2^2-1\right)+\nu\left(\lambda_1^2-1\right)\right) \quad \ldots (5.41b)$$

which may then be used in equations 5.8a to 5.8c to give

$$f_1 = \frac{\partial T_1}{\partial \lambda_1} = \frac{Eh_o}{2\left(1-\nu^2\right)}\left\{3\lambda_1^2+\nu\lambda_2^2-\left(1+\nu\right)\right\} \quad \ldots (5.42a)$$

$$f_2 = \frac{\partial T_1}{\partial \lambda_2} = \frac{Eh_o}{2\left(1-\nu^2\right)}\frac{\lambda_1}{\lambda_2^2}\left\{\nu\lambda_2^2-\lambda_1^2+\left(1+\nu\right)\right\} \quad \ldots (5.42b)$$

$$f_3 = T_1 - T_2 = \frac{Eh_o}{2\left(1-\nu^2\right)}\left\{\frac{\lambda_1}{\lambda_2}\left[\lambda_1^2-\left(1+\nu\right)\right]-\frac{\lambda_2}{\lambda_1}\left[\lambda_2^2-\left(1+\nu\right)\right]\right\} \quad \ldots (5.42c)$$

If incompressibility is assumed, i.e. v = 0.5, equations 5.42a to 5.42c become

$$f_1 = \frac{\partial T_1}{\partial \lambda_1} = \frac{Eh_o}{\lambda_2}\left\{2\lambda_1^2 + \frac{\lambda_2^2}{3} - 1\right\} \quad \ldots (5.43a)$$

$$f_2 = \frac{\partial T_1}{\partial \lambda_2} = Eh_o \frac{\lambda_1}{\lambda_2^2}\left\{\frac{\lambda_2^2}{3} - \frac{2}{3}\lambda_1^2 + 1\right\} \quad \ldots (5.43b)$$

$$f_3 = T_1 - T_2 = \frac{2Eh_o}{3}\left\{\frac{\lambda_1}{\lambda_2}\left[\lambda_1^2 - \frac{3}{2}\right] - \frac{\lambda_2}{\lambda_1}\left[\lambda_2^2 - \frac{3}{2}\right]\right\} \quad \ldots (5.43c)$$

Hencky (logarithmic) Strain

Using this measure of strain, most appropriate for large deformations and large strains, the required stress is the Kirchhoff stress. This is related to the Cauchy stress by

$$\tau_i = J\sigma_i \quad \ldots (5.25)$$

The principal components are once again

$$\sigma_1 = \frac{\lambda_1}{J}\frac{\partial W}{\partial \lambda_1} \quad \text{and} \quad \sigma_2 = \frac{\lambda_2}{J}\frac{\partial W}{\partial \lambda_2} \quad \ldots (5.35a, 5.35b)$$

and, allowing for wall thinning, the tensions are

$$T_1 = \frac{h_o}{\lambda_2}\frac{\partial W}{\partial \lambda_1} \quad \text{and} \quad T_2 = \frac{h_o}{\lambda_1}\frac{\partial W}{\partial \lambda_2} \quad \ldots (5.38a, 5.38b)$$

In terms of principal stretch ratios, using equation 5.11, the strain energy function in equation 5.24 becomes

$$W = \frac{E}{2(1-\nu^2)}\left((\ln\lambda_1)^2 + (\ln\lambda_2)^2 + 2\nu\ln\lambda_1\ln\lambda_2\right) \quad \ldots (5.44)$$

Differentiating with respect to each principal stretch ratio and substituting in equations 5.38a and 5.38b

$$T_1 = \frac{Eh_o}{\lambda_1\lambda_2(1-\nu^2)}\left(\ln(\lambda_1) + \nu\ln(\lambda_2)\right) \quad \ldots (5.45a)$$

$$T_2 = \frac{Eh_o}{\lambda_1\lambda_2(1-\nu^2)}\left(\ln(\lambda_2) + \nu\ln(\lambda_1)\right) \quad \ldots (5.45b)$$

which may then be used in equations 5.8a to 5.8c to give

$$f_1 = \frac{\partial T_1}{\partial\lambda_1} = \frac{Eh_o}{\lambda_1^2\lambda_2(1-\nu^2)}\left\{1 - \ln(\lambda_1) - \nu\ln(\lambda_2)\right\} \quad \ldots (5.46a)$$

$$f_2 = \frac{\partial T_1}{\partial\lambda_2} = \frac{Eh_o}{\lambda_1\lambda_2^2(1-\nu^2)}\left\{\nu - \nu\ln(\lambda_2) - \ln(\lambda_1)\right\} \quad \ldots (5.46b)$$

$$f_3 = T_1 - T_2 = \frac{Eh_o}{\lambda_1\lambda_2(1+\nu)}\ln\left\{\frac{\lambda_1}{\lambda_2}\right\} \quad \ldots (5.46c)$$

For the incompressible case used in this work

$$f_1 = \frac{\partial T_1}{\partial \lambda_1} = \frac{2Eh_o}{3\lambda_1^2\lambda_2}\left\{2 - \ln\left(\lambda_1^2\lambda_2\right)\right\} \quad \ldots (5.47a)$$

$$f_2 = \frac{\partial T_1}{\partial \lambda_2} = \frac{2Eh_o}{3\lambda_1\lambda_2^2}\left\{1 - \ln\left(\lambda_1^2\lambda_2\right)\right\} \quad \ldots (5.47b)$$

$$f_3 = T_1 - T_2 = \frac{2Eh_o}{3\lambda_1\lambda_2}\ln\left\{\frac{\lambda_1}{\lambda_2}\right\} \quad \ldots (5.47c)$$

The expressions in 5.32, 5.42 and 5.46 (or 5.33, 5.43 and 5.47 for the incompressible case) provide the functions required to solve equations 5.1 to 5.7, using the following boundary conditions (Liu *et al.*, 1996):

$$\psi = 0, \lambda_1 = \lambda_2 = \lambda_o$$

$$\psi = \Gamma, \lambda_1\left(contact\ region\right) = \lambda_1\left(non\text{ - }contact\ region\right)$$

$$\psi = \Gamma, \lambda_2\left(contact\ region\right) = \lambda_2\left(non\text{ - }contact\ region\right)$$

$$\psi = \Gamma, \eta = \overline{\eta}$$

$$\psi = \Gamma, \eta' = 0 \text{ or } \omega = \lambda_1$$

$$\psi = \frac{\pi}{2}, \omega = 0$$

where Γ identifies the angle of the points on the edge of the contact region between the compression surface and the cell, η is the horizontal coordinates and $\overline{\eta}$ is the distance between the compression surface and the equatorial plane (see Figure 5.2).

In this work, it was decided to assume incompressibility of the cell walls as there is no information available on this parameter, and this follows the approach of most previous workers, as described earlier. However, the more general equations 5.33, 5.43 and 5.47 would allow this assumption to be revisited if better information on Poisson's ratio should become available. The significance of this incompressibility assumption to the determination of the elastic modulus is discussed later.

5.4. Numerical simulation

The governing equations were solved by the Runge-Kutta method using the MATLAB ode45 solver (The MathWorks Inc., Cambridge, UK). The method for solving these equations has been outlined in Wang *et al.* (2004). The program code for the mathematical model is given in Appendix 11. The cell wall material is considered to be time independent (i.e. negligible viscoelasticity) which allowed the simulation to be solved as a series of static equilibrium problems. In each step of the simulation the probe is displaced the set amount depending on the time length of each step and the speed of compression. This probe displacement compresses and deforms the cell a certain amount following which the pressure inside the cell is adjusted until a number of boundary conditions are met including a constant cell volume. It is important to note here that the analytical model is using a single step from the inflated un-deformed state to the compressed state (Section 5.2). The fluid contents of the cell are assumed to be incompressible and the cell wall is assumed to be impermeable. The solution method for equations 5.1 to 5.7 is outlined in the following flow chart. The same procedure was followed for all the material models.

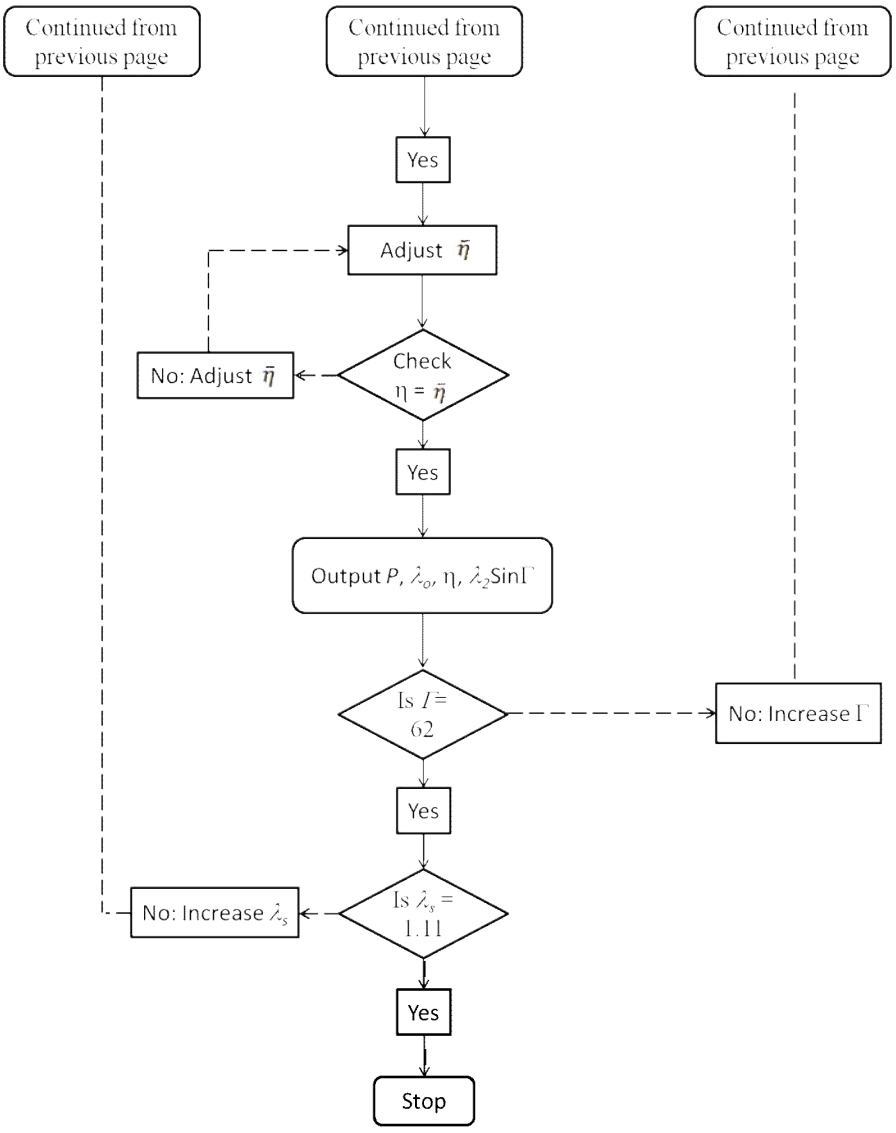

Flowchart 5.1: Flow chart for solving the membrane model equations. E = elastic modulus of the cell wall, r_o = cell radius, h_o = cell wall thickness, P = internal pressure of the cell, λ_o = stretch ratio, λ_s = initial stretch ratio, V_o = initial volume of the cell, V = volume of the cell following step.

At the end of each step the volume of the cell is determined and the cell boundary co-ordinates ρ and η calculated. In all cases the error in volume after each increase in contact angle was found to be less than 10^{-7} of the initial volume.

Once all of the boundary conditions have been satisfied corresponding values for the pressure (P) and the deformation ($\bar{\eta}$) are generated. From this force (F) and deformation (X) data can be obtained using the following equations:

$$F = PA_c \quad \ldots (5.48)$$

where P is the turgor pressure and A_c is the contact area between the probe and the cell calculated using:

$$A_c = \pi\left(r_o \lambda_2 \sin\Gamma\right)^2 \quad \ldots (5.49)$$

The deformation of the cell is defined using:

$$X = \frac{z}{r_o \lambda_s} = 1 - \frac{\bar{\eta}}{r_o \lambda_s} \quad \ldots (5.50)$$

where z is half the distance that the cell has been compressed (Figure 5.2).

Following this procedure dimensional force - deformation data was produced whose shape and magnitude was dependent on the initial modelling parameters.

5.5. Comparison of infinitesimal, Green and Hencky strain models

The elastic membrane models that have been developed in Section 5.3 are compared to determine the effect that the different strain definitions have on the numerical simulation results.

5.5.1. Force - deformation data

Figure 5.5 compares force - deformation data produced using the three different strain definitions. As an illustration the elastic modulus (E = 100 MPa), initial stretch ratio (λ_s = 1.04), cell radius (r_o = 2.5 μm), cell wall thickness (h_o = 92.5 nm) and Poisson ratio (ν = 0.5) were assigned to allow the output from the different models to be compared. The appropriateness of these parameters will be discussed in detail later (Section 5.7). Dimensionless parameters, which are also discussed later (Section 5.7), were used for this comparison.

It can be seen that the choice of strain measure is important, especially for the higher deformations needed to induce cell breakage.

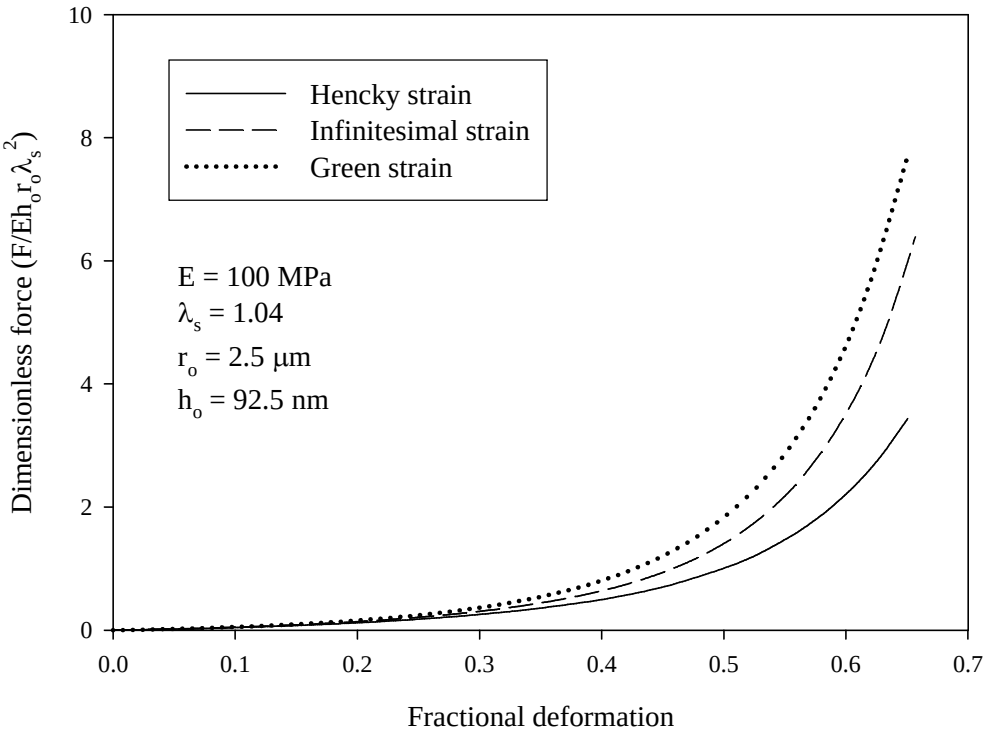

Figure 5.5: Comparison of the force - deformation results obtained from numerical simulations. E = 100 MPa, λ_s = 1.04, r_o = 2.5 μm, h_o = 92.5 nm

Figure 5.5 shows that at a given deformation the strain definition chosen in the material model will lead to a significantly different dimensionless force. This result may imply that different material properties will be obtained from modelling experimental data, which will be investigated later (Section 6.1.4). As described previously (Section 5.2) the infinitesimal strains are intended as an approximation suitable only for small deformations where the strain is of the order of 0.1 %. At higher strains, the infinitesimal strain model does not allow properly for rigid body movements, i.e. rotation and translation. Such movements may lead to incorrect estimates of force at higher deformations, leading to underestimation of the elastic modulus. The Green strain model is better, as it is able to take into account rigid body motion; although it should not be applied when large deformations are accompanied by large strains. However, if this model is used over small increments of

deformation, as in incremental finite element analyses, it should give results close to that of the Hencky strain (Figure 5.4 - effect of incremental stretch on strain).

As has been previously discussed (Section 5.2) when large increments of deformation are used the choice of strain is important. As was shown in Figure 5.3 (Section 5.2) up to a stretch of 1.05 the strain calculated using the three different measurements is indistinguishable and above this value differ greatly. The numerical simulations showed that at high fractional deformations the circumferential (hoop direction) stretch ratio in the wall at the equator of the cell will be significantly higher than 1.05 as shown in Figure 5.6.

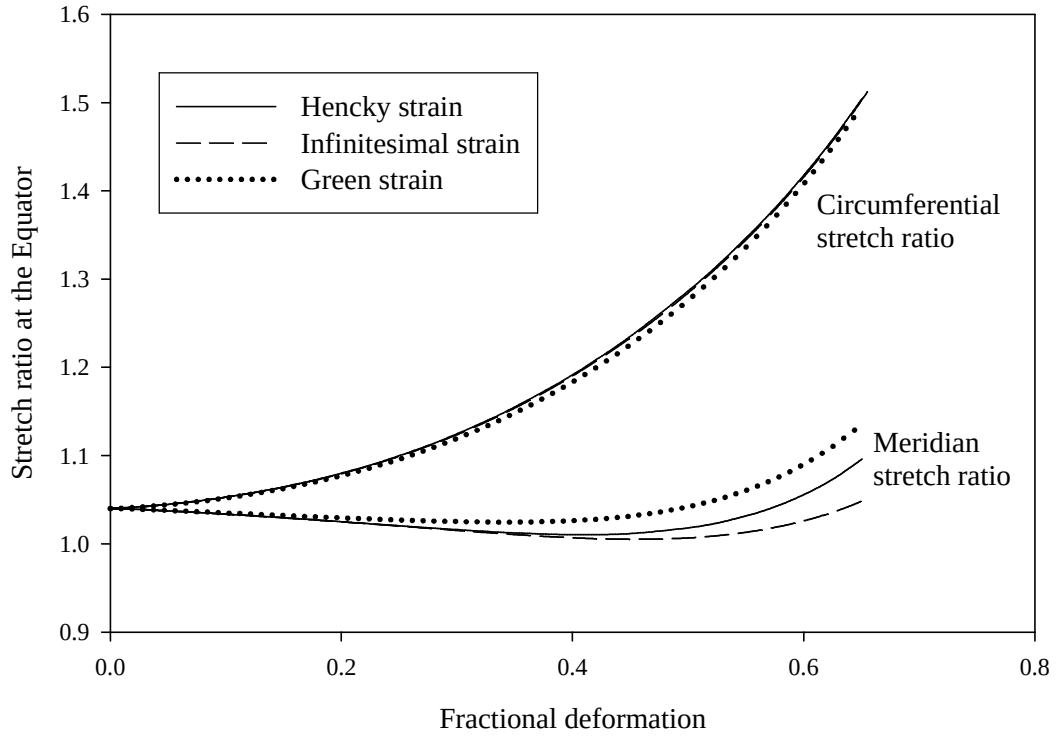

Figure 5.6: Stretch ratio at the equator of the cell during compression from numerical simulations. E = 100 MPa, λ_s = 1.04, r_o = 2.5 μm, h_o = 92.5 nm, ν = 0.5

As is clearly shown (Figure 5.6) the stretch ratio in the circumferential direction of the cell is higher than 1.5 and in the meridian direction 1.1. These stretch values are significantly

higher than 1.05 at which the three strain definitions begin to diverge. This result along with Figure 5.3 (Section 5.2) explains the large differences in the force - deformation curves obtained from the numerical simulations.

5.5.2. Strain and stress

Using any of the models, the strains in the meridian and the circumferential directions at any location on the cell boundary can be calculated, for any deformation. In particular the values at the equator were found as this is where cell wall failure is thought to occur. Both the strain and the stress in the cell wall are of interest as the mechanism of failure is as yet unkown. Figure 5.7 shows the equatorial strains in the circumferential and meridian direction over the compression calculated using equations 5.7, 5.8 and 5.9.

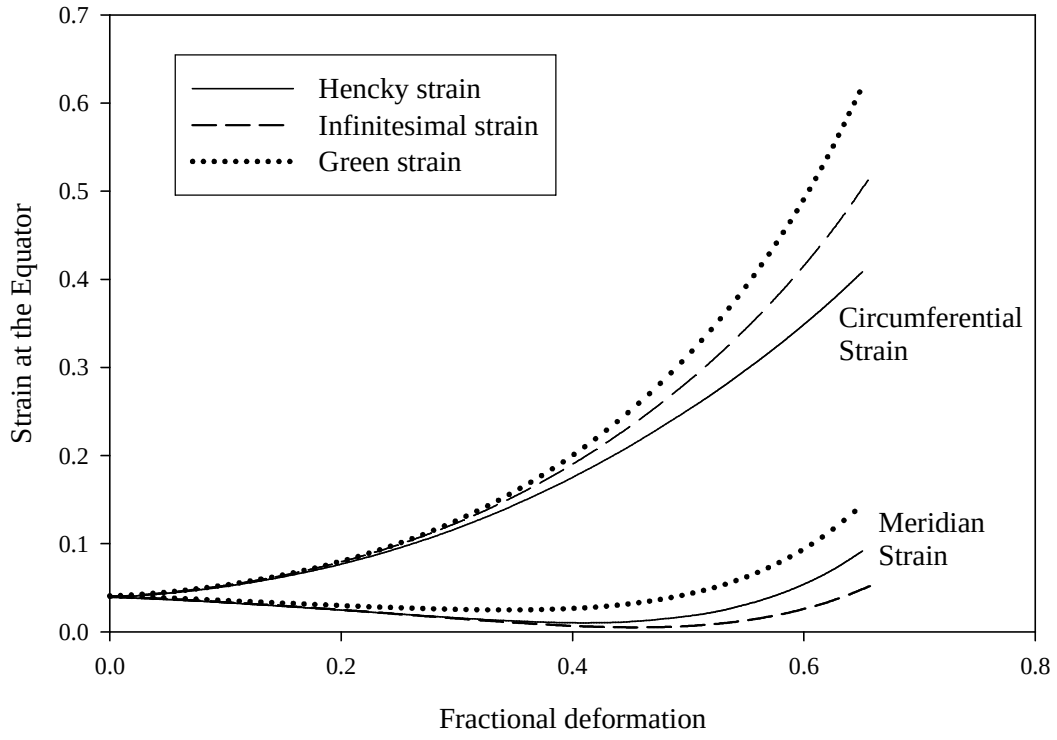

Figure 5.7: Strain at the equator of the cell during deformation. E = 100 MPa,

$\lambda_s = 1.04$, $r_o = 2.5\ \mu m$, $h_o = 92.5\ nm$, $\nu = 0.5$

Figure 5.7 shows the strain in the cell wall at the equator of the cell during compression using the stretch data from Figure 5.6. At small deformations the meridian strain actually decreases while the circumferential strain increases. Also the circumferential strain can be up to 5 fold greater than the meridian strain. It was found that for deformations above 30 % the largest strain always occurred at the equator of the cell a result confirming similar observations of Cheng (1987b). Lardner and Pujara (1980) found that the tensions in the wall are highest at the equator for deformations above 40 %. However, Feng and Yang (1973) found that the tensions in the wall are always highest at the equator of the cell. This may occur as Feng and Yang (1973) do not assume that the enclosed volume of the cell should remain constant during compression; instead their analysis assumes a constant pressure is maintained. This may be the reason for the differences seen between the tensions

calculated by Lardner and Pujara (1980) and Feng and Yang (1973) as the rest of the model formulation was identical.

Using the data in Figure 5.7 it is possible to calculate the stress at the equator of the cell during compression.

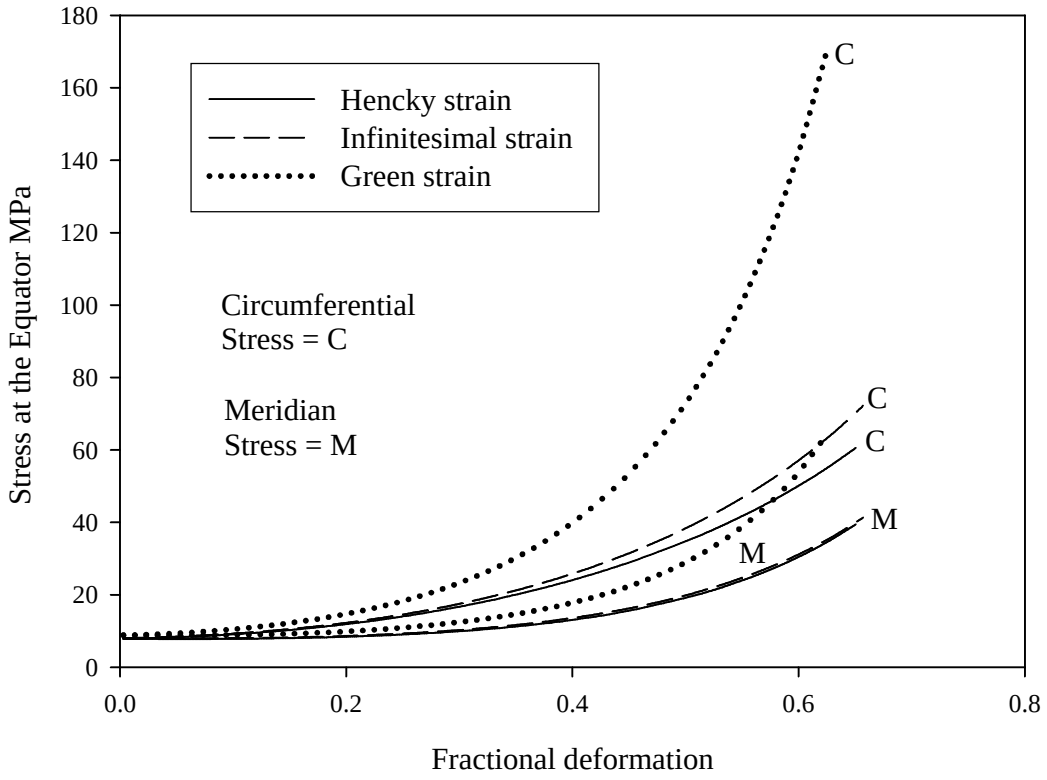

Figure 5.8: Stress at the equator of the cell during compression. E = 100 MPa,

$\lambda_s = 1.04$, $r_o = 2.5\ \mu m$, $h_o = 92.5\ nm$, $\nu = 0.5$

It is clear that like the strains the circumferential stress is higher than the stress in the meridian direction. As with the strain the wall stresses are far from homogeneous. Unlike meridian strain the stress does not decrease at the lower fractional deformations. This occurs as the stresses are calculated using both the circumferential and meridian strains (equations 5.35b and 5.44) which are up to 5 fold different (Figure 5.7).

5.5.3. Cell profile

The simulations also provided profiles of the compressed cell, with a typical example shown in Figure 5.9. In order to determine if the strain definition most appropriate for use with yeast cells could be independently verified by visual observation of cells during compression experiments, the effect on the cell profiles from the model was investigated. The profiles are axisymmetric about the axis of compression and symmetrical across the equatorial plane, allowing them to be fully characterised with just one quadrant. In these simulations, the same force and deformation was used, to match a specific experimental condition. The profiles were all generated at a deformation of 62 %, initial stretch ratio of 1.04, cell radius 2.5 μm and a cell wall thickness of 92.5 nm. The elastic modulus of the Hencky strain model was set at 100 MPa with the elastic modulus of the Infinitesimal and Green strain models adjusted to fit. The same relationships could be shown at all deformations, cell radius and cell wall thickness. As can be seen in Figure 5.9 the cell profiles are similar for all of the different strain definitions although there are small differences at the point of contact between the probe and the cell and close to the equator of the cell. However, the resolution required during compression testing to distinguish between these models is currently far beyond that possible for yeast cells using the equipment described in Section 3.2.3. Unfortunately this means that independent verification of the correctness of the Hencky strain model using image analysis of the cell shape is impractical.

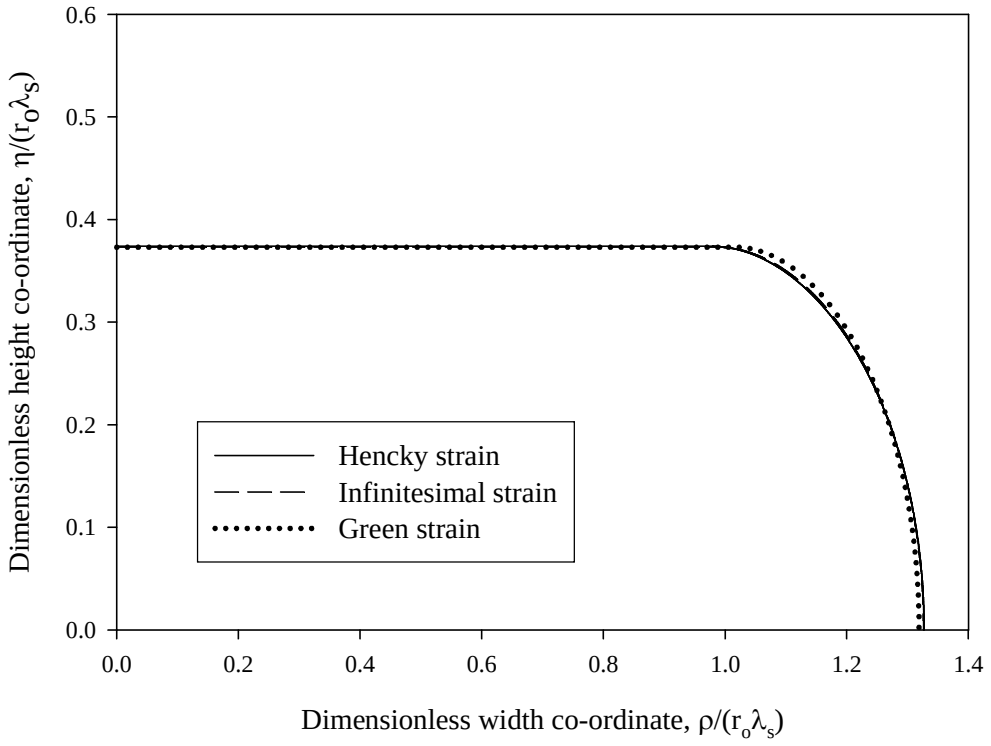

Figure 5.9: Cell profiles at the same deformation using Hencky, Infinitesimal and Green strain models. E= 100 MPa, r_o = 2.5 μm, h_o= 92.5 nm, λ_s= 1.04, ν = 0.5

5.6. Comparison of preferred Hencky strain model with the previously developed finite element model.

A dimensionless force - deformation curve from the Hencky strain analytical model is shown in Figure 5.10 along with the results obtained from two finite element packages using the same parameter values. The purpose was to examine how the different methods of simulation compare. Simulated force - deformation data for compression testing was taken from Smith *et al.* (1999; 2000b) who used LUSAS finite element software (LUSAS v12.1, FEA (Australia) Pty Ltd, Cheltenham, Victoria, Australia). In this model the probe and cell were represented by 4-noded solid elements which include membrane forces and in-plane

shear but neglect out of plane shear and bending moments. Incompressibility in the cell wall was approximated by setting Poisson ratio to 0.499. An Eulerian formulation using logarithmic strains and Cauchy stresses is used in LUCAS, which are updated during each increment of deformation. The cell wall material was taken to be time independent and the compression was solved as a series of static equilibrium problems.

In addition, simulated force - deformation data was produced using ABAQUS finite element software (SIMULIA UK, Warrington, UK) by Bac Nguyen (unpublished work – personal communication). Both these packages used linear elastic material models with Hencky strains and Cauchy stresses and assumed incompressibility of the cell wall.

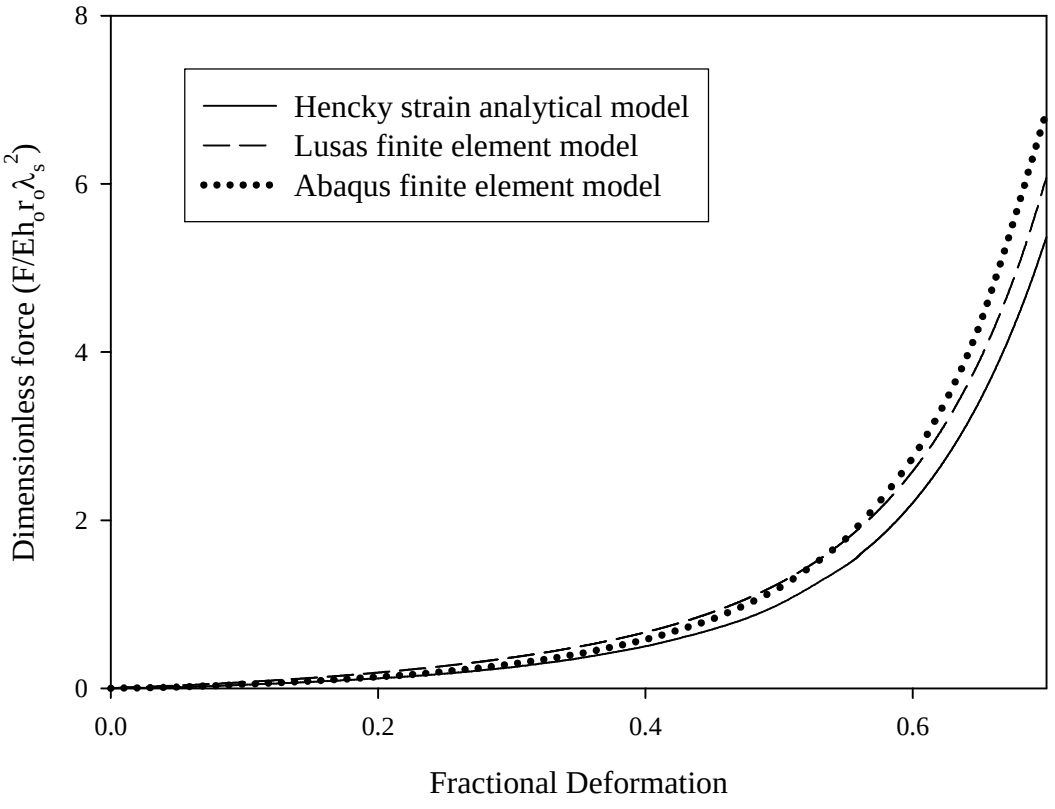

Figure 5.10: Comparison of the Hencky strain analytical model with LUCAS and ABAQUS Finite element packages. E= 100 MPa, r_o = 2.5 μm, h_o= 92.5 nm, λ_s= 1.04, ν = 0.5.

Figure 5.10 shows that the finite element models and the Hencky strain analytical model produce different outputs using the same initial modelling parameters. As shown by the difference in the two finite element simulations, even with the same strain definitions it appears that other assumptions, such as the element composition and mesh density, influence the result. Analytical models have the advantage of being easily understood by workers from a wide range of research fields with all assumptions of the model being fully describable. In contrast finite element analysis is often used as a "black box" except by expert users. Ideally, all finite element models would be validated with an appropriate analytical model to confirm correct formulation. The data in Figure 5.10 show that the finite element models did not validate each other as well as not agreeing with the analytical model.

The analytical model developed in this work is very simple and might not be expected to be identical to the finite element models. One simplifying assumption of the former is the use of a constant Poisson ratio over large deformations (see comment after equation 5.22). In general, it is unclear why there are differences between the models. However, all of the models would produce elastic modulus from experimental data of similar magnitude.

5.7. Data analysis

Numerical simulations produce force - deformation curves whose magnitude and shape are determined by the initial model parameters including the cell radius (r_o), cell wall thickness (h_o), elastic modulus (E), initial stretch ratio (λ_s), cell permeability (Lp) and the Poisson ratio (ν). These parameters can be determined by fitting the force - deformation curves obtained from the numerical simulations to the experimental data. However, there may be non-unique

solutions, i.e. different combinations of model parameter values can produce matching simulation results (at least within the precision of the experiments). To prevent such non-unique solutions being obtained, direct measurements of at least two of Lp, λ_s, and h_o are required, even if the wall can be assumed *a priori* to be linear elastic. The remaining parameters are then adjustable and can be determined by model fitting (Smith *et al.*, 1998).

In the following sections a series of simulations were run to see how variations in the initial parameters affect the magnitude and shape of the force - deformation curves. In addition to this the dimensionless groups used for fitting and the assumption of incompressibility (Poisson ratio set to 0.5) were investigated.

5.7.1. Dimensionless groups

In the process of matching simulations to experimental data, comparisons are made of the simulated and experimental forces in dimensionless form. Dimensionless groups were defined by Feng and Yang (1973) for a model that used a Mooney Rivlin constitutive equation. The dimensionless force and fractional deformation used in this work were defined by Lardner and Pujara (1980; 1979) and have been used by other authors in this field of study (Wang *et al.*, 2004; Liu *et al.*, 1996). In addition to this the dimensionless force proposed by Smith *et al.* (2000b) was also investigated.

Dimensionless group	**Form**
Lardner and Pujara (1980; 1979) :	
Force - $\hat{F}$	$\frac{F}{\left(Eh_o r_o \lambda_s^2\right)}$
Fractional deformation - X	$\frac{z}{r_o \lambda_s}$
Cell wall thickness to cell radius ratio - τ	$\frac{h_o}{r_o}$
Initial stretch ratio - λ_s	$\frac{r_i}{r_o}$
Smith *et al.* (2000b):	
Force - F_{smith}	$\frac{F}{\left(Er_i^2\right)}$

Table 5.2: Dimensionless groups used in this work. E = elastic modulus, h_o = cell wall thickness, r_o = cell radius, z = half the displacement of the probe.

Section 5.7.2 shows the dimensional and dimensionless force - deformation curves obtained from the numerical simulations using the initial parameters shown in Table 5.3. For all of this work fractional deformation and not displacement is used. Also only the data obtained using the Hencky strain analytical model is presented.

Parameter	**Symbol**	**Value**
Initial stretch ratio	λ_s	1.01, 1.04, 1.07, 1.1
Un-inflated cell radius	r_o	2.5 μm, 5 μm, 7.5 μm
Elastic modulus	E	100 MPa, 200 Mpa, 500 Mpa
Cell wall thickness	h_o	45 nm, 92.5 nm, 138 nm
Volume loss during compression	Lp	Zero
Poisson ratio	ν	0.5, 0.4, 0.3

Table 5.3: Initial modelling parameters used in the parametric study

Water loss due to cell permeability has been shown previously to be a function of the compression speed, at least for plant cells (Wang *et al.*, 2004). Due to this it was decided to consider only speeds of compression at which the effects of cell permeability could be considered negligible. No force - deformation curves involving water loss are presented here.

5.7.2. *Elastic modulus, cell size, and cell wall thickness*

Elastic modulus

Prior to the fitting of the numerical simulations to the experimental data the elastic modulus was unknown. Previous authors have given values of the elastic modulus ranging from 124 MPa up to 165 MPa (Smith, 1999). On this basis, numerical simulations were run with an elastic modulus value ranging from 100 MPa to 500 MPa. The dimensional and dimensionless data obtained from this are shown in Figure 5.11.

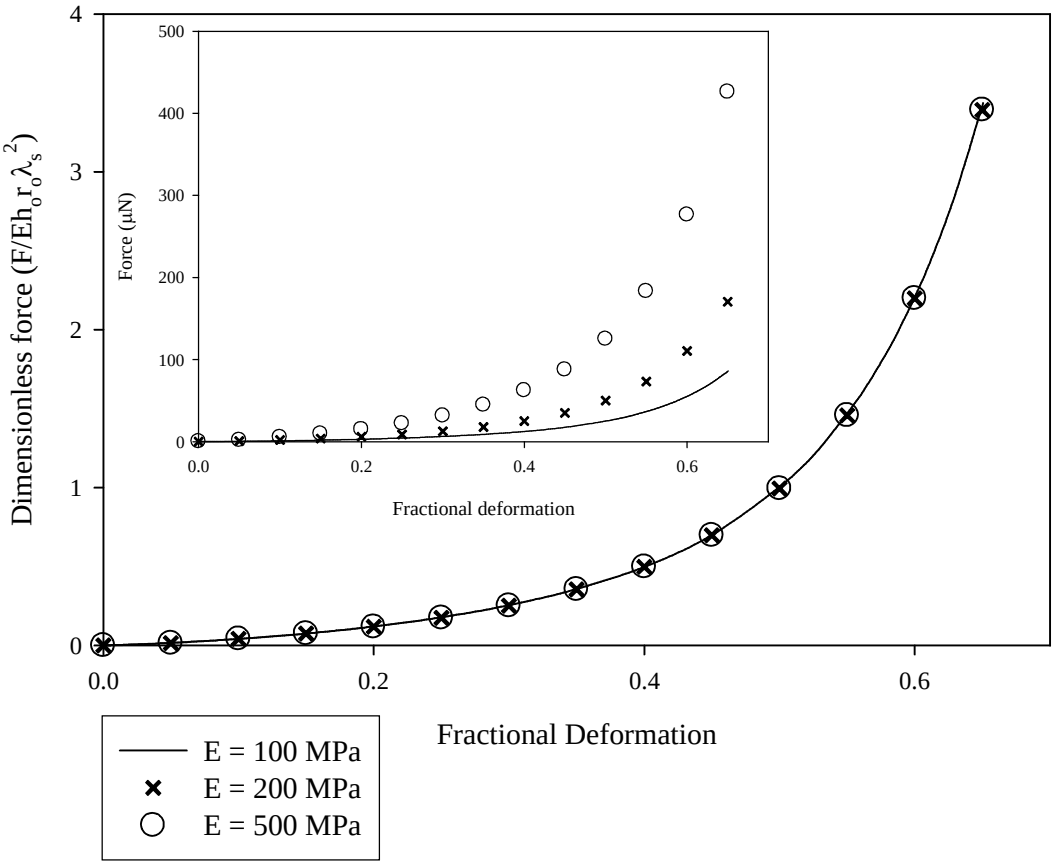

Figure 5.11: Effect of changing the elastic modulus on the force - deformation data and the dimensionless force. E = 100, 200, 500 MPa, r_o = 2.5 μm, h_o= 92.5 nm, λ_s= 1.04, ν = 0.5

As is clear in the inset to Figure 5.11, increasing the elastic modulus significantly increased the magnitude of the force for a given deformation. This increase occurred as an increase in elastic modulus leads to an increase in the stiffness of the cell wall and so resistance to deformation. When the dimensionless force was used all of the data lay on the same line. This result means it is possible to compare dimensionless data from the numerical simulations to dimensionless experimental data with a different elastic modulus. The fitting process is discussed in detail later (Chapter 6). In all the following simulations presented in this Chapter an elastic modulus of 100 MPa was used.

A similar result to that shown in Figure 5.11 was found when using the dimensionless group (F/Er_i^2).

Cell size

The cell radius was measured directly from the experimental compression data (Section 3.2.4). As has been shown previously, yeast cells vary greatly in diameter between 3 and 8 μm depending on the cell strain (Srinorakutara, 1997; Kleinig *et al.*, 1997). Due to this a wide range of cell sizes were used in the numerical simulation up to a cell diameter of 15 μm. Figure 5.12 shows the force - deformation curves and dimensionless force - deformation curves with different cell radius.

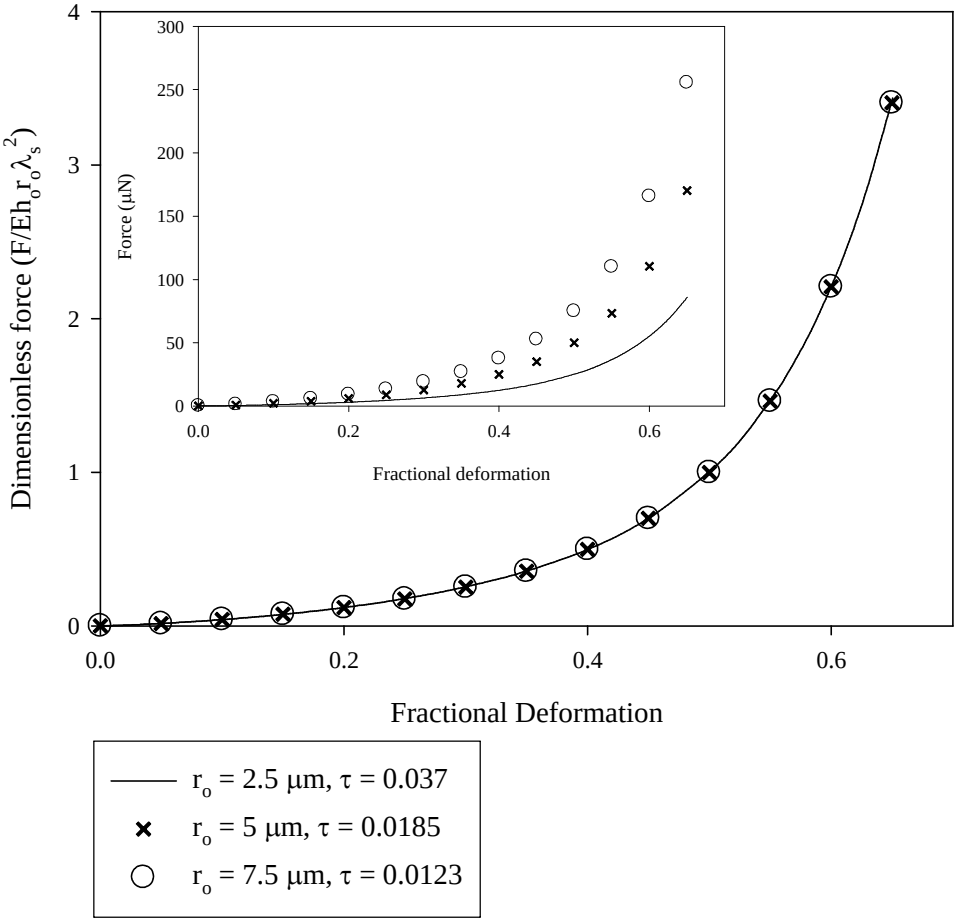

Figure 5.12: Simulated dimensionless force - deformation data and force - deformation data (inset) with varying cell diameter. E= 100 MPa, r_o = 2.5, 5 and 7.5 μm, h_o= 92.5 nm, λ_s= 1.04, ν = 0.5

As can be seen in Figure 5.12 the change in cell radius had a significant effect on the force - deformation data from the numerical simulations. As expected an increase in the cell radius significantly increased the force at equivalent deformations. As can also be seen in Figure 5.12 , when the dimensionless force was used the simulations produced the same curve. This is important as it means that it is possible to compare dimensionless data from the numerical simulations with cell radii different to those used to obtain the dimensionless experimental data. It should be noted that using different cell radii whilst keeping the cell wall thickness

constant has the effect of using a size dependent τ. The effect of varying the τ is discussed in the next section. A similar result to that shown in Figure 5.12 was found when using the dimensionless group (F/Er_i^2).

From the force - deformation data (inset in Figure 5.12) it can be seen that if the cells fail at the same force then this would occur in larger cells at a lower deformation than smaller cells. This relationship is discussed further in Section 7.2.6.1.

Cell wall thickness

The cell wall thickness could be calculated using a previously determined cell wall thickness to cell radius ratio, an average for the sample of cells (Section 6.1.2).

As can be seen in Figure 5.13, the assumption about cell wall thickness will have a major impact on any results obtained from modelling of experimental data. As described by Cheng (1987b) what is actually controlling the model result is Eh_o and so it is important that the effect of h_o is investigated. Previous techniques have assumed a reasonable value for the cell wall thickness and used this for all experimental data (Wang *et al.,* 2004) in effect varying the ratio τ with cell size. In this work the cell size was measured directly from the experimental data and the cell wall thickness calculated using a constant ratio of τ (Section 6.1.2). If τ were to be kept constant identical curves would again have been generated by the numerical simulation using the dimensionless group ($F/Eh_o r_o \lambda_s^2$); (data not shown).

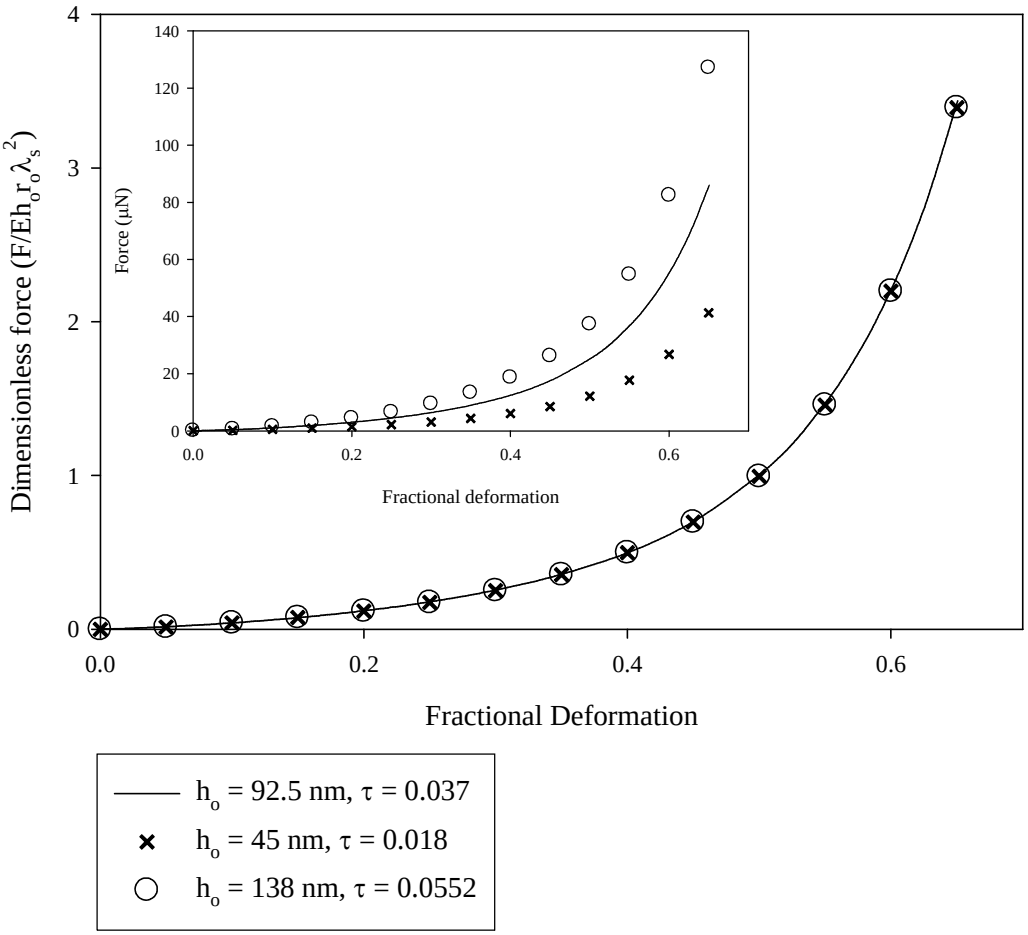

Figure 5.13: Simulated dimensionless force - deformation data and force - deformation data (inset) with varying cell wall thickness. E= 100 MPa, r_o = 2.5 μm, h_o= 45 nm, 92.5 nm, and 138 nm λ_s= 1.04, ν = 0.5

Smith *et al.* (2000b) suggested a different dimensionless group (F/Er_i^2) which could also be used for data analysis.

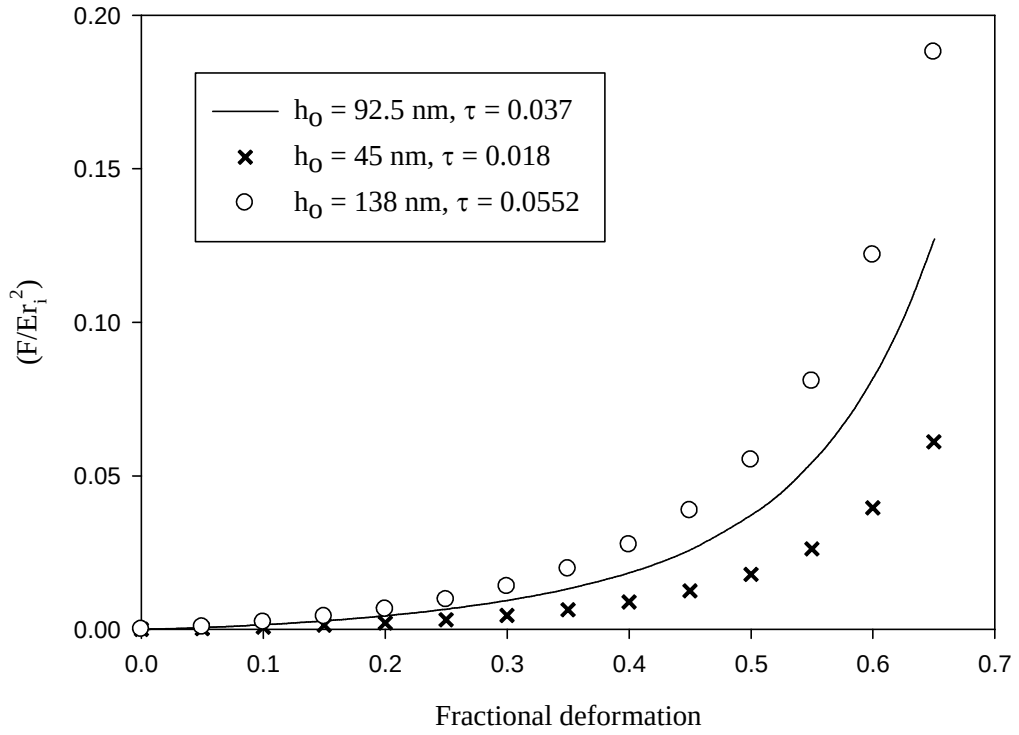

Figure 5.14: Simulated dimensionless force - deformation data generated using the group defined by Smith et al. (2000), (F/Er_i^2). E= 100 MPa, r_o = 2.5 μm, h_o=45 nm, 92.5 nm, 138 nm, λ_s= 1.04, ν = 0.5

Figure 5.14 demonstrates that using Smith *et al.* (2000b) dimensionless groups with a size dependent τ led to significantly different force - deformation curves, unlike the results shown in Figure 5.13. If a constant τ was used then an identical force (F/Er_i^2) deformation curve would be produced. This result suggests that when τ is unknown it is most appropriate to use the group ($F/Eh_or_o\lambda_s^2$). In this work, although τ was known, ($F/Eh_or_o\lambda_s^2$) was used as the effect of the cell wall thickness to cell radius assumption will be investigated later (Section 7.2.5).

5.7.2.1. *Summary*

As has been previously mentioned experimental data leads directly to measurements of the force at cell failure. Figures 5.11 to 5.13 have shown clearly how changes in the cell parameters can lead to significantly altered force - deformation curves without necessarily changing the elastic modulus, as is the case with the cell size and cell wall thickness. This demonstrates the need for modelling the experimental results to obtain intrinsic material properties that are not dependent on these parameters.

5.7.3. Initial stretch ratio

If the initial stretch ratio were to be treated as an adjustable parameter within the model this would allow it to be determined for individual cells while still allowing for unique solutions from the compression data.

Tests independent of the compression method have shown that the initial stretch ratio of a cell population suspended in a solution with an osmotic pressure of 0.8 MPa is about 1.04 (Section 3.3) but might be as high as 1.08 (Meikle *et al.*,1988). For the different models, numerical simulations were produced with the initial stretch ratio ranging from 1.00 to 1.11 a selection of which is shown in Figure 5.15.

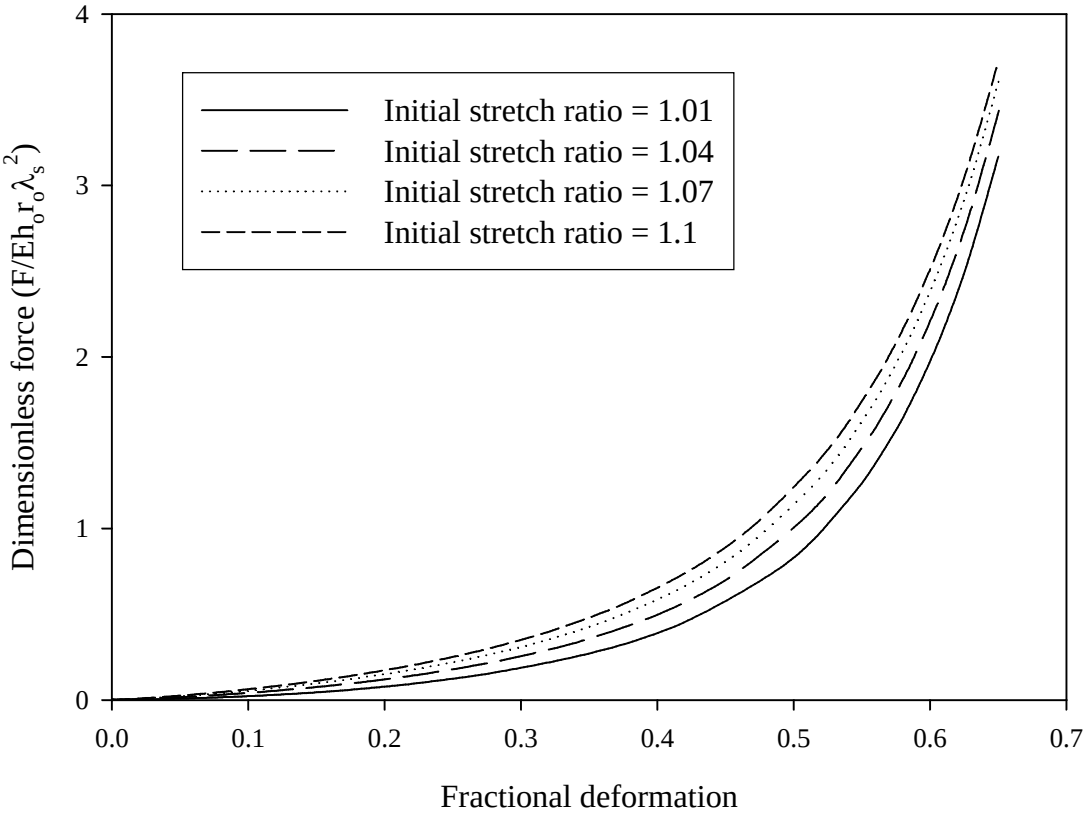

Figure 5.15: Dimensionless force - deformation data with different initial stretch ratios.

E= 100 MPa, r_o = 2.5 μm, h_o= 92.5 nm, λ_s= 1.01, 1.04, 1.07, and 1.1, ν = 0.5

The results shown in Figure 5.15 were found to be the same for the dimensional and dimensionless force - deformation data. As can be seen changing the initial stretch ratio led to different force - deformation data being obtained from the numerical simulations. This occurred as, unlike alterations in the elastic modulus, cell size, and cell wall thickness, changes in the initial stretch ratio altered the shape of the force - deformation curve and not simply the magnitude. This effect on curve shape can be seen when a scaling factor (α) was introduced so that the force - deformation curves lay on top of each other at lower deformations, the result of which is shown Figure 5.16. This comparison was made to

emphasise the change in shape of the force - deformation curves caused by altering the initial stretch ratio.

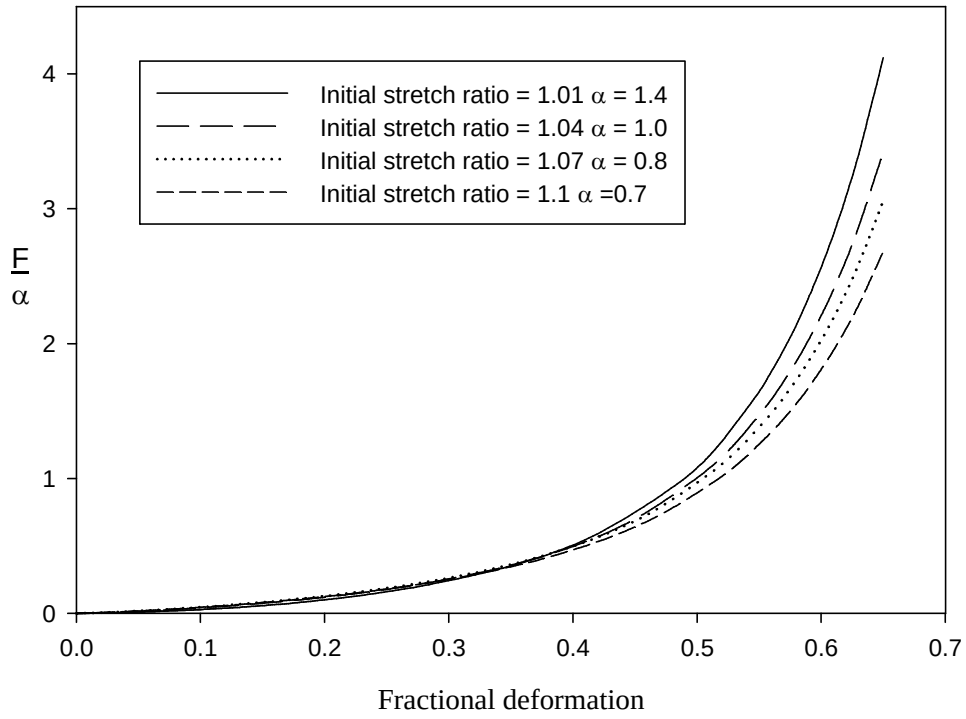

Figure 5.16: Effect of initial stretch ratio when a scaling factor (α) is used to fit all force - deformation curves at low deformations. E= 100 MPa, r_o = 2.5 μm, h_o= 92.5 nm, λ_s= 1.01, 1.04, 1.07, and 1.1, ν = 0.5. The force - deformation curve with λ_s = 1.04 has α set at 1.00 with all other force - deformation curves fitted to this.

For this comparison the force - deformation curve with λ_s = 1.04 used α set to 1 and all the other curves used a value of α adjusted to fit at the lower deformations. Changes in the initial stretch ratio dramatically affected the shape of the force - deformation curves above approximately 40% fractional deformation. Given the significance of the initial stretch ratio on the force - deformation curves it was decided to treat this as an adjustable parameter to be determined by model fitting (Chapter 6).

5.6.4. Poisson ratio

It is not possible at present to test the assumption of a constant Poisson's ratio for all strains (equation 5.20), but it is possible to simulate the effect of choosing different values of this parameter on the force - deformation curves.

Figure 5.17 shows such simulations for given values of all the other parameters, and it would seem that the effect is significant for a sensible range of Poisson ratios.

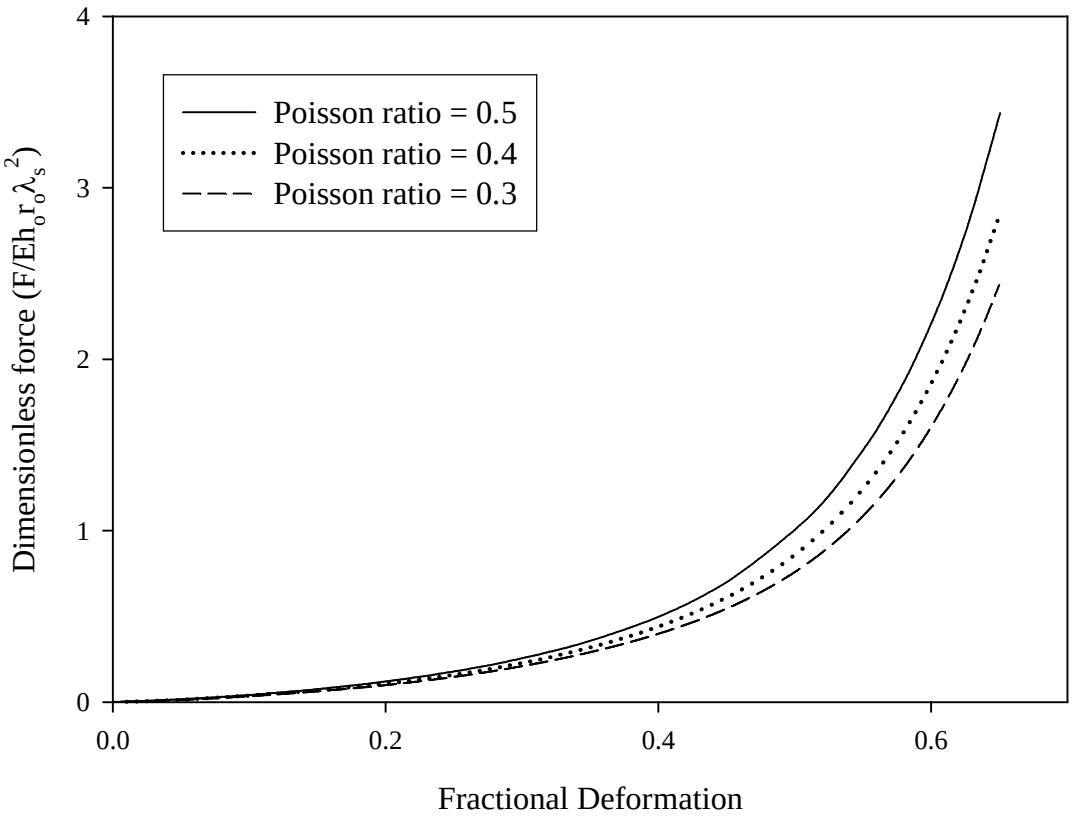

Figure 5.17: Dimensionless force - deformation data with differing Poisson ratios.

E= 100 MPa, r_o = 2.5 μm, h_o= 92.5 nm, λ_s= 1.04, ν = 0.3, 0.4, and 0.5

This would indicate that the compressibility of the cell wall should not be ignored. However, as mentioned previously there is no reliable information in the literature for the Poisson ratio of yeast cell walls. In addition all previous modelling work with yeast cells had set the Poisson ratio to 0.5. The material equations have been derived allowing for compressibility within the wall for use by other workers in the future. The effect of compressibility of the cell wall on the calculated elastic modulus will be investigated further in Section 6.4.

5.7. Conclusions

A Hencky strain model with constant elastic modulus has been developed that can be used to extract intrinsic material properties from compression experiments performed on single suspended yeast cells. It is believed that this is the only correctly formulated analytical model for this situation, which should also apply to cells other than yeast cells, and to microcapsules.

The elastic modulus which would be found by fitting this or any other models (including finite element analysis) to experimental data is dependent on the choice of Poisson's ratio and cell wall thickness, neither of which are particularly amenable to experimental determination. However, the modulus values are determined in a consistent manner and might therefore be used in other studies, for example of the relationship between cell wall composition and the material properties. The model should be valuable in studying the mechanisms of cell disruption in bioprocessing, and in improving current understanding of the mechanisms of yeast cell wall growth and form.

Chapter Six:
Fitting procedure and choice of strain model

To obtain intrinsic material properties from yeast compression data it was necessary to fit the experimental data presented in Chapter 4 to the Hencky strain model developed in Chapter 5. In order to use these intrinsic properties to compare different cell populations it was essential that the fitting procedure was consistent. This Chapter outlines the fitting procedures that were followed throughout this work.

6.1. Dimensionless groups

In the process of matching simulations to experimental data, comparisons were made of simulated and experimental forces in dimensionless form. Using dimensionless groups simplified the fitting procedure and allowed cells with different properties to be compared (Chapter 5). The method by which data was converted into dimensionless form was different for the force data from the two sources (numerical simulation and experimental data) and therefore the methods are described separately.

6.1.1. Numerical simulation

Numerical simulations produce force - deformation curves whose magnitude and shape are controlled by the initial modelling parameters including the elastic modulus (E) and the initial stretch ratio (λ_s).

The dimensionless force is defined as:

$$\hat{F} = \frac{F}{\left(Eh_o r_o \lambda_s^2\right)} \quad \ldots (6.1)$$

and the fractional deformation is defined as:

$$X = \frac{z}{\left(r_o \lambda_s\right)} \quad \ldots (6.2)$$

where z represents half the displacement of the probe, r_o is the uninflated cell radius, h_o is the uninflated cell wall thickness, F is the force, E is the elastic modulus and λ_s is the initial stretch ratio. Lardner and Pujara (1978; 1980) defined these dimensionless groups which were also used by Wang *et al.* (2004) and Liu *et al.* (1996). For numerical simulations the parameters E, r_o, h_o, and λ_s were assigned in the model and the effect on the force - deformation data investigated, as described previously (Chapter 5).

The result of the numerical simulations was a set of dimensionless force - deformation curves, one for each initial stretch ratio λ_s, with a range of the latter from 1 to 1.11 at intervals of 0.01 (Figure 5.15).

6.1.2. Experimental data

In the experimental work the compressive force (F) and the displacement (d) of the probe were recorded directly for each cell using the methods described in Section 3.2.4. From this

the inflated cell radius (r_i) was measured directly. The inflated cell radius r_i is equal to the un-inflated cell radius multiplied by the initial stretch ratio (equation 6.3).

$$r_i = r_o \lambda_s \quad \ldots (6.3)$$

The displacement, *d*, was output directly from the compression experiment and is equal to *2z*. Using equations 6.2 and 6.3 it was possible to calculate the fractional deformation of the cell.

In order to calculate the dimensionless force it was necessary to know the cell wall thickness (h_o), elastic modulus (E), and the initial stretch ratio (λ_s) for each cell (equation 6.1). The cell wall thickness was determined using a cell wall thickness to cell radius ratio, τ, which was measured using the transmission electron microscopy (TEM) method described in Section 3.5. TEM images were produced which allowed the cell wall thickness and the radius of individual cells to be measured. Table 6.1 presents the results for the mean corrected cell wall thickness ($\overline{H}$) and mean cell radius ($\overline{R}$) analysis. The method used to calculate these corrected mean parameters is outlined in Appendix 9.

	$\overline{H}$ (nm)	$2\overline{R}$ (μm)	$\overline{H}/\overline{R} = \tau$
Mean	91	4.9	0.037
Standard deviation	–	–	± 0.001

Table 6.1: Summary of the image analysis results from TEM of yeast cells. $\overline{H}$ = corrected mean cell wall thickness, $\overline{R}$ = corrected mean cell radius, τ = cell wall thickness to cell radius ratio.

The cell wall thickness was measured at the osmotic pressure of the fixative solution, and corresponds to an initial stretch ratio of 1.00 (Figure 3.14). From Table 6.1 the cell wall thickness to cell radius ratio (τ) was assigned a value of 0.037. This is the same value as used by Smith *et al.* (2000a) also for Fermipan dried Baker's yeast. This choice of a fixed value of τ means that the calculated cell wall thickness was size dependent (i.e. increased with cell size). The importance of this assumption is discussed in detail in Section 7.2.5. From these data it was also possible to obtain data on the mean aspect ratio of the cells. In this case it was found to be 1.09 which suggests the assumption of sphericity of the cells was reasonable.

The initial stretch ratio was unknown before fitting, although this parameter is related to the cell radius (equation 6.3) and therefore the cell wall thickness through τ. As previously described the inflated radius (r_i) was obtained directly from the experimental data. Using the ratio τ it was possible to find the combined parameter $h_o\lambda_s = \tau r_i$. Therefore, by using the parameters r_i and τr_i it was possible to calculate the dimensionless force from compression data without having defined the λ_s value:

$$\hat{F} = \frac{F}{\left(Eh_o r_o \lambda_s^2\right)} = \frac{F}{\left(Er_i\left(h_o\lambda_s\right)\right)} = \frac{F}{\left(E\tau r_i^2\right)} \qquad \ldots (6.4)$$

From equation 6.4 the experimental compression data were converted into dimensionless form by assuming a reasonable initial E value, i.e. 100 MPa. Using equations 6.2 to 6.4 it was possible to produce dimensionless force - deformation data for each of the compression tests with this assumed E value, before adjusting E to make the experimental data fit the dimensionless numerical simulation data (Section 6.2).

6.2. Fitting the experimental data to the numerical simulation

In order to fit the experimental data to the dimensionless numerical simulation's a polynomial was regressed to the simulated dimensionless force - deformation data This simplified the fitting procedure.

Dimensionless experimental data were fitted to the numerical simulation polynomials (for each λ_s) by adjusting the values of E used to calculate the former. This was done in increments of 1 MPa from the initial value of 100 MPa. The correlation coefficient (Pearson R^2) was used to determine how well the dimensionless experimental data fitted the numerical simulations at each value of E. This process continued in order to maximise the correlation coefficient between the experimental data and numerical simulations for each λ_s value. For each set of experimental force - deformation data, this process produced a best fit estimate of the elastic modulus (E) for each initial stretch ratio (λ_s) with a corresponding R^2 value.

From this the E and λ_s parameters were found that produced the maximum R^2 value overall, and these were taken as the best estimates of the properties for the experimental compression data. This allowed the variables E, λ_s, r_o, and h_o to be defined for the experimental data. Figure 6.1 shows an example of this fitting method for a typical set of experimental data, with $\lambda_s = 1.04$.

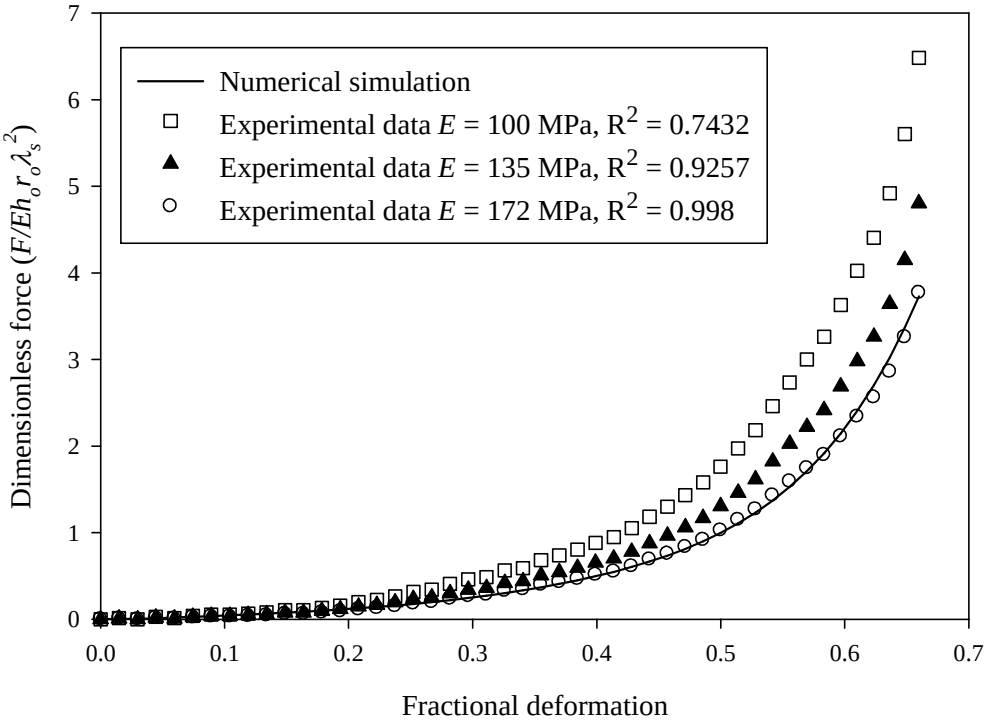

Figure 6.1: Typical example of results produced by the fitting process. Numerical simulation parameters: r_o = 2.5 µm, h_o = 92.5 nm, λ_s = 1.04, E = 100. Experimental data parameters: r_i = 2.37, τ = 0.037, E with corresponding R^2 values shown in the legend.

As can be seen in Figure 6.1 as the elastic modulus was increased the dimensionless experimental force - deformation data moved closer to the numerical simulation which had the effect of increasing R^2. In this case it was found that the R^2 was maximised when *E* was set at 172 MPa.

An example of the R^2 data generated by the overall fitting process is shown as a surface plot in Figure 6.2.

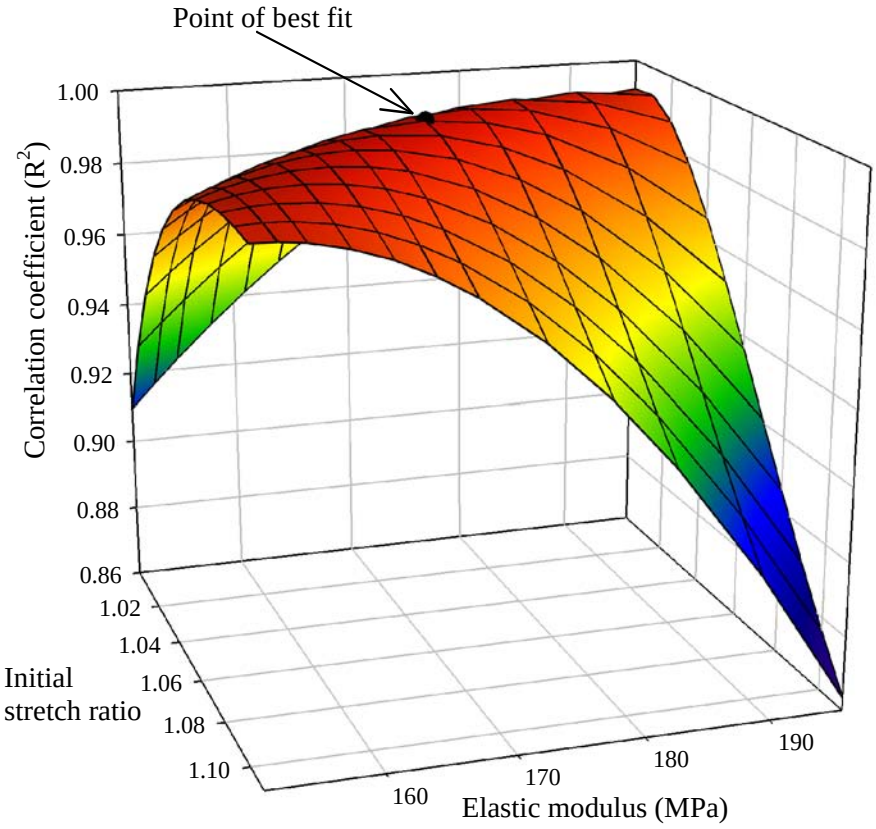

Figure 6.2: Surface plot showing an example of data generated by the fitting process. The black point shows the best fit (E = 172 MPa, λ_s = 1.04, R^2 = 0.998)

Along the "spine" of the surface in Figure 6.2 the correlation coefficient remained consistently high, above 0.99. Although the correlation coefficient was high at all parts on the spine, when the initial stretch ratio or the elastic modulus was fixed, adjusting the other parameter decreased R^2 significantly. Figure 6.3 shows the data from the spine of the surface plot in Figure 6.2.

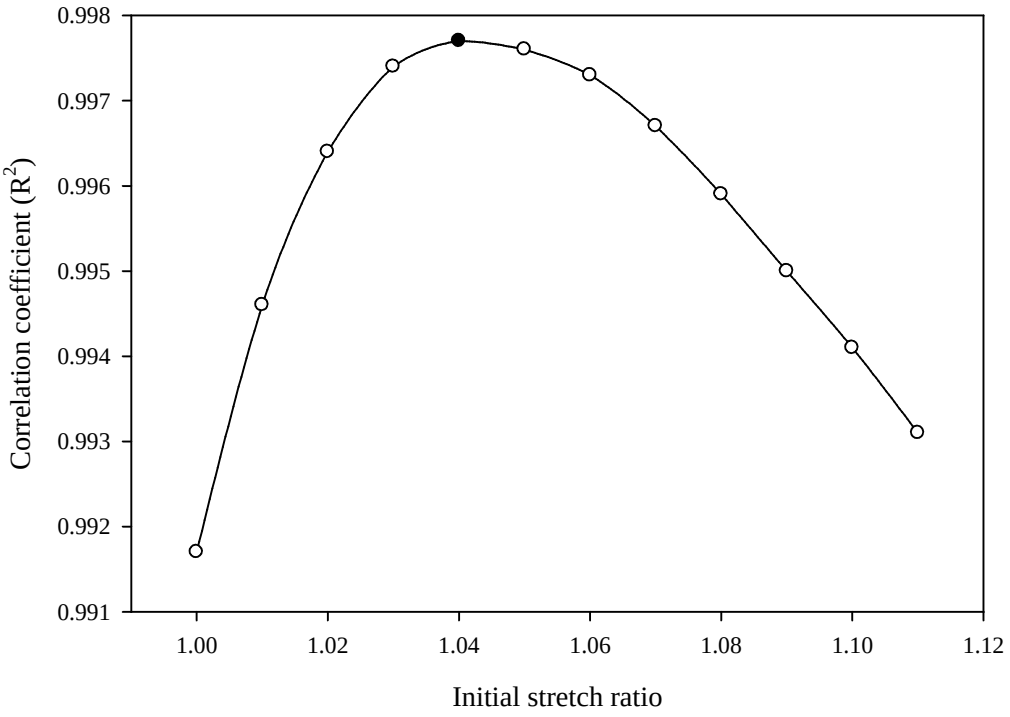

Figure 6.3: Effect of initial stretch ratio on the correlation coefficient (R^2) for points on the data spine observable in Figure 6.2. The black point indicates the point of best fit ($E = 172$ MPa, $\lambda_s = 1.04$, $R^2 = 0.998$)

Figure 6.3 shows the R^2 value for the best fit at each numerical simulation with a different given inital stretch ratio. The correlation coefficient remained high, though the point of best fit was distinct.

The data in Figure 6.3 allowed some estimate of the errors in the fitting procedure. If the intial stretch ratio had been taken to be 1.03 or 1.05, this would have led to an elastic moduli of 177 MPa and 167 MPa respectively. This result suggests that as the initial stretch ratio of a population of cells was found to be 1.04 ± 0.01 (see Section 3.3.1) then the error in the elastic modulus might be ± 5 MPa, giving an elastic modulus of 172 ± 5 MPa.

From Section 3.2.4 a possible source of error of up to 3 % in the determination of the cell size was discussed. An error of this magnitude in the cell size would lead to an error similar in magnitude to that shown for the initial stretch ratio. However, as is demonstrated in Section 3.2.4 the point of initial contact was clear during compression so this error should be kept to a minimum over a large number of data sets.

Fitting was also performed using the dimensionless group defined by Smith *et al.* (2000b) (equation 6.5).

$$F_{Smith} = \frac{F}{Er_i^2} \qquad \ldots (6.5)$$

It was found that the same result could be obtained from modelling when using this dimensionless group, which is unsurprising if τ can be considered a constant (compare equation 6.5 to 6.4). The advantage in using the dimensionless group defined in equation 6.1 is that the cell wall thickness assumption can be altered without having to reproduce all of the numerical simulations (Section 5.7.2).

As well as this the fitting methods were further confirmed by using force - deformation data directly rather than dimensionless groups. This process was significantly more time consuming than using dimensionless groups as the force - deformation data is size dependent so individual simulations had to be produced for each cell size. However, the same results were again obtained from the modelling (data not shown).

6.3. Investigation the fitting of Hencky strain, infinitesimal strain and Green strain models to experimental data

Preliminary results showed that the simulations were unable to fit approximately 5 % of the experimental data adequately and these were discarded (Section 4.1.5). All of the remaining data could be fitted up to cell bursting, presumably at cell wall failure. These data are presented in detail in Chapter 7.

As part of the investigation into the influence of different strain measures the three strain models derived in Chapter 5 were fitted to typical experimental compression data. Figure 6.4 compares simulations using the models with the parameters that were determined for the Hencky strain model ($\lambda_s = 1.04$, $E = 172$ MPa, $r_o = 2.28$ μm, $h_o = 84$ nm).

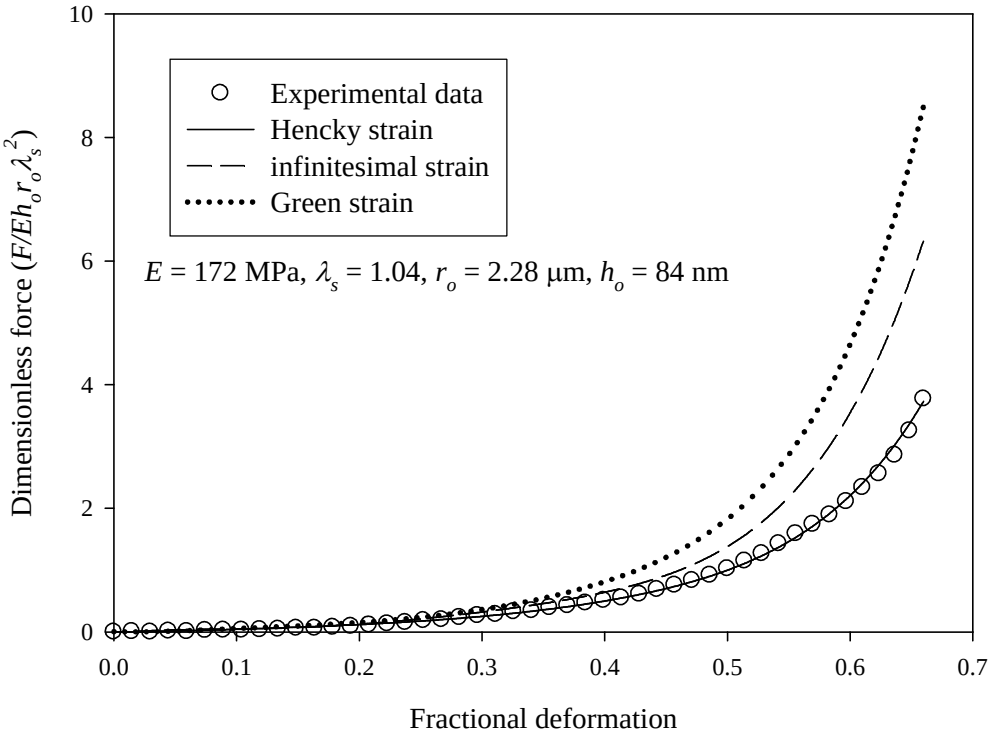

Figure 6.4: Typical example of the Hencky strain model fitting experimental data up to the point of cell failure, with the Infinitesimal and Green strain models produced using the same parameters. (Parameters for the Hencky strain model: Elastic modulus of the cell wall 172 MPa, initial stretch ratio 1.04, cell radius 2.28 μm, correlation coefficient 0.998).

It can be seen that the choice of strain measure is important, especially for the higher deformations needed to induce cell breakage. Failure was at a deformation of about 67 %, which was typical. Up to approximately 30 % deformation the infinitesimal and Green strain models appeared to fit the experimental data well using the parameters from the Hencky strain fit. Above this deformation they differed significantly.

In Chapter 5 it was stated that infinitesimal strains are really only suitable for small deformations where the strain is approximately 0.1%. Figure 6.4 shows that this led to incorrect estimates of force at higher deformations, causing an underestimation of the elastic

modulus. The Green strain model was better although it should not be applied when large deformations are accompanied by large strains. A detailed comparison of these models from a theoretical viewpoint was outlined in Chapter 5.

As a comparison, the experimental data shown in Figure 6.4 were also fitted using the infinitesimal strain and Green strain models with the initial stretch ratio and the elastic modulus treated as adjustable parameters. The best fit using the infinitesimal strain model led to an elastic modulus of 80 ± 3 MPa, and an initial stretch ratio of 1.11. The correlation coefficient was found to be 0.996. For the Green strain model the elastic modulus was 60 ± 2 MPa, the intitial stretch ratio 1.11, and the correlation coeffcient 0.995.

It is clear that all the models were able to fit the data well, and that small changes in correlation coefficient may not be sufficient to justify choosing one model over another, although the preferred Hencky strain model is marginally the best. Nevertheless, the choice of strain measure is important, as it determines the elastic modulus. There is a significantly higher value for the Hencky model because it gives lower strains for given stretch ratios (Section 5.2). In view of this and the results previously presented in Chapter 5, the Hencky strain model was used for modelling the results from the compression testing experiments.

It should be noted that the modulus value depends on the choice of wall thickness, and it might be best to treat Eh_0 as a single parameter to be determined by modelling. It is likely that this combination of parameters would also appear in any application of the data. The effect of the cell wall thickness on the results is investigated further in Section 7.2.5.

6.4. Effect of the Poisson ratio

It is not possible at present to test the assumption of a constant Poisson's ratio for all strains (Chapter 5, equation 5.14), but it is possible to simulate the effect of choosing different values of this parameter on the force - deformation curves. Figure 5.17 showed that the effect is significant for a sensible range of Poisson ratio.

If the best fit to the experimental data in Figure 6.2 is found for each Poisson ratio, the values of the elastic modulus are 238 ± 5 MPa (ν = 0.3) and 205 ± 5 MPa (ν = 0.4), compared to the value for the incompressible case (172 ± 5 MPa). The elastic modulus found by fitting this or any other models (including finite element analysis) to experimental data is clearly dependent on the choice of Poisson's ratio as well as the cell wall thickness, neither of which are particularly amenable to experimental determination. It is possible some alternative method of characterising the mechanical properties of yeast cells would resolve these issues, and such a method should be sought. The modulus values found here were determined in a consistent manner. They might therefore be used in other studies, for example in investigating how cell wall material properties depend on cell wall composition and structure.

6.5. Conclusions

The methods outlined in this Section have detailed how the experimental data was fitted to the numerical simulation to obtain intrinsic material properties of the yeast cell wall. In Chapter 7 these methods are employed using the data in Chapter 4 to produce the elastic modulus, initial stretch ratio and some failure criteria for samples of cells.

Chapter Seven: Parameters from modelling experimental compression data

In the work described in this chapter, the methods developed in Chapters 3, 5 and 6 were applied to samples of cells to obtain population data. The compression testing technique described in Chapter 3 was used to obtain force - deformation data from yeast cells. The model developed in Chapter 5 was then implemented to determine intrinsic material properties of the yeast cell wall using the fitting procedure described in Chapter 6. The effects of compression speed and the effects of water loss during compression were determined. If water loss could be considered negligible because of the high speed of compression, then it should be possible to determine the intrinsic material properties from force - deformation data by modelling. If the linear elastic material model is representative of the cell wall at all strains then it should be possible to fit the numerical simulation up to cell failure, allowing failure criteria to be determined as well (Chapter 6). The analysis also allowed the initial stretch ratio to be determined uniquely for each cell. As a key step in verification of the modelling and fitting procedures, image analysis was used to measure the initial stretch ratio of individual cells, independently of compression testing.

7.1. Effect of compression speed on the "pseudo elastic modulus"

It was expected that at lower speeds of compression force - deformation data would be influenced by water loss from the cell (Smith *et al.*, 2000a). Yeast cells have been shown to have a very high hydraulic conductivity (0.31×10^{-12} $ms^{-1}Pa^{-1}$; Smith *et al.*, 2000b). This suggested that the speed of compression could have a major effect on the elastic modulus,

estimated by modelling. In order to determine the effect of water loss on the elastic modulus the model developed in Chapter 5 was fitted to experimental data (using a range of compression speeds) assuming no water loss was occurring. Lower compression speeds were expected to change the shape and magnitude of the force - deformation curves due to water loss from the cell during compression (Smith *et al.,* 1998). Data for cells compressed at speeds ranging from 8 to 308 μms^{-1} (Chapter 4) were analysed.

In each case it was assumed that the elastic modulus could be determined as if there was no water loss, giving a "pseudo elastic modulus". Within the numerical simulations the cell wall permeability was therefore set at zero. Furthermore, the initial stretch ratio was fixed at 1.04 because fitting for this parameter when water loss was occurring would be meaningless. A value of 1.04 was chosen after measuring the initial stretch ratio for a population of cells using the Malvern Mastersizer (Figure 3.14). This method is described in detail in Section 3.3.2 and its reliability discussed in Section 7.2.6.

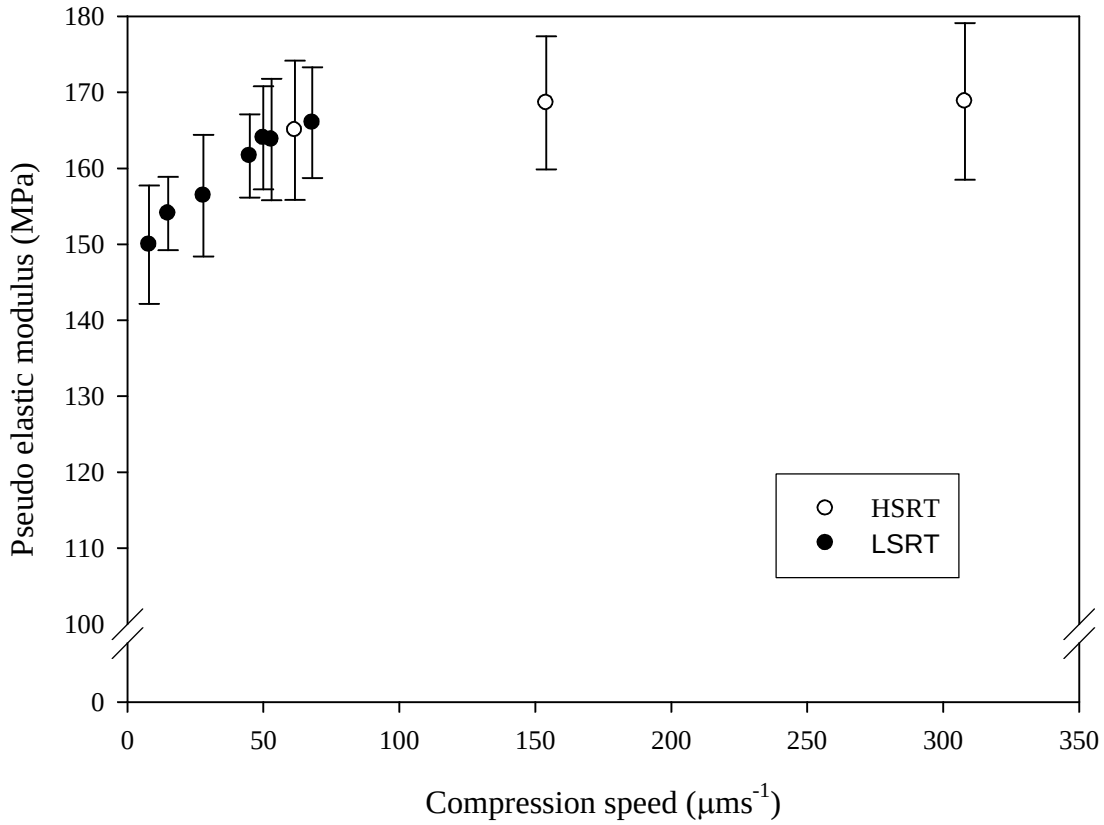

Figure 7.1: Effect of compression speed on the mean "pseudo elastic modulus" from fitting numerical simulations. In each case the initial stretch ratio was fixed at 1.04, and the elastic modulus was an adjustable parameter within the model. Approximately 100 cells were tested at each compression speed. LSRT = Low strain rate tester, HSRT = High strain rate tester for speeds higher than 68 μms^{-1}. Errors are standard errors.

Figure 7.1 shows the effect of compression speed on the "pseudo elastic modulus", which was estimated assuming no water loss had occurred during compression. It can be seen that the modulus was essentially constant for compression speeds of around 45 μms^{-1} or higher. This indicates that when cells were compressed above this speed the effects of water loss from the cell during compression could be considered negligible. A t - test at the 5 % level was performed between the data obtained at 308 μms^{-1} and that at 8 μms^{-1}. This led to a P -

value of 0.11 suggesting the results are statistically similar. However, the trend shown in Figure 7.1 clearly indicates that the "pseudo elastic modulus" was decreasing at slower compression speeds. To ensure that no time dependent behaviour was affecting the results it seemed reasonable to use a compression speed of 68 μms^{-1}. Figure 7.1 suggested that this compression speed would be high enough for water loss to be assumed negligible in the modelling. As this speed was within the capability of the LSRT (Section 3.2.3.1), this machine was used at 68 μms^{-1} for all subsequent work.

In order to confirm that 68 μms^{-1} was a sufficiently high compression speed, numerical simulations (Chapter 5) were performed in which the cell wall was taken to be permeable. Although the fluid contents of the cell were still assumed incompressible, the volume of the cell decreased during compression due to water loss. Equation 7.1 describes the volume change during cell compression:

$$\frac{dV}{dz} = \frac{2Lp}{v} A(\Delta P - \Delta \pi) \qquad \ldots (7.1)$$

where V is the instantaneous internal volume, z is half the displacement of the probe, Lp is the hydraulic conductivity, A is the area available for flow, v is the velocity of compression, $\Delta P = P_{external} - P_{internal}$ is the hydrostatic pressure difference, and $\Delta \pi = \pi_{external} - \pi_{internal}$ is the osmotic pressure difference (Smith, 1999; Wang *et al.*, 2004). This method of accounting for water loss during compression testing was based on the work of Kedem and Katchalky (1958).

The hydraulic conductivity was taken to be 0.3 $\times 10^{-12}$ $ms^{-1}Pa^{-1}$ (Smith *et al.*, 2000b) and compression speeds of 8 μms^{-1} and 68 μms^{-1} were assigned. Figure 7.2 shows a comparison of simulations with and without water loss.

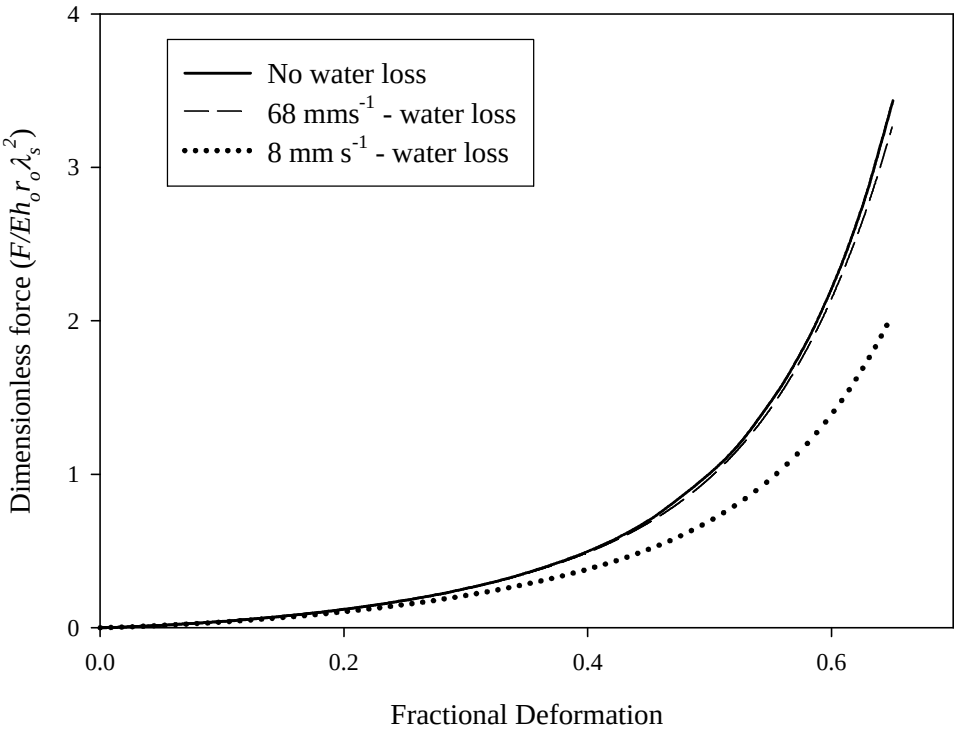

Figure 7.2: Comparison of simulations produced with water loss and without water loss. $E = 100$ MPa, $\lambda_s = 1.04$, $r_o = 2.5\ \mu m$, $h_o = 92.5$ nm, $Lp = 0.3 \times 10^{-21}\ ms^{-1}Pa^{-1}$, compression speeds = 8 and 68 μms^{-1}.

The curves for no water loss and for the compression speed of 68 μms^{-1} are close but both are significantly different to the curve for 8 μms^{-1}. This confirms that it was reasonable to assume negligible water loss during compression for speeds of 68 μms^{-1} and above.

To determine the effect on the estimated elastic modulus of neglecting water loss, simulation data produced assuming no water loss was fitted to the curve produced at

8 μms^{-1}. The elastic modulus was found to be 27 MPa lower for the water loss curve. This compares well to the data shown in Figure 7.1 where the elastic modulus at 8 μms^{-1} was found to be 18 MPa lower than that produced at 68 μms^{-1}.

Implications

The results presented in this section show that if the compression speed was sufficiently high then any cell volume changes during compression could be considered negligible. This result has important implications for the subsequent analysis of the force - deformation data obtained by compression testing. As has been discussed previously (Chapter 5), a number of parameters need to be determined in order to obtain unique solutions from the fitting of numerical simulations to experimental data. As it is possible to set the cell volume changes during deformation to be zero this allows the initial stretch ratio (λ_s) to be treated as an adjustable parameter while still allowing unique results from the modelling. This is the first time that it has been possible to obtain information about the initial stretch ratio of individual cells from compression testing.

7.2. Yeast cell wall mechanical properties

The numerical simulation was fitted to force - deformation data produced at a compression speed of 68 μms^{-1} using the elastic modulus and the initial stretch ratio as adjustable parameters. An example of this force - deformation data is shown in Chapter 6 (Figure 6.4). A large elastic modulus indicates a stiff material while a smaller elastic modulus would imply a more flexible material. The trends shown in the following sections were similar for all repeat experiments at high compression speeds. All errors in the following Sections are

95 % confidence limits. In Sections 7.2.1 – 7.2.5 the results from the modelling are outlined and some initial comparisons are given. Section 7.2.6 then discusses these results.

7.2.1. Using the initial stretch ratio and elastic modulus as adjustable parameters

The numerical simulations were fitted to the experimental data using the technique of maximising the correlation coefficient described in Chapter 6. These fitting processes were performed on the force - deformation data produced by the compression of 103 cells. This process produced a mean elastic modulus of 185 ± 15 MPa and a mean initial stretch ratio of 1.039 ± 0.006. This result compares well to the data shown in Figure 7.1 where a mean elastic modulus of 166 ± 15 MPa was obtained with the initial stretch ratio fixed at 1.04. These results also compare well with results presented by Smith *et al.* (2000b) of 150 ± 15 MPa, also for Fermipan yeast cells, with the initial stretch ratio fixed at 1.04 ± 0.01. Smith *et al.* (2000b) used finite element analysis to obtain these results, and it is believed that their method also used Hencky strains, making the results directly comparable. As was shown in Chapter 5 (Figure 5.10) the finite element model and Hencky strain numerical simulation produced different force - deformation curves for the same parameter values. It is unclear why this should occur. It is presumed such differences were responsible for the different mean elastic moduli found by Smith *et al.,* (2000b). These results are discussed further in Section 7.2.6.

In addition to using the Hencky strain model the infinitesimal and Green strain models (Chapter 5) were also fitted using the elastic modulus and initial stretch ratio as adjustable parameters. The infinitesimal strain model led to a mean elastic modulus of 103 ± 10 MPa with a mean initial stretch ratio of 1.079 ± 0.007. This compares to the Green strain model

with a mean elastic modulus of 78 ± 7 MPa with a mean initial stretch ratio of 1.084 ± 0.007. The reason for the different modelling results has been discussed in detail previously (Chapter 5). This further demonstrates that if the incorrect strain definition is used within the material model then significantly different results will be obtained. The results produced by the infinitesimal and Green strain models will not be considered further in this thesis.

Using the Hencky strain model it was found that the elastic modulus obtained by compression testing was not dependent on the cell size (Figure 7.3).

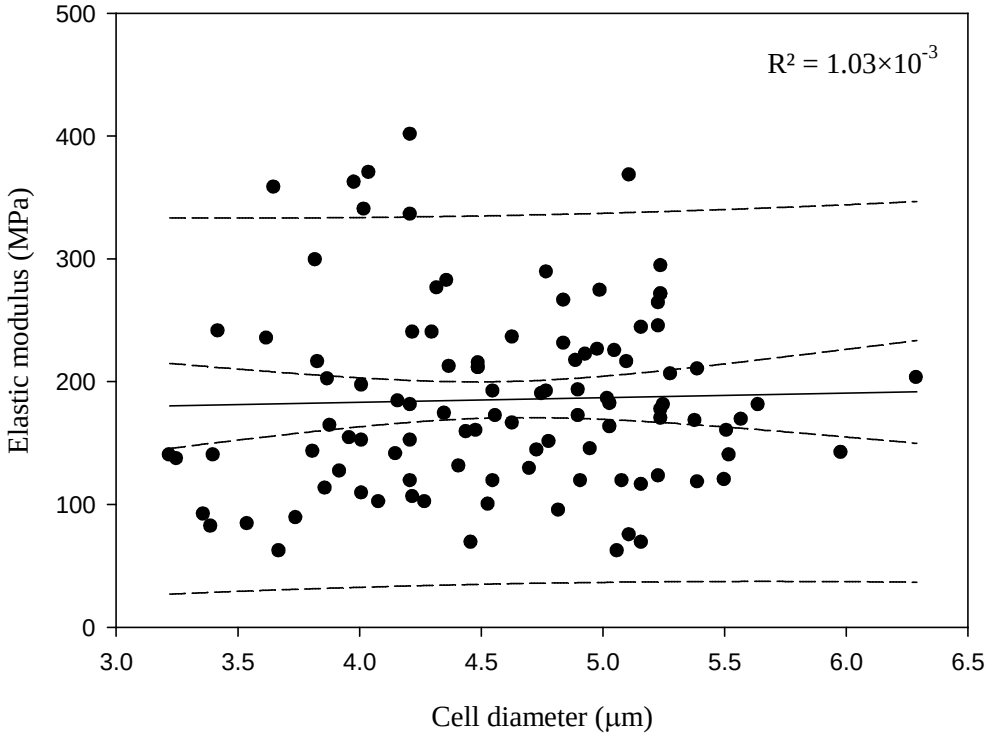

Figure 7.3: Trend between the cell diameter and the elastic modulus. Dashed lines represent the 95 % confidence limits for the mean and the individual measurements.

It was found that the elastic modulus decreased with increasing deformation at failure (Figure 7.4) and force at failure (Figure 7.5). These force and deformation data are the same as those presented in Figures 4.7 and 4.9.

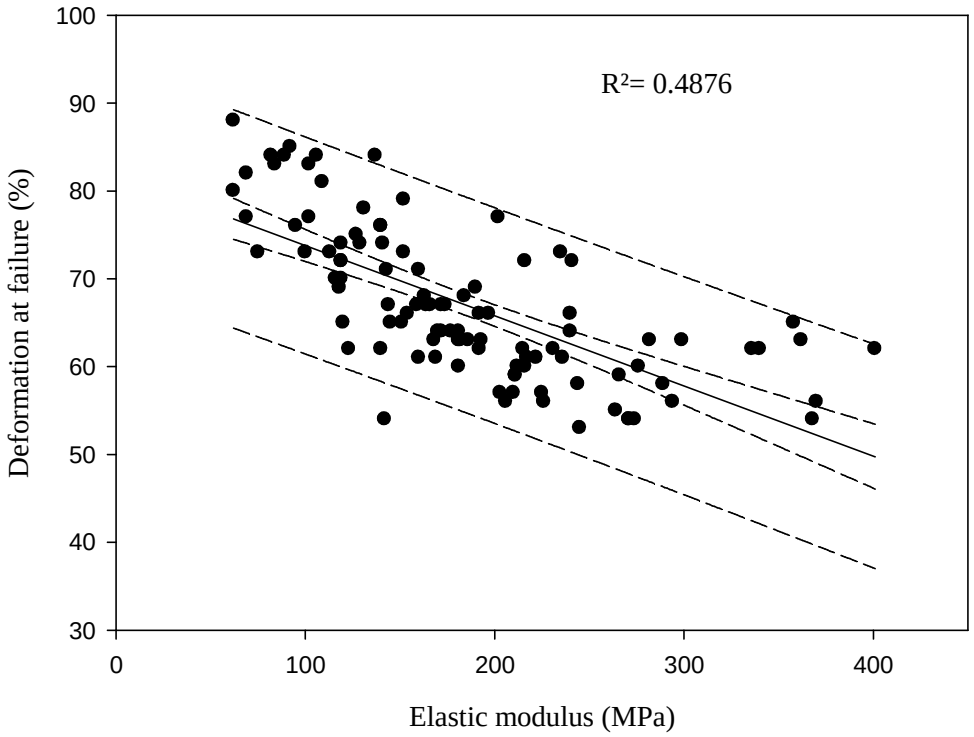

Figure 7.4: Trend between the elastic modulus and the deformation at failure. Dashed lines represent the 95 % confidence limits for the mean and the individual measurements.

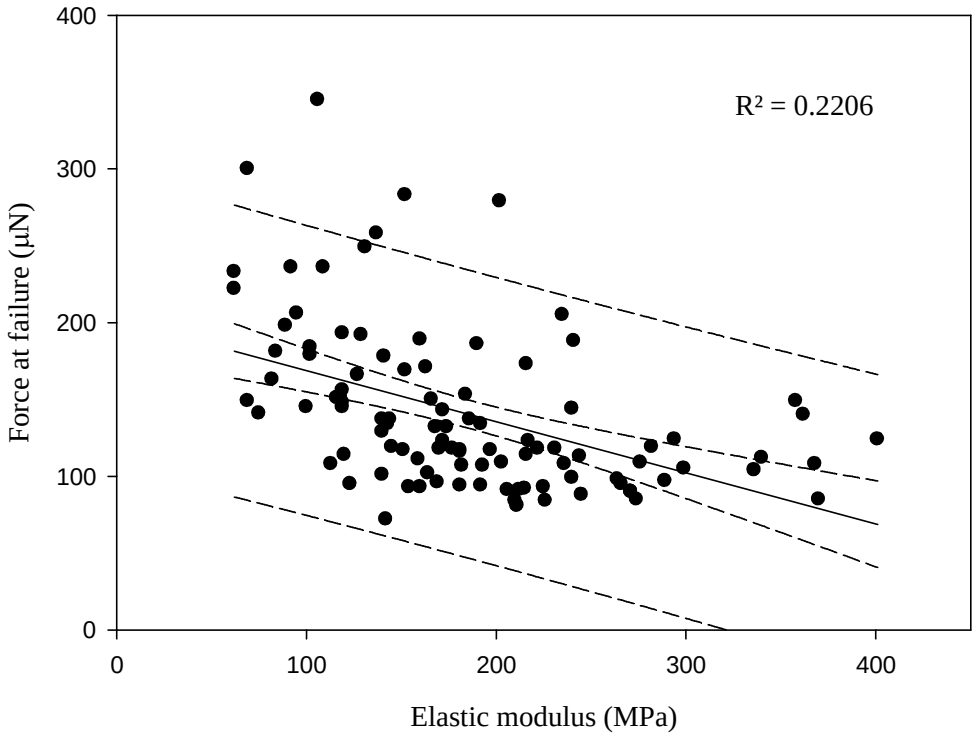

Figure 7.5: Trend between the elastic modulus and the force at failure. Dashed lines represent the 95 % confidence limits for the mean and the individual measurements.

Figure 7.4 is an important result as cells that are deformed more also have a lower elastic modulus of the cell wall. This suggests that the more flexible (i.e. less stiff, but not necessarily weaker) cells will deform further before failure. This result is expected to be due to changes occurring within the cell wall composition and structure during the cell cycle. These changes and their effect on the results produced by modelling are discussed later (Section 7.2.6).

7.2.2. Initial stretch ratio – Model fitting

The mean initial stretch ratio found by modelling the experimental data was 1.039 ± 0.006 (Section 7.2.1). This result was consistent with that found using the Malvern Mastersizer

(Section 3.3.1) where the initial stretch ratio of a population of cells was found to be 1.040 ± 0.007 (Figure 3.14). These results also compare well with those presented by Smith *et al.* (2000a) of 1.04 ± 0.01, also for Fermipan yeast cells. It was found that the initial stretch ratio was not dependent on the cell size (Figure 7.6). Also the deformation at failure (%) (Figure 7.7) and force at failure (Figure 7.8) were not dependent on the initial stretch ratio.

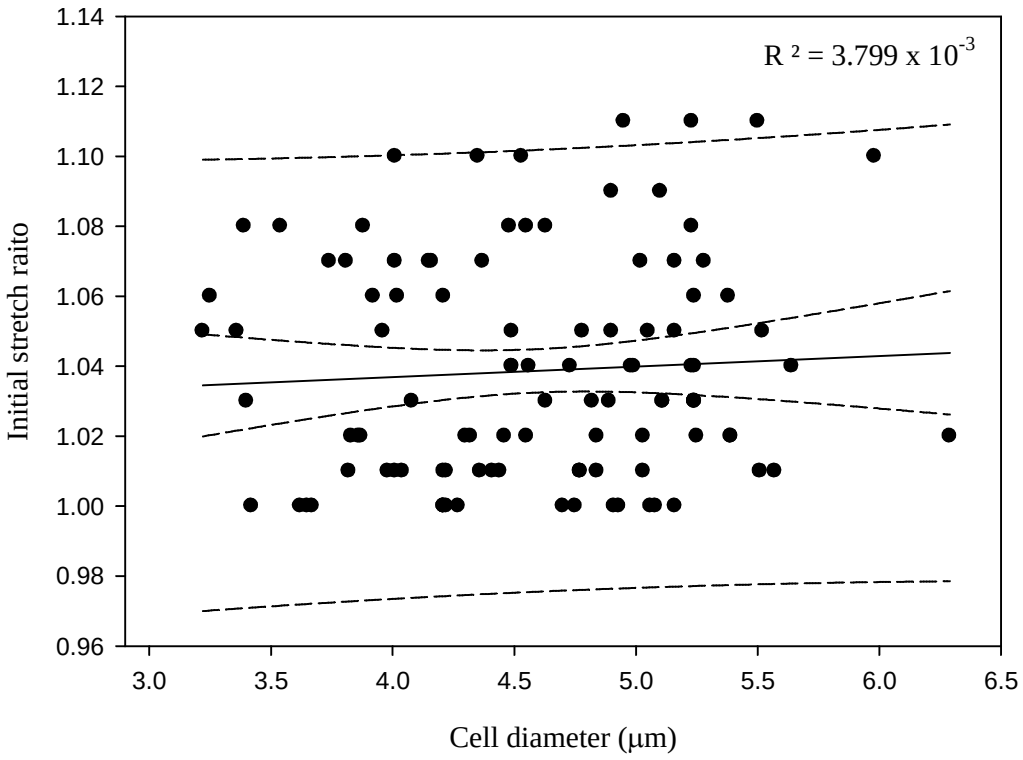

Figure 7.6: Trend between the initial stretch ratio and the cell diameter. Dashed lines represent the 95 % confidence limits for the mean and the individual measurements.

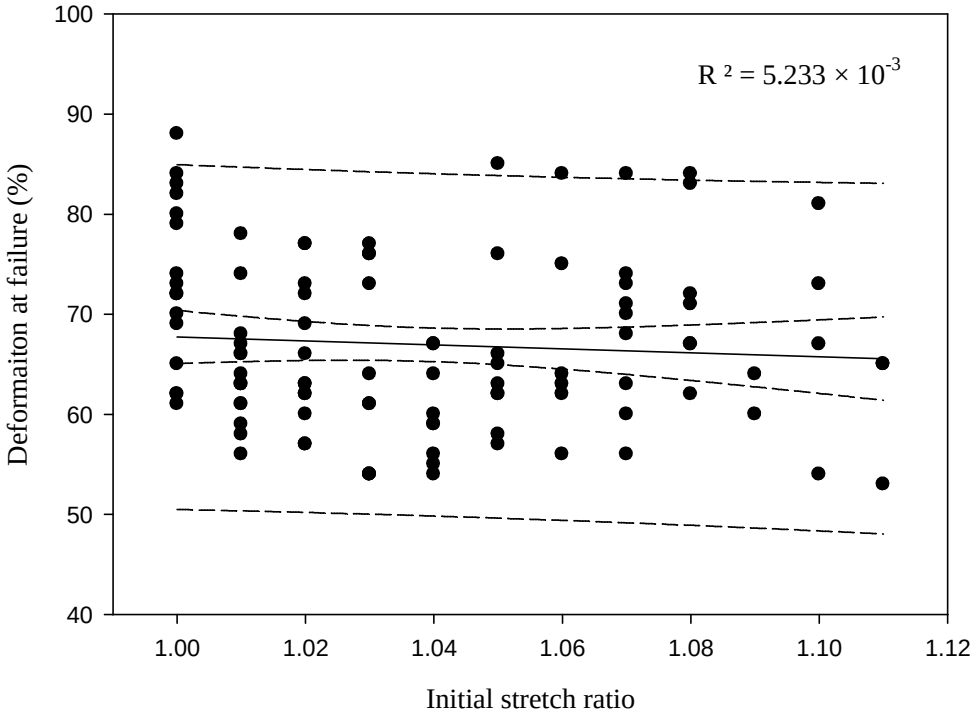

Figure 7.7: Trend between the initial stretch ratio and the deformation at failure (%). Dashed lines represent the 95 % confidence limits for the mean and the individual measurements.

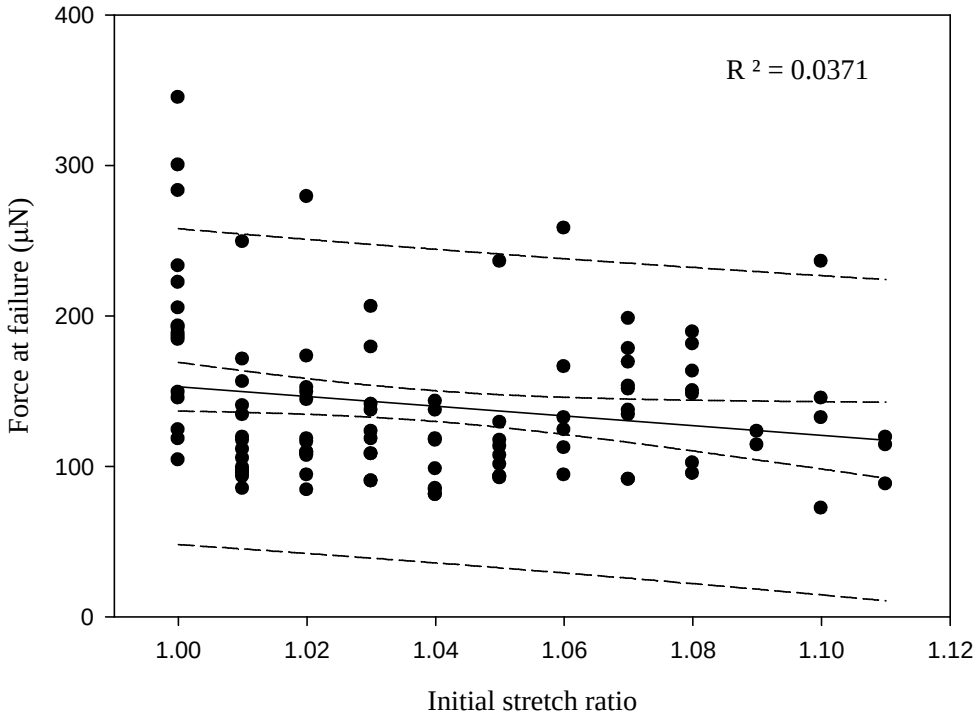

Figure 7.8: Trend between the initial stretch ratio and the force at failure. Dashed lines represent the 95 % confidence limits for the mean and the individual measurements.

The size independence of the initial stretch ratio has been observed previously by Martínez de Marañón (1996) using a visualisation chamber method similar to that described in Section 3.3.2.

In addition to this the elastic modulus did not depend strongly on the initial stretch ratio (Figure 7.9).

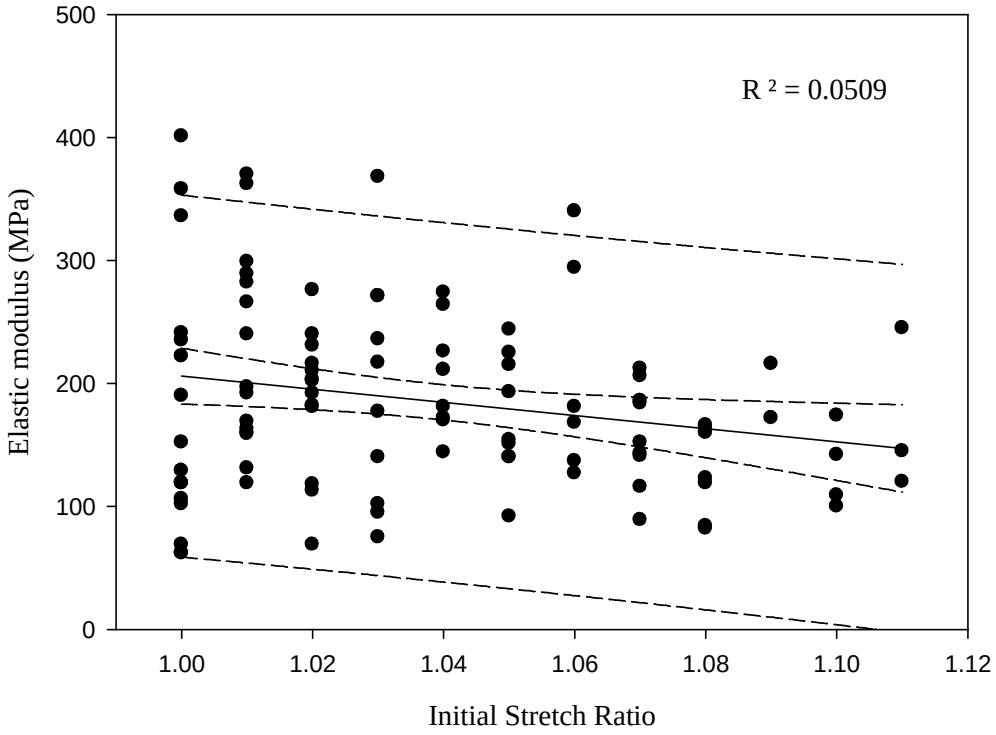

Figure 7.9: Trend between the elastic modulus and the initial stretch ratio. Dashed lines represent the 95 % confidence limits for the mean and the individual measurements.

As the initial stretch ratio is also size independent it seems reasonable for the initial stretch ratio and elastic modulus not to be strongly correlated. However, it might be expected that the initial stretch ratio depends on the elastic modulus by a simple force balance on a spherical shell. The results presented here suggest that the osmotic pressure difference and

the structure of the wall are not constant. The reasons for these relationships will be discussed further in Section 7.2.6.2.

It was possible to calculate the volumetric or bulk elastic modulus from the relationship shown below. Although the bulk elastic modulus is not an intrinsic material property, it is used widely in the plant biomechanics field.

$$\varepsilon_{Bulk} = \frac{dP}{dV}V \qquad \ldots (7.2)$$

where V is the cell volume, dV is the change in total volume of the cell and dP is the change cell turgor pressure. Using mean values, the bulk elastic modulus (ε_{Bulk}) from compression testing was calculated to be 8.78 MPa (Appendix 12). These values do not compare well with Meikle (1988) who derived values of 1.95 MPa for stationary phase cells and 3.25 MPa for mid-exponential phase cells. Levin *et al.* (1979) derived a value of 4.7 MPa from the data of Conway and Armstrong (1961). However, as has been previously stated (Section 2.3) the bulk elastic modulus has been described by Wu *et al.* (1985) as being a meaningless parameter because it treats the cell as a homogeneous sphere, and does not give direct information about the cell wall. The result presented here seems to further confirm this view of the volumetric elastic modulus.

7.2.3. Initial stretch ratio - Visualisation chamber

It was unknown if the initial stretch ratios shown in Figures 7.6 – 7.9 were reasonable. The visualisation chamber experiment was designed to allow the initial stretch ratio of individual cells to be determined independently of the compression testing experiment. The description of the technique is found in Section 3.3.2. Figure 7.10 a) and b) shows an example of the data obtained for an individual cell from the visualisation chamber.

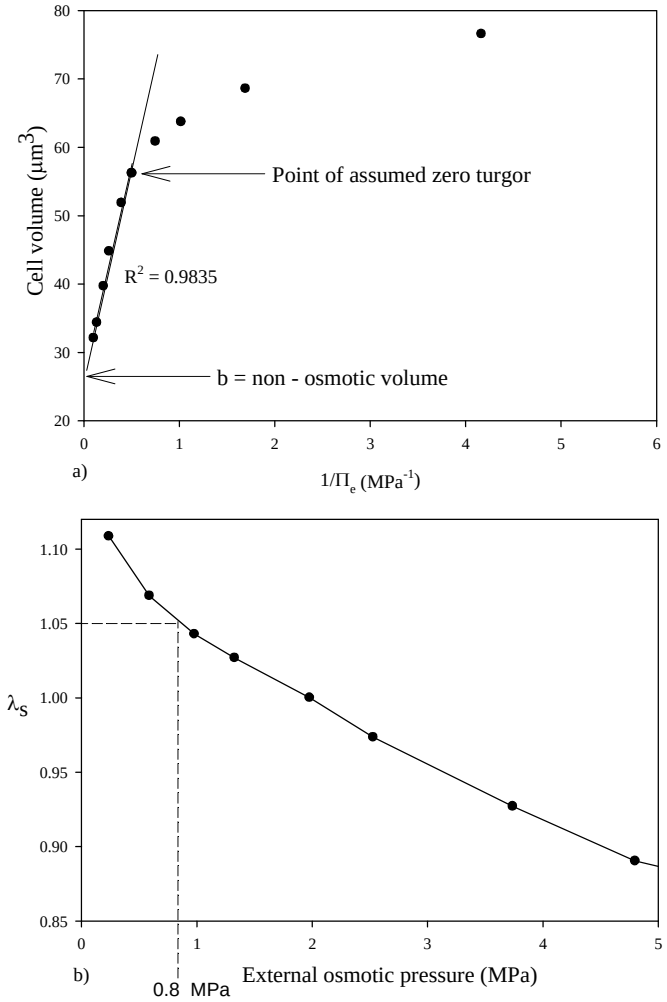

Figure 7.10 a) and b): Example of the data obtained directly from the visualisation chamber. a) Plot of the cell volume against the reciprocal of the external osmotic pressure ($1/\Pi_e$). In this case $V_0 = 56\ \mu m^3$ b) Plot of the initial stretch ratio against the external osmotic pressure. The initial stretch ratio of the cell suspended in Isoton II (0.8 MPa) is shown to be 1.05.

Figure 7.10 a) shows the cell volumes measured from the visualisation chamber at a range of external osmotic pressures for an individual cell. It was presumed that the abolition of cell turgor was indicated as the point at which the data at high external osmotic pressures was no longer linearly related to the volume of the cell, in this case at 56 μm^3. In addition to this it is possible to obtain the non - osmotic volume of each cell from the point at which the linear relationship between the cell volume and the reciprocal of the external osmotic pressure intercepts the cell volume axis. These assumptions are discussed in detail in Section 7.2.6. From Figure 7.10 b) the initial stretch ratio of the individual cell suspended in Isoton II (0.8 MPa) is shown to be 1.05. This process was repeated for 175 cells to allow a comparison of the initial stretch ratio measured by compression testing and using the visualisation chamber as shown in Figure 7.11.

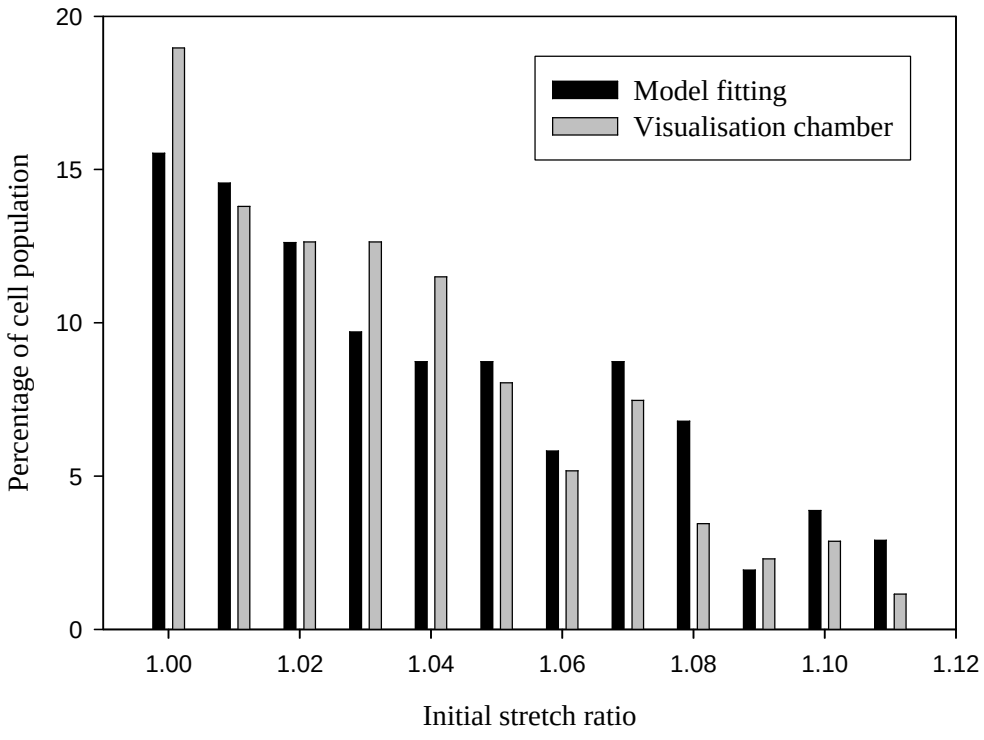

Figure 7.11: Comparison of the initial stretch ratio determined by compression testing and using the visualisation chamber. Number of cells shown as the percentage of the total population of the cells tested.

Using the visualisation chamber the mean initial stretch ratio of the population of cells was determined to be 1.033 ± 0.008. This compares well with the result from the compression testing where the mean initial stretch ratio was determined to be 1.039 ± 0.006 and that using the Malvern Mastersizer of 1.040 ± 0.007 (Data shown in Figure 3.14). Chi squared tests were performed on the data in Figure 7.11 and these showed that the distributions were statistically similar at the 5 % level. This demonstrates that the wide range of initial stretch ratios obtained by compression testing is reasonable. In addition to this the visualisation chamber data also demonstrated that the initial stretch ratio was not dependent on the cell size, as found by compression testing.

By combining equations 3.6 and 3.7 from Chapter 3 (repeated below for clarity) it is possible to calculate the turgor pressure of the cells when suspended in Isoton II ($\Pi_e = 0.8\text{MPa}$).

$$V = \frac{\Pi_{e,\Delta P=0}\left(V_{\Delta P=0} - b\right)}{\Delta P + \Pi_e} + b \qquad \ldots (3.6)$$

$$\lambda_s = \left(\frac{V}{V_{\Delta P=0}}\right)^{\frac{1}{3}} \qquad \ldots (3.7)$$

As mentioned previously it is also possible to calculate the non - osmotic volume of the cells, which is the total volume of the internal contents that are not water. From the visualisation chamber data the mean external osmotic pressure at which turgor was abolished ($\Pi_{e,\Delta P=0}$) was found to be at 1.66 MPa and the mean non-osmotic volume (*b*) was found to be 57 % of the cell volume at zero turgor pressure. Using these data the mean

turgor pressure (ΔP) of the cell was found to be 0.36 MPa when suspended in Isoton II ($\Pi_e = 0.8MPa$).

Using the data from the Malvern Mastersizer (data shown in Figures 3.13 and 3.14) the mean external osmotic pressure at which turgor was abolished was estimated as 1.4 MPa, the mean non-osmotic volume was 47 % and from this the mean internal turgor pressure was 0.28 MPa. This compares well with similar Malvern Mastersizer data from Smith *et al.* (2000a) where the turgor pressure was found to be 0.43 MPa when the cells were suspended in Isoton II. The turgor pressure of Baker's yeast (*Saccharomyces cerevisiae*) has been shown by Martínez de Marañón *et al.* (1996) to be abolished at an external osmotic pressure of 1.43 MPa for exponential cells and 1.58 MPa in stationary phase cells. Also the non – osmotic volume of exponential and stationary cells was found to be 53.5 % and 62 % respectively which correspond favourably with the data shown here.

The use of micromanipulation to measure the turgor pressure of plant cells directly has been shown to produce reliable results by comparison with the pressure probe (Wang *et al.*, 2006b). However, to do this it is necessary to be able to measure the contact area between the probe and the cell. As discussed earlier (Chapter 3) it is not possible to accurately visualise yeast cell during compression testing due to their small size, so the turgor pressure could not be calculated in this way.

7.2.4. Cell wall failure criteria

Because the models fit the experimental data well up to failure (e.g. Figure 6.1), it was possible to estimate the stresses and strains at failure. To be able to determine which of the failure criteria was most appropriate it would be necessary to have independent information on the mechanism of failure. It is not even clear whether the mode of failure of the walls is ductile or brittle, and because of the small size of yeast cells, it has proved impossible to confirm the mechanism of failure experimentally.

The numerical simulations allow the stress and strain at cell wall failure to be determined. Chapter 5 has shown that the stress and strain were up to 5 times greater in the circumferential (hoop) direction of the cell than in the meridian direction. Due to this it was assumed that cell wall failure propagated along the meridian direction. As the elastic model (with linear relationship between the stress and the strain) is able to fit the experimental data up to failure, it is assumed that negligible plasticity occurs prior to failure. Also above a deformation of 40 % the strain and stress in the wall were found to always be highest at the equator of the cell (Section 5.5.2) so this is where failure was assumed to occur. It would seem reasonable to characterise the stress at failure as the corresponding circumferential Kirchhoff stress, or the Cauchy stress for the incompressible case as used here (equation 5.35b in Chapter 5). The principal strain in the circumferential direction was calculated using the Hencky definition (equation 5.11 in Chapter 5). From this the mean circumferential stress at failure was found to be 115 ± 5 MPa and the mean circumferential strain at failure was found to be 0.46 ± 0.03. Size dependent effects of these parameters are shown in Figures 7.12 and 7.13.

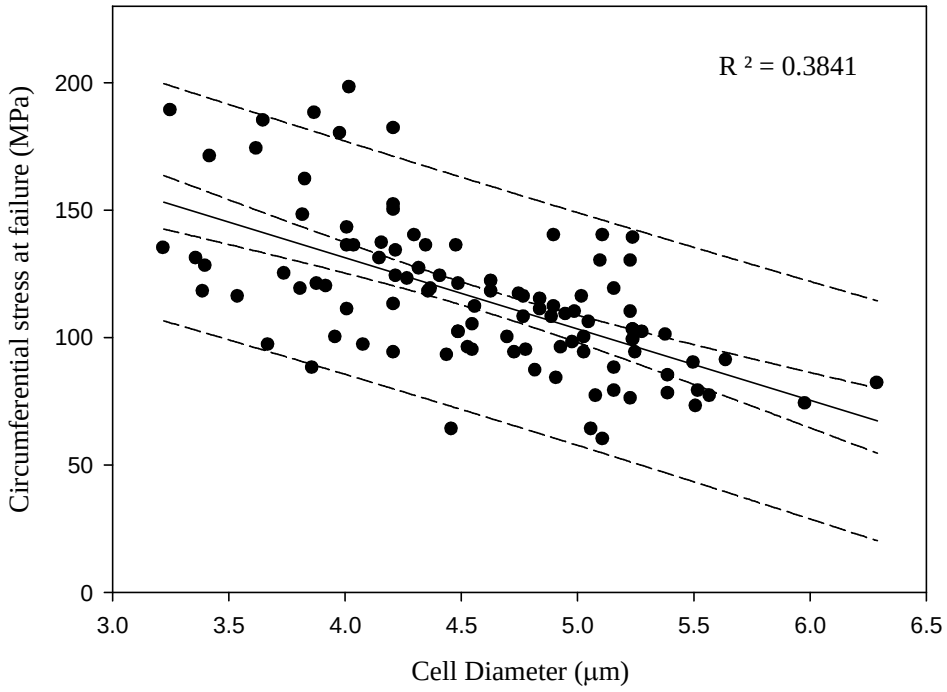

Figure 7.12: Trend between the Cauchy stress at failure and the cell diameter. Dashed lines represent the 95 % confidence limits for the mean and the individual measurements.

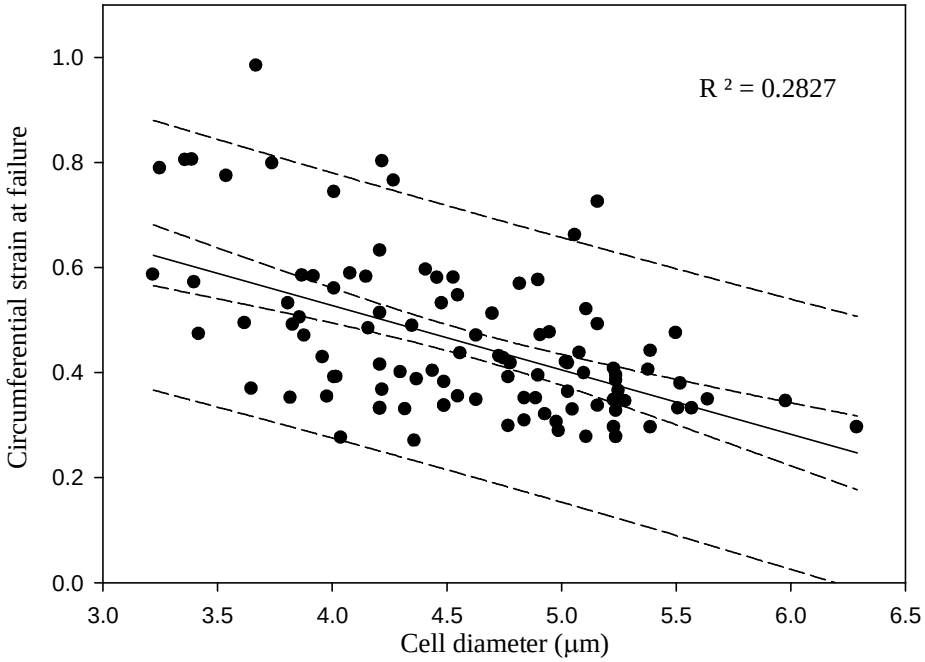

Figure 7.13: Trend between the strain at failure and the cell diameter. Dashed lines represent the 95 % confidence limits for the mean and the individual measurements.

Figure 7.12 and 7.13 show that the principal stress and strain in the cell wall at failure are decreasing functions of the cell diameter.

Other possible failure criteria that could be used are the von Mises stress and strain as used by Smith *et al.* (2000b). von Mises stress is often used to determine the yielding point at which a ductile material, such as metal, begins to deform plastically. For plane stress conditions the von Mises stress can be calculated from the stress components using:

$$\sigma_{vm} = \sqrt{\sigma_1^2 - \sigma_1\sigma_2 + \sigma_2^2} \quad \ldots (7.3)$$

and the equivalent von Mises strain, assuming incompressibility, can be calculated using:

$$\sigma_{vm} = \frac{2}{3} E\varepsilon_{vm} \quad \ldots (7.4)$$

where σ_1 and σ_2 are the meridian and circumferential stress respectively, E is the elastic modulus, σ_{vm} is the von Mises stress at failure and ε_{vm} is the von Mises strain at failure. If a von Mises failure criteria was assumed in this work the corresponding stress and strain at failure were found to be 102 ± 5 MPa and 0.94 ± 0.08. These values are different to those given by Smith *et al.* (2000b) who found the mean von Mises stress at failure to be 70 ± 4 MPa and mean von Mises strain at failure to be 0.75 ± 0.08. Similarly to the principal stress and strain the von Mises failure criteria were found to also be decreasing functions of the cell diameter (Appendix 13), presumably for the same reason.

Another possibility is the strain energy per unit volume at failure, on the assumption that any cell breakage in processing would require the energy stored in the cell wall to exceed some critical level. This failure measure might be useful when considering the breakage of yeast cells in disruption processes such as homogenisation. The strain energy per unit volume (equation 5.44) at failure W_f for the incompressible case is given by:

$$W_f = \frac{2E}{3}\left(H_{1f}^2 + H_{2f}^2 + H_{1f}H_{2f}\right) \quad \ldots (7.5)$$

where H_{1f} and H_{2f} are the Hencky strains at failure (i.e. percentage deformation at failure) in the meridian and circumferential direction, respectively. The value for this criterion was found to be 30 ± 3 MPa (MJm^{-3}). The cell size dependent effects of the strain energy per unit volume at failure are shown in Figure 7.14.

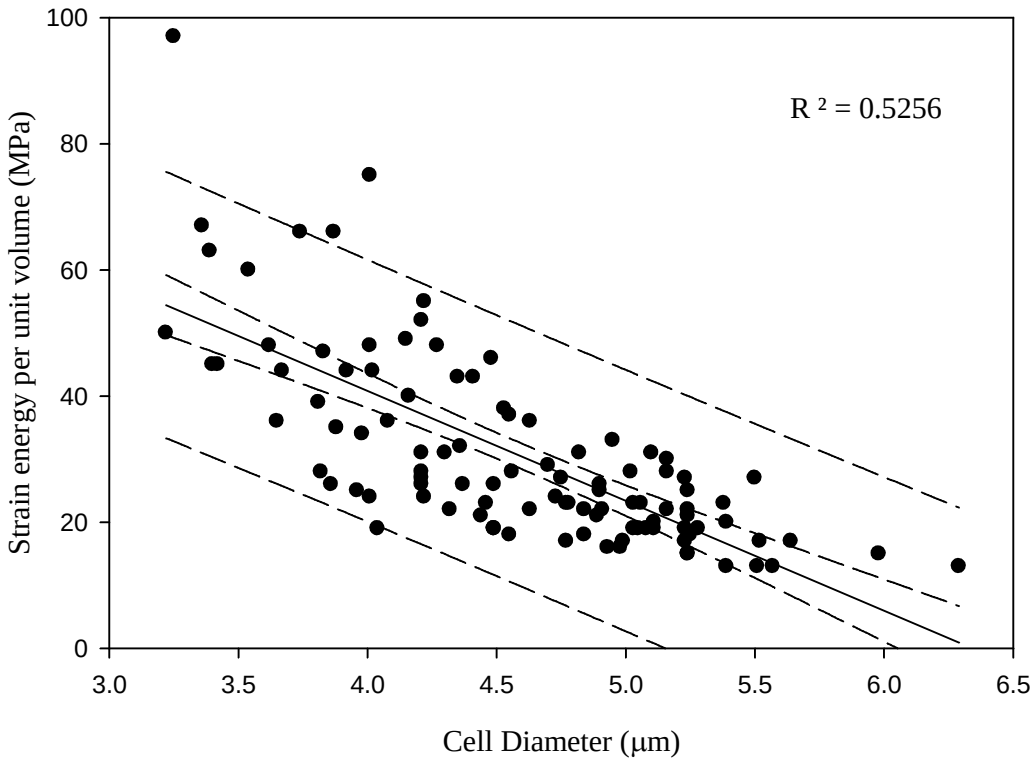

Figure 7.14: Trend between the strain energy per unit volume at failure and the cell diameter. Dashed lines represent the 95 % confidence limits for the mean and the individual measurements.

As with all of the other failure criteria the strain energy per unit volume at failure was a decreasing function of the cell diameter. The possible reasons for these relationships will be discussed further in Section 7.2.6.

7.2.5. Effect of the cell wall thickness assumptions

As mentioned earlier, it was impractical to determine the cell wall thickness of individual cells during compression testing, so a constant cell wall thickness to cell radius ratio was used. Cheng (1987a) and Smith *et al.* (2000b) stated that it is the "surface modulus" Eh_o that actually determines the mechanical properties of the cell wall. Eh_o controls the magnitude of

the dimensionless experimental data and not purely E. As shown in Chapter 5 when τ (the cell wall thickness to cell radius ratio) was varied it did not affect the dimensionless force curve of the numerical simulations. However, if the incorrect cell wall thickness were used (i.e. an incorrect τ assumption) when converting the force data to dimensionless form, then the magnitude of the curve would change. This would lead to a different E being calculated. Even though an incorrect h_o would lead to a different E value, the same Eh_o (surface modulus) would be obtained regardless of the τ assumption.

A surface modulus of 15.3 ± 1.2 Nm^{-1} was calculated here, in comparison to previously reported values of 11.4 ± 0.4 Nm^{-1} (Smith *et al.,* 2000b). The surface modulus calculated in this work was shown to be only weakly correlated with the cell diameter (Figure 7.15).

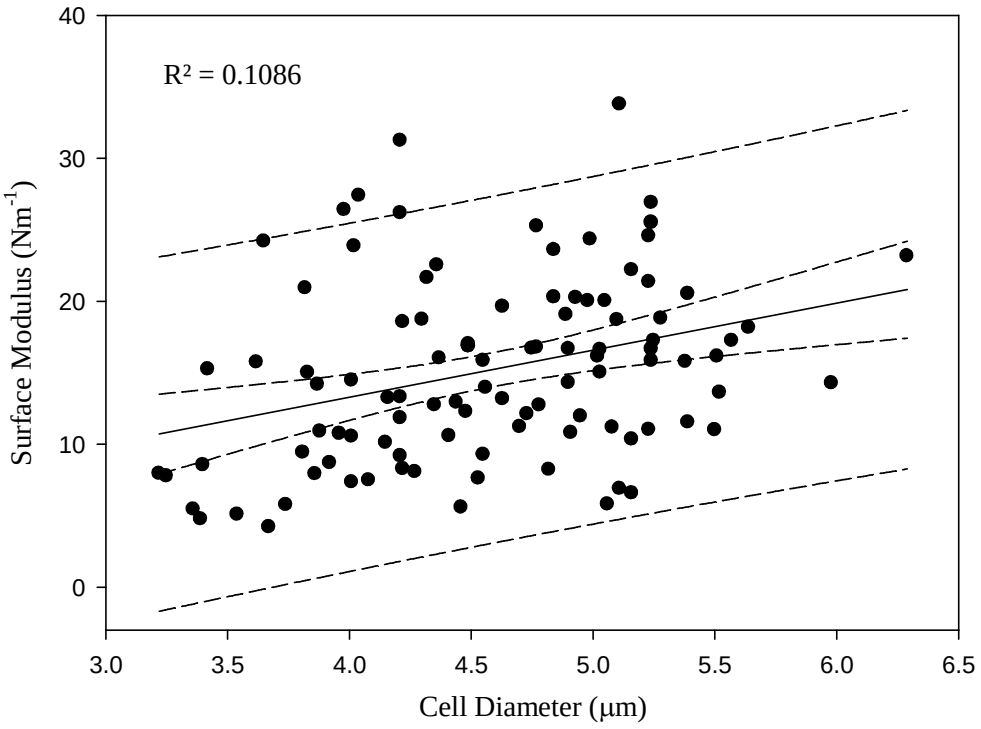

Figure 7.15: Trend between the surface modulus and the cell diameter. Dashed lines represent the 95 % confidence limits for the mean and the individual measurements.

If the data for a compression speed of 68 μms^{-1} from Figure 7.1 were used (λ_s fixed at 1.04 as with Smith *et al.* (2000b)) then a surface modulus of 13.9 ± 1.1 Nm^{-1} could be determined, which should be directly comparable to Smith *et al.* (2000b) who gave a value of 11.4 ± 0.4 Nm^{-1}.

In addition to this it is possible to examine the effects of eliminating the cell wall thickness assumption on the failure criteria. From the literature it does not appear that this parameter has an established name. This will be in effect treating the strain energy per unit volume (defined previously as W_f) as the strain energy per unit area. In this work this failure criteria will be called the surface strain energy at failure (W_{sf}).

The surface strain energy at failure W_{sf} for the incompressible case is given by

$$W_{sf} = \frac{2Eh_o}{3}\left(H_{1f}^2 + H_{2f}^2 + H_{1f}H_{2f}\right) \qquad \ldots (7.6)$$

where H_{1f} and H_{2f} are the Hencky strains at failure in the meridian and circumferential direction, respectively. Figure 7.16 shows the surface strain energy at failure against the cell diameter.

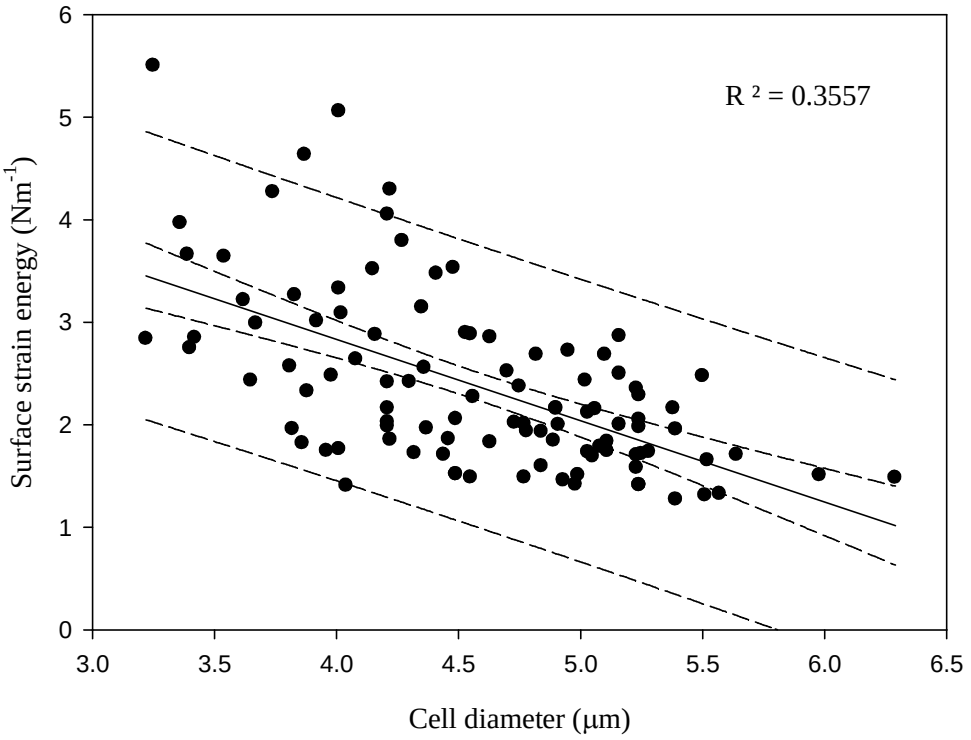

Figure 7.16: Trend between the surface strain energy and the cell diameter. Dashed lines represent the 95 % confidence limits for the mean and the individual measurements.

From the data in Figure 7.16 a mean surface strain energy of 2.4 ± 0.2 Nm^{-1} was determined. Unlike the strain energy per unit volume function this parameter was not dependent on the cell wall thickness assumption and so was more appropriate as a comparison between cell populations. Unfortunately there do not appear to be any similar results in the literature with which to compare this value.

It is believed that only the inner β 1,3 - glucan layer provides mechanical support to the cell wall (Klis *et al.,* 2006) so it may actually be inappropriate to use the whole cell wall thickness in modelling. Also if the outer layers of the cell wall were stripped away by enzymic treatment (Zlotnik *et al.,* 1984) then the cell wall thickness assumption used in this

work would no longer be valid. As well as this, although the cell wall thickness to cell radius ratio used in this work (Section 3.5 and Section 6.1.2) is a good estimate there was still a variation in cell wall thickness within the cell population which cannot be fully accounted for. By using the surface modulus and the surface strain energy the uncertainty in cell wall thickness can be eliminated. However, to use these parameters it is essential that the dimensionless groups used to fit the numerical simulation to the experimental data are correct. By using the dimensionless group in this work ($F/Er_o h_o \lambda_s^2$) it was possible to make incorrect assumptions about the cell wall thickness and still obtain the same surface modulus and surface strain energy values.

By using the surface modulus and the surface strain energy it was also possible to make comparative measurements between cell populations with different histories. This technique was used in experiments described in Chapter 8.

7.2.6. Discussion

In Section 7.2.6.1 the elastic modulus determined by modelling is compared to previously reported results for Baker's yeast cells and similar organisms. In addition, the relationships between the failure criteria and the cell size and elastic modulus are considered.

Following this, the initial stretch ratios produced by modelling and from the visualisation chamber experiments are discussed. Finally, biological differences that occur within the cell population and the effect that these might have on mechanical properties are described.

7.2.6.1. Elastic modulus and failure criteria

In this Section the elastic modulus produced by modelling is compared to previously reported values. Ideally comparisons between surface modulus values would also be made, but this parameter is not widely used so it is not possible to do this.

There are few studies available in the literature on the mechanical properties of fungal cell walls. Using atomic force microscopy (AFM) the elastic modulus of *Aspergillus nidulans* has been determined to range between 110 MPa and 200 MPa depending on the distance from the hyphal tip and on the growth media (Zhao *et al.,* 2005). This is an important result as both the yeast used in this study, *Saccharomyces cerevisiae,* and *A. nidulans* have similar chemical and structural properties (Bull, 1970) so an elastic modulus of similar magnitude would be expected.

Smith *et al.* (2000b) obtained an elastic modulus of 150 ± 15 MPa for Baker's yeast in comparison to a value of 185 ± 15 MPa from the current work. One of the major reasons for this difference is that Smith *et al.* (2000b) assigned λ_s a value of 1.04, the mean value for the population obtained from the Malvern Mastersizer (Smith *et al.,* 2000a). In this work when λ_s is fixed at 1.04 an elastic modulus of 166 ± 15 MPa was obtained. This suggests that by fixing λ_s and not treating it as an adjustable parameter the results obtained by Smith *et al.* (2000b) underestimated the true elastic modulus. This result suggests that the effect of the initial stretch ratio on the elastic modulus is not symmetrical, a relationship which is confirmed in Appendix 14.

In addition to this, Smith *et al.* (2000b) stated that the elastic modulus decreases with cell size in contrast to this work where the elastic modulus was size independent. When comparisons were made using the surface modulus this parameter was found to be size independent by Smith *et al.* (2000b) and weakly positively correlated with the cell size in this work (Figure 7.15). This suggested that any cell size dependent relationships for the elastic modulus might be entirely due to the assumptions made about the cell wall thickness to cell radius ratio (τ).

Also, any remaining differences observed between this work and that of Smith *et al.* (2000a; 2000b) might be attributed to the very low cell population viability of ~ 70 % stated by Smith *et al.* (2000a) whereas in this work the cell population viability was found to be in excess of 95 %. Both of these studies used Fermipan Baker's yeast cells (Fermipan Red, DSM Bakery Ingredients, Dordrecht, Holland). The large difference in population viability suggests the cell population in Smith's work had been perturbed in some way which might have affected the modulus determination as well as the viability.

From the relationships outlined in this Chapter it can be seen that the initial stretch ratio was not dependent upon any other measured parameter (Figure 7.6 – 7.9). Due to this, the initial stretch ratio is not considered initially when discussing the relationships between the parameters. Relationships with the initial stretch ratio are described in Section 7.2.6.2.

In order to understand the relationships between the parameters it is important to consider the structure of the Baker's yeast cell wall. The inner β 1,3 - glucan layer is believed to be the cell wall constituent that provides the majority of the mechanical strength to the cell (Klis *et al.,* 2006). As described in Section 2.2.1.1 β 1,3 - glucan chains are highly elastic

due to their hollow helix structure. Within the cell wall chitin is deposited in the lateral cell walls and cross linked with β 1,3 - glucan and β 1,6 - glucan of cells following cytokinesis (Shaw *et al.*, 1991). However, it is generally not present in the growing bud walls at all, suggesting that chitin is not essential for the stability and mechanical strength of the cell walls. The majority of chitin is found in the bud scars of mother cells following cell cytokinesis. It has been shown by AFM that the chitin within the bud scar has an elastic modulus up to 10 times greater than the mannoprotein surface (Touhami *et al.*, 2003). Although this work uses a Hertzian model (used for small elastic deformation where the contact area is small compared to the radius), the comparison of the magnitude of the results still seems valid. When the highly elastic β 1,3 - glucan layer is cross-linked with the significantly stiffer chitin (elastic modulus 80 GPa, tensile strength 4 GPa, breaking strain 8-10%: Harris, 1980) the ability of the cell wall to stretch during compression is expected to be reduced (Lesage and Bussey, 2006).

An hypothesis may be proposed such that the relationships found between the parameters can be seen to be consequences of the changes that occur within the cell wall during the growth cycle of yeast cells. It is believed that this occurs mainly due to the increased number of chitin bud scars that develop in the cell wall following cytokinesis. It is expected that the larger cells will be older and so contain a higher number of bud scars leading to the cell size effects seen in this work. In order to help better understand the relationships between the parameters the relevant results are reproduced below together with the relevant numerical simulation results. It is accepted for the purpose of this discussion that the β 1,3 - glucan layer is the primary component responsible for the strength of the cell wall (Klis *et al.*, 2006) although this may change as the cells age.

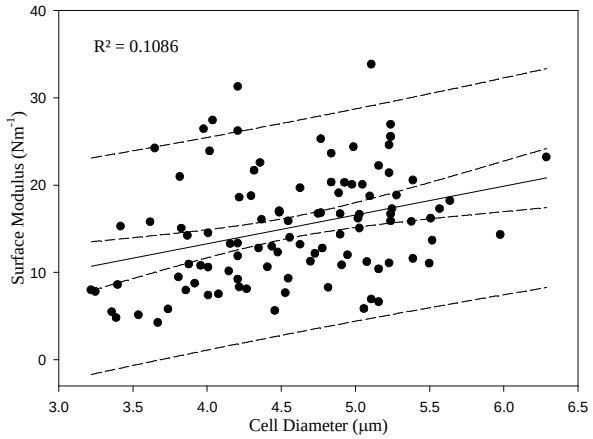

Figure 7.15: Trend between the surface modulus and the cell diameter.

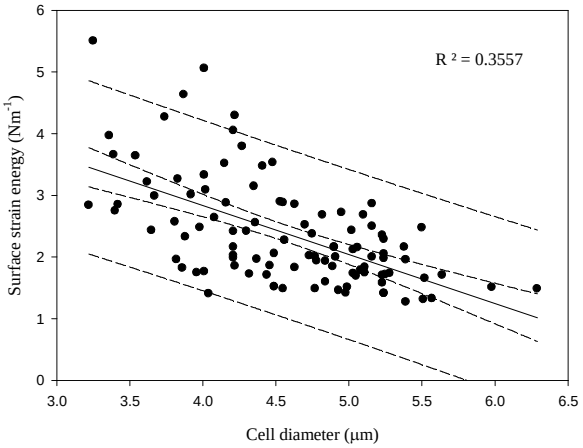

Figure 7.16: Trend between the surface strain energy at failure and the cell diameter.

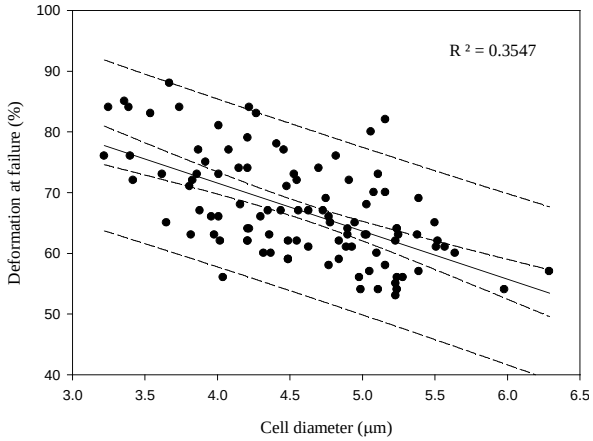

Figure 4.9: Trend between the deformation at failure and cell diameter.

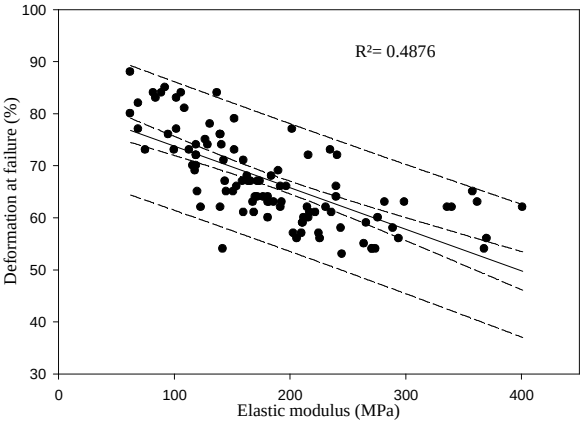

Figure 7.4: Trend between the deformation at failure and the elastic modulus.

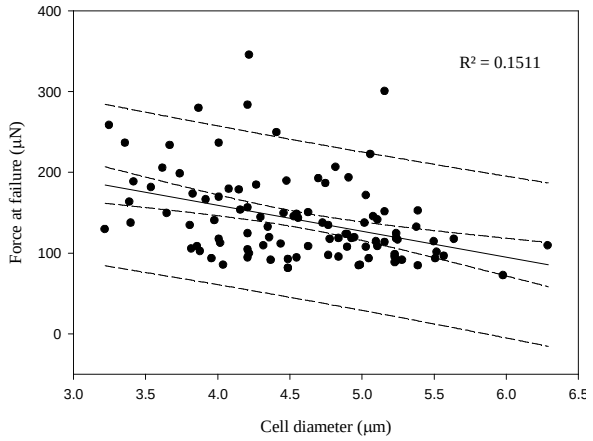

Figure 4.7: Trend between the force at failure and cell diameter.

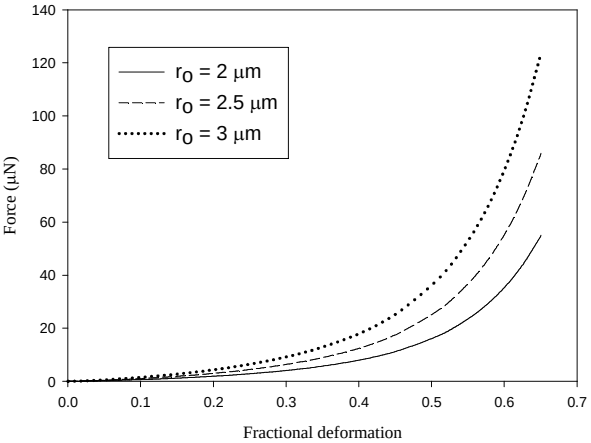

Figure 7.17: Effect of changing cell size on the force - deformation data produced from numerical simulations. E = 100 MPa, $\lambda_s = 1.04$, $\tau = 0.037$.

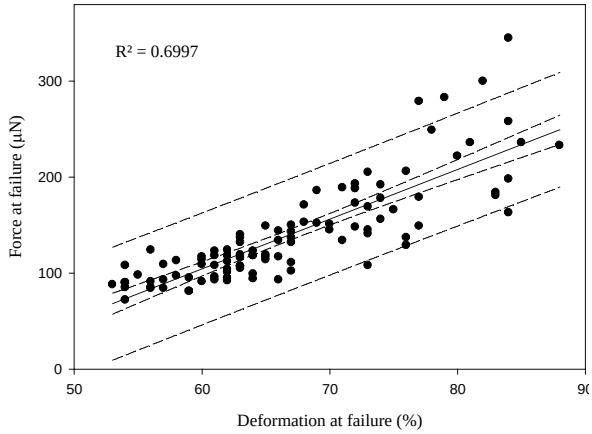

Figure 4.8: Trend between the force and deformation at failure.

Firstly, it is assumed that the larger cells are older and therefore contain chitin bud scars that display a greater mechanical stiffness than the remainder of the cell wall. The evidence for this increased stiffness is found in AFM studies (Touhami *et al.*, 2003). As described by Smits *et al.* (2006) and Powell *et al.* (2003) the bud scar is a rigid structure that expands little or not at all as the cell grows. From Figure 7.15 it can be seen that the surface modulus was weakly correlated with increasing cell size. This suggests that addition of the chitin bud scars into the cell wall did increase the stiffness of the larger cells, although any effect was small. This might be because there were relatively few bud scars even on the larger cells.

From Figure 7.16 it can be seen that the surface strain energy at failure was negatively correlated with the cell size. As the surface modulus increases with cell size, then, for a homogeneous material, if all cells failed at the same strain it would be expected that the surface strain energy would also increase with cell size. This is not found in this work so some other explanation needs to be found. It is possible that, stress concentrations occur around the bud scars, or possibly some other flaws appear in the β 1,3 - glucan layer of older cells. If the surface strain energy at failure reduces with cell size and the surface modulus increases, this means the strains at failure must also reduce with cell size. This would

explain why the percentage deformation at failure is correlated (negatively) with the cell size, as in Figure 4.9, and also, why the elastic modulus shows a similar correlation with the deformation at failure (Figure 7.4).

From Figures 4.7 it can be seen that the force at failure is weakly negatively correlated to cell size. In general, larger cells of the same material will require a larger force to reach a given fractional deformation, as a greater volume of material is being deformed, and this is evident in Figure 7.17. In addition the force at failure is strongly correlated with the deformation at failure as shown in Figure 4.8. However, interpretation of these figures must be done with care, because in Figure 4.8 a higher deformation does not correspond to a larger cell, in fact the opposite is found. So, although at a given deformation a larger force is required for a larger cell, the force at failure is usually smaller for a larger cell because the latter fail at a lower deformation. It is hypothesised here that this is because of stress concentration effects induced by the bud scars in the larger cells. By using the cell diameter and fractional deformation at failure of the experimental data it is possible to use the numerical simulation results, such as those in Figure 7.17, to predict the force at failure.

The hypothesis outlined previously suggests that the changes in the measured parameters occurred because of compositional changes within the cell wall. As outlined above it seems reasonable from the relationships between the parameters to assume that as the cell increases in size the number of bud scars also increases. This leads to the material of the cell wall becoming stiffer (i.e. higher surface modulus) and there may be some stress concentration affects near bud scars that cause the surface strain energy at failure to decrease with cell size. However, as it is currently not possible to determine the composition

and structure of each cell being compressed it is possible that these relationships could be due to some other unknown factors.

7.2.6.2. Initial stretch ratio

As has been shown it is possible to calculate the initial stretch ratio from the compression testing data (Section 7.2.2) and using osmotic pressure changes (Section 7.2.3).

7.2.6.2.1. Compression testing

The initial stretch ratio (λ_s) is a measure of the stretch of the cell wall. Therefore it might have been expected that some relationship would exist between λ_s and the deformation at failure on the grounds that a higher initial stretch would mean that a smaller deformation would be required to stretch the wall to failure. The lack of a relationship between the deformation at failure and the initial stretch ratio (Figure 7.7) differs from that implied by Smith *et al.* (2000a) who found that cells compressed in distilled water (λ_s = 1.1) had a lower mean deformation at failure than cells in Isoton II (λ_s = 1.04). However, the result presented in Smith *et al.* (2000a) is a population average of cells suspended in different solutions and so one might not expect to see the same result here for the small number of cells that had such high initial stretch ratios. The key point is that in this work the biological variability within the sample was being investigated, while in the work of Smith *et al.* (2000b) it was an explicit change in the external osmotic pressure that was being investigated.

When considering the initial stretch ratio (λ_s) the interpretation of the results is not straight forward as it does not appear to correlate with any other parameters. For a cell to have a higher λ_s it is expected that the strain within the wall prior to deformation would be higher. During compression testing by micromanipulation the strain in the wall increases as the cell is compressed until failure occurs. It might therefore be expected that cells with a higher initial stretch ratio would exceed this failure criterion at a lower force due to the higher initial strain within the wall. However, this is only true if all the cells have the same material properties, which the results in Section 7.2 show is not the case. As λ_s is a measure of the stretch of the cell wall it may have been expected that the larger cells with more bud scars would lead to a lower λ_s as they are less able to stretch. However, the surface modulus is only weakly correlated with cell diameter (Figure 7.15) and also it is not necessarily the case that the internal turgor pressure of every cell is the same. As λ_s is a function of both the internal environment of the cell and the cell wall structure it might be unreasonable to expect correlations with λ_s.

In a cell population the cell wall composition and structure as well as the internal environment of the cells can vary widely leading to different initial stretch ratios. Meikle *et al.* (1988) demonstrated this by showing cells from the stationary phase and the exponential phase, which will have a different composition and structure, will have different mean initial stretch ratios.

The cell wall thicknesses of mother cells are known to be thicker than those of the smaller daughter cells, leading to the assumption of a constant τ used in this work (Chapter 6). Due to this it may have been expected that a different response to osmotic pressure variations would be dependent on the cell size. However as has been shown here and by others

(Martínez de Marañón *et al.,* 1997) the initial stretch ratio is not dependent on the cell size or therefore the cell wall thickness. This result suggests that factors other than cell wall thickness are controlling the initial stretch ratio.

7.2.6.2.2. Osmotic pressure changes

In order to confirm that the initial stretch ratio results produced by compression testing were reliable, independent experiments were performed using changes in the external osmotic pressure (Section 3.3). To calculate the initial stretch ratio using the osmotic pressure changes it was necessary to use the Boyle van't Hoff relationship described in Section 3.3.1. It is clear from the data in Figure 3.13 that as the osmotic pressure of the external solution was altered so the volume of the cell changed. The most interesting observations in this experiment were that as the external osmotic pressure increased past the point identified earlier as "plasmolysis" (point A in Figure 3.13) so the cell volume continued to decrease. One might have expected the volume to be essentially constant at high external osmotic pressures, as happens with plant cells (Nobel, 1991; Blewett, 2000). For yeast cells Morris *et al.* (1983) stated that as the volume of the protoplast decreases due to osmotic water loss, the wall will shrink with the plasma membrane until the tension in the wall is zero at which point the cell membrane may separate from the cell wall. Gervais *et al.* (1996) suggested that following plasmolysis in yeast the cell turgor pressure would be zero.

Although it is known that the protoplast shrinks with the cell wall at high external osmotic pressures (Niedermyer *et al.,* 1977), it is still not entirely clear as to what happens. The cell membrane appears by both optical and electron microscopy (Niedermyer *et al.,* 1977; Morris *et al.,* 1983) to remain closely pressed against the cell wall during external osmotic

pressure changes. This would suggest the protoplast is somehow anchored to the cell wall causing its shrinkage. If this were the case it would imply that the protoplast is mechanically strong enough to compress the cell wall as it shrinks at high osmotic pressures. This seems unlikely. It would also indicate some form of structural bonding between the two structures that has not yet been identified.

An alternative idea is that the cell wall also acts an ideal osmometer, even when there is zero turgor in the protoplast. High levels of the external osmotic pressure could still cause the wall to shrink if it acts as an osmometer.

Another suggestion is the cell wall may become dehydrated at higher external osmotic pressures leading to its shrinkage. However, no direct evidence of this has been found.

Finally, another explanation for the continued shrinking of the cell was given by Jennings (1995). It was proposed in this work that the cell membrane will remain close to the cell wall if the structure is only able to allow solutes to move slowly through it. It has been previously noted by (Oertli, 1986) that if a walled cell is subjected to a high external osmotic pressure solute then a negative pressure will be generated in the wall. This can be demonstrated using the following equation:

$$\Delta P_w - \Delta \Pi_w = \Delta P_m - \Delta \Pi_m \qquad \ldots (7.8)$$

where $\Delta \Pi_w$ is the osmotic pressure of the wall, $\Delta \Pi_m$ is the osmotic pressure of the cell membrane, ΔP_w is the turgor pressure of the wall and ΔP_m is the turgor pressure of the cell membrane. From equation 7.8, if $\Delta \Pi_w > \Delta \Pi_m$ then $\Delta P_w < \Delta P_m$ as the solute cannot penetrate

the wall, meaning that the turgor pressure in the wall would be lower than the pressure in the membrane. This difference in the pressure would keep the cell membrane pushed against the wall but there would also be a negative pressure in the wall. This negative pressure could be responsible for the cell shrinkage. Niedermeyer *et al.* (1977) have observed the penetration of glycerol through the cell wall at high external osmotic pressures. As one of the major functions of the mannoprotein in the yeast cell wall is to control the movement of macromolecules and play a role in water retention (Klis *et al.*, 2006), it is possible that this structure also affects the cell volume changes. As described in Chapter 2 the cell wall can be described as a fibrous network. It is conceivable that if the outer mannoprotein layer is able to control the internal environment of the cell then the structural components of the wall may 'mesh' closer together at high pressures to maintain the equilibrium.

Niedermeyer *et al.* (1977) observed at high osmotic pressures large depressions and invagination of the cell membrane though no effect on the cell wall was observed. Morris *et al.* (1983) showed that the surface of *S. cerevisiae* was unaffected at high osmotic pressures but the cell wall increased in thickness. It was also noted that the cytoplasmic side (inner surface) of the cell wall buckled with irregular projections into the cytoplasam. This suggests that significant structural changes were occurring within the wall. A similar process known as cytorrhysis occurs in plant cells where at high external osmotic pressures the cell wall will collapse (Pryce – Jones *et al.*, 1999).

Regardless of the reason for the shrinkage, decreases in cell wall size at high external osmotic pressures suggest that there may be compressive forces in the wall. This is a very important point as an initial stretch ratio of 1 is supposed to indicate zero tension within the cell wall. This means it is quite important to identify the point of "incipient plasmolysis" or

rather the point at which the tension in the wall became zero as the external osmotic pressure increased.

As well the problems in identifying exactly what is happening when *S. cerevisiae* is exposed to high osmotic pressures there are also possible problems with the Boyle van't Hoff plot itself. As previously mentioned one of the most difficult aspects is identifying the point at which the tension in the cell wall is zero (apparent incipient plasmolysis).

Using the Boyle van't Hoff relationship it is possible to show the relationship between the volume of the cell and the reciprocal of the external osmotic pressure. This was done as it is the convention in the literature when using the Boyle van't Hoff relationship (Gervais *et al.*, 1996; Meikle *et al.* (1988); Munns *et al.* (1983). The derivation of the Boyle van't Hoff relationship used to justify this is given in Appendix 15. Figure 7.10 a) is repeated below to allow easier discussion of the results.

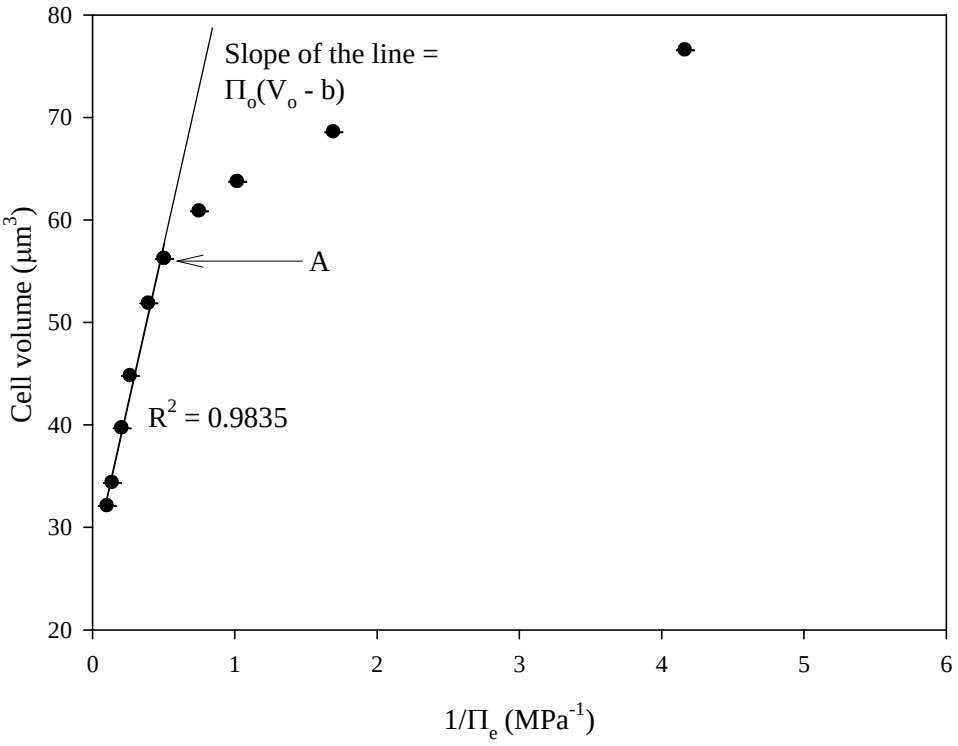

Figure 7.10 a): Comparison of the experimental data from the visualisation chamber and the Boyle van't Hoff model.

Figure 7.10 a) shows what appears to be a nearly linear relationship between the cell volume and high external osmotic pressures. This is followed by a curved region which presumably asymptotes or at least tends towards a value for Π_e at zero (i.e. the osmotic pressure of water). Smith *et al.* (2000a), Meikle *et al.* (1988) and Munns *et al.* (1983) chose the point of plasmolysis as the point where there is no longer a linear relationship between the reciprocal of the external osmotic pressure and the cell volume (Point A in Figure 7.10 a)). This value is designated Π_o, the point at which turgor is abolished. It is unclear from the work of Gervais *et al.* (1996) how they identified the point at which turgor is abolished. Due to the small size of yeast cells and because the protoplast does not separate from the cell wall it is not possible to use direct measurement techniques (i.e. plant cell pressure probe) for independent confirmation of the point of zero turgor.

One of the major assumptions of the initial stretch ratio calculation is that the cell is able to behave as an ideal osmometer at osmotic pressures higher than the point at which turgor is abolished. This assumption is used to account for the linearity of the volume relationship at high external osmotic pressures. Gervais *et al.* (1996) stated that the linear relationship between the point of zero turgor and the maximum osmotic pressure is only theoretically justified if the solution can be considered dilute, which corresponds to a maximum osmotic pressure of 13 MPa. This is higher than the maximum osmotic pressure used here so a linear relationship was expected. As was shown in Appendix 15 and Figure 7.10 a) the theoretical Boyle van't Hoff relationship is approximately linear at the highest osmotic pressures. This suggests that the prediction of a linear relationship between the volume and the osmotic pressure is correct. Therefore it appears that the cell does act as an ideal osmometer at osmotic pressures above zero turgor. It seems reasonable then to take the point of zero turgor as the point at which the linear relationship between the cell volume and the reciprocal of the external osmotic pressure starts to deviate.

As well as using the Boyle van't Hoff relationship the initial stretch ratio was also determined independently using mathematical fitting of experimental compression data producing very similar results (Figure 7.11). The similarity of the results produced by these two independent techniques seems to confirm that the data being obtained by both is reliable. However, as previously discussed it is still not entirely clear exactly what is happening to the cell at high external osmotic pressures. The physical response of the yeast cells to high osmotic pressures is an area of work that requires further investigation.

7.2.6.3. Biological variability and changes in the cell wall composition and structure

The scatter observed in the Figures shown in this Chapter is assumed to be due to the biological variability of the cell population. There are an estimated 1200 genes of *S. cerevisiae* which affect the composition and organisation of the cell wall (Klis *et al.*, 2006). The expression of these genes during the cell cycle is a tightly controlled process with many of the genes being interdependent. This has been shown by microarray analysis which indicated that approximately 50 % of the cell wall proteins are regulated by the cell cycle (Spellman *et al.*, 1998). In addition, the mechanisms and processes of growth will change during the cell cycle between isotropic (growth over whole of cell surface) and apical (growth at the tip during bud formation). The process of apical growth during bud formation will lead to the deposition of chitin bud scars in the cell wall with older cells expected to have an increased number of bud scars. It is also known that changes in the growth medium, growth temperature, external pH and oxygen levels will significantly affect the thickness, composition and structure of the cell wall (Aguilar-Uscanga and Francois, 2003). Also within a population while two individual cells might be of an equivalent age this does not mean that there cell wall construction and composition will be identical. This has been shown in this work where cells that are of equivalent size have produced different measured properties (i.e. elastic modulus). Significant advances have been made in recent years to understand how the cell wall structure and composition is controlled. However, knowledge of the temporal and spatial construction of the cell wall during the cell cycle is far from complete.

The Baker's yeast cells (*Saccharomyces cerevisiae*) used in this work have been shown to be late stationary phase (Kleinig, 1997). When cells enter the stationary phase their cell

walls change becoming thicker and more impermeable to macromolecules (Klis *et al.*, 2002; 2006). Also the number of disulphide bridges in the cell wall increases by 6-7 times from that of exponential cells (De Nobel *et al.*, 1990). The thickness of the yeast cell wall is also cell size dependent with mother cells (largest cells) being thicker than those of the daughter cells (smallest cells). This relationship is simulated by the size independent measurement τ used in this work. The importance of this is that it would imply that the material deposited in the wall contributes equally to the material properties which may not be the case. Mannoprotein and chitin are deposited in the cell wall late in the cell cycle with mannoprotein believed not to play a role in the mechanical strength. However, there has been no direct confirmation of this, only indirect osmotic studies (Zlotnik *et al.*, 1984). If it is assumed that mannoproteins do not contribute to the mechanical properties of the yeast cell wall, and the thickness is taken as being only that of the β 1,3 - glucan layer, then the elastic modulus and consequently the strain energy per unit volume at failure value would be significantly higher than those presented here (See Figure 5.13). However, as previously stated the surface modulus and the surface strain energy will be unaffected.

As the cell wall structure and composition of the individual cell being compressed was unknown it is possible that the relationships found here are due to some other factors. Further investigation of the effect of chitin on the relationships found by compression testing could use mutants lacking the chitin synthases (Shaw *et al.*, 1991). In addition, as the cell wall thickness, composition and structure of individual cells being compressed was unknown all further work should be done using the surface modulus and surface strain energy.

7.3. Conclusions

The compression testing technique has been used to produce force - deformation data from the compression of yeast cells at a wide range of speeds. This was combined with the numerical model developed in Chapter 5 to obtain intrinsic material properties and failure criterion of the yeast cell wall.

This result confirms that a thin walled sphere with a linear elastic constitutive equation for the cell wall can represent the yeast cell. Uniquely investigations into the effects of compression speed have shown that compression speeds are attainable that allowed the cell wall permeability to be treated as negligible and so allow the initial stretch ratio of individual cells to be measured for the first time by micromanipulation. This study has given mean cell wall properties for late stationary phase Baker's yeast of: elastic modulus 185 ± 15 MPa, initial stretch ratio 1.039 ± 0.006, circumferential stress at failure 115 ± 5 MPa, circumferential strain at failure of 0.46 ± 0.03, strain energy per unit volume at failure of 30 ± 3 MPa, surface modulus 15.3 ± 1.2 Nm^{-1}, and surface strain energy of 2.37 ± 0.16 Nm^{-1}.

Chapter Eight: Effect of dithiothreitol and sonication on the mechanical properties of Baker's yeast cells

In the preceding Chapters the mathematical model and the experimental techniques necessary to measure the intrinsic material properties of yeast cells were established. This made it possible to measure the effect of chemical and mechanical treatment on the intrinsic material properties of the yeast cell wall. To do this it was necessary to use independent methods to measure the level of cell disruption (Section 3.4.3) as well as compression testing. These methods have allowed the contribution of different constituents of the cell wall to its mechanical properties to be investigated for the first time.

8.1. Treatment of Baker's yeast cells with dithiothreitol (DTT)

8.1.1. Why investigate the use of DTT on the mechanical properties?

As has been discussed previously (Chapter 2) the yeast cell wall is constructed of two main layers covalently linked together. The inner skeletal layer is made up of a porous network of polysaccharides which is believed to be responsible for the mechanical strength of the cell. The outer fibrous layer consists of mannoproteins which are not believed to contribute to the mechanical properties of the cell wall (Klis *et al.,* 2006). Within the outer mannoprotein layer a number of cell wall proteins are not linked directly to the skeletal layer but instead are linked through disulphide bridges to the outer layer. The external protein layer limits the permeability of the cell wall to macromolecules. In addition to this the mannoprotein layer prevents the loss of soluble cell wall associated proteins such as invertase. Disulphide

bridges are believed to play a role in the retention of proteins in the cell wall and the number of disulphide bridges is known to be six-fold higher in cell walls of stationary phase cells when compared to exponential phase cells (De Noble *et al.*, 1990). The associated cell wall proteins can be released by breaking the disulphide bonds in the wall with reducing agents such as dithiothreitol (DTT) and β-mercaptoethanol. Capellaro *et al.* (1998) have studied the effect of the reducing agent DTT on the release of cell wall proteins from living cells. It was found in their work that several cell wall proteins could be released from *Saccharomyces cerevisiae* (Baker's yeast). Klis *et al.* (2007) stated that the treatment of yeast cells with DTT is expected to release: a) disulphide bridge linked cell wall proteins; b) non - covalently linked cell wall proteins; c) periplasmic proteins due to increased permeability; and d) ionically associated proteins.

It was decided to determine the effect of disrupting the disulphide bonds in the cell wall by DTT on the mechanical properties and failure criteria of Baker's yeast.

8.1.2. DTT experimental methods

In order to investigate the effect of DTT treatment the release of total soluble protein and invertase was measured. Treatment with DTT should not lead to significant amounts of total protein being released from the cell though a small amount is to be expected (Capellaro *et al.*, 1998). Invertase is a sucrase enzyme produced by Baker's yeast that hydrolyses sucrose to glucose and fructose. There are two forms of invertase within the yeast cell, invertase located in the cell wall known as external invertase and that located in the cytoplasm known as internal invertase. The majority of invertase is located in the cell wall with the internal invertase only making up 2 – 6 % of the total present in the cell (Gascon *et al.*, 1968).

Gascon *et al.* (1968) found that the external invertase was stable between pH 3 – 7.5 while the internal invertase was stable between pH 6 – 9 and became inactivated at acidic pH. In this work the invertase assay (Section 3.4.3.3) was performed at pH 5.5 to try and ensure that only the release of the external enzyme was being measured. The release of invertase from *S. cerevisiae* by reducing agents has been widely investigated by Sommer and Lewis (1971), Smith and Ballou (1974), and Kidby and Davis (1970a; 1970b).

A suspension of Baker's yeast cells (Section 3.1) was treated with 10 mM DTT for 60 minutes and the resultant release of invertase and soluble protein from the cell wall measured (Section 3.4.3). The mechanical properties of the treated cells were then investigated using compression testing by micromanipulation at a speed of 68 μms^{-1}. This speed has been shown in Section 7.1 to allow the effects of water loss during compression to be considered negligible. The experimental data was then fitted to the numerical simulations using the surface modulus (Eh_o) and the initial stretch ratio (λ_s) as adjustable parameters (Chapter 6). Again the correlation coefficient (R^2) was maximised to indicate the best fit between the experimental data and the numerical simulations.

8.1.3. Results of treatment with DTT

Analysis showed that the viability of the DTT treated cells was similar to the control group using methylene blue testing. This was confirmed by compression testing where more than 95 % of cells compressed produced a bursting event confirming an assumed viability (Section 4.1.5).

8.1.3.1. Enzyme and protein release due to DTT

Using the techniques described in Section 3.4.3.4 the amount of total soluble protein released was measured using the Bradford method. The amount of invertase released by treatment with DTT was measured using the assay described in Section 3.4.3.3. These measurements were compared to the maximum amount of total soluble protein and invertase released by disruption with the sonication probe which is discussed later (Section 8.2.2.2). As is clearly shown in Table 8.1 treatment of yeast cells with DTT released soluble protein and invertase from the cell wall.

	Treated for 60 minutes with DTT	**Percentage of total available protein/invertase**
Total soluble protein released	2.3 mg/gram of yeast dry cell weight	0.6 %
Invertase released	409000 units per gram of yeast dry cell weight. Assuming 300 units/mg (Sigma-Aldrich, Cat. No. I4504) gives an estimated 1.3 mg/gram of yeast dry cell weight.	17.4 %

Table 8.1: Release of protein and invertase from cells following DTT treatment. One unit of invertase is defined as the amount of enzyme, which hydrolyses 1 micromole of sucrose in one minute at 55 ^{o}C in sodium acetate buffer of pH 5.5.

The total amount of protein released was not significant suggesting that the cell wall was not significantly damaged, a result supported by the viability tests. However, significant amounts of invertase were released from the yeast cell wall by DTT. The percentage of the maximum available invertase released is of a similar magnitude to that found by DTT

treatment in the literature (Smith and Ballou, 1974). The release of invertase confirms that the DTT broke the disulphide bonds in the cell wall as expected.

8.1.3.2. Compression testing by micromanipulation of DTT treated cells

As has been previously described (Section 8.1.3) bursting events were obtained from the compression testing data for cells treated with DTT. It was found that these cells were 'stickier' than untreated cells meaning that during the compression experiments the micromanipulation probe would frequently have to be cleaned. This meant that the time to compress a large number of cells increased significantly and it took approximately 5 hours to compress 75 cells. However, no correlation was found between the order of compression and the results (Appendix 16).

8.1.3.3. Whole population measurements

As described in Chapter 4 a number of measurements can be made directly from the compression testing data which are summarised in Table 8.2. Correlations similar to those with untreated cells (Chapter 4) were found between the cell size and the force and deformation at failure (Appendix 16). It was found that the viability of the cell populations remained constant during the experiment. t – tests were performed at the 5% level to compare the significance of the differences between the control and the DTT treated cells.

	Control	**DTT treated cells**	**P – value**
Mean cell diameter	4.6 ± 0.1 μm	4.8 ± 0.1 μm	0.08
Mean force at failure	131 ± 9 μN	113 ± 6 μN	2×10^{-3}
Mean deformation at failure	66 ± 2 %	63 ± 2 %	0.03

Table 8.2: Effect of DTT treatment on whole cell measurement with 95% confidence limits.

As can be seen from the data in Table 8.2 the cell diameters of the DTT treated and the control populations are not statistically different at the 5 % level. However, there does appear to be a slight increase in the cell diameter of the DTT treated cells. It is possible that DTT is affecting the internal environment of the cells leading to this change in the cell diameter. This effect will be described later (Section 8.1.4).

The force at failure is found to be significantly lower in the DTT treated cells than the control. As well as this the deformation at failure was found to be lower in the DTT treated cells but not significantly at the 1 % level.

As has been previously discussed (Chapter 4) the whole cell measurement results are not intrinsic material properties and so should not be used to determine the effect of DTT treatment on cell wall properties. However, the results are interesting as the significant decrease in the force at failure has not previously been observed. This result suggests significant changes have occurred within the cell or within the cell wall.

8.1.3.4. Results from modelling compression data

As with Chapter 7 the data obtained from compression testing was fitted to numerical simulations using a maximised R^2 to find the best fit. For this work the surface modulus (Eh_o) and the initial stretch ratio (λ_s) were used as fitting parameters. This process also allowed the surface strain energy at failure (W_{sf}) to be calculated, shown in Table 8.3.

	Control	**DTT treated cells**	**P – value**
Mean surface modulus (Eh_o)	16 ± 1 Nm^{-1}	16 ± 2 Nm^{-1}	0.97
Mean initial stretch ratio (λ_s)	1.038 ± 0.007	1.052 ± 0.010	0.02
Mean surface strain energy at failure (W_{sf})	2.3 ± 0.2 Nm^{-1}	2.2 ± 0.2 Nm^{-1}	0.45

Table 8.3: Effect of DTT treatment on modelling results with 95 % confidence limits.

As can be observed in Table 8.3 the mean surface modulus and mean surface strain energy at failure are statistically similar for the control and DTT treated cells. These results are also statistically similar to the results presented in Chapter 7. However, the mean initial stretch ratio was found to be significantly different for the DTT treated cells at the 5 % level. This result appears to suggest that treatment of cells with DTT caused them to swell. Although it was not possible to independently verify the initial stretch ratio calculated here, in Chapter 7 it was shown that compression testing produces reliable values. From the data in Table 8.3 it is possible to extract the un-inflated cell diameter by using the initial stretch ratio dimensionless group in equation 8.1:

$$\lambda_s = \frac{r_i}{r_o} \qquad \ldots (8.1)$$

where r_i is the inflated radius (measured from compression testing), r_o is the un-inflated radius and λ_s is the initial stretch ratio (from fitting experimental data to numerical simulations). By using equation 8.1 the un-inflated diameter of the DTT treated cells was found to be 4.6 ± 0.1 μm and the un-inflated diameter of the control was found to be 4.5 ± 0.1 μm. These led to a P-value of 0.3 at the 5 % level suggesting that the un-inflated cell diameters are similar. This result suggests that the treatment of cells with DTT will not affect the cell diameter but will cause an increase in the initial stretch ratio. The effect of DTT on the initial stretch ratio is discussed further in Section 8.1.4.

Figures 8.1 and 8.2 show the trends between the surface modulus and surface strain energy at failure with the cell diameter for DTT treated cells. Similar relationships were found for the untreated control cells. As can be seen the relationships obtained in this work are very similar to those shown in Chapter 7. This seems to suggest that the treatment of cells with DTT does not significantly affect the intrinsic material properties of the yeast cell wall.

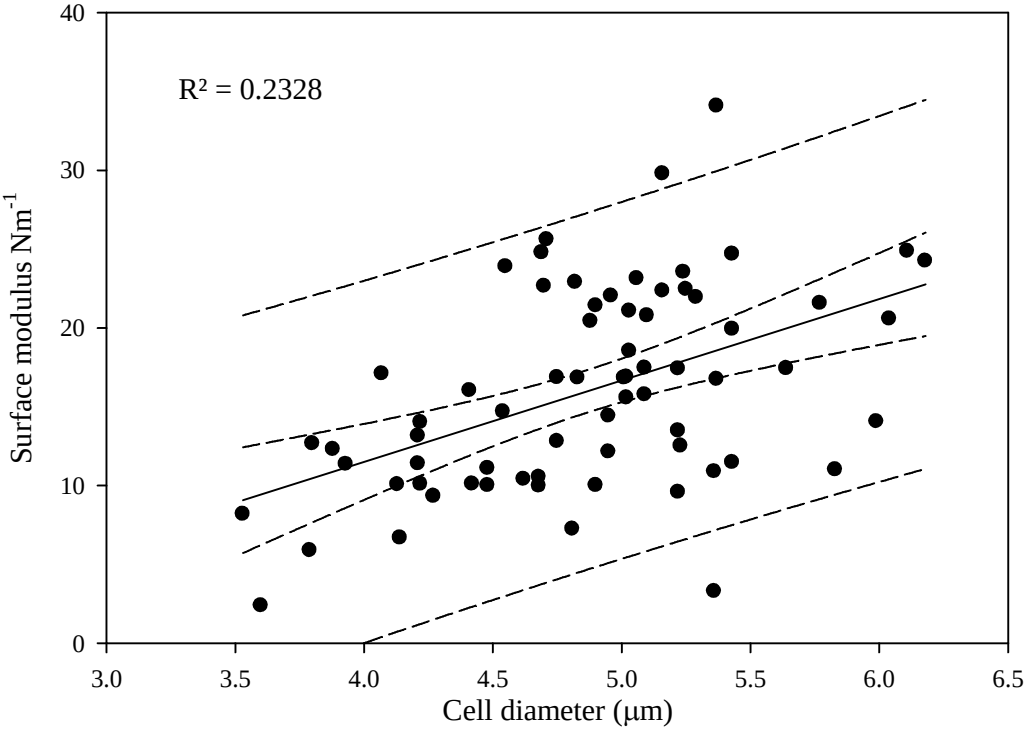

Figure 8.1: Relationship between the surface modulus and the cell diameter for cells treated with DTT. Dashed lines represent the 95 % confidence limits for the mean and the individual measurements.

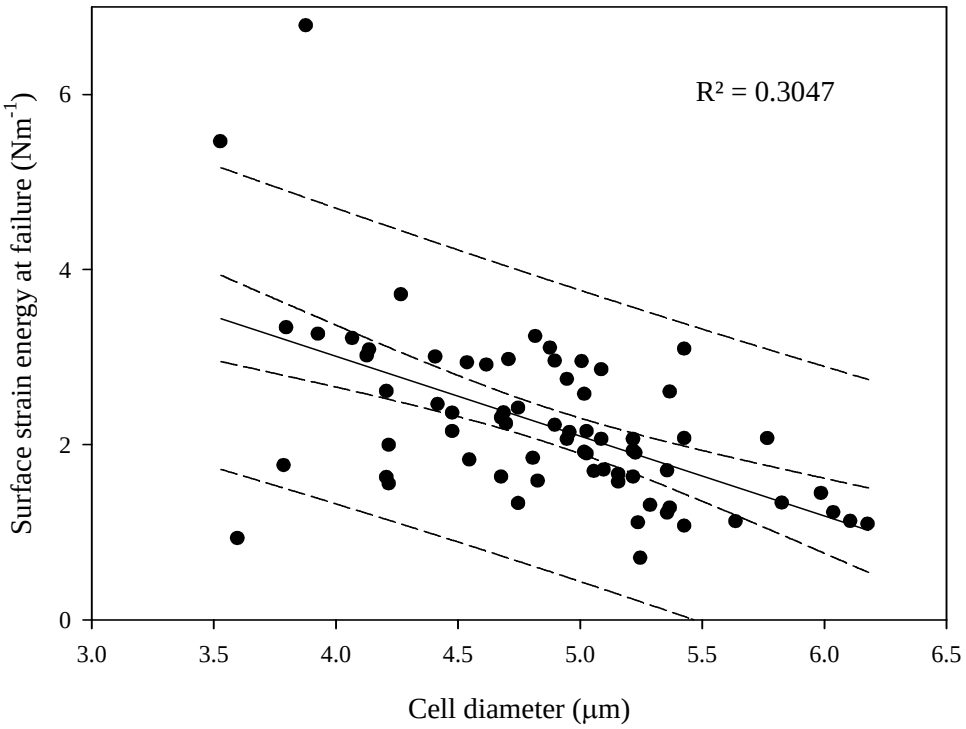

Figure 8.2: Relationship between the surface strain energy at failure and the cell diameter for cells treated with DTT. Dashed lines represent the 95 % confidence limits for the mean and the individual measurements.

8.1.4. Discussion

In this Chapter, a 10 mM concentration of DTT was used at approximately 25 ^{o}C for 60 minutes under conditions of gentle agitation. From this 0.6 % of the total cell protein available was released into the supernatant corresponding to 2.3 mg/gram of dry cell yeast. This data suggest that the treatment of cells with DTT led to the limited release of cytosolic proteins. It was thought that treatment with DTT would not structurally damage the cell wall as it is used widely for the selective release of cell wall proteins. This has been confirmed here by the small levels of total protein released compared to the significant quantities of invertase released.

The mean surface modulus obtained through modelling the compression data showed that treatment with DTT did not have a significant effect on the intrinsic material properties of the yeast cell wall. In addition, it was found that the mean surface strain energy at failure also was not affected by treatment with DTT.

As can be seen by the enzyme analysis (Section 8.1.3.1) it was found that the treatment of the yeast cells with DTT was able to remove significant quantities of invertase from the yeast cell wall. Although this method of measurement does not account for the loss of other materials from the cell wall it is still a useful measure of the effect that DTT has on the structural integrity of the wall. As described earlier this enzyme is located almost entirely within the cell wall with only minor quantities being found inside the cell (Gascon *et al.,* 1968). As well as limiting the transport of proteins across the cell boundary the outer mannoprotein layer is also known to limit the cell wall permeability (Klis *et al.,* 2006). It is possible that treatment with DTT would allow water loss from the cell during compression.

However, as the mean surface modulus is statistically similar to the control it seems reasonable to assume that any water loss from the DTT treated cells could be considered negligible.

Recently Klis *et al.* (2007) have found that the use of reducing agents β – mercaptoethanol and DTT may perturb the plasma membrane causing the release of cytosolic proteins at high extraction temperatures, high concentrations, and over long treatment times. It was also found by Gasch *et al.* (2000) that DTT will cross the plasma membrane and enter the endoplasmic reticulum (ER) of the cell within 15 minutes of the start of treatment. By entering the ER, DTT is known to induce the unfolded protein response (UPR) in yeast cells by denaturation of accumulated proteins (Payne *et al.*, 2008). The specific response of the internal environment of Baker's yeast cells to treatment with DTT is beyond the scope of this thesis. However, it is possible that this response leads to the changes in the initial stretch ratio seen here by lowering the internal osmotic pressure. This will cause water to flow into the cells so increasing the cell turgor pressure and therefore the initial stretch ratio. It has been claimed previously by Morris *et al.* (1983) that the osmotic response of cells is not affected by treatment with DTT. However, in Morris *et al.* (1983) the response of only a very small number of cells (5 cells repeated three times) was measured so this effect could have been missed.

8.1.5. Conclusions

This is the first time that the contribution of a specific component to the intrinsic material properties of the Baker's yeast cell wall has been measured. It was found that the disruption of disulphide bonds in the cell wall by DTT did not decrease the surface modulus or failure

criteria of the cell significantly. It is possible that the compression testing technique is not sensitive enough for very minor changes in the wall properties to be observed.

8.2. Sonication of Baker's yeast cells

8.2.1. Why investigate the effect of sonication on the mechanical properties?

The disruption of cells is one of the most important steps in the downstream processing of a product produced by microorganisms. There are many different mechanisms by which cells can be broken and these are separated into two main types, mechanical and non - mechanical disruption (physical, chemical and enzymic disruption) (see Chapter 2).

Sonication is the physical cell disruption technique that operates by the creation of high frequency sound (ultrasound) that is produced electronically and transferred to the cell suspension. Ultrasound is any sound that is above the frequency that may be detected by human ears (greater than 16 kHz). The effect of sonication on the mechanical structure of the cell wall has been attributed to cavitation as described in Chapter 2. In this process pressure waves are generated by the high frequency mechanical vibration of the sonication probe (Section 3.4.1) which leads to the formation of microscopic bubbles. At high frequencies these bubbles implode violently causing cell disruption. During the sonication process reactive free radicals are also generated by the collapse of bubbles. The extent of their production depends on the intensity of the sonication process which can be controlled by varying the operating conditions such as the initial concentration of the cell suspension, temperature (Ciccolini *et al,* 1997) and the power input (Guerrero *et al.,* 2001).

When these processes occur in a suspension of cells it could lead to mechanical damage occurring in the cell wall. In Baker's yeast cells a number of effects have been observed including the pitting of the cell wall surface, the modification of cellular activity, the mechanical erosion of the cell wall, and possible internal cavitation within cells (Ciccolini *et*

al, 1997; Guerrero *et al.*, 2001). This internal cavitation damage would not appear using optical microscopy. The cells would appear undamaged but the cell membrane, and internal contents would be disrupted. Due to this it would not be possible to identify cells which have been internally disrupted using the compression testing equipment. However, using TEM it should be possible to observe these damaged cells.

The effect of sonication on the mechanical strength of the yeast cell wall was of interest to see how the partial disruption affected the intrinsic material properties. This experiment was designed to discover if the cell wall structure was degraded gradually or if it was suddenly ruptured during the sonication process. Due to the mechanical effects of sonication it is possible that the inner structural β - glucan layer could be damaged leading to a weakening of the cell wall prior to cell failure. The effect of this should be shown in the overall material and failure parameters obtained from compression testing and modelling.

8.2.2. Sonication experimental methods

In order to determine the effect of sonication, the surface modulus (Eh_o) the surface strain energy (W_{sf}) was determined for cells exposed to 20 kHz sonication power for 5 and 10 minutes. This should have meant that there was still a significant quantity of viable cells to be compressed to failure.

In order to determine the level of cell disruption and the effect of sonication on the yeast cell wall the release of enzymes from different locations within the cell wall and from the cytoplasm of the cell were investigated (Section 3.4.3). These techniques were chosen as they have been used previously to quantify the level of disruption of yeast cells subjected to

the cavitation process (Balasundaram and Harrison, 2006). Using these techniques it would be possible to compare the relative levels of disruption. In addition to this methylene blue staining and the percentage of bursting events that occurred during compression testing would give an indication of the level of cell viability. This is of particular interest for cells that have had their internal contents disrupted but still have an intact cell wall.

8.2.3. Disruption results

8.2.3.1. Effect of sonication on the structure of the yeast cell wall

To determine the effect of sonication on the physical structure of the yeast cell wall TEM images were taken of the cells following 10 minutes of sonication treatment. Shown below is a summary of the points of interest from these images.

Figure 8.3 shows two example cells which have had their internal contents disrupted.

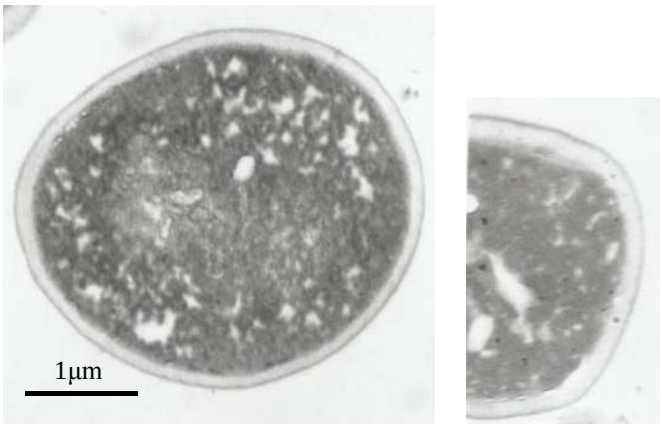

Figure 8.3: Two examples of cells which have had the internal contents of the cell disrupted but still have an intact cell wall. Magnification × 6000. (Images have been rescaled).

The internal contents of the cell have been disrupted, possibly by internal cavitation effects, while the cell wall still maintains its integrity. It was expected that when such cells were compressed they would not produce a bursting event as the cell membrane was not believed to be intact and so would be unable to resist the flow of the cell contents out of the cell.

Figure 8.4 is an example of a cell which has a hole punctured in the side of the cell wall.

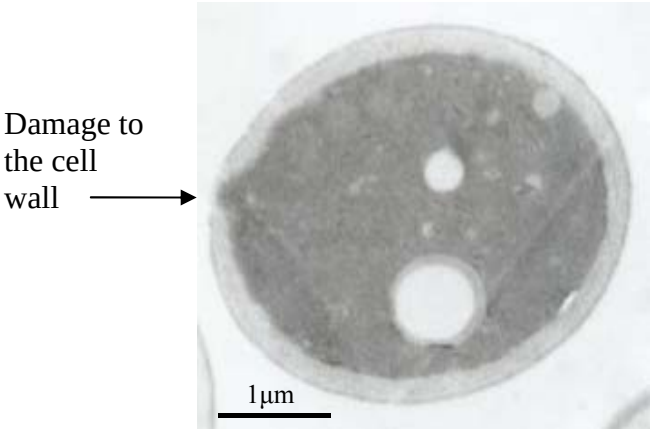

Figure 8.4: Example of cell which has a hole punctured into the side of the cell wall but still maintains the majority of the internal cell contents. Magnification × 6000.

(Image has been rescaled)

When compared to Figure 3.17 (example of cell bud scar) this confirms that the structure here was not a bud scar. It is believed that the cell wall had been partly punctured by cavitation and while the cell membrane was still intact it was now pushing towards the outside of the cell wall. It is expected that cells such as this would lead to a bursting event though this might be at a lower force and deformation than untreated cells. However, it was not possible to confirm cell viability using methylene blue staining.

Figure 8.5 a) is an example of a cell which might have been distorted by the focused energy dissipation on a small part of the yeast cell wall. Figure 8.5 b) is an example of a distorted cell which is stained with methylene blue. This suggests that these distorted cells would not lead to a bursting event as they are non-viable.

a) 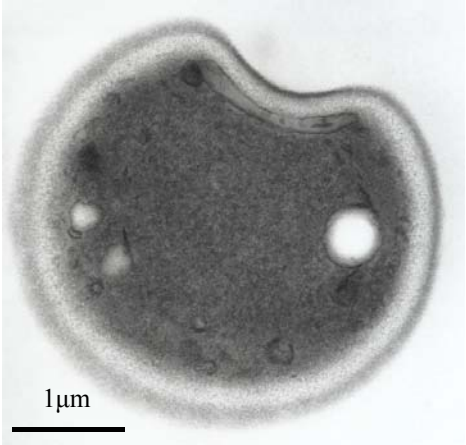

b) 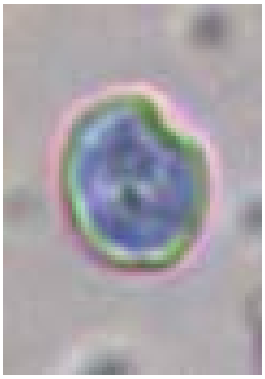

Figure 8.5a) and b): Example of cells, which might have been distorted as a result of the focused energy dissipation on a small part of the yeast cell. a) TEM image of distorted cell. Magnification × 6000. (Image has been rescaled) b) Optical image of distorted cell stained with methylene blue.

Figure 8.6 is an example of a cell where part of the cell wall has separated from the rest of the cell boundary.

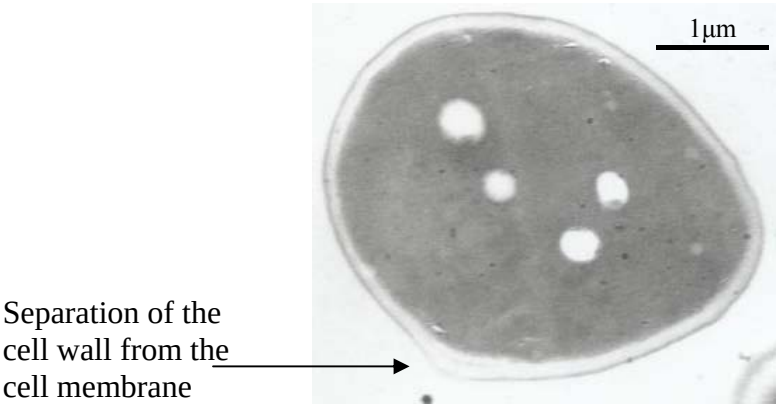

Figure 8.6: Example of a cell that has had part of the cell wall separated from the cell membrane. Magnification × 6000. (Image has been rescaled).

The outer mannoprotein layer appears to have separated from the inner structural β 1,3 - glucan layer. It is possible that the mannoprotein layer has actually broken though this is not entirely clear in the image. It is stated in the literature that the outer mannoprotein layer does not contribute to the structural strength of the yeast cell wall so this process should not affect the mechanical response of the cell to compression testing. It is believed that cells which are disrupted in this way would lead to a bursting event. However, as with the example in Figure 8.4 it was not possible to use methylene blue staining to confirm this.

Figure 8.7 a) and b) shows two examples of cells, which have been fully ruptured by sonication.

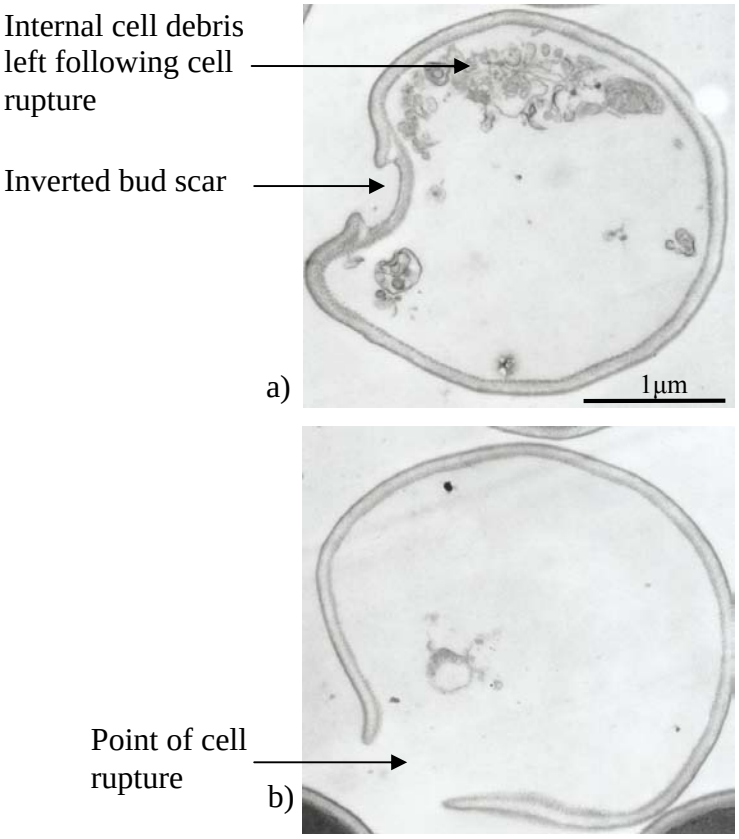

Figure 8.7a) and b): Two examples of cells which have been ruptured by sonication and had the majority of the internal contents removed leaving only the cell wall remnants. Magnification × 7500. (Image has been rescaled).

In example Figure 8.7 a) the cell has been ruptured but some of the internal contents of the cell are still inside the cell. Also it appears that following rupture a bud scar had been inverted into the cell. Figure 8.7 b) shows a cell that had been fully ruptured with all of the internal contents of the cell released into the suspension.

Figures 8.3 to 8.7 show cells that have been disrupted by the sonication process. During compression testing it was not possible to identify individual cells which had been partially or fully ruptured. However, only cells which were able to produce a bursting event and were assumed to be viable were modelled. This means that the compression testing data presented in this Section is a mean of all the various states of physical disruption in a treated suspension and cannot be directly related to one particular state.

8.2.3.2. Enzyme analysis

As previously described it is not possible to determine the individual state of each cell being compressed. The release of enzymes into the suspension from different locations within the cell gave an indication of the amount of disruption that had occurred. Enzymes which are located within the cytoplasm were assumed to be released only when cell rupture had occurred and periplasmic enzymes were assumed to be released following only partial disruption.

Figure 8.8 shows the total amount of soluble protein released into the suspension over increasing sonication time.

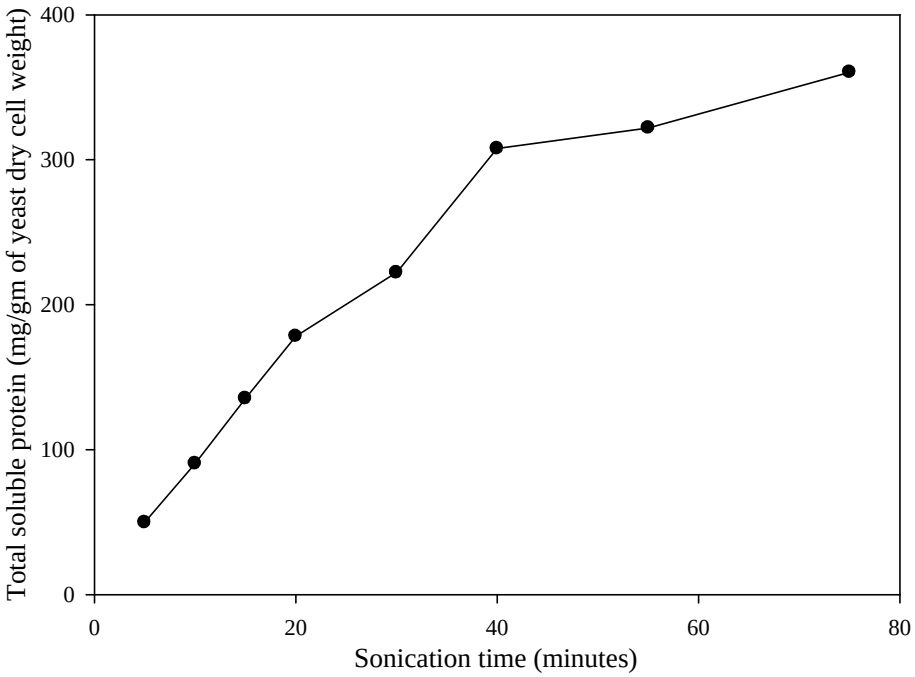

Figure 8.8:Effect of sonication time on the release of total soluble protein from the cell wall.

From Figure 8.8 it can be observed that with increased sonication time the total amount of soluble protein released also increased. Up to 20 minutes of treatment the rate of protein release was constant suggesting that this was occurring from the rupturing of cells. Following this, the rate of protein release continued but, after 40 minutes of sonication, at a reduced rate. This might be due to the cell wall debris being increasingly disrupted.

Figures 8.9 and 8.10 show the levels of invertase and α – glucosidase released from the cell population over the sonication period.

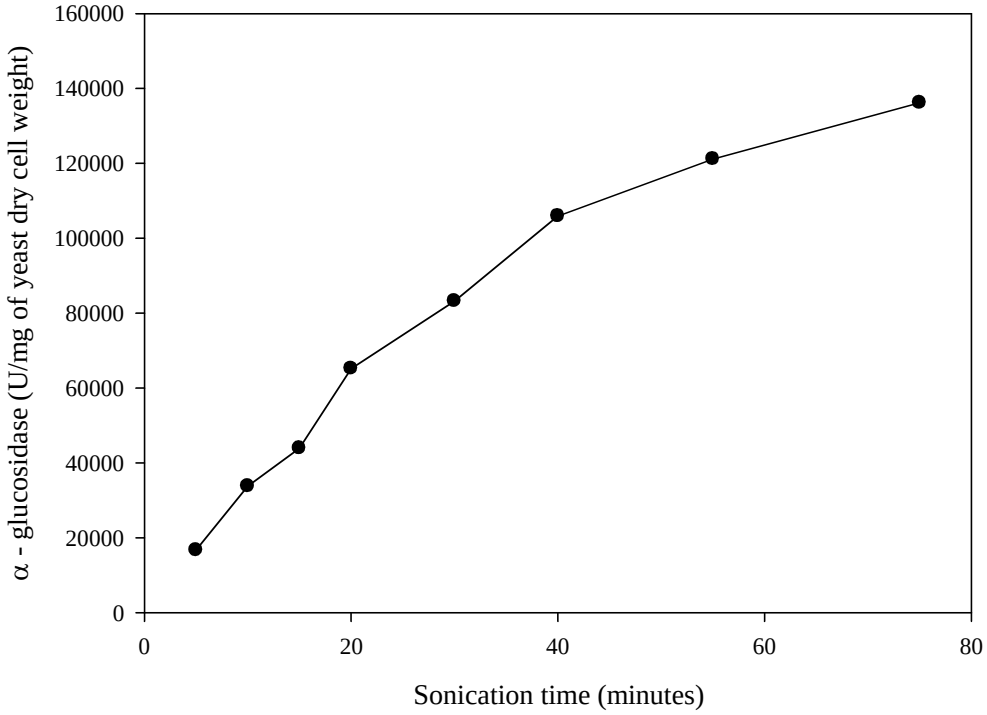

Figure 8.9: Effect of sonication time on the release of α – glucosidase from periplasmic space

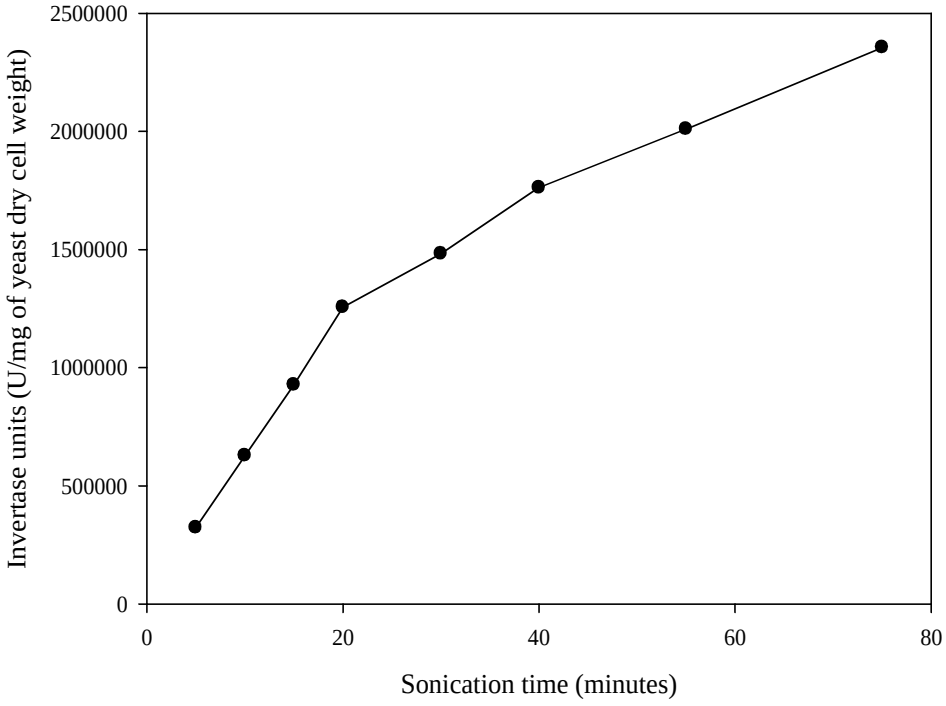

Figure 8.10: Effect of sonication time on the release of Invertase from the cell wall.

α - glucosidase is located in the periplasmic space of the yeast cell and was increasingly released with prolonged sonication. The majority of cell wall associated invertase is trapped in the outer layer of the cell wall by disulphide bonds (Sommer and Lewis, 1979). Presumably generation of the reactive species during sonication led to the release of invertase by breaking the disulphide bonds. Also the physical disruption of the cell walls was expected to lead to invertase being released into the suspension. The release of these two enzymes indicates that the cell walls were being broken in such a way that these periplasmic and cell wall enzymes were being released into the suspension. However, this does not necessarily mean that the cell is being ruptured or that they were no longer viable. A comparison can be made with the results obtained by treatment with DTT (Section 8.1.3) where significant amounts of invertase were released from the wall but the viability of the cell population was unaffected. Previous authors had noted that the release rate of invertase is constant and independent of the time of sonication treatment (Balasundarum and Pandit, 2001a). This result is supported here where up to the 20 minutes the release of invertase was linearly related to the treatment time. The release of both these enzymes indicates that significant damage had occurred to the cell wall by sonication.

Figure 8.11 shows the release of ADH from the cytoplasm of the yeast cell over prolonged sonication.

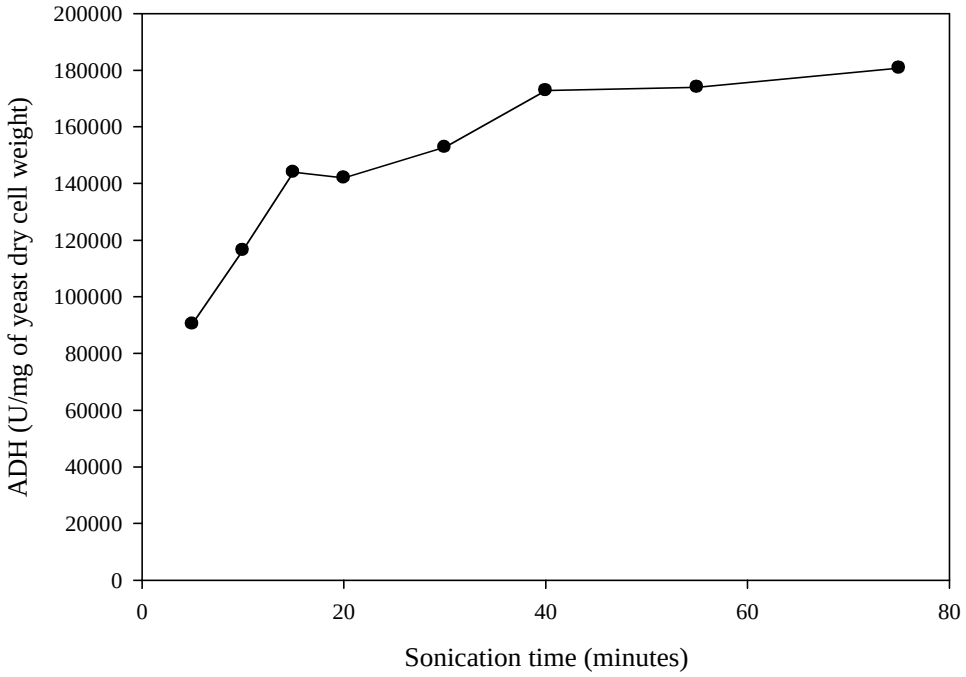

Figure 8.11: Effect of sonication time on the release of Alcohol Dehydrogenase (ADH) from the cell cytoplasm.

ADH is released from the cytoplasm of the yeast cell when total cell rupture occurs. As can be seen in Figure 8.11 the level of ADH increased significantly in the first 15 minutes of sonication before reaching a maximum after 40 minutes of disruption. This suggests that the majority of cells were ruptured following just 15 –20 minutes of sonication. The amount of ADH released following 5 minutes of sonication seems to be very high considering only limited cell disruption was assumed to have occurred (See Section 8.2.3.3). It is not immediately clear why such a large amount of ADH has been released and this would need to be investigated further if additional studies of cell disruption are to be performed.

From the results for enzyme and protein release during sonication it appears that the majority of the cell rupture occurred during the first 20 minutes of the sonication process.

Following this the release of the protein and enzymes from the cells was occurring due to the breakdown of the remaining cell debris. If this proposition is correct then it would be expected that the percentage of viable cells would decrease significantly over the first 20 minutes and be at a relatively low level following this time. This would mean that it would be almost impossible to perform compression testing on cells sonicated for longer than 20 minutes.

8.2.3.3. Compression testing

Compression testing was performed on cells that had been sonicated for 5 and 10 minutes. It was found that the incidence of cell bursting events were lower for cells that had been sonicated. During compression testing it was not possible to distinguish between cells that were damaged and still viable and cells which were not viable but maintained there shape. This had the effect of significantly increasing the time to perform the compression experiments, especially for the cell suspension which had been sonicated for 10 minutes. However, it was still found that the order in which the cells were compressed did not influence the results (Appendices 17 and 18).

As with the DTT experiments in Section 8.1 the same fitting procedure was used with the surface modulus (Eh_o) and the initial stretch ratio (λ_s) being used as fitting parameters and maximised R^2 indicating the best fit. As with the data in Chapters 4 and 7 it was possible to obtain both whole cell measurements (cell diameter, force and deformation at failure) and intrinsic material properties (surface modulus and surface strain energy at failure) from the compression testing data. The data in this Section compare the compression of approximately 100 cells following both 5 and 10 minutes of sonication with a control set.

In order to determine the population viability methylene blue staining was used (Section 3.1.1) as well as recording the number of cells that led to a bursting event during compression testing.

As in Chapter 4 the viability of the control cell population was found to be in excess of 95 %. With the cells that had been sonicated for 5 minutes it was found that the viability of the cell population was approximately 75 %. For cells which had been sonicated for 10 minutes the viability of the cell population was found to be approximately 40 % both determined by methylene blue staining and compression testing. This decrease in population viability had a direct effect on the time taken for the compression of 100 cells. For the cells which had been sonicated for 10 minutes it took about 5 hours to compress the required number of cells. This occurred due to the high number of compressions which did not produce a bursting event. Also cells sonicated for 10 minutes were a lot 'sticker' than the control sample requiring the probe to be cleaned regularly. It is unknown why this occurs but it is possibly due to the increased level of internal cell contents released from ruptured cells into the suspending solution. It is also possible that this occurs due to the breakdown of the outer mannoprotein layer as a similar phenomenon was observed when cells were treated with DTT (Section 8.1.3.2).

For cells which had been sonicated for longer than 10 minutes it was not possible to compress the required number of cells due to the decreasing number of viable cells in the population. If it had been possible to identify the viable cells and the non viable cells in the compression testing equipment then it might have been possible to do this. Currently it is not possible to do this.

Whole cell measurements

To compare the results obtained by cells which had been subjected to sonication and the control, t –tests at the 5 % level were performed. All parameters measured for the control are statistically similar to the data shown in Chapter 4.

	Control	**5 mins sonication**	**P – value**
Mean cell diameter	4.6 ± 0.1 μm	4.6 ± 0.1 μm	0.85
Mean bursting force	131 ± 9 μN	116 ± 8 μN	0.03
Mean deformation at failure	66 ± 2 %	66 ± 2 %	0.83

Table 8.4: Effect of 5 minutes sonication treatment on whole cell measurements with 95 % confidence limits.

Table 8.4 shows that after cells have been sonicated for 5 minutes the mean cell diameter and the mean deformation at failure were statistically similar to the control set. The mean force at failure has decreased significantly at the 5 % level but is still similar at the 1 % level.

	Control	**10 mins sonication**	**P – value**
Mean cell diameter	4.6 ± 0.1μm	4.5 ± 0.1 μm	0.11
Mean bursting force	131 ± 9 μN	107 ± 5 μN	6.5×10^{-6}
Mean deformation at failure	66 ± 2 %	67 ± 2 %	0.49

Table 8.5: Effect of 10 minutes sonication treatment on whole cell measurements with 95 % confidence limits.

Table 8.5 shows that following 10 minutes of sonication the mean cell diameter and mean deformation at failure are still statistically similar to the control at the 5 % level. The mean force at failure is now significantly different at the 5 % and the 1 % level.

The whole cell results indicate that the mean cell diameter and the mean deformation at failure were unaffected by prolonged sonication while the mean force at failure was significantly changed.

Modelling results

Tables 8.6 and 8.7 show a comparison of the results obtained by modelling the compression data using the surface modulus (Eh_o) and the initial stretch ratio (λ_s) as adjustable parameters.

	Control	**5 mins sonication**	**P - value**
Mean surface modulus (Eh_o)	16 ± 1 Nm^{-1}	14 ± 1 Nm^{-1}	0.02
Mean initial stretch ratio (λ_s)	1.038 ± 0.007	1.050 ± 0.008	0.02
Mean surface strain energy at failure (W_{sf})	2.3 ± 0.2 Nm^{-1}	2.3 ± 0.2 Nm^{-1}	0.84

Table 8.6: Effect of 5 minutes sonication treatment on results obtained from modelling with 95 % confidence limits.

The mean surface modulus and mean initial stretch ratio for cells sonicated for 5 minutes were found to be significantly different from the control at the 5 % level though they are statistically similar at the 1 % level. However, the mean surface strain energy at failure was found to be statistically similar to the control population.

	Control	**10 mins sonication**	**P - value**
Mean surface modulus (Eh_o)	16 ± 1 Nm^{-1}	13 ± 1 Nm^{-1}	5×10^{-04}
Mean initial stretch ratio (λ_s)	1.038 ± 0.007	1.070 ± 0.008	1.35×10^{-08}
Mean surface strain energy at failure (W_{sf})	2.3 ± 0.2 Nm^{-1}	2.2 ± 0.1 Nm^{-1}	0.21

Table 8.7: Effect of 10 minutes sonication treatment on results obtained from modelling with 95 % confidence limits.

From table 8.7 it can be observed that the mean surface modulus and mean initial stretch ratio for the cells which have been sonicated for 10 minutes are statistically different to the control at the 5 % level. As with the results shown in table 8.6 it can be seen that the mean surface strain energy at failure is similar to the control set.

The data shown in Figures 8.12 and 8.13 are from cells which have been subjected to 5 minutes sonication. The relationships presented here were found to be similar for the control and the 10 minute sonication data. The correlations match well the results shown in Chapter 7.

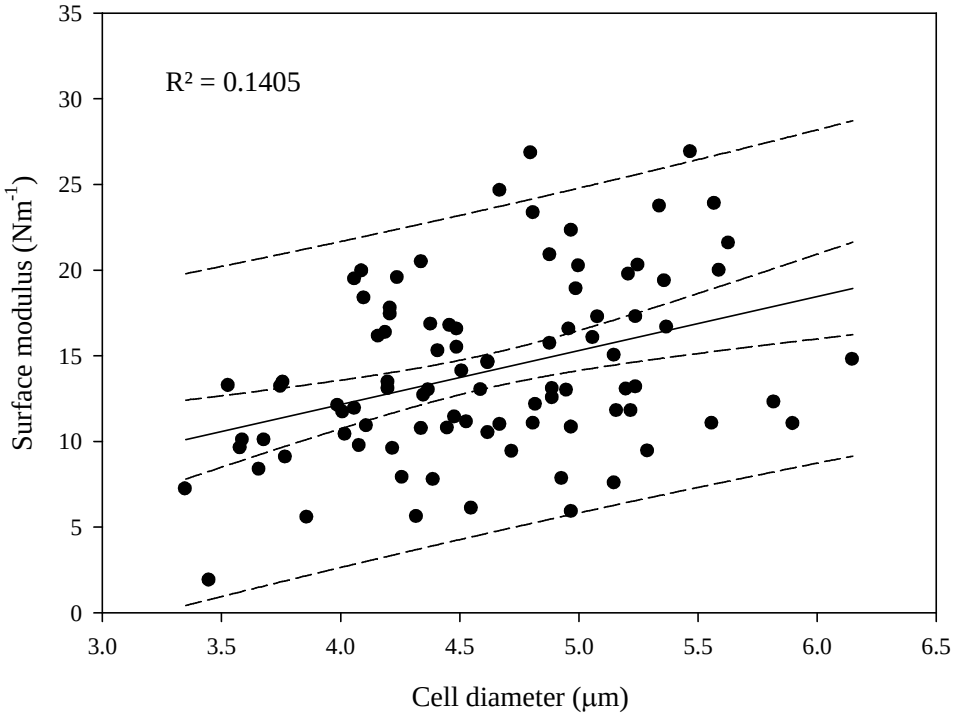

Figure 8.12: Trend between the surface modulus and the cell diameter for cells subjected to 5 minutes sonication. Dashed lines represent the 95 % confidence limits for the mean and the individual measurements.

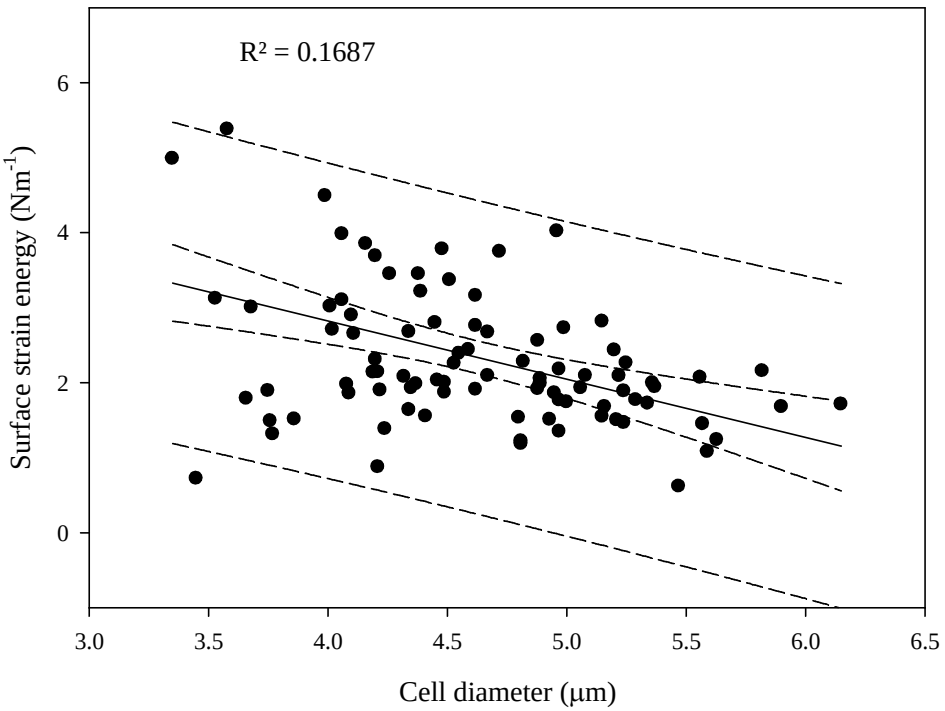

Figure 8.13: Trend between the surface strain energy and the cell diameter for cells subjected to 5 minutes sonication. Dashed lines represent the 95 % confidence limits for the mean and the individual measurements.

8.2.4. Discussion

The decrease in the cell viability over time indicates the physical effects of sonication were disrupting the Baker's yeast cells. Due to this the release of soluble proteins and specific yeast associated enzymes were found to increase when the time of sonication was increased.

The images in Figure 8.3 to 8.7 show the structural damage that was occurring to the Baker's yeast cells over prolonged sonication time. There were several physical effects on the yeast cells, both to the cell wall and the internal cytological contents. This result was important as it shows that the erosion of the cell wall was not the only mechanism responsible for causing damage to Baker's yeast since the inner structure of the cell was significantly affected. Using optical microscopy within the micromanipulation equipment the sonicated cells appeared undamaged but did not lead to a bursting event, indicating damage at the subcellular level which could not be determined by light microscopy. In order to measure the mechanical strength of cells that had been treated for longer than 10 minutes (leading to an increased percentage of the population which was not viable) then it would be necessary to identify the viable cells from the non viable. With the current micromanipulation equipment it is not possible to do this.

In studies of cavitation effects on metals it was found that multiple pits by corrosion rather than one big pit would be formed when a large number of bubbles collapse (Balasundaram and Harrison, 2006). Therefore it can be postulated that a large number of smaller holes may develop in the yeast wall resulting the release of periplasmic proteins. However, if the pore size is small this may restrict the leaching out of the macromolecules.

As with the treatment of yeast cells with DTT, cell wall bound invertase was released from the cell wall. This is believed to be due to the breaking of thiol bonds within the wall due to the production of reactive species as well as mechanical disruption through sonication. Previously it has been reported that cavitation (Balasundaram and Pandit, 2001b) is able to selectively release cell wall enzymes due to this combined mechanical and chemical effect on the cell wall.

Compression testing results

From the data in Table 8.3 it appears that the mean force at failure decreased with increased sonication time while the mean deformation at failure appears to be unchanged. While the force at failure is not an intrinsic material property it does indicate that the yeast cells were being altered over the increased sonication time. The results presented in Section 8.2.2 suggest that sonication had the effect of decreasing the mean surface modulus with increased treatment time. However, the mean surface strain energy at failure remained unchanged over the sonication time. It is possible that the surface modulus of the cell wall had been reduced due to the damage of the β 1,3-glucan layer with increased sonication time. However, the constant mean surface strain energy at failure suggests that the cause of cell failure is not affected by sonication. In Chapter 7 it was hypothesised that the bud scars were responsible for causing cell wall failure possibly by stress concentration. If these bud scars are relatively unaffected by sonication due to the presence of high levels of chitin, then it seems reasonable for the failure criteria to remain constant. However, without being able to determine the specific damage that has occurred to the cell being compressed it is not possible to confirm this.

It is also possible that the effects seen in the mean surface modulus were due to water loss from the cell during compression and not mechanical damage to the β 1,3-glucan layer. In Chapter 7 it was shown that compression speeds of 68 μms^{-1} were suitable to consider the effects of water loss negligible. It was expected that the sonication process caused damage to the mannoprotein layer, which is believed to play a role in the water retention of the cell. Damage to the mannoprotein layer might increase the hydraulic conductivity of the cell wall leading to the compression speed of 68 μms^{-1} not being sufficient to allow water loss to be considered negligible. This increase in the hydraulic conductivity might lead to the decrease in surface modulus seen here. It was not possible to perform trials similar to those in Chapter 7 on the effect of speed on the results obtained by modelling due to the length of time it takes to do the compression experiments.

If this work was repeated in addition to determining the effect of compression speed on the mean surface modulus it would also be advisable to have a much finer time scale for testing samples, especially below 10 minutes sonication time. This might help confirm if the β 1,3-glucan layer is responsible for the mechanical strength of the cell wall by releasing only the cell wall associated invertase at the shortest sonication times.

8.2.5. *Conclusions*

These results seem to suggest that the cells were not increasingly weakened over the sonication process. This means that sonication did not increasingly weaken the cells by disruption prior to cell rupture but instead it would seem that the cells were broken in one event. However, due to the nature of sonication it was not possible to define exactly how the cells being compressed had been affected. While it is known that all the cells being

compressed were viable, due to their ability to produce a bursting event, their physical state was unknown. The cells being compressed could be:

a) unaffected by sonication and so in the same state as the control;

b) have a partly ruptured cell wall (Figure 8.4);

c) had the outer layer separated from the inner structural layer (Figure 8.6);

d) been effected by the production of reactive species;

e) had the surface pitting effect disrupting the outer mannoprotein layer.

As it is currently not possible to distinguish the physical state of each cell being compressed it is not possible to state explicitly how sonication affects the mechanical properties of the cell wall.

8.3. Conclusions and implications of the DTT and sonication work

Section 8.1 outlines the effect of treatment with DTT on the intrinsic material properties of the yeast cell wall, which were not found to change significantly. This is the first direct measurement of the effect a specific component of the cell wall has on the intrinsic material properties of the Baker's yeast cell. This work demonstrates the potential of the compression testing by micromanipulation technique to determine the effects of the composition and structure of the wall on the mechanical properties of the cell wall.

While the sonication work is an interesting addition, due to the inability to distinguish between the effects on the cells it is not possible to draw significant conclusions from this work. However, it was found that the mean surface strain energy required to cause cell failure did remain constant during the sonication process. This suggests the cell wall maintains its structural integrity during sonication.

Chapter Nine: Conclusions

The aim of this study was to determine intrinsic cell wall mechanical properties of Baker's yeast (*Saccharomyces cerevisiae*) cells. These data are essential to help improve the optimisation and design of cell disruption equipment. This Chapter outlines the main conclusions that have arisen from this work.

9.1. Compression testing was successfully utilised to investigate the mechanical properties of Baker's yeast cells (*Saccharomyces cerevisiae*). The method generated force - displacement data which allowed the cell size, force and fractional deformation at failure of each cell to be obtained.

9.2. It was found that the force at failure, and fractional deformation at failure were not affected by the speed of compression. In addition, it was found that these parameters did not change significantly over 18 months for samples prepared from a dried stock and that the temperature at which the cells were compressed did not influence the results. Also as expected, it was shown that the order in which the cells were compressed did not influence the results.

9.3. The mean cell diameter was measured by three methods, compression testing by micromanipulation, image analysis (TEM) and the Malvern Mastersizer, and it was found that there were no significant differences. This confirmed that the diameter of a cell measured during compression testing by micromanipulation could be used to characterise

the cell size. This was important, as it is essential to have an accurate cell diameter for each cell being compressed for modelling.

9.4. In all situations, it was found that the force at failure was not strongly correlated with the cell diameter and that the deformation at failure was weakly correlated with the cell diameter. Also as expected, it was shown that the deformation at failure is strongly correlated with the force at failure.

9.5. Numerical models were developed to extract intrinsic material properties and failure criteria from the experimental force - deformation data. Three different strain definitions, infinitesimal strain, Green strain and the Hencky strain, were used in this development. Detailed comparisons of the models were performed and the reasons for the differences sought. It was shown that numerical simulations using any of these strain definitions could fit the experimental data well up to the point of cell failure. This suggested that the assumption of a linear elastic constitutive relationship (i.e. a linear relationship between the stress and the strain) was representative of the actual constitutive relationship of the cell wall.

9.6. Compression and release experiments showed that significant volume loss occurred during the time it took for the motor to change direction making it impossible for hysteresis tests to be performed. Instead repeat compression experiments were performed which generated similar force - deformation data in each case. This also indicated that the assumption of a linear elastic constitutive equation was appropriate.

9.7. The numerical model was fitted to experimental data produced at a range of compression speeds with the initial stretch ratio fixed at 1.04. The compression speed appeared to have an effect on the "pseudo elastic modulus" of the cell wall. At and above speeds of approximately 45 μms^{-1}, the pseudo elastic moduli were found to be essentially constant. Due to this all further compressions were performed at a speed of 68 μms^{-1}. It was assumed that this compression speed was sufficient to allow water loss during compression to be considered negligible.

9.8. For experimental data produced at 68 μms^{-1} the initial stretch ratio and the elastic modulus were treated as adjustable parameters during the fitting process. This study has given mean cell wall properties for late stationary phase Baker's yeast of: elastic modulus 185 ± 15 MPa, initial stretch ratio 1.039 ± 0.006, circumferential stress at failure 115 ± 5 MPa, circumferential strain at failure of 0.46 ± 0.03, and strain energy per unit volume at failure of 30 ± 3 MPa. The elastic modulus and initial stretch ratio were both found to be independent of the cell size while all of the failure criteria were found to decrease with increasing cell size.

9.9. A protocol was established for determining the initial stretch ratio of individual cells by visualisation chamber experiments independent of compression testing by micromanipulation. This method successfully confirmed that the initial stretch ratio obtained by fitting of numerical simulations to experimental data was reasonable. In addition to this the initial stretch ratio measured with the visualisation chamber was found to be size independent.

9.10. In order to eliminate the effect of the cell wall thickness assumption the surface modulus (15.3 ± 1.2 Nm^{-1}) and the surface strain energy (2.37 ± 0.16 Nm^{-1}) were determined. The surface modulus was found to correlate weakly with the cell diameter while the surface strain energy at failure was found to be a decreasing function of the cell diameter.

9.11. It is believed that the cell size dependent effects are due to the changes that occur in the cell wall during the yeast cell cycle, specifically the increasing inclusion of bud scars following cytokinesis in the larger cells. It is possible that, stress concentrations occur around these bud scars during compression testing. This leads to the larger cells, which presumably contain more bud scars, failing at a lower deformation and strain energy than smaller cells.

9.12. It was found that treating Baker's yeast cells with dithiothreitol (DTT), which breaks disulphide bonds in the cell wall, did not have a significant effect on the surface modulus or the surface strain energy at failure. This represents the first investigation into the effect of a specific component of the Baker's yeast cell wall on intrinsic material properties and failure criteria produced from compression testing experiments.

9.13. Disruption of Baker's yeast cells by sonication showed a decrease in the surface modulus and constant surface strain energy at failure over increased treatment time. However, as it was not possible to describe the structure of the cell wall of the cells after sonication it was not possible to draw explicit conclusions from this work.

Chapter Ten: Recommendations

10.1. The micromanipulation technique was able to produce useful information from the compression of Baker's yeast. However, it was clear that there are still aspects of the technique that need improvement if further insight into the material properties of the cell wall are to be determined.

10.2. Improvement to the visualization of the sample would enable the operator to observe more clearly the cell undergoing compression and to confirm visually that cell breakage had occurred. Clearly observing the cell during breakage might also allow information about the mechanism of failure to be obtained. In addition, significant improvement of visualisation would allow cells which are mechanically damaged or non-viable to be identified. Improvement of the side view microscope should also allow independent estimates of the water loss from the cell during compression testing.

10.3. Analysis of the cell wall might be performed in conjunction with micromanipulation and cell physiological measurements to investigate the effect of wall composition on biomechanics. This objective could be completed using either biochemical analysis or a technique that gives the mechanical structure of each cell being compressed, such as raman confocal spectroscopy. This would allow more explicit statements to be made about how the different components of the cell wall contribute to the mechanical strength of the cell.

10.4. Functional genomics could be used to eliminate specific structural genes that are expected to contribute to the mechanical strength of the cell wall. However, caution needs to be used in this approach as altering essential genes in the yeast cell may lead to other unforeseen changes to the wall composition and structure.

10.5. The effect of many other factors such as antibiotics, chemical agents, different growth conditions, etc. on the mechanical properties could also be examined. This process also needs to be performed in conjunction with the detailed biochemical analysis of the cell wall.

10.6. The large variations in the results are most likely due to biological variation. In order to detect small differences in the population, significantly greater number of measurements would be needed. The rate at which micromanipulation measurements are obtained could be increased by automation of the rig. In order to detect small differences in the elastic modulus due to removal of the outer mannoprotein layer, or to use a functional genomics approach, significantly more cells would need to be compressed (~ 512 cells to detect a difference of 5 MPa).

10.7. It has been hypothesised in this work that the cell size dependent relationships found between the parameters is due to the increased number of bud scars in the cell wall of larger cells. This hypothesis could be testing by separating the cell population according to the number of bud scars in the cell wall. It is possible that this could be done using cell stains such as Calcoflour white and flow cytometry. However, it would need to be ensured that the

sorting technique does not interfere with the mechanical properties of the cell wall, which Calcoflour may do.

10.8. Further development of the mathematical model is required if it is to be applied to other biological materials which are not linear - elastic in nature, such as tomato cells. Alternatively it may be more appropriate to employ finite element modelling where non - spherical cells and non - isotropic cell walls can also be investigated.

Chapter Eleven: References

Aguilar-Uscanga, B., Francois, J.M. (2003). **A study of the yeast cell wall composition and structure in response to growth conditions and mode of cultivation**. *Letters in Applied Microbiology*. 37 268-274

Alessandrini, A. and Facci, P. (2005). **AFM: a versatile tool in biophysics.** *Measurement Science and Technology, 16,* 65-92.

Balasundarum, B. (2004). **A detailed investigation of Microbial Cell Disruption by Hydrodynamic Cavitation for Selective Product Release**. PhD, University of Cape Town, SA.

Balasundarum, B., and Pandit, A.B. (2001a). **Selective release of invertase by hydrodynamic cavitation.** *Biochemical Engineering Journal, 8,* 251-256.

Balasundarum, B., and Pandit, A.B. (2001b). **Significance of location of enzymes on their release during microbial cell disruption.** *Biotechnology and Bioengineering, 75,* 607-614.

Balasundarum, B. and Harrison, S.T.L. (2006). **Disruption of Brewers' yeast by Hydrodynamic Cavitation: Process variables and their influence on selective release**. *Biotechnology and Bioengineering, 94,* 303-311.

Berner, J.L. and Gervais, P. (1994). **A new visualization chamber to study the transient volumetric response of yeast cells submitted to osmotic shifts**. *Biotechnology and Bioengineering, 43,* 165-170.

Blewett, J.M. (2000). **Micromanipulation of Plant Cell Mechanical Properties**. Ph.D thesis, University of Birmingham, UK.

Blewett, J.M., Burrows, K., & Thomas, C.R. (2000). **A micromanipulation method to measure the mechanical properties of single tomato suspension cells.** *Biotechnology Letters, 22,* 1877-1883.

Boudou, T., Ohayon, J., Arntz, Y., Finet, G., Picart, C., and Tracqui, P. (2006). **An extended modelling of the micropipette aspiration experiment for the characterisation of the Young's modulus and Poisson's ratio of adherent thin biological sample: Numerical and experimental studies.** *Journal of Biomechanics, 39,* 1677-1685.

Bowen, W.R., Lovitt, R.W. and Wright, C.J. (2001). **Atomic force microscopy study of the adhesion of *Saccharomyces cerevisiae.*** *Journal of Colloid and Intersurface Science, 237,* 54-61.

Bryant, Z., Stone, M.D., Gore, J., Smith, S.B., Cozzarelli, N.R. and Bustamante, C. (2003). **Structural transitions and elasticity from torque measurements on DNA.** *Nature, 424,* 338-341.

Bull, A.T. (1970). **Chemical composition of wild-type and mutant Aspergillus nidulans cell walls. The nature of polysaccharide and melanin constituents.** *Journal of General Microbiology, 63,* 75-94.

Cabib, E., Drgonová, J., and Drgon, T. (1998). **Role of Small G Proteins in Yeast Cell Polarization and wall Biosynthesis.** *Annual Review of Biochemistry, 67,* 307-333

Cabib E, Roh DH, Schmidt M, Crotti L, and Varma A. (2001). **The yeast cell wall and septum as paradigms of cell growth and morphogenesis.** *The Journal of Biological Chemistry. 276,* 19679-19682.

Cappellaro, C., Mrsa, V., and Tanner, W. (1998). **New potential cell wall glucanases of *Saccharomyces cerevisiae* and their involvement in mating.** *Journal of Bacteriology, 180,* 5030-5037.

Castillo, L., Martinez, A.I., Garcerá, A., Elorza, M.V., Valentín, E., Sentandreu, R. (2003). **Functional analysis of the cysteine residues and the repetitive sequence of Saccharomyces cerevisiae Pir4/Cis3: the repetitive sequence is needed for binding to the cell wall β-1,3-Glucan.** *Yeast., 20,* 973-83.

Carpita C.C. (1985). **Tensile strength of living cells.** *Plant Physiology, 79,* 485-488.

Champluvier, B., Kamp, B., and Rouxhet, P.G. (1989). **Immobilization of β-galactosidase retained in yeast: Adhesion of the cells on a support.** *Applied Microbiology and Biotechnology, 27,* 464-469.

Cheng, L.Y. (1987a). **Deformation analyses in cell and development biology. Part I - Formal methodology.** *Transactions of the American Society of Mechanical Engineers: Journal of Biomedical Engineering, 109,* 10-17.

Cheng, L.Y. (1987b). **Deformation analyses in cell and development biology. Part II - Mechanical experiments on cells.** *Transactions of the American Society of Mechanical Engineers: Journal of Biomedical Engineering, 109,* 18-24.

Ciccolini, L., Taillandier, P., Wilhem, A.M., Delmas, H., and Strhaiano, P. (1997). **Low frequency thermo-ultrasonication of *Saccharomyces cerevisiae* suspensions: effect of temperature and of ultrasonic power.** *Chemical Engineering Journal, 65,* 145-149.

Cole, K.S. (1932). **Surface forces of the arbacia egg.** *Journal of Cellular and Comparative Physiology, 1,* 1-9.

D'haeseleer, P. (2005). **Closing the circle of osmoregulation.** *Nature Biotechnology, 23,* 941-942.

Dallies, N., Francois, J., Paquet, V. (1998). **A new method for quantitative determination of polysaccharides in the yeast cell wall. Application to the cell wall defective mutants of *Saccharomyces cerevisiae*.** *Yeast, 14,* 1297-1306

De Nobel, J.G., Klis, F.M., Priem, J., Munnik, T., and Van Den Ende, H. (1990). **The glucanase – soluble Mannoproteins limit cell wall porosity in *Saccharomyces cerevisiae.*** *Yeast, 6,* 491-499.

Farkade, V.D., Harrison, S.T.L, and Pandit, A.B. (2005). **Heat induced translocation of proteins and enzymes within the cell: an effective way to optimise the microbial cell disruption process.** *Biochemical Engineering Journal, 23,* 247-257.

Feng, W.W. and Yang, W.H. (1973). **On the contact problem of an inflated spherical nonlinear membrane.** *Transaction of the American Society of Mechanical Engineers: Journal of Applied Mechanics, 40,* 209-214.

Fraser, D. (1951). **Bursting bacteria by release of gas pressure.** *Nature, 167,* 33-4.

Gaboriaud, F. and Dufrene, Y.F. (2007). **Atomic force microscopy of microbial cells: Application to nanomechanical properties, surface forces, and molecular recognition forces.** *Colloids and Surfaces B: Biointerfaces, 54,* 10-19.

Gasch, A.P., Spelman, P.T., Kao, C.M., Carmel-Harel, O., Eisen, M.B., Storz, G., Botstein, D, and Brown, P.O. (2000). **Genomic expression programs in the response of yeast cells to environmental changes.** *Molecular Biology of the Cell, 22,* 4241-4257.

Gascon, S., Neumann, N.P., and Lampen, J.O. (1968). **Comparitive study of the Properties of the Purified Internal and External Invertases from Yeast.** *The Journal of Biological Chemistry, 243,* 1573-1577.

Gervais, P., Molin, P., Marechal, P.A., and Herail-Foussereau, C. (1996). **Thermodynamics of yeast cell osmoregulation: Passive mechanisms.** *Journal of Biological Physics, 22,* 73-86.

Guerrero, S., Lopez-Malo, A., and Alzamora, S.M. (2001). **Effect of ultrasound on the survival of *Saccharomyces cerevisiae:* influence of temperature, pH and amplitude**. *Innovative Food Science and Emerging Technologies, 2,* 31-39.

Harold, F.M. (2007). **Bacterial morphogenesis: learing how cells make cells**. *Current Opinions in Microbiology, 10,* 591-595.

Harris, B. (1980). **The Mechanical Behaviour of Composite Materials,** in *The Mechanical Properties of Biological Materials,* Symposia of the Society for Experimental Biology (XXXIV), Cambridge University Press, 37-74.

Hartland, R.P., Vermeulen, C.A., Klis, F.M., Sietsma, J.H., and Wessels, J.G. (1994). **The linkage of (1-3)-β-Glucan to chitin during cell wall assemble in Saccharomyces cerevisiae.** *Yeast, 10,* 1591-1599.

Hiramoto, Y. (1963). **Mechanical properties of sea urchin eggs: I – Surface force and elastic modulus of the cell membrane.** *Experimental Cell Research, 32,* 59-76.

Hochmuth, R.M., (2000). **Micropipette aspiration of living cells.** *Journal of Biomechanics, 33,* 15-22.

Hunter, M. J. and Commerford, S. L., (1961). **Pressure homogenization of mammalian tissues.** *Biochimica et Biophysica Acta, 47,* 580-586.

Iorio, E., Torosantucci, A., Bromuro, C., Chiani, P., Ferretti, A., Giannini, M., Cassone, A., and Podo, F. (2008).**Candida albicans cell wall comprises a branched β-d-(1→6)-glucan with β-d-(1→3)-side chains.** *Carbohydrate Research,* 343, 1050-1061.

Jennings, D.H. (1995). **The Physiology of Fungal Nutrition.** *Cambridge University Press,* UK.

Jentoft ,N. (1990). **Why are proteins O-glycosylated?** *Trends in Biochemical Sciences, 15,* 291-294

Kedem, O., and Katchalsky, A., (1958). **Thermodynamics analysis of the permeability of biological membranes to non-electrolytes.** *Biochimica et Biophysica Acta, 27,* 229-246.

Kapteyn, J.C., ter Riet, B., Vink, E., Blad, S., De Nobel, H., Van Den Ende, H., and Klis, F.M. (2001). **Low external pH induces HOG1-dependent changes in the organization of the *Saccharomyces cerevisiae* cell wall.** *Molecular Microbiology, 39,* 469-479.

Kelly, D., and Kelly. S. (2003). **Rewiring yeast for drug synthesis**. *Nature Biotechnology, 21,* 133-134.

Kidby, D.K., and Davies, R. (1970a). **Thiol induced release of invertase from cell walls of *Saccharomyces fragilis.*** *Biochimica et Biophysica Acta, 24,* 261-266.

Kidby, D.K., and Davies, R. (1970b). **Invertase and disulphide bridges in the yeast wall.** *Journal of General Microbiology, 61,* 327-333.

Kleinig, A.R. (1997). ***Cell disruption mechanics***. Ph.D. thesis, University of Adelaide, Australia.

Kleinig, A.R. and Middelberg, A.P.J. (1996). **The correlation of cell disruption with homogeniser valve pressure gradient determined by computational fluid dynamics.** *Chemical Engineering Science, 51,* 5103-5110.

Kleinig, A.R. and Middelberg, A.P.J. (1998). **On the mechanism of microbial cell disruption in high-pressure homogenisation.** *Chemical Engineering Science, 53,* 891-898.

Klipp, E., Nordlander, B., Kruger, R., Gennemark, P., and Hohmann, S. (2005). **Integrative model of the response of yeast to osmotic shock.** *Nature Biotechnology, 23,* 975-982.

Klis, F.M., Mol, P., Hellingwerf, K., and Brul, S. (2002). **Dynamics of cell wall structure in Saccharomyces cerevisiae.** *FEMS Microbiology Reviews,* 26, 239-256.

Klis, F.M., Boorsma, A., and de Groot, P.W.J. (2006). **Cell wall construction in *Saccharomyces cerevisiae.*** *Yeast,* 23,185-202.

Klis, F.M., de Jong, M., Brul, S., and de Groot, P.W.J. (2007). **Extraction of cell surface associated proteins from living yeast cells.** *Yeast, 24,* 253-258.

Kollar, R., Petrakova, E., Ashwell, G., Robbin, P.W. and Cabib, E. (1995). **Architecture of the yeast cell wall.** *Journal of Biological Chemistry, 270,* 1170-1178.

Kollar, R., Reinhold, B., Petrakova, E., Yeh, h., Ashwell, G., Drgonova, J., Kapteyn, J., Klis, F.M., Cabib, E. (1997). **Architecture of the yeast cell wall.** *Journal of Biological Chemistry. 272,* 17762-17775.

Krainer, E., Stark, R.E., Naider, F., Alagramam, K., and Becker, J.M. (1994). **Direct observation of cell wall glucans in whole cells of *Saccharomyces cerevisiae* by magic-angle spinning ^{13}C-NMR.** *Biopolymers, 34,* 1627-1635.

Kuznetsova, T.G., Starodubtseva, M.N., Yegorenkov, N.I., Chizhik, S.A. and Zhdanov, R.I. (2007). **Atomic force microscopy probing of cell elasticity.** *Micron, 38,* 824-833.

Lardner, T.J. and Pujara, P. (1978). **On the contact problem of a highly inflated nonlinear membrane.** *Journal of Applied Mechanics, 45,* 202-203.

Lardner, T.J. and Pujara, P. (1980). **Compression of spherical cells.** *Mechanics Today, 5,* 161-176.

Lemaitre J. and Chaboche, J.L. (1994). **Mechanics of Solid Materials**. (p. 125) Cambridge University Press.

Lesage, G. and Bussey, H. (2006). **Cell wall assembly in *Saccharomyces cerevisiae.*** *Microbiology and Molecular Biology Reviews, 70,* 317-343.

Levin, R.L. (1979). **Water permeability of yeast cells at sub-zero temperatures.** *Membrane Biology, 46,* 91-124.

Lim, C.T., Zhou, E.H., Li, A., Vedula, S.R.K., and Fu, H.X. (2006). **Experimental techniques for single cell and single molecule biomechanics.** *Materials Science and Engineering, 26,* 1278-1288.

Lipke P.N and Ovalle R. (1998). **Cell wall architecture in yeast: New structure and new challenges.** *Journal of Bacteriology,* 180, 375-3740.

Liu, K.K. (1995). ***The deformation of cellular entities*.** Ph.D thesis, University of London, UK.

Liu, K.K., Williams, D.R., and Briscoe, B.J. (1996). **Compressive deformation of a single microscope.** *Physical Review E, 54,* 6673-6680.

Liu T. and Zhang Z. (2004). **Mechanical properties of desiccated ragweed pollen grains determined by micromanipulation and theoretical modelling.** *Biotechnology and Bioengineering, 8,* 770-775.

Loewus, M.W. and Loewus,F., (1971). **The isolation and characterization of d-glucose 6-phosphate cycloaldolase (NDAdependent) from acer pseudoplatanus L. cell cultures**. *Plant. Physiol. 48,* 255-260.

Malvern L.E. (1969). **Introduction to the Mechanics of a Continuous Medium**, (pp. 223), Prentice-Hall.

Marechal, P.A., Martinez de Maranon, I., Molin, P., and Gervais, P. (1995). **Yeast cell response to water potential variations,** *International Journal of Food Microbiology, 28,* 277-287.

Martinez de Maranon, I., Gervais, P., and Molin, P. (1997). **Determination of cells' water membrane permeability : unexpected high osmotic permeability of *Saccharomyces cerevisiae.*** *Biotechnology and Bioengineering, 56,* 62-70.

Mashmoushy, H., Zhang, Z. and Thomas C.R. (1998). **Micromanipulation measurement of the mechanical properties of baker's yeast cells.** *Biotechnology Techniques, 12,* 925-929.

McAleer, W.J., Buynak, E.B., Maigetter, R.Z., Wampler, D.E., Miller, W.J., and Hilleman, M.R. (1984). **Human hepatitis B vaccine from recombinant yeast.** *Nature,* 307, 178-180.

Meikle, A.J., Reed, R.H. and Gadd, G.M. (1988). **Osmotic adjustment and the accumulation of organic solutes in whole cells and protoplasts of *Saccharomyces cerevisiae*.** *Journal of General Microbiology, 134,* 3049-3060.

Mendelson, N.H., Sarlls, J.E., Wolgemuth, C.W., and Goldstein, R.E. (2000). **Chiral self-propulsion of growing bacterial macrofibers on a solid surface.** *Physical Review Letters, 84,* 1627-1630.

Middelberg, A.P.J. (1995). **Process scale disruption of microorganisms**. *Biotechnology Advances, 13,* 491-551.

Mills, J.P., Qie, L., Dao, M., Lim, C.T. and Suresh, S. (2004). **Nonlinear elastic and viscoelastic deformation of the human red blood cell with optical tweezers.** *Molecular Cell Biology, 1,* 169-180.

Molano, J., Bowers, B., and Cabib, E. (1980). **Distribution of Chitin in the yeast cell wall. An ultrastructural and chemical study.** *Journal of Cell Biology, 85,* 199-212.

Morris, G.J., Winters, L., Coulson, G.E., and Clarke, K.J. (1983). **Effect of osmotic stress on the ultrastucture and viability of the yeast cell *Saccharomyces cerevisiae.*** *Journal of General Microbiology , 129,* 2023-2034.

Muller, A., Ensley, R., McNamee, R., Jones, E., Mclaughlin, E., Chandley, W., Browder, W., Lowman, D., and Williams, D. (1997). **The application of protic acids to the extraction of β 1,3-glucan from *Saccharomyces cerevisiae.*** *Carbohydrate Research, 299,* 203-208.

Munns, R., Greenway, H., Setter, T.L., and Kuo, J. (1983). **Turgor Pressure, Volumetric elastic modulus and ultrastructure of *Chlorella emersonii* Grown at High and Low External NaCl.** *Journal of Experimental Botany, 34,* 144-155.

Neidermeyer, W., Parish, G.R., and Moor, H. (1977). **Reactions of Yeast Cells to Glycerol Treatment Alterations to Membrane Structure and Glycerol Uptake.** *Protoplasma, 92,* 177-193.

Nobel, P.S. (1969). **The Boyle van't Hoff relationship.** *Journal of Theoretical Biology, 23,* 375-379.

Nobel, P.S. (1991). **Physicochemical and Environmental Plant Physiology.** Academic Press Inc.

Ohashi, T., Ishii, Y. Matsumoto, T. and Sato, M. (2002). **Experimental and numerical analyses of local mechanical properties measured by atomic force microscopy for sheared endothelial cells.** *Bio-medical Materials and Engineering, 12,* 319-327.

Oertli, J.J. (1986).**The effect of cell size on cell collapse under negative turgor pressure.** *Journal of Plant Physiology,124,* 365-370.

Osumi, M., (1998). **The ultrastructure of yeast: Cell Wall structure and formation.** *Micron, 29,* 207-233.

Payne, T., Hanfrey, C., Bishop, A.L., Michael, A.J., Avery, S.V., and Archer, B.D. (2008). **Transcript – specific translational regulation in the unfolded protein response of *Saccharomyces cerevisiae.*** *FEBS Letters, 582,* 503-509.

Peeters, E.A.G., Bouten, C.V.C., Oomens, C.W.J., and Baaijens, F.P.T. (2003). **Monitoring the biomechanical response of individual cells under compression: a new compression device.** *Medical and Biological Engineering and Computing, 41*, 498–503.

Peeters, E.A.G., Oomens, C.W.J., Bouten, C.V.C., Bader, D.L., and Baaijens, F.P.T. (2005). **Mechanical properties of single attached cells under compression.** *Journal of Biomechanics, 38,* 1685-1693.

Pelling, A.E., Sehati, S., Gralla, E.B., Valentine, J.S. and Gimzewski, J.K. (2004). **Local nanomechanical motion of the cell wall of *Saccharomyces cerevisiae.*** *Science, 305,* 1147-1150.

Powell, C.D., Quain, D.E. and Smart, K.A. (2003). **Chitin scar breaks in aged *Saccharomyces cerevisiae.*** *Microbiology, 149,* 3129-3137.

Pryce-Jones, E., Carver, T., and Gurr, S.J. (1999). **The roles of cellulose enzymes and mechanical force in host penetration by *Erysiphe graminisf.sp. hordei.*** *Physiological and Molecular Plant Physiology, 55,* 175-182.

Ruiz, C., Cid, V.J., Lussier, M., Molina, M., and Nombela, C. (1999). **A large-scale sonication assay for cell wall mutant analysis in yeast.** *Yeast, 15,* 1001-1008.

Santos, H.M., and Capelo, J.L. (2007). **Trends in ultrasonic based equipment for anyalytical sample treatment.** *Talanta, 73,* 795-802.

Shahinian, S., and Bussey, H. (2000). **β-1,6-Glucan synthesis in *Saccharomyces cerevisiae.*** *Molecular Microbiology, 35,* 477-489.

Shaw, J.A., Mol, P.C., Bowers, B., Silverman, S.J., Valiviesco, M.H., Durdn, A., and Cabib, E. (1991). **The function of chitin synthases 2 and 3 in the *Saccharomyces cerevisiae* cell cycle.** *Journal of Cell Biology, 114,* 111-123.

Shiu, C. (2000). ***Mechanical properties of Bacteria.*** Ph.D thesis, University of Birmingham, UK.

Shiu, C., Zhang, Z., and Thomas, C.R. (1999). **A novel technique for the study of bacterial cell mechanical properties.** *Biotechnology Letters, 13,* 707-713.

Sinclair, D., Mills, K., and Guarente, L. (1998). **Ageing in *Saccharomyces cerevisiae.*** *Annual Review of Microbiology, 52.* 533-560.

Skalak, R., Tozeren, A., Zarda, R.P., & Chien, S. (1973). **Strain energy function of red blood cell membranes**. *Biophysical Journal, 13*, 245-263.

Smith, A.E. (1999). ***Cell wall mechanical properties of Saccharomyces cerevisiae***. Ph.D thesis, University of Adelaide, Australia.

Smith, A.E., Moxham, K.E. and Middelberg, A.P.J. (1998). **On uniquely determining cell-wall material properties with the compression experiment.** *Chemical Engineering Science, 53,* 3913-3922.

Smith, A.E., Zhang, Z. and Thomas, C.R. (2000a). **Wall material properties of yeast cells: Part 1. Cell measurements and compression experiments.** *Chemical Engineering Science, 55,* 2031-2041.

Smith, A.E., Moxham, K.E. and Middelberg, A.P.J. (2000b). **Wall material properties of yeast cells. Part II. Analysis.** *Chemical Engineering Science, 55,* 2043-2053.

Smith, A.E., Zhang, Z., Thomas, C.R., Moxham, K.E. and Middelberg, A.P.J. (2000c). **The mechanical properties of *Saccharomyces cerevisiae*.** *Proceedings of the National Academy of Sciences, 97,* 9871-9874.

Smith, S.B., Cui, Y., and Bustamante, C. (1996). **Overstretching B-DNA: The Elastic Response of Individual Double-Stranded and Single-Stranded DNA Molecules.** *Science, 271,* 795-799.

Smith, W.L., and Ballou, C.E. (1974). **The effect of dithiothreitol on external yeast invertase.** *Biochemical and Biophysical Research Communication,* 59, 314-321.

Smits, G.J., Kapteyn, J.C., Van Den Ende, H., and Klis, F.M. (1999). **Cell wall dynamics in yeast.** *Current Opinion in Microbiology, 2,* 348-352.

Smits, G.J., van den Ende, H., and Klis, F.M. (2001). **Differential regulation of cell wall biogenesis during growth and development in yeast.** *Microbiology, 147,* 781-794.

Smits, G.J., Schenkman, L.R., Brul, S., Pringle, J.R., and Klis, F.M. (2006). **Role of cell-cycle regulated expression in the localised incorporation of cell wall proteins in yeast.** *Molecular Biology of the Cell, 17,* 3267-3280.

Sommer, A., Lewis, M.J. (1971). **Effect of Dithiothreitol on yeast: Sphaeroplast Formation and Invertase Release.** *Journal of General Microbiology, 68,* 327-335.

Spellman, P.T., Sherlock, M., Zhang, M.Q., Lyer, V.R., Anders, K., Eisen, M.B., Brown, P.O., Botstein, D., and Futcher, B. (1998). **Comprehensive identification of cell-cycle regulated genes of the yeast cell *Saccharomyces cerevisiae* microarray hybridisation,** *Molecular Biology of the Cell, 9,* 3273-3297.

Srinorakutara, T. (1997). ***Mechanical strength of Yeasts.*** Ph.D thesis, University of Birmingham, UK.

Stocks, S.M. and Thomas, C.R. (2001). **Viability, strength and fragmentation of *Saccharopolyspora erythraea* in submerged fermentation.** *Biotechnology and Bioengineering, 75,* 702-709.

Stokke, B.T., Elgsaeter, A., Hara, C., Kitamura, S., and Takeo, K. (1993). **Physicochemical properties of (1→6)-branched (1→ 3)-β-D-Glucans. 1. Physical dimensions estimated from hydrodynamic electron microscopic data.** *Biopolymers, 33,* 561-573.

Thomas, C.R., and Zhang. Z. (1998). **The effect of hydrodynamics on biological materials.** *Advances in Bioprocessing II,* (page 137-170), London: Kluwer academic publishers.

Thomas, C.R., Zhang, Z., and Cowen, C. (2000). **Micromanipulation measurements of biological materials.** *Biotechnology Letters, 22,* 531-537.

Tomos, A.D., Leigh, R.A. (1999). **The Pressure Probe: A versatile toll in plant cell physiology.** *Annual review of Plant Physiology Plant Molecular Biology.50,* 447-472.

Tomos, D. (2000). **The Plant Cell Pressure Probe.** *Biotechnology Letters, 22,* 437-442.

Touhami, A., Nysten, B., and Dufrene, Y.F. (2003). **Nanoscale mapping of the elasticity of microbial cells by atomic force microscopy.** *Langmuir, 19,* 4539-4543.

Wang, C.X., Wang, L. and Thomas, C.R. (2004). **Modelling the mechanical properties of single suspension-cultured tomato cells.** *Annals Botany, 93,* 443-453.

Wang, C.X., Cowen, C., Zhang, Z., and Thomas, C.R. (2005). **High-speed compression of single alginate microspheres.** *Chemical Engineering Science, 60,* 6649-6657.

Wang, C.X., Pritchard, C.R. and Thomas, C.R. (2006a). **Investigation of the mechanics of single tomato fruit cells.** *Journal of Texture Studies, 37,* 597–606.

Wang, L., Hukin, D., Pritchard, J., and Thomas, C.R. (2006b). **Comparison of plant cell turgor pressure measurement by pressure probe and micromanipulation**. *Biotechnology Letters, 28,* 1147-1150.

Williams, D.L., McNamee, R.B., Jones, E.L., Pretus, H.A., Ensley, H.E., Browder, I.W., Di Luzio, N.R. (1991). **A method for the solubilization of a (1----3)-beta-D-glucan isolated from Saccharomyces cerevisiae.** *Carbohydrate research. 219,* 203-213.

Wolf, A.V., Brown, M.G., and Prrentiss, P.G. (1980). In: CRC Handbook of Chemistry and Physics, 60th edition.

Wu, H., Spence, R. D., Sharpe, P.J.H., Goeschl, J.D. (1985). **Cell wall elasticity: A critique of the bulk elastic modulus and an analysis using polymer elastic principles.** *Plant, Cell and Environment, 8,* 563-570.

Xiao, H. and Chen, L.S. (2002) **Hencky's elasticity model and linear stress-strain relations in isotropic finite hyperelasticity**. *Acta Mechanica, 157,* 51-60.

Yoneda, M. (1964). **Tension at the surface of sea-urchin egg: a critical examination of Cole's experiment,** *Journal of Experimental Biology, 41,* 893-906.

Yoneda, M. (1973). **Tension at the surface of sea-urchin eggs on the basis of 'liquid-drop' concept.** *Advances in Biopysics, 4,* 153-190.

Zeng, Q., Qiu, F., and Yuan, L. (2008). **Production of artemisinin by genetically modified microbes.** *Biotechnology Letters, 30,* 581-592

Zhang, Z., Ferenczi, M.A., Lush, A.C. and Thomas, C.R. (1991). **A novel micromanipulation technique for measuring the bursting strength of single mammalian cells.** *Applied Microbiology and Biotechnology, 36,* 208-210.

Zhang, Z., Ferenczi, M.A. and Thomas, C.R. (1992). **A micromanipulation technique with a theoretical cell model for determining mechanical properties of single mammalian cells.** *Chemical Engineering Science, 47,* 1347-1354.

Zhang, Z., Blewett, J.M., and Thomas, C.R. (1999). **Modelling the effect of osmolality on the bursting strength of yeast cells.** *Journal of Biotechnology, 71,* 17-24.

Zhao, L. Schaefer, D., Xu, HJ., Modi, S.J., Lacourse, W.R. and Marten, M.R. (2005). **Elastic properties of the cell wall of *Aspergillus nidulans* studied with atomic force microscopy**. *Biotechnology Progress, 21,* 292-299.

Zlotnik, H., Fernandez, M.P., Bowers, B., Cabib, E. (1984). ***Saccharomyces cerevisiae* Mannoproteins form an external cell layer that determines wall porosity.** *Journal of Bacteriology. 159,* 1018-1026

Appendices

Appendix 1: Force transducer

Figure A 1 is a schematic of the force transducer used to measure the compression of materials. The transducer contains two cantilever beams, these are a measurement beam and a reference beam.

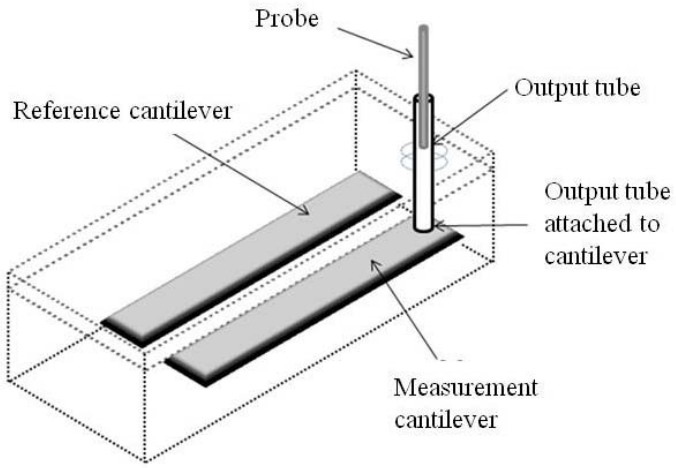

Figure A 1: Diagram of force transducer

Appendix 2: Sensitivity of transducer

The 403A series transducer (Aurora Scientific Inc) is able to measure 0.5 grams force by deflection of the cantilever beam. The bending of the beam is presumed to correlate directly to the force which is imposed on the beam. In order to correlate this bending of the beam it is necessary to determine the grams per voltage change, known as the sensitivity of the transducer. According to the manufacturer, the sensitivity should be 0.5 mN/V. It is essential to check the sensitivity as this value may change over usage and age. To measure this parameter known weights are applied to the measurement beam of the transducer and the voltage recorded. If an amplifier is to be used for compressions, as here, then the sensitivity and compliance should be measured with this attached.

Calculation of the transducer sensitivity

1. Attach the transducer to a flat stable desk with the output tube vertical.
2. Produce a range of paper weights ranging from 0.005 g to 0.025 g accurately measured using scales accurate to 0.001 g. These weights will need to be adjusted if a transducer with a different force range is used. The small paper pieces are folded in quarters until there is a hollow peak that is able to balance on top of the output tube. For the larger weights Blue tac is attached to these weights.
3. A baseline is initially recorded with the offset being used to make this value as close to zero as possible.
4. Balance a paper weight on the output tube and record the voltage change that occurs. It is essential the weight is square on the output tube and that there are no draughts. Repeat this process for the whole series of weights.

5. The baseline value is subtracted from all of the recorded voltage values which leads to a series of weight verses voltage output data as shown in Figure A 2.

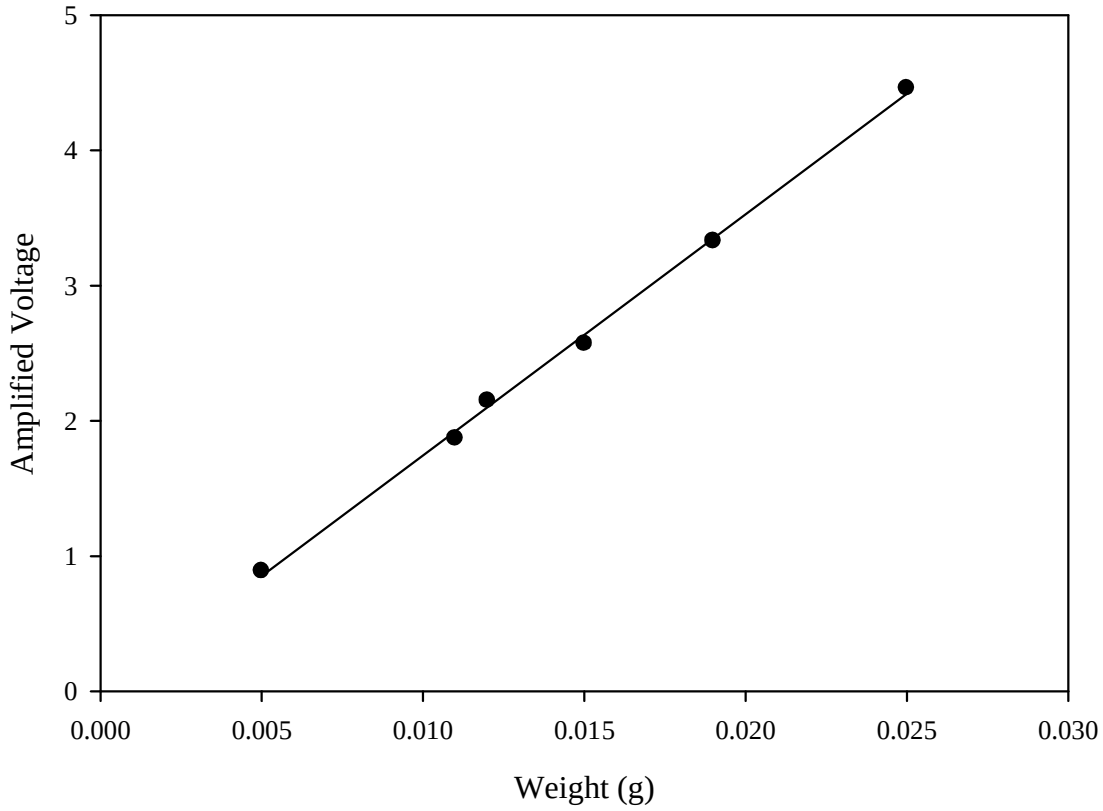

Figure A 2: Voltage verses weight data used to calculate the sensitivity of the transducer.

6. From Figure A 2 the gradient of the line is shown to be 19.3. This leads to a corresponding sensitivity value of 0.518 mN/V which is similar to the value provided of 0.5 mN/V. This value is used to calculate the compliance and force - displacement data.

If the data in Figure A 2 is found not to be linear then the transducer should not be used as this would indicate possible permanent deformation of the measurement beam or some other problem.

Appendix 3: Calculation of the compliance of the transducer.

During the compression process the measurement cantilever beam deflects leading to alterations in the voltage output. The higher forces result in more bending of the cantilever beam and a greater voltage output. The distance that the probe has moved is calculated by multiplying the speed of compression with the time of the displacement. However, the actual displacement of the probe is not the same as the distance moved as the cantilever beam bends in the opposite direction during the compression due to the imposed force. Due to this the bending of the beam that occurs must be calculated and subtracted from the distance calculated. This beam bending is considered to be a small deflection, in the case of the 403A transducer a recommended value of 1 μm mN^{-1} is given by the manufacture (Aurora Scientific Inc). This technique will lead to accurate and precise calculations of force - displacement data.

Figure A 3 shows voltage - time data that is calculated by compressing a probe attached to the force transducer at a known speed against a solid glass slide.

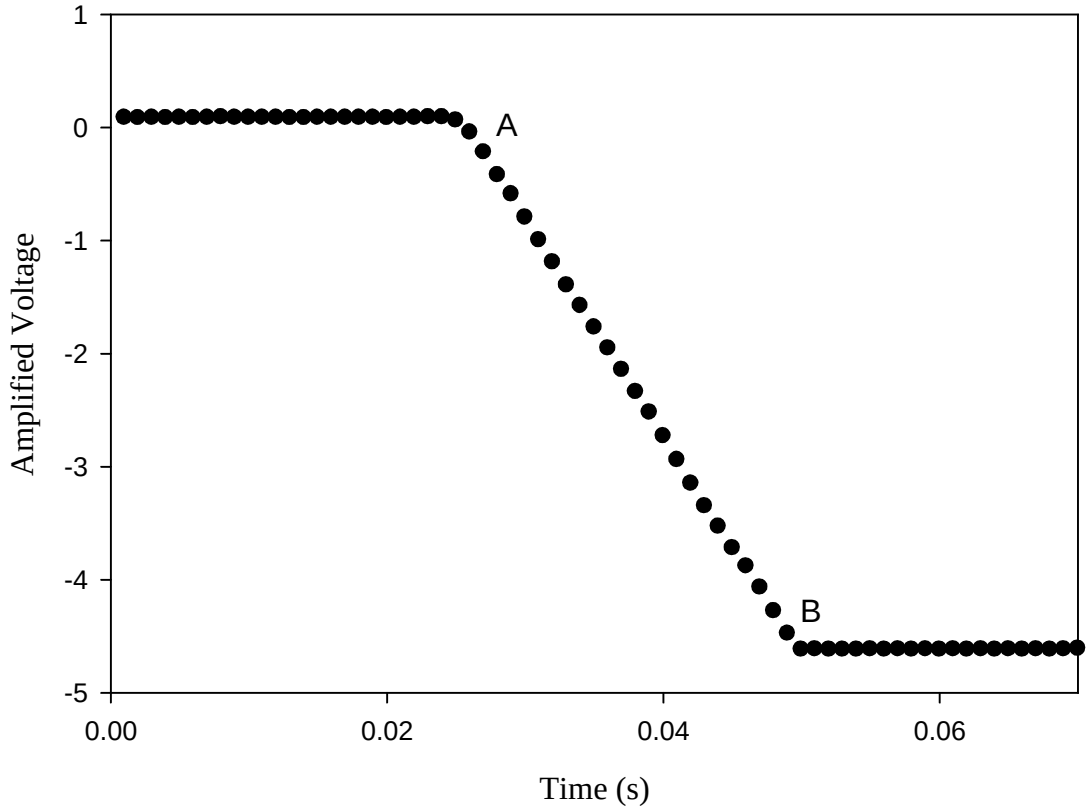

Figure A 3: Voltage verses time data obtained from the compression of a solid glass slide at a known compression speed to allow the compliance to be calculated.

The compliance of the transducer is calculated between points A and B in Figure A 3 which is where the probe is pressing against the slide.

The compliance is calculated using the equations below:

speed [μm/s] × Δt = distance moved by the probe [μm]

distance moved by the probe [μm] ÷ ΔV = μm/V

μm/V ÷ sensitivity of transducer [mN/V] = compliance in μm/mN

Appendix 4: Full table of the control commands for the LSRT stepping motor

The stepping motor used to lower the probe in the LSRT micromanipulator is controlled through Hyperterminal. The port settings assigned in Hyperterminal are outlined below.

Port settings: Baud Rate 9600
Bata Bits 8
Parity none
Stop bits one
Flow control none

Command	Action
Version	Returns the version number of the unit. Should return version 2.0 if working correctly.
C	Sets the number of steps for the motor to move (e.g. c,2000). Input 'C' and the number of assigned steps will be returned.
Wait	Sets the delay between the steps which has the effect of controlling the speed of compression. (e.g. wait,50). Input 'wait' and the assigned wait value will be returned.
U	Moves the motor down the by the set number of steps
D	Moves the motor up by the set number of steps
Z	Sets the position to zero
M	Sends the motor to the zero position
P	Returns the position in steps
K	Kills all movement

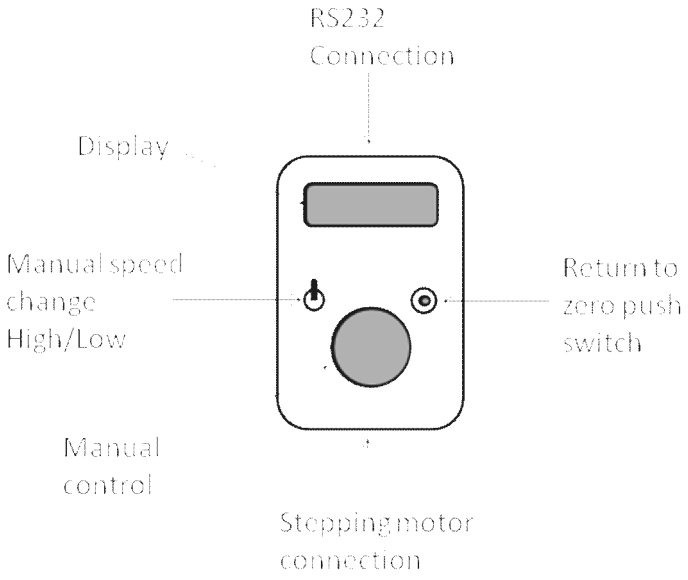

Figure A 4 : LSRT control box for stepping motor

From this the number of steps can be easily set using the ‘c’ command. The command ‘wait’ is used to assign a value for a period of time between each of the steps and has the effect of controlling the speed of the compression. This method of speed control allows significantly more control than previous methods which defined the required speed as a percentage of the possible top speed.

Appendix 5: Stepping motor calibration

1. The micromanipulation rig was set up with the objectives necessary to observe yeast cells during the compression experiments and the image observed on the attached monitors.
2. A measurement graticule 100 μm in length with 1 μm intervals was placed so that it could be seen clearly through the objective.
3. A clear ruler was photocopied onto a clear acetate OHP.
4. This OHP clear acetate was fixed to the monitor screen and using an OHP pen, the distances between each 10 μm point were marked on the ruler.
5. This allowed the distance that 1 μm would represent to be determined.
6. The probe was positioned at the 0 μm mark on the monitor using the OHP.
7. The motor was set to move 10000 steps and the motor initiated.
8. The distance that the probe had moved was then recorded off the graticule and found to be 120 μm. This leads to a step size of 0.012 μm.
9. Once the probe has been initiated to move down and the distance recorded the probe should be initiated to move back up to the 0 μm mark. The probe will not return to the 0 μm point exactly due to backlash. To return the probe to the 0 μm point the motor needs to be moved up from this point and then back down again.

Appendix 6: Calculation of the stepping motor speed for the low strain rate tester (LSRT) and the high strain rate tester (HSRT).

LSRT

To measure the speed of compression the probe is firstly manually lowered until it is visible on the monitor. The graticule produced in Appendix 5 is used to mark out a distance of 120 µm on the monitor over which the probe can be observed moving. Using HyperTerminal the probe is set to move 120 µm at a known 'wait'. The time taken to move over this distance is recorded with the process being repeated at least 10 times for each wait value. The speed is measured at a large range of wait values. As observed in Figure A 5 the speed of compression is not linearly related to the assigned wait. This means that to ensure an accurate speed is used, verification using this method needs to be done at each assigned wait value.

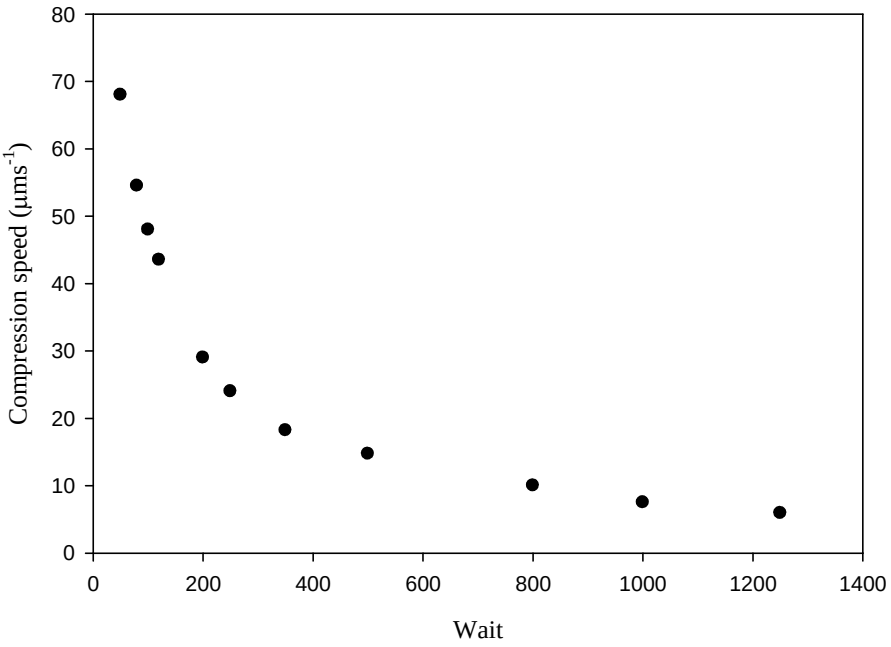

Figure A 5: Compression speed determined at a range of assigned 'wait' values

In addition to this Blewett (2000) observed that the speed of compression alters depending on the distance over which the probe travels. To compress yeast cells the motor will be need to travel between 10 and 30 μm so the speed over these distances needed to be confirmed. It is not possible to use the technique previously described to measure the speed as the probe will travel over the distance too quickly to be accurately timed. Due to this an image analysis technique was used. The probe was visualised on the monitor using a × 50 objective and its movement over a distance between 10 and 30 μm recorded. This then allowed the speed to be accurately determined over this shorter distance. It was found that the speed was the same when calculated over 120 μm, 30 μm or 10 μm.

HSRT

The Speed for the HSRT stepping motor was calibrated in the same way as with the LSRT. The speed was assigned as a percentage of the maximum possible speed. The results are shown in Figure A 6.

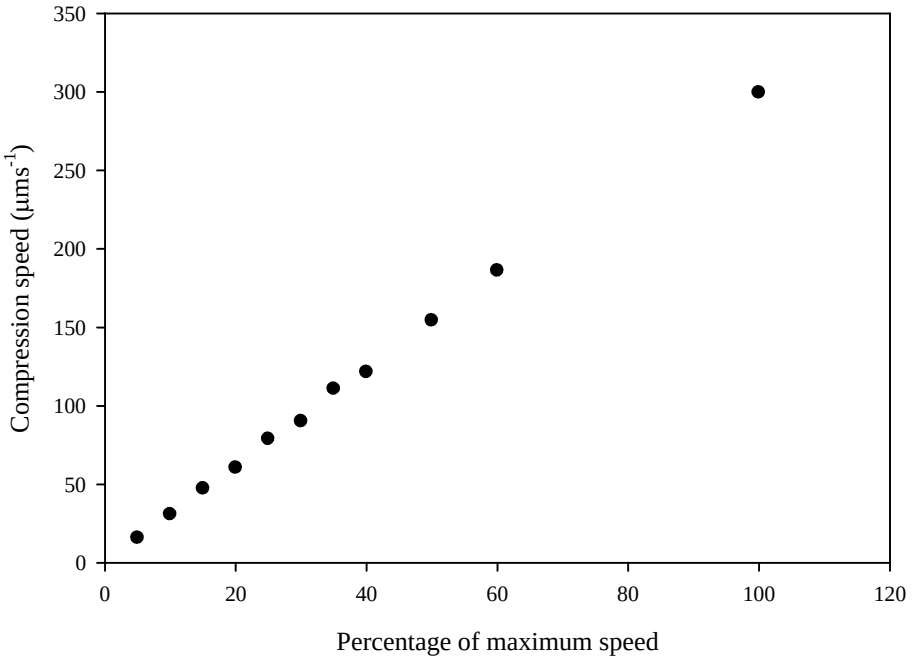

Figure A 6: Speed calibration for the high strain rate micro compression tester.

Appendix 7: Vapour pressure osmometer

The osmolality of the medium was measured using a vapour pressure osmometer (model Wescor 5500, Chemlab Scientific Products Ltd, Hornchurch, UK). The instrument needed to be left for at least 60 minutes to warm-up and stabilise prior to use. Standard solutions (Wescor, Utah, USA) of known osmolality, 100, 250 and 1000 mmol/kg were used to calibrate the osmometer following the instructions outlined in the manual. The osmolarity was determined by loading undiluted 10 µl samples onto cellulose discs.

Appendix 8: Enzyme and protein analysis techniques

The techniques outlined in this Appendix describe in detail the enzyme analysis methods used to assess the level of cell disruption by mechanical or chemical treatments.

Prior to use, any of the reagents that have been refrigerated should be warmed to room temperature. The samples obtained from the disruption methods are separated using micro-centrifugation.

α-glucosidase

As mentioned previously the α-glucosidase is located within the periplasmic space of the cell wall and will indicate partial disruption of the cell wall.

Reagents

5.0 mM	p-nitrophenol-α-D-glucosidase in 0.05M phosphate buffer pH 6.8 room temperature. This reagent needs to be prepared each time prior to use as it cannot be stored.
0.05 M	Phosphate buffer pH 6.8
0.1 M	Sodium carbonate (Na_2CO_3) solution in distilled water.

Method

1. Pipette out 100 µl of yeast cell supernatant into a clean test tube.
2. Add 2 ml of 5.0 mM p-nitrophenol-α-D-glucosidase dissolved in phosphate buffer pH 6.8
3. Incubate test tube at 30 ^{o}C for 15 minutes.
4. Add 2 ml of 0.l M sodium carbonate solution as a stop reagent and remove from the water bath

5. Measure the absorbance at 410 nm against a blank (distilled water) treated in a similar manner.

Calibration of p-nitrophenol-α-D-glucosidase

1. Standard solution of p-nitrophenol-α-D-glucosidase with concentrations ranging from 1-5 M dissolved in 0.1 M sodium carbonate solution.
2. Measure the absorbance at 410 nm against a blank sample.
3. Produce a calibration curve of the net absorbance against the number of moles of p – nitrophenol (Figure A 7).

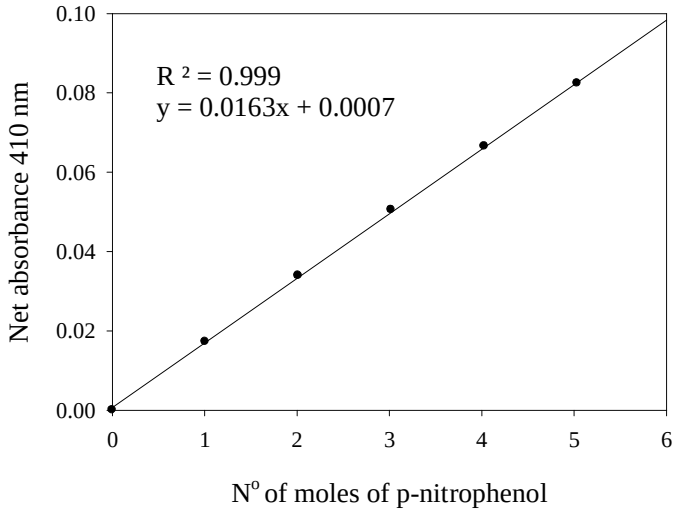

Figure A 7: p-nitrophenol calibration curvefor α-glucosidase

Alcohol dehydrogenase (ADH, cytoplasmic)

Alcohol dehydrogenase catalyses the conversion of acetaldehyde to ethanol in yeast cells.

Reagents

0.06 M	Sodium pyrophosphate pH 8.5
0.1 M	Nicotine adenine di-nucleotide (NAD) in distilled water
0.1 M	Ethanol in distilled water

Method

1. Pipette 2.2 ml of distilled water into a quartz cuvette
2. Add 0.5 ml of 0.06 M pyrophosphate buffer
3. Add 0.1 ml of 0.1 M ethanol
4. Add 0.1 ml of 0.1 M NAD
5. Add 0.1 ml of enzyme supernatant diluted the appropriate amount
6. Place the cuvette in the spectrophotometer and record the absorbance at intervals of 15 seconds for 2 minutes at 340 nm using a blank of distilled water treated the same way.

Protein release (Bradford method)

The release of protein from cell disruption is measured using the Bradford Coomassie dye binding protein assay (Sigma-Aldrich product number B6916). This product comes ready to use with no dilution or mixing required.

1. Pipette 100 µl of smaple supernatant into a 2 ml plastic cuvette.
2. Add 1 ml of the Bradford reagent and incubate for 2-5 minutes at room temperature.
3. Read the absorbance at 595 nm after 10 minutes and compare against a blank treated in a similar manner.
4. Produce a calibration curve of the net absorbance against the BSA concentration (Figure A 8).

Bovine serum albium (BSA) is used as the standard with standards made up from 0.2 – 1.0 $mgml^{-1}$ measured against a blank of distilled water.

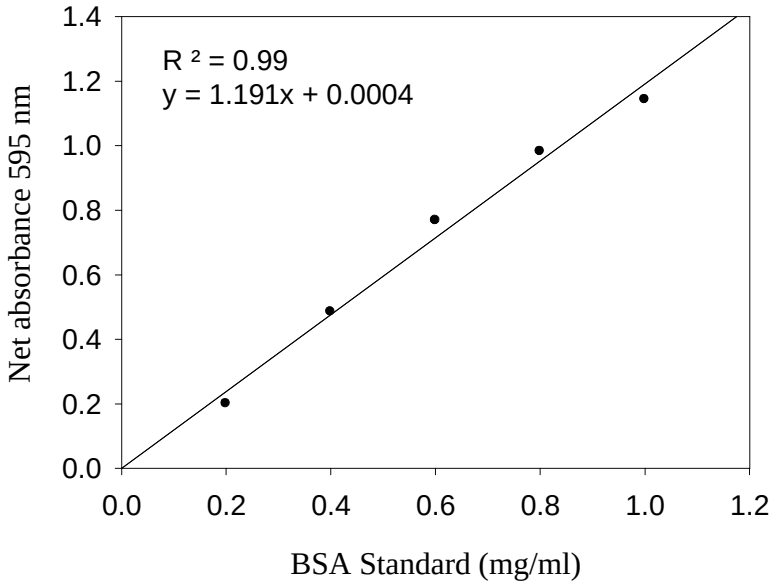

Figure A 8: BSA calibration curve for the Bradford method

Invertase assay

Invertase is a cell wall associated sucrase enzyme that is able to catalyse the breakdown of the disaccharide sucrose to glucose and fructose.

Reagents

0.1 M	Sodium acetate buffer pH 5.5
0.5 M	Sucrose dissolved in water
0.2 M	Potassium di-hydrogen phosphate (KH_2PO_4) in water
DNSA reagent	Dissolve 150 grams of sodium potassium tartrate in 250 ml distilled water. Add 0.5 ml of phenol and 0.5 grams of sodium sulphate. Dissolve 5 gms of 3, 5 di-nitrosalicylic acid in 100 ml of 0.4 M NaOH. Mix the above two solutions and make up to 500 ml with distilled water (Miller G, 1959). Modified from paper

Method

1. Pipette 0.5 ml of sample from the supernatant into a clean test tube
2. Add 1.5 ml of 0.1 M acetate buffer of pH 5.5
3. Add 0.5 ml of 0.5 M sucrose
4. Incubated at 55 ^{o}C for 10 minutes in a water bath.
5. After 10 minutes add 3 ml of 0.2 M KH_2PO_4 to terminate the reaction
6. Place the reaction mixture in boiling water bath for 3 minutes.
7. Pipette out 1 ml of this reaction mixture into another clean test tube
8. Add 1 ml of DNSA reagent and place in a boiling water bath for 10 minutes
9. Remove and add 10 ml of distilled water to the above reaction mixture
10. Read the absorbance at 540 nm against blank (buffer pH 7.0) treated similar to the sample

To determine the levels of cell disruption it is also necessary to generate a calibration curve for a range of glucose concentrations using the DNSA.

Method

1. Prepare a range of glucose standard solutions from 0.01 – 0.05 mM
2. Pipette out 1 ml of each standard solution into a clean test tube
3. Add one ml of DNSA reagent
4. Place the test tubes in a boiling water bath for 10 minutes
5. Add 10 ml of distilled water
6. Read the absorbance at 540 nm against blank (distilled water) treated similar to the sample.

7. Produce a calibration curve of the net absorbance against the glucose concentration (Figure A 9).

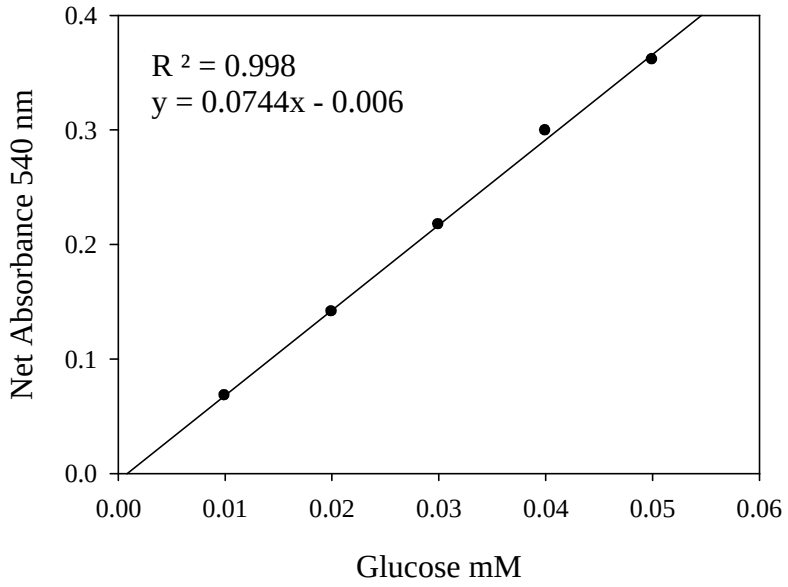

Figure A 9: Glucose calibration curve for the Invertase assay

Appendix 9: Mathematical analysis of TEM images

The cell size and cell wall thickness measured by TEM images did not take into account the random angle at which the cells were cut. The mathematical model used by Smith *et al.* (2000a) was developed by Professor Z Zhang (School of Chemical Engineering, The University of Birmingham). This model used the mean and standard deviation of the measured cell size and cell wall thickness to correct for the random angle at which the cells were cut. The uncorrected and corrected values are shown in Table A 3.9. The model was solved using Mathcad 13 (Mathsoft Inc., Cambridge, MA, USA) and the procedure is shown below.

TEM sectioning cuts cells at a random distance from their centre. Due to this the cell size and cell wall thickness measured directly from TEM is a function of this distance. Figure A 10 shows the geometry for a sphere of uniform thickness that is used in the mathematical model.

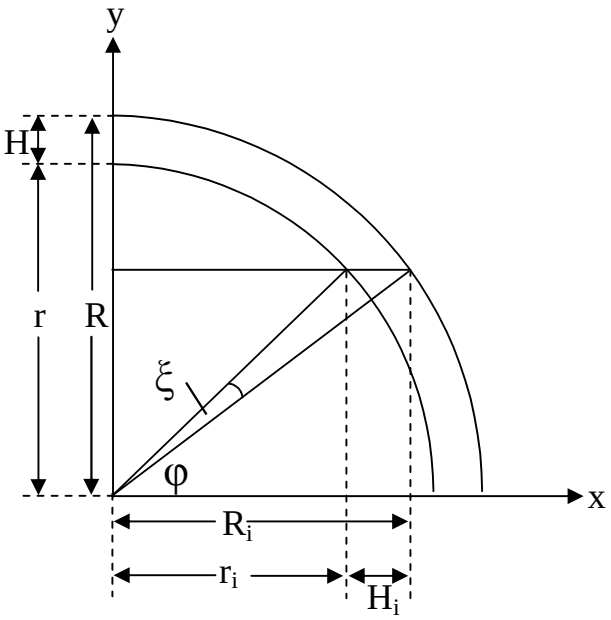

Figure A 10: Definition of geometry for a sphere of uniform thickness used in the mathematical correction for random slicing along the y – axis during TEM sample preparation.

By assuming that the cells are spherical the measured thickness (Hi) can be found using equation A 3.1:

$$H_i = R_i - r_i \quad \ldots \text{(A 3.1)}$$

where R_i is the measured outer radius and r_i is the measured inner radius.

The following relationships are derived from Figure A 10.

$$r_i = r\cos(\xi + \varphi) \quad \ldots \text{(A 3.2)}$$

$$H_i = R^2 + r^2 - 2Rr\cos(\xi) \quad \ldots \text{(A 3.3)}$$

$$r\sin(\xi) = H_i \sin(\varphi) \quad \ldots \text{(A 3.4)}$$

$$R_i = R\cos(\varphi) \quad \ldots \text{(A 3.5)}$$

$$H_i = R_i - r_i \quad \ldots \text{(A 3.6)}$$

$$H = R - r \quad \ldots \text{(A 3.7)}$$

Rearrangement gives the corrected wall thickness H as functions of H_i, R_i and the angle φ.

$$H = \left(\frac{R_i}{\cos(\varphi)}\right) - \sqrt{H_i^2 - \left(\frac{R_i}{\cos(\varphi)}\right)^2 + 2R_i\left(\frac{R_i - H_i\cos^2(\varphi)}{\cos^2(\varphi)}\right)} \quad \ldots \text{(A 3.8)}$$

The mean corrected thickness is then given by solving equation A 3.9.

$$\overline{H} = \int_{-\varphi_{limit}}^{+\varphi_{limit}} \int_{R_{i,min}}^{R_{1,amx}} \int_{H_{i,min}}^{H_{i,max}} H(R_i, H_{i,}\varphi).f_1(R_i).f_2(H_i).f_3(\varphi).dR_i.dH_i.d\varphi \quad \ldots \text{(A 3.9)}$$

where $f_1(R_i)$, $f_2(H_i)$, and $f_3(\varphi)$ are the probability density functions of R_i., H_i and φ respectively. $f_1(R_i)$ and $f_2(H_i)$ are assumed to be normally distributed which means that they can be described by the mean and standard deviation of the measured sizes from TEM image analysis. It is assumed that there is an equal probability of slicing the cells at any angle so $f_3(\varphi)=1/\pi$.

The mean corrected outer radius is calculated using equation A 3.10.

$$\overline{R} = \frac{\pi}{2}\left(\overline{R}_i - \overline{H}_i\right) + \overline{H} \qquad \ldots \text{(A 3.10)}$$

The limits of the integration were taken to be mean ± 4 standard deviations for Ri and Hi.

The results produced by this procedure are shown below in Table A 3.9.

	R_i	H_i	$\overline{R}$	$\overline{H}$	τ
Mean	1.65 µm	150 nm	2.447 µm	91 nm	0.037
Standard deviation	0.6 µm	0.35 nm	–	–	± 0.001

Table A 3.9: Results for the measured and corrected cell size and cell wall thickness.

Mathcad worksheet

$Ri := 1.65$ $\sigma Ri := 0.60$ $Rmean := Ri$

$Rimin := Ri - 4 \cdot \sigma Ri$ $Rimin = -0.75$

$Rimax := Ri + 4 \cdot \sigma Ri$ $Rimax = 4.05$

$$f1(Ri) := \frac{1}{\sigma Ri \cdot \sqrt{2 \cdot \pi}} e^{\frac{-(Ri - Rmean)^2}{2 \cdot \sigma Ri^2}}$$

$Hi := 0.150$ $\sigma Hi := 0.35$ $Hmean := Hi$

$Himin := Hi - 4 \cdot \sigma Hi$ $Himin = -1.25$

$Himax := Hi + 4 \cdot \sigma Hi$ $Himax = 1.55$

$$f2(Hi) := \frac{1}{\sigma Hi \cdot \sqrt{2 \cdot \pi}} e^{\frac{-(Hi - Hmean)^2}{2 \cdot \sigma Hi^2}}$$

$$\phi := \frac{\pi}{2.421} \qquad f3(\phi) := \frac{1}{\pi}$$

$$H(Ri, Hi, \phi) := \frac{Ri}{\cos(\phi)} - \sqrt{Hi^2 - \left(\frac{Ri}{\cos(\phi)}\right)^2 + 2 \cdot Ri \cdot \left(\frac{Ri - Hi \cdot \cos(\phi)^2}{\cos(\phi)^2}\right)}$$

$$Hav := \int_{-\phi}^{\phi} \int_{Rimin}^{Rimax} \int_{Himin}^{Himax} H(Ri, Hi, \phi) \cdot f1(Rr) \cdot f2(Hr) \cdot f3(\phi)\, dHr\, dRr\, d\phi \qquad Hav = 0.091$$

$Rav := \frac{\pi}{2} \cdot (Ri - Hi) + Hav$ $Rav = 2.447$

$\phi limit := \operatorname{asin}\left(\frac{Rav - Hav}{Rav}\right)$ $\phi limit = 1.298$ $\phi = 1.298$

$adeg := \frac{180}{\pi} \cdot \phi$ $adeg = 74.349$

$Dcorrected := Rav \cdot 2$ $Hcorrected := Hav$ $tau := \frac{Hcorrected}{\frac{Dcorrected}{2}}$

$Dcorrected = 4.894$ $Hcorrected = 0.091$ $tau = 0.037$

Appendix 10: Derivation of the governing equations

This Appendix will show the derivation of the governing equations given in Chapter 5 that are used in the material model to control the geometry of the cell during compression. Initially in Part a) the correct governing equations defined by Wang *et al.* (2004) are derived in full. This is done as in the published literature the steps used to derive these relationships are often obscure and difficult to follow. So while some of this work may seem basic it can generally be used by workers without knowledge of its origin.

Following this the original derivation of the governing equations by Feng and Yang (1970) will be shown and the errors highlighted. This process was performed as Feng and Yang (1970) do not explicitly state the governing equations that are used. Finally any other errors in the literature concerning the governing equations will be described.

Part a) Derivation of relationships given by Wang et al. (2004)

Membrane boundary assumptions

Membrane

It is assumed that the cell wall behaves as a structural membrane (N.B. not biological membrane). This means that the wall material only supports in-plane normal stress. This membrane structure does not allow for bending moments or shear between membrane layers. It is possible to ignore these factors only when the material is very thin.

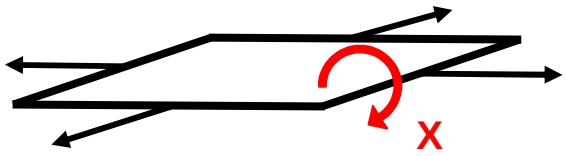

Figure A 11: Thin walled membrane with no bending moments.

Stress

Stress is a measure of the applied force exerted per unit area that strains or deforms a body depending on the internal resistance of the material. Stress can be described as the force applied per unit area with units Nm^{-2}. During compression testing pressure is developed inside the cell. Pressure is a normal stress which acts perpendicular to the surface. When the membrane is stretched there are stresses normal to the membrane edge. For structural membranes, as the membrane is assumed to be thin, these are often expressed as tensions (Figure A 12).

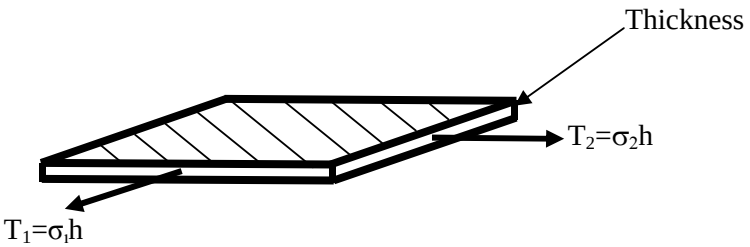

Figure A 12: Thin walled membrane with tension within the wall.

Model assumptions

There are a number of assumptions within the model that need to be satisfied for this approach to be applicable.

1. A spherical membrane is compressed between two parallel rigid platens of infinite size with frictionless contact (Figure A 13).

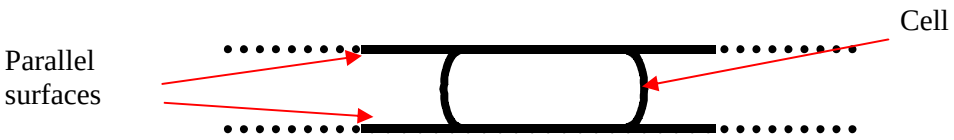

Figure A 13: Cell compressed between two parallel plates.

2. The profile of the deformed particle (Figure A 14a) between the two platens is symmetrical across the equatorial plane allowing the particle to be fully characterised with just the positive η axis (Figure A 14b). The particle is axisymmetrical about the η-axis allowing it to be represented fully by a curve in a 2-D plane (Figure A 14c).

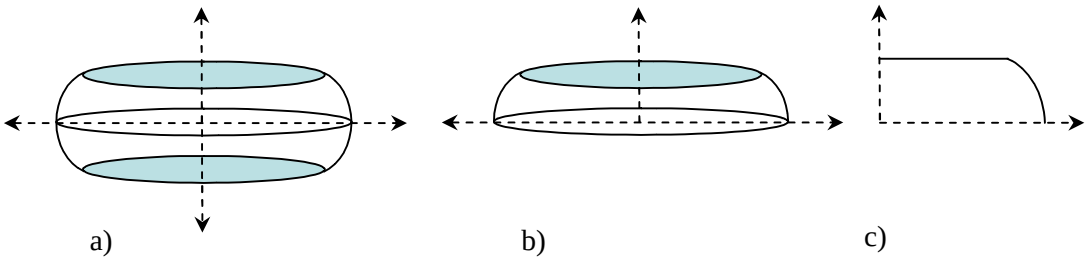

Figure A 14: a) deformed particle between two platens; b) positive η axis; c) axisymmetry.

3. Sphere filled with incompressible fluid.

4. Sphere is initially inflated by a uniform internal pressure.

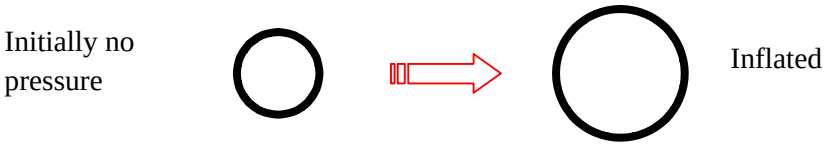

Figure A 15: Inflated cell

5. Membrane is: Homogeneous (uniform composition)

Isotropic (material properties do not depend on direction)

Uniform thickness

6. Membrane material properties are time independent (i.e. negligible viscoelasticity)

7. The deformation is reversible and isothermal.

Model formulation

Due to the axisymmetric representation of the compressed particle the stresses can be represented by two directions – the meridian (subscript 1) and circumferential (subscript 2). The meridian direction is described as any vertical plane which intersects the poles and is parallel to the η-axis. The circumferential direction is described as any horizontal plane that is parallel to the ρ-axis (Figure A 16).

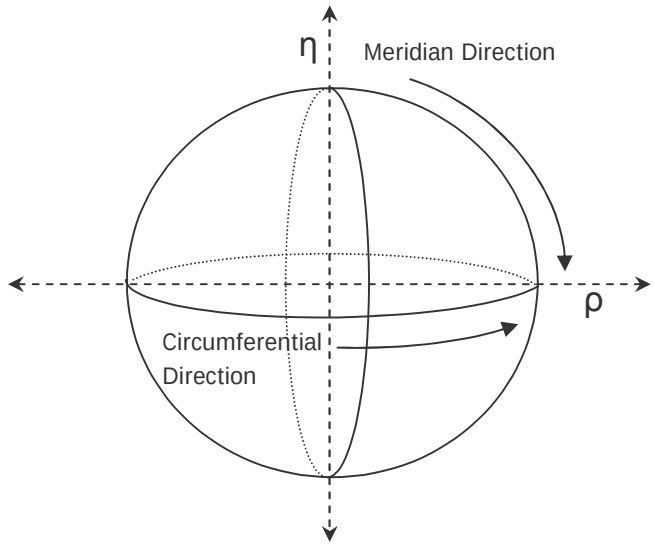

Figure A 16: Meridian and circumferential directions

Initial Geometry

The membrane is inflated by the initial pressure P to change the radius of the sphere from r_o (uninflated radius) to r_i (inflated radius). The internal pressure is always above or equal to the external pressure, and P is expressed against the external pressure (i.e. it is at gauge pressure).

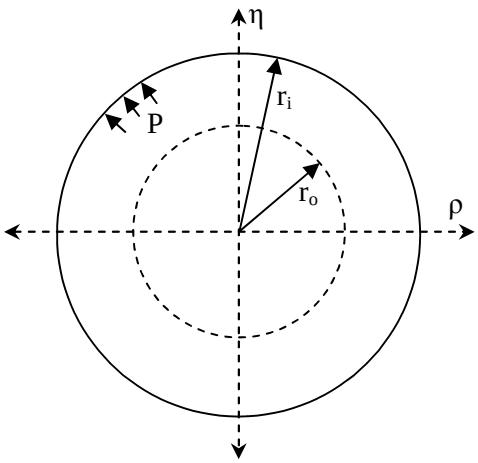

Figure A 17: Initials geometry of the cell

Compression

The parallel plates compress the spherical membrane along the η axis and this compression causes an extension of the particle in the ρ axis. Each of the plates exerts an equal pressure over the contact area.

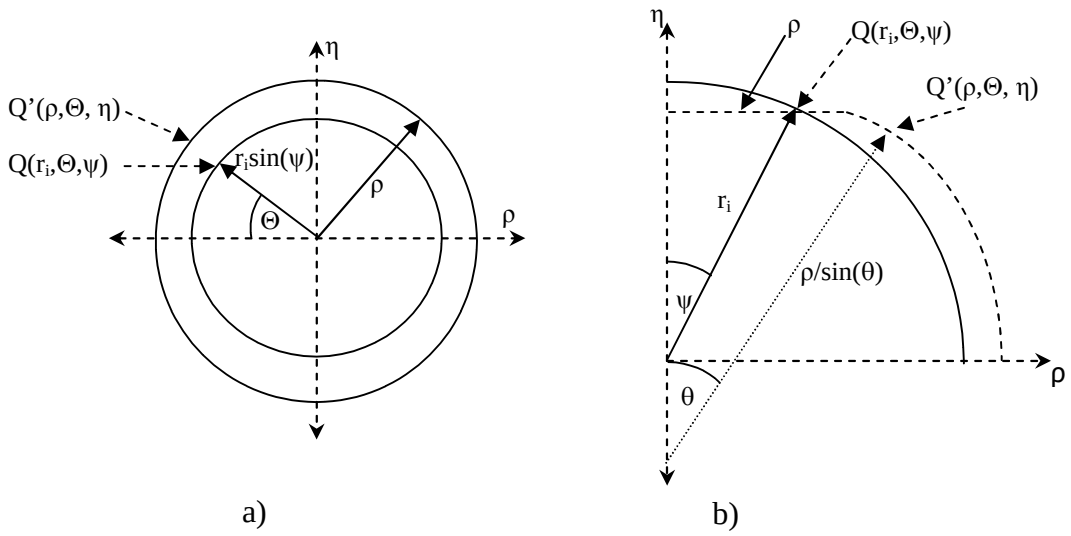

Figure A 18: a) top view; b) side view. ρ = horizontal coordinate, η = vertical coordinate, r_i = inflated radius of the cell θ = angle between the normal to the surface at Q' and the η axis following compression,Θ = angle of rotation in the circumferential direction, ψ = angle between the normal to the surface at Q and the η axis prior to compression.

Figure A 18a and b show that the compression of the particle between the plates causes the radius to increase from $r_i\sin(\psi)$ to ρ. Point Q with coordinates (r_i,Θ,ψ) is a position on the cell surface prior to compression, point Q' with coordinates (ρ,Θ, η) is the point following compression.

Contact and non-contact region

The compression analysis requires two regions within the cell membrane to be considered, the contact and non-contact regions. The contact area is taken to be the part of the cell wall that is in contact with the compression surfaces.

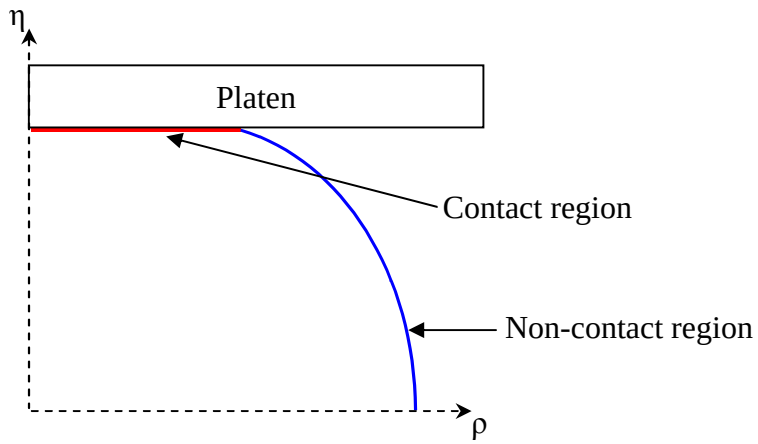

Figure A 19: Figure showing the contact and non – contact regions.

Equilibrium equations

The equilibrium equations link the tensions in the wall to the local shape of the membrane in both the contact and non-contact regions. It is assumed that there are no external forces acting tangentially to the membrane

Derivation of forces normal to the element

The equilibrium equations link the tensions in the wall to the local shape of the membrane.

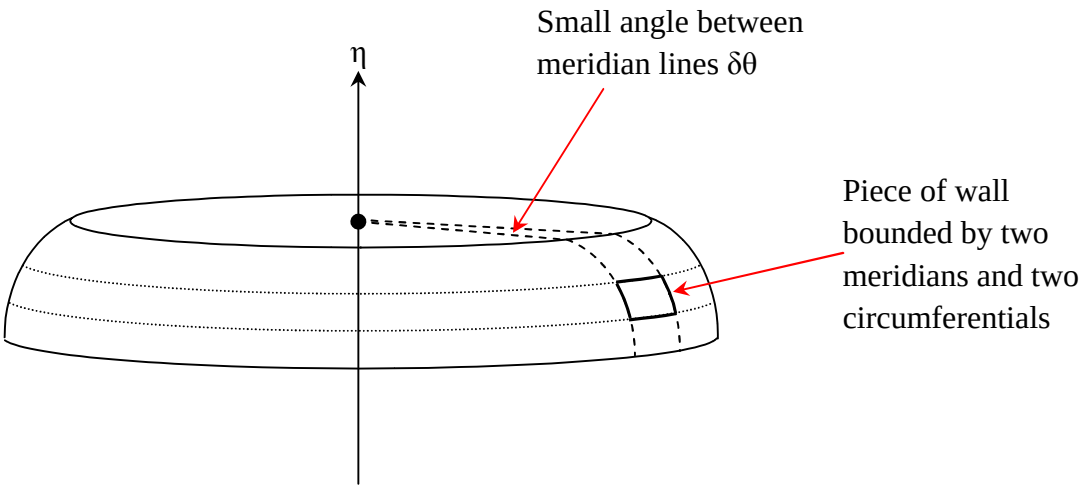

Figure A 20: Identifying an element of the wall in a deformed cell

Geometry of the element

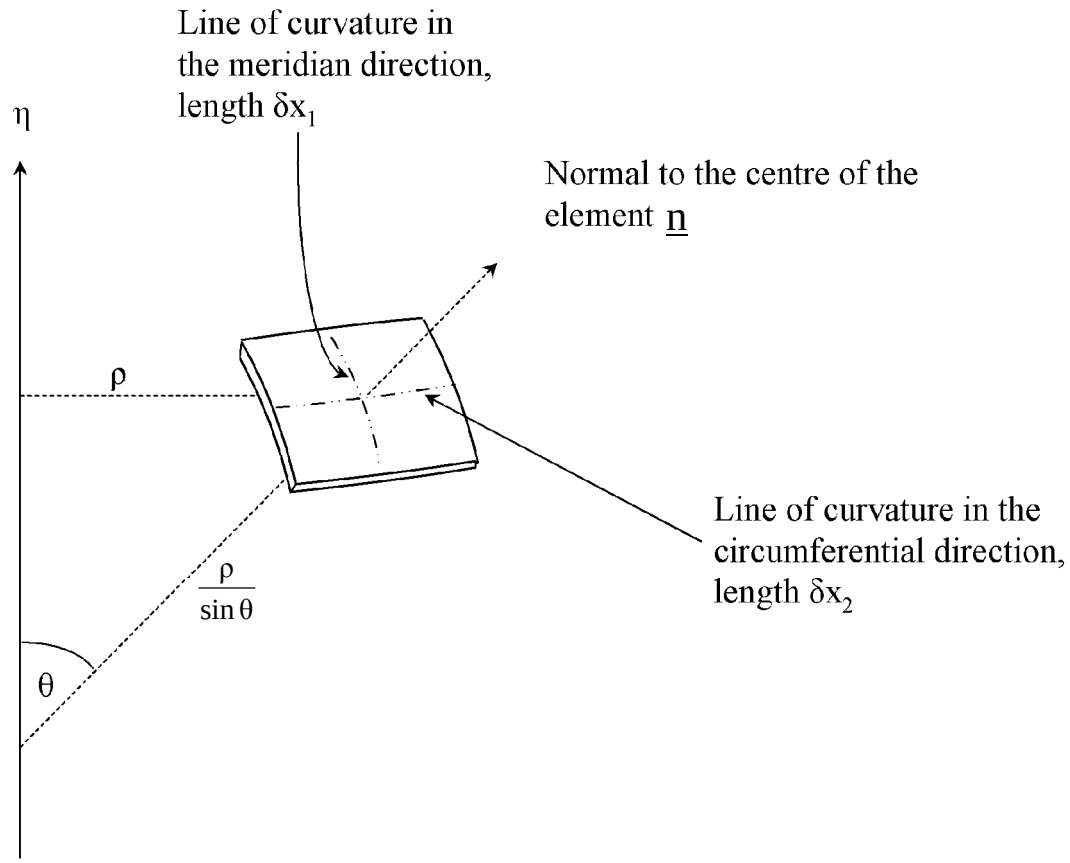

Figure A 21: Wall element

Because of symmetry, curvature in the circumferential direction is given by:

$$\kappa_2 = \frac{\sin\theta}{\rho}$$

So the distance from the centre of curvature to the centre of the element is $\frac{\rho}{\sin\theta}$

The curvature in the meridian direction is:

$\kappa_1 = \frac{d\theta}{dS}$ where S is the length of the wall element in the meridian direction.

Let the distance across the element in the circumferential direction be δx_2, and in the meridian direction be δx_1. The element is not quite rectangular nor flat, which affects the equilibrium relationships for forces acting on it.

Let the tensions in the meridian and circumferential direction be T_1 and T_2 respectively. As these are tensions, the corresponding forces are found by multiplying by the edge lengths. The pressure is a normal force acting outwards. As T_1 and T_2 are principal tensions, there are no shear stresses acting on the element edges.

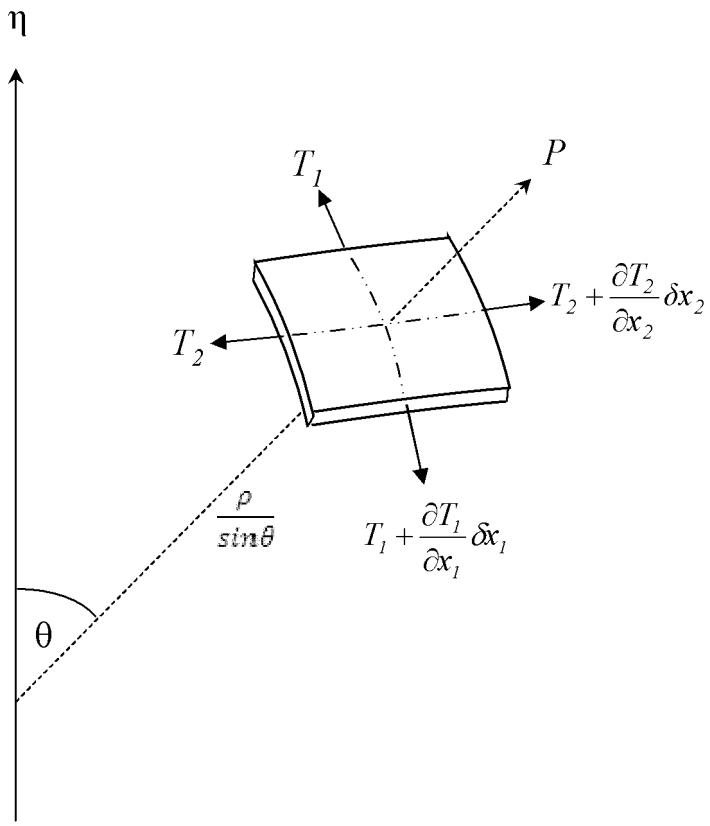

Figure A 22: Tensions acting on the wall element. δx_1 = line of curvature in the meridian direction, δx_2 = line of curvature in the circumferential direction, T_1 = tension in the meridian direction, T_2 = tension in the circumferential direction.

A side view of the wall element along a circumferential line is used to derive the equilibrium equations.

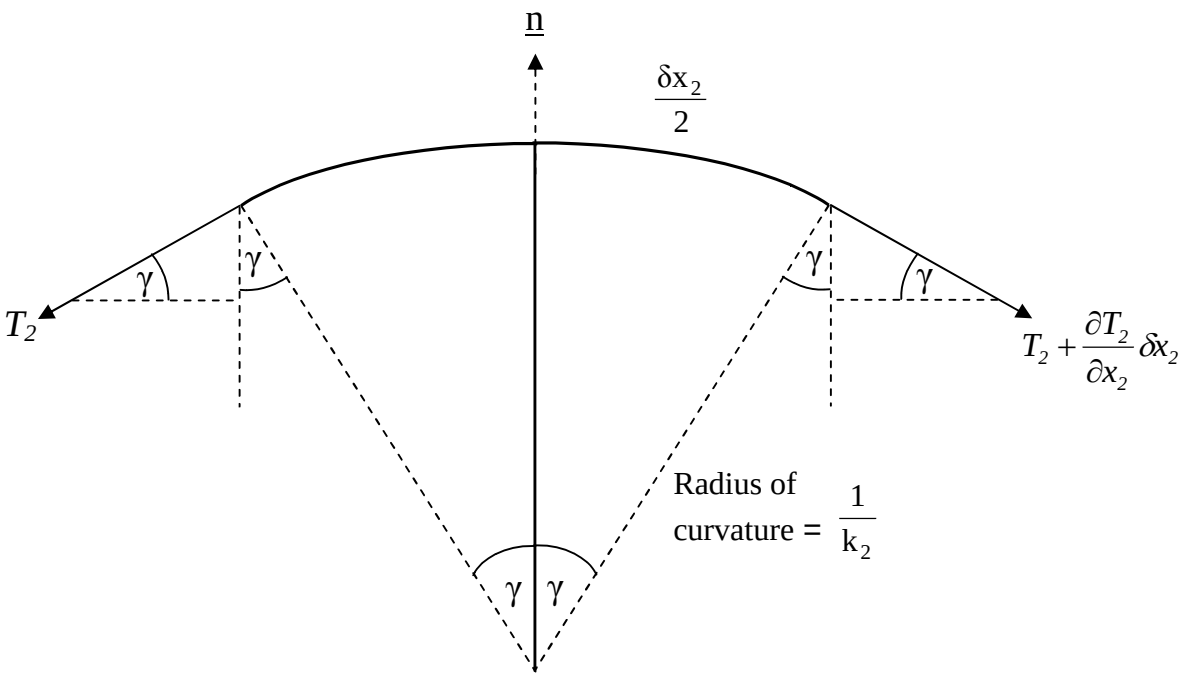

Figure A 23: Side view in the latitudinal direction. γ = half the angle subtended by the edge of the centre of curvature.

γ is the half angle subtended by the edge at the centre of curvature. The tensions have a normal component and assuming γ is a small angle it is given by:

$$\frac{\gamma}{\kappa_2} \approx \frac{\delta x_2}{2} \qquad \text{so,} \qquad \gamma \approx \frac{\delta x_2 \kappa_2}{2} \qquad \ldots \text{(A 5.1)}$$

The tension T_2 acts on an edge of the length δx_1, so the normal force due to the circumferential tensions is:

$$T_2 \frac{\delta x_2 \kappa_2}{2} \delta x_1 + \left(T_2 + \frac{\partial T_2}{\partial x_2} \delta x_2 \right) \frac{\delta x_2 \kappa_2}{2} \delta x_1 \approx \kappa_2 T_2 \delta x_2 \delta x_1 \qquad \ldots \text{(A 5.2)}$$

Second order terms are ignored here.

By a similar argument the normal component of the meridian force is $K_1 T_1 \delta x_2 \delta x_1$. P acts along the normal $\underline{n}$ and the area of the element upon which P acts is $\delta x_1 \, \delta x_2$.

So the force balance becomes:

$$\kappa_1 T_1 \delta x_1 \delta x_2 + \kappa_2 T_2 \delta x_1 \delta x_2 = P \delta x_1 \delta x_2 \quad \ldots \text{(A 5.3)}$$

$$\text{So, } \kappa_1 T_1 + \kappa_2 T_2 = P \quad \ldots \text{(A 5.4)}$$

Derivation of the forces in the plane to the element

Now consider the forces in a plane with normal also $\underline{n}$. The element can be projected out of the plane and it will not be rectangular as the edges in the meridian direction are not parallel. It should also be noted that the projection of this element is flat.

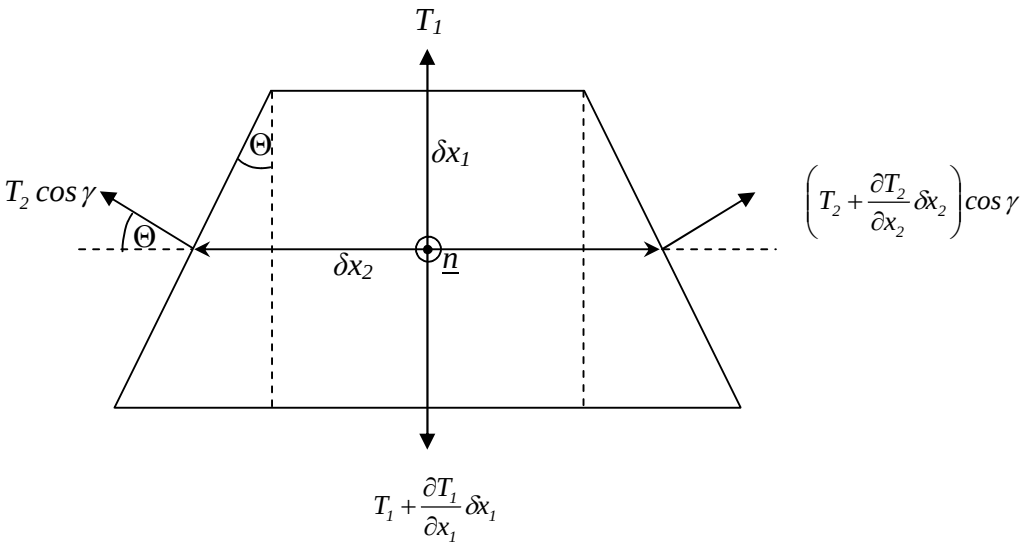

Figure A 24: In plane wall element

By using the series definitions of cos, the component of T_2 in this plane is:

$$T_2 \cos\gamma \approx T_2\left(1-\frac{\gamma^2}{2}\right) \qquad \text{where} \quad \gamma = \kappa_2 \frac{\delta x_2}{2} \qquad \ldots \text{(A 5.5)}$$

γ^2 is a second order term, so the tensions can actually be taken as T_2 and $\left(T_2 + \frac{\partial T_2}{\partial x_2}\delta x_2\right)$.

However, they are not aligned along the x_1 direction because of the edges not being parallel.

The angle $\Theta = \frac{1}{2}\frac{\partial(\delta x_2)}{\partial x_1}$ so the component of T_2 in the x_1 direction is

$T_2 \sin\Theta \approx T_2\Theta = \frac{T_2}{2}\frac{\partial(\delta x_2)}{\partial x_1}$.

The corresponding force is $\left(\frac{T_2}{2}\frac{\partial(\delta x_2)}{\partial x_1}\partial x_1\right)$

For the tension $\left(T_2 + \frac{\partial T_2}{\partial x_2}\delta x_2\right)$ the corresponding force will also be $\left(\frac{T_2}{2}\frac{\partial(\delta x_2)}{\partial x_1}\partial x_1\right)$ as second order terms are ignored.

Considering the force balances, the forces in the circumferential direction will balance as $\delta x_2 \rightarrow 0$.

For the balance in the meridian direction, we need to consider all the edges.

The length of the top edge is approximately $\left(\delta x_2 - \frac{\delta x_1}{2} \frac{\partial(\delta x_2)}{\partial x_1} \right)$. The force is therefore $T_1 \left(\delta x_2 - \frac{1}{2} \frac{\partial(\delta x_2)}{\partial x_1} \delta x_1 \right)$.

The force on the bottom edge is:

$$\left(T_1 + \frac{\partial T_1}{\partial x_1} \delta x_1 \right) \left(\delta x_2 + \frac{1}{2} \frac{\partial(\delta x_2)}{\partial x_1} \delta x_1 \right) \quad \ldots \text{(A 5.6)}$$

From previously, the force in the x_1 direction from the edges delineated by the meridians is

$$T_2 \frac{\partial(\delta x_2)}{\partial x_1} \partial x_1 . \quad \ldots \text{(A 5.7)}$$

Assuming no external forces tangential to the membrane a force balance gives:

$$T_1 \left(\delta x_2 - \frac{1}{2} \frac{\partial(\delta x_2)}{\partial x_1} \delta x_1 \right) + \left(T_2 \frac{\partial(\delta x_2)}{\partial x_1} \partial x_1 \right) = \left(T_1 + \frac{\partial T_1}{\partial x_1} \delta x_1 \right) \left(\delta x_2 + \frac{1}{2} \frac{\partial(\delta x_2)}{\partial x_1} \delta x_1 \right) \quad \ldots \text{(A 5.8)}$$

Hence

$$\begin{aligned} & T_1 \delta x_2 - \frac{T_1}{2} \frac{\partial(\delta x_2)}{\partial x_1} \delta x_1 + T_2 \frac{\partial(\delta x_2)}{\partial x_1} \partial x_1 = \ldots \\ & T_1 \delta x_2 + \frac{T_1}{2} \frac{\partial(\delta x_2)}{\partial x_1} \delta x_1 + \frac{\partial T_1}{\partial x_1} \delta x_1 \delta x_2 + \frac{1}{2} \frac{\partial T_1}{\partial x_1} \frac{\partial(\delta x_2)}{\partial x_1} \delta x_1 \delta x_1 \end{aligned} \quad \ldots \text{(A 5.9)}$$

Rearranging gives:

$$(T_2 - T_1)\frac{\partial(\delta x_2)}{\partial x_1} = \frac{\partial T_1}{\partial x_1}\delta x_2 + \frac{1}{2}\frac{\partial T_1}{\partial x_1}\frac{\partial(\delta x_2)}{\partial x_1}\delta x_1 \qquad \ldots \text{(A 5.10)}$$

$$(T_2 - T_1)\frac{\partial(\delta x_2)}{\partial x_1} = \frac{\partial T_1}{\partial x_1}\left(\delta x_2 + \frac{1}{2}\frac{\partial(\delta x_2)}{\partial x_1}\delta x_1\right) \qquad \ldots \text{(A 5.11)}$$

Now as $\delta x_2 = \rho\delta\Theta$, so:

$$(T_2 - T_1)\frac{\partial \rho}{\partial x_1}\delta\Theta = \frac{\partial T_1}{\partial x_1}\left(\rho\delta\Theta + \frac{1}{2}\frac{\partial \rho}{\partial x_1}\delta\Theta\delta x_1\right) \qquad \ldots \text{(A 5.12)}$$

So by cancelling second order terms and $\delta\Theta$ gives:

$$(T_2 - T_1)\frac{\partial \rho}{\partial x_1} = \rho\frac{\partial T_1}{\partial x_1} \qquad \ldots \text{(A 5.13)}$$

Also, it should be noted that ρ does not depend on x_2 so $\frac{\partial \rho}{\partial x_1} = \frac{d\rho}{dx_1}$ and T_1 does not depend on x_2

so

$$\frac{\partial T_1}{\partial x_1} = \frac{dT_1}{dx_1} \qquad \ldots \text{(A 5.14)}$$

Hence:

$$\left(T_2 - T_1\right)\frac{d\rho}{dx_1} = \rho\frac{dT_1}{dx_1} \quad \ldots \text{(A 5.15)}$$

Hence:

$$\frac{1}{\rho}\left(T_2 - T_1\right) = \frac{dT_1}{d\rho} \quad \ldots \text{(A 5.16)}$$

$$\frac{dT_1}{d\rho} + \frac{1}{\rho}\left(T_1 - T_2\right) = 0 \quad \ldots \text{(A 5.17)}$$

This equation needs modifying to allow the tensions in the wall to be related to the stretch ratios in the meridian and circumferential direction as well the angle ψ:

$$\frac{dT_1}{d\psi}\frac{d\psi}{d\rho} + \frac{1}{\rho}\left(T_1 - T_2\right) = 0 \quad \ldots \text{(A 5.18)}$$

$$\frac{dT_1}{d\psi} = \frac{\rho'}{\rho}\left(T_2 - T_1\right) \quad \ldots \text{(A 5.19)}$$

where the prime represents a derivative with respect to ψ.

The tension T_1 will depend on both the stretch ratios so:

$$\frac{\partial T_1}{\partial \lambda_1}\frac{\partial \lambda_1}{\partial \psi} + \frac{\partial T_1}{\partial \lambda_2}\frac{\partial \lambda_2}{\partial \psi} = \frac{\rho'}{\rho}\left(T_2 - T_1\right) \quad \ldots \text{(A 5.20)}$$

Summary of the equilibrium equations

$$\frac{\partial T_1}{\partial \lambda_1}\frac{\partial \lambda_1}{\partial \psi} + \frac{\partial T_1}{\partial \lambda_2}\frac{\partial \lambda_2}{\partial \psi} = \frac{\rho'}{\rho}\left(T_2 - T_1\right) \qquad \ldots \text{(A 5.21)}$$

$$\kappa_1 T_1 + \kappa_2 T_2 = P \qquad \ldots \text{(A 5.22)}$$

where T_1 and T_2 are the meridian and circumferential tensions, κ_1 and κ_2 are the corresponding principal curvatures, and P is the normal force per unit area, here the internal pressure.

Stretch ratio derivations

During compression the membrane is stretched causing strains within the wall. These strains are represented by stretch ratios (λ). Stretch ratios represent the relative changes in the length of the membrane in the meridian and circumferential directions. The meridian stretch ratio (λ_1) is the length of an infinitesimal length ds in the meridian direction compared to its inflated and deformed length dS. The circumferential stretch ratio (λ_2) is:

$$\lambda_2 = \frac{\rho}{r_o \sin\psi}$$

were r_o is the initial radius, and ρ is the inflated and deformed radius.

Derivation of λ_1

Consider a small element on the surface of the membrane of length δs which is deformed to δS after the membrane is inflated and deformed.

The meridian stretch ratio (λ_1) is the length of an infinitesimal length ds in the meridian direction compared to its inflated and deformed length dS.

An approximation of the stretch in the meridian direction is:

$$\lambda_1 \approx \frac{\delta S}{\delta s} \qquad \ldots \text{(A 5.23)}$$

As δs $\rightarrow$ 0:

$$\lambda_1 = \frac{dS}{ds} \qquad \ldots \text{(A 5.24)}$$

By using the chain rule for derivatives:

$$\frac{dS}{ds} = \frac{\left(\frac{dS}{d\psi}\right)}{\left(\frac{ds}{d\psi}\right)} \qquad \ldots \text{(A 5.25)}$$

Therefore it is necessary to determine $\frac{dS}{d\psi}$ and $\frac{ds}{d\psi}$ in terms of the coordinates ρ and η of the boundary.

Initial membrane length δs

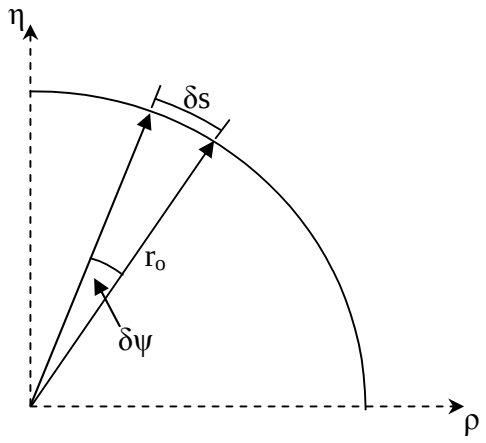

Figure A 25: Initial uninflated membrane

From figure A 25 it can be seen that δs subtends the angle δψ and the radius of the sphere is r_o.

Therefore:

$$\delta s = r_o \delta \psi$$

$$\frac{\delta s}{\delta \psi} = r_o \qquad \ldots \text{(A 5.26)}$$

As the length δs tends to zero so δψ also tends to zero giving:

$$\frac{ds}{d\psi} = r_o \qquad \ldots \text{(A 5.27)}$$

Following inflation of the membrane and deformation the element δs is deformed to δS.

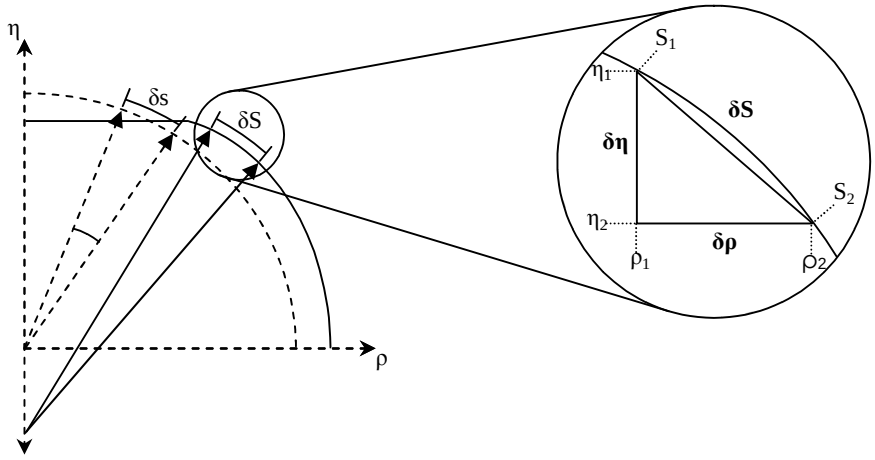

Figure A 26: Meridian stretch ratio (λ_1)

In Figure A 26 the ends of the deformed element δS is represented on the membrane surface by the coordinates S_1 (ρ_1,η_1) and S_2 (ρ_2, η_2). From this the horizontal distance between points S_1 and S_2 is given by the distance δρ and the vertical distance is defined as δη. Using Pythagoras theorem it can be seen that:

$$\delta S^2 \approx \delta \rho^2 + \delta \eta^2$$

Dividing by $\delta\psi^2$ gives:

$$\left(\frac{\delta S}{\delta\psi}\right)^2 \approx \left(\frac{\delta\rho}{\delta\psi}\right)^2 + \left(\frac{\delta\eta}{\delta\psi}\right)^2 \quad \ldots \text{(A 5.28)}$$

Again as the arc length δS tends to zero so $\frac{\delta S}{\delta\psi} \to \frac{dS}{d\psi}, \frac{\delta\rho}{\delta\psi} \to \frac{d\rho}{d\psi}, \frac{\delta\eta}{\delta\psi} \to \frac{d\eta}{d\psi}$.

$$\frac{dS}{d\psi} = \sqrt{\left(\frac{d\rho}{d\psi}\right)^2 + \left(\frac{d\eta}{d\psi}\right)^2} \quad \ldots \text{(A 5.29)}$$

$$Let\ \rho' = \frac{d\rho}{d\psi}\ and\ \eta' = \frac{d\eta}{d\psi}$$

$$Then\ \frac{dS}{d\psi} = \left(\rho'^2 + \eta'^2\right)^{\frac{1}{2}} \quad \ldots \text{(A 5.30)}$$

This equation links changes of membrane length S to the coordinates ρ and η (all 3 as derivatives with respect to ψ).

Substituting equation's A 5.30 and A 5.27 in to equation A 5.24 leads to:

$$\lambda_1 = \frac{dS}{ds} = \frac{\sqrt{\left(\rho'^2 + \eta'^2\right)}}{r_0} \quad \ldots \text{(A 5.31)}$$

Derivation of λ_2

The circumferential stretch ratio (λ_2) is defined as the ratio of the radius of the inflated and deformed membrane to that of the initial uninflated membrane.

Initial radius $= r_o \sin\psi$

Inflated and deformed radius $= \rho$

So $\lambda_2 = \dfrac{\rho}{r_o \sin\psi}$ . . . (A 5.32)

Principal curvature derivations

Principal curvatures are the angular equivalent of the stretch ratios and are measures of how much a line curves in the principal direction. In a circle the curvature is equal to the reciprocal of the radius, and the curvature at the point on a more general curve is the reciprocal of the radius of the osculating circle. A surface has curvatures in two directions, in this case taken as the principal directions. κ_1 is the principle curvature in the meridian direction and is the rate of change of length around a meridian with change of the angle of the normal (to the surface) to the η axis.

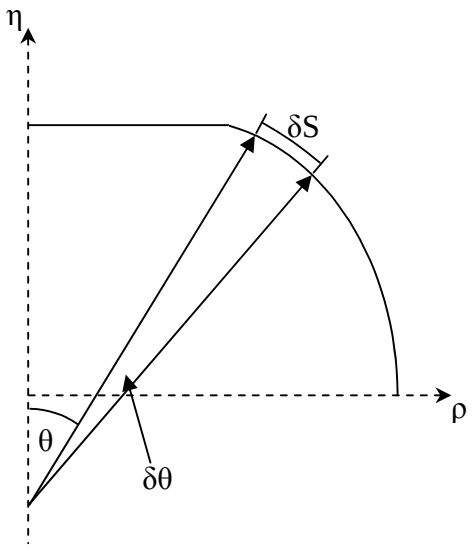

Figure A 27: Meridian curvature

Where θ is the angle measured in the clockwise direction from the vertical axis of symmetry to the small element of interest along the line of the normal.

$$\delta S = \frac{\delta\theta}{\kappa_1} \qquad \text{i.e. } \kappa_1 \approx \frac{\delta\theta}{\delta S} \qquad \ldots \text{(A 5.33)}$$

As δS tends towards zero so $\kappa_1 \rightarrow \frac{d\theta}{dS}$ . . . (A 5.34)

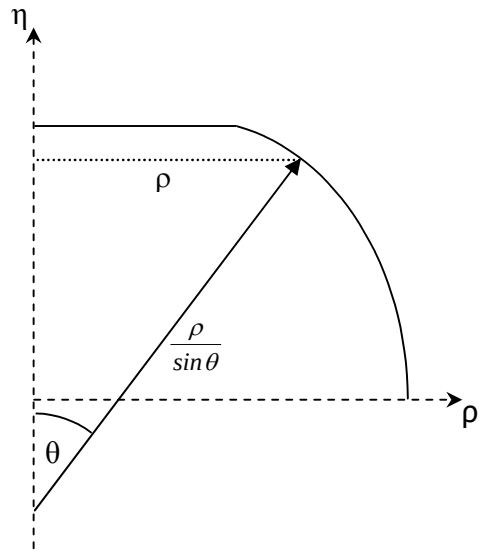

Figure A 28: Circumferential curvature

For the circumferential direction, the distance from the η axis to the surface along a normal is a constant for a given θ. As can be seen in Figure A 28, this distance is $\frac{\rho}{\sin\theta}$. Hence:

$$\kappa_2 = \frac{\sin\theta}{\rho} \qquad \ldots \text{(A 5.35)}$$

However for further analysis we need to find κ_i in terms of the stretch ratios (λ_1, λ_2) and the angle ψ. To be able to do this firstly we need to define κ_1 with respect to η and ρ and not θ.

By the chain rule:

$$\kappa_1 = \frac{d\theta}{dS} = \frac{d\theta}{d\psi} \cdot \frac{d\psi}{dS} \qquad \ldots \text{(A 5.36)}$$

We already know $\frac{d\psi}{dS}$ from deriving the stretch ratio, so now need to derive an expression for $\frac{d\theta}{d\psi}$.

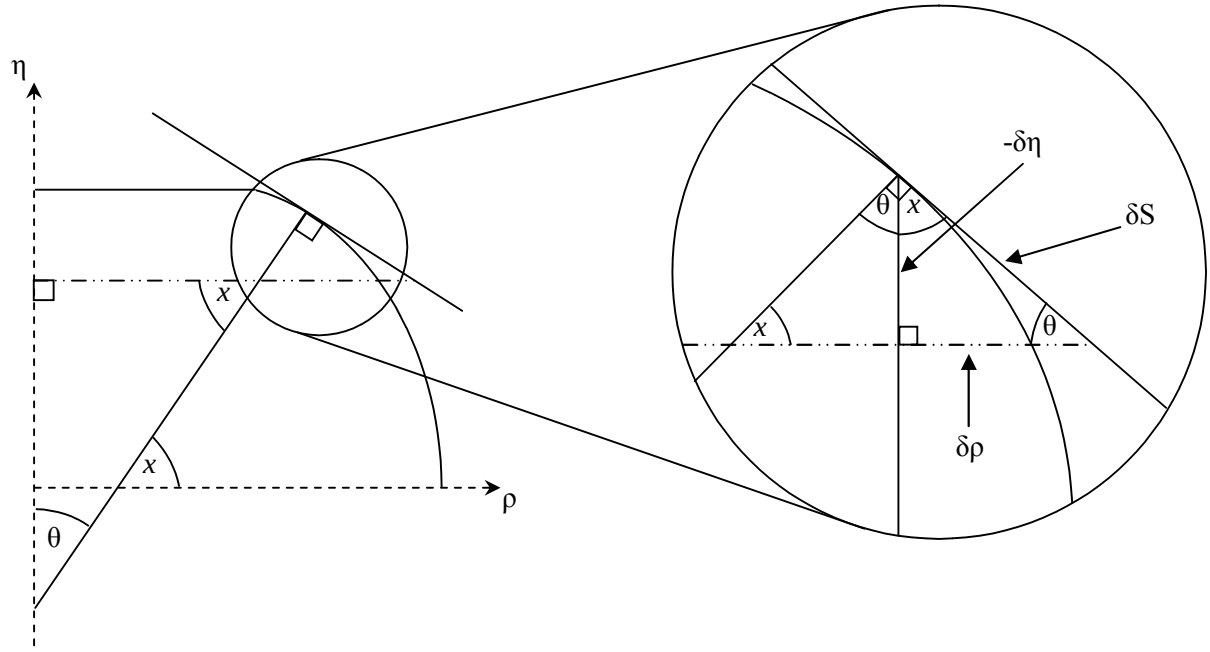

Figure A 29: Trigonometric relationship between angle θ and the deformed surface dS

Using the standard trigonometric relationships from Figure A 29 taking the limits as δS →0, it can be seen that the angle θ is related to the deformed surface by:

$$\cos\theta = \frac{d\rho}{dS} \qquad \sin\theta = -\frac{d\eta}{dS} \qquad \tan\theta = -\frac{d\eta}{d\rho} \qquad \ldots \text{(A 5.37)}$$

As $$\tan\theta = \frac{\sin\theta}{\cos\theta} = \frac{-d\eta/dS}{d\rho/dS} \qquad \ldots \text{(A 5.38)}$$

Substitute in $dS = \left(\rho'^2 + \eta'^2\right)^{\frac{1}{2}} d\psi$ . . . (A 5.30)

So $tan\theta = \dfrac{-d\eta / dS}{d\rho / dS} = \dfrac{-d\eta / \left(\rho'^2 + \eta'^2\right)^{\frac{1}{2}} d\psi}{d\rho / \left(\rho'^2 + \eta'^2\right)^{\frac{1}{2}} d\psi} = \dfrac{-d\eta / d\psi}{d\rho / d\psi} = -\dfrac{\eta'}{\rho'}$ . . . (A 5.39)

By applying the quotient rule:

$$\frac{d(tan\theta)}{d\psi} = \frac{d\left(-\eta'/\rho'\right)}{d\psi} = \frac{-\eta''\rho' + \eta'\rho''}{\rho'^2} \qquad \text{. . . (A 5.40)}$$

Using the basic trigonometric relationships and the chain rule:

$$\frac{d(tan\theta)}{d\psi} = sec^2\theta \cdot \frac{d\theta}{d\psi} \qquad \text{. . . (A 5.41)}$$

As $sec^2\theta = \left(1 + tan^2\theta\right)$ . . . (A 5.42)

$$\frac{d(\tan\theta)}{d\psi} = \left(1 + \tan^2\theta\right) \cdot \frac{d\theta}{d\psi}$$

Using $\tan^2\theta = \left(-\dfrac{\eta'}{\rho'}\right)^2 = \dfrac{\eta'^2}{\rho'^2}$

$$= \left(1 + \frac{\eta'^2}{\rho'^2}\right) \cdot \frac{d\theta}{d\psi}$$

$$= \left(\frac{\rho'^2 + \eta'^2}{\rho'^2}\right) \cdot \frac{d\theta}{d\psi} \qquad \text{. . . (A 5.43)}$$

From this equation A 5.40 becomes:

$$\left(\frac{\rho'^2+\eta'^2}{\rho'^2}\right)\cdot\frac{d\theta}{d\psi}=\frac{-\eta''\rho'+\eta'\rho''}{\rho'^2} \qquad \ldots \text{(A 5.44)}$$

Rearranging this leads to:

$$\frac{d\theta}{d\psi}=\frac{-\eta''\rho'+\eta'\rho''}{\rho'^2+\eta'^2} \qquad \ldots \text{(A 5.45)}$$

This equation tells us how the angle of the normal to the compressed membrane θ changes with the uninflated angle ψ, using the membrane coordinates.

Substituting equation A 5.30 and A 5.45 into equation A 5.34:

$$\kappa_1=\frac{\mathrm{d}\theta}{\mathrm{dS}}$$
$$=\frac{d\theta}{d\psi}\cdot\frac{d\psi}{dS}$$

$$\kappa_1=\frac{-\eta''\rho'+\eta'\rho''}{\rho'^2+\eta'^2}\cdot\frac{1}{\left(\rho'^2+\eta'^2\right)^{1/2}}$$
$$=\frac{-\eta''\rho'+\eta'\rho''}{\left(\rho'^2+\eta'^2\right)^{3/2}} \qquad \ldots \text{(A 5.46)}$$

Note: The form of this equation given in Feng and Yang (1973) appears to be incorrect.

Following this the principal curvature in the circumferential direction can be determined using equation A 5.35:

$$\kappa_2 = \frac{\sin\theta}{\rho}$$

Firstly determine sin θ in terms of ρ and η:

$$\begin{aligned}\sin\theta &= \frac{-d\eta}{dS} \\ &= \frac{-d\eta/d\psi}{dS/d\psi} \\ &= \frac{-\eta'}{\left(\rho'^2+\eta'^2\right)^{1/2}}\end{aligned} \qquad \ldots \text{(A 5.47)}$$

$$\text{So } \kappa_2 = \frac{-\eta'}{\rho\left(\rho'^2+\eta'^2\right)^{1/2}} \qquad \ldots \text{(A 5.48)}$$

To be able to represent the principal curvatures in terms of λ and ψ we need to define the first and second derivatives of ρ and η.

From equation A 5.31 and equation A 5.32:

$$\lambda_1 = \frac{\left(\rho'^2+\eta'^2\right)^{1/2}}{r_o}$$

$$\lambda_1 r_o = \left(\rho'^2+\eta'^2\right)^{1/2}$$

$$\left(\lambda_1 r_o\right)^2 - \rho'^2 = \eta'^2 \qquad \textit{substituting in A5.32 } \rho = r_o\lambda_2 \sin\psi$$

$$\left(\lambda_1 r_o\right)^2 - \left(r_o\lambda_2 \sin\psi\right)'^2 = \eta'^2$$

$$r_o^{\,2}\left(\lambda_1^{\,2}-\left(\lambda_2\,sin\psi\right)'^{2}\right)=\eta'^{2} \qquad \ldots \text{(A 5.49)}$$

From this the negative root of η prime should be taken since η is decreasing while ψ is increasing from the axis of symmetry.

$$\eta'=-r_o\sqrt{\left(\lambda_1^{\,2}-\left(\lambda_2\,sin\psi\right)'^{2}\right)} \qquad \ldots \text{(A 5.50)}$$

From this:

$$\eta''=\frac{-r_o\left(\lambda_1\lambda_1'-\left(\lambda_2\,sin\psi\right)'\left(\lambda_2\,sin\psi\right)''\right)}{\sqrt{\lambda_1^2-\left(\lambda_2\,sin\psi\right)'^{2}}} \qquad \ldots \text{(A 5.51)}$$

$$\rho=r_o\lambda_2\,sin\psi \qquad \ldots \text{(A 5.32)}$$

$$\rho'=r_o\lambda_2'\,sin\psi+r_o\lambda_2\,cos\psi=r_o\left(\lambda_2\,sin\psi\right)' \qquad \ldots \text{(A 5.52)}$$

$$\rho''=r_o\lambda_2''\,sin\psi+2r_o\lambda_2'\,cos\psi-r_o\lambda_2'\,sin\psi=r_o\left(\lambda_2\,sin\psi\right)'' \qquad \ldots \text{(A 5.53)}$$

These equations connect the ρ and η coordinate's and their derivatives to the stretch ratio λ_2 and the angle ψ.

Substituting equations A 5.50, A 5.51, A 5.52 and A 5.53 into equation A 5.46:

$$\kappa_1=\frac{-\eta''\rho'+\eta'\rho''}{\left(\rho'^{2}+\eta'^{2}\right)^{3/2}} \qquad \ldots \text{(A 5.46)}$$

$$\kappa_1 = \frac{r_o(\lambda_2 \sin\psi)'' \cdot -r_o\sqrt{\left(\lambda_1{}^2 - (\lambda_2 \sin\psi)'^2\right)} - r_o(\lambda_2 \sin\psi)' \dfrac{-r_o\left(\lambda_1\lambda_1{}' - (\lambda_2 \sin\psi)'(\lambda_2 \sin\psi)''\right)}{\sqrt{\lambda_1^2 - (\lambda_2 \sin\psi)'^2}}}{\left(\rho'^2 + \eta'^2\right)^{3/2}}$$

. . . (A 5.54)

As $\left(\rho'^2 + \eta'^2\right)^{1/2} = \lambda_1 r_o$

$$\kappa_1 = \frac{r_o(\lambda_2 \sin\psi)'' \cdot -r_o\sqrt{\left(\lambda_1{}^2 - (\lambda_2 \sin\psi)'^2\right)} - r_o(\lambda_2 \sin\psi)' \dfrac{-r_o\left(\lambda_1\lambda_1{}' - (\lambda_2 \sin\psi)'(\lambda_2 \sin\psi)''\right)}{\sqrt{\lambda_1^2 - (\lambda_2 \sin\psi)'^2}}}{(\lambda_1 r_o)^3}$$

. . . (A 5.55)

Taking out common factors:

$$\kappa_1 = -\frac{1}{\lambda_1^3 r_0 \sqrt{\lambda_1^2 - (\lambda_2 \sin\psi)'^2}} \ldots.$$
$$\left[(\lambda_2 \sin\psi)''\left(\lambda_1{}^2 - (\lambda_2 \sin\psi)'^2\right) - (\lambda_2 \sin\psi)'\left(\lambda_1\lambda_1{}' - (\lambda_2 \sin\psi)'(\lambda_2 \sin\psi)''\right)\right] \quad \text{. . . (A 5.56)}$$

Expand the equations:

$$\kappa_1 = -\frac{1}{\lambda_1^3 r_0 \sqrt{\lambda_1^2 - (\lambda_2 \sin\psi)'^2}} \ldots.$$
$$\left[\lambda_1{}^2(\lambda_2 \sin\psi)'' - (\lambda_2 \sin\psi)'^2(\lambda_2 \sin\psi)'' - \lambda_1\lambda_1{}'(\lambda_2 \sin\psi)' + (\lambda_2 \sin\psi)'^2(\lambda_2 \sin\psi)''\right]$$

. . . (A 5.57)

$$\kappa_1 = -\frac{1}{\lambda_1^3 r_0 \sqrt{\lambda_1^2 - (\lambda_2 \sin\psi)'^2}}\left[\lambda_1{}^2(\lambda_2 \sin\psi)'' - \lambda_1\lambda_1{}'(\lambda_2 \sin\psi)'\right] \quad \text{. . . (A 5.58)}$$

Multiply through by $-\frac{1}{\lambda_1^3}$:

$$\kappa_1 = \frac{1}{r_0\sqrt{\lambda_1^2 - (\lambda_2 \sin\psi)'^2}}\left[\frac{\lambda_1'(\lambda_2 \sin\psi)'}{\lambda_1^2} - \frac{(\lambda_2 \sin\psi)''}{\lambda_1}\right] \quad \ldots \text{(A 5.59)}$$

From equation A 5.48 the relationship between the circumferential curvatures can be defined using λ and ψ.

$$\kappa_2 = \frac{-\eta'}{\rho\left(\rho'^2 + \eta'^2\right)^{1/2}} \quad \ldots \text{(A 5.48)}$$

As $\left(\rho'^2 + \eta'^2\right)^{1/2} = \lambda_1 r_o$

$$\kappa_2 = \frac{-\eta'}{\rho\lambda_1 r_o}$$

Inserting $\eta' = -r_o\sqrt{\lambda_1^{\,2} - (\lambda_2 \sin\psi)'^2}$

$$\kappa_2 = \frac{-\left(-r_o\sqrt{\lambda_1^{\,2} - (\lambda_2 \sin\psi)'^2}\right)}{r_0\lambda_2 \sin\psi(\lambda_2 r_o)} \quad \ldots \text{(A 5.60)}$$

Therefore the principle curvature in the circumferential direction is given by:

$$\kappa_2 = \frac{\sqrt{\lambda_1^2 - (\lambda_2 \sin\psi)'^2}}{r_0\lambda_1\lambda_2 \sin\psi} \quad \ldots \text{(A 5.61)}$$

Summary

In this section the principal curvatures in terms of the stretch ratios and the angle ψ have been derived and are summarised below. In the following section the principal curvatures will be used in conjunction with the equilibrium equations and the stretch ratios to derive governing equations for the contact and non-contact regions.

$$\kappa_1 = \frac{1}{r_0\sqrt{\lambda_1^2 - \left(\lambda_2 \sin\psi\right)'^2}}\left[\frac{\lambda_1'\left(\lambda_2 \sin\psi\right)'}{\lambda_1^2} - \frac{\left(\lambda_2 \sin\psi\right)''}{\lambda_1}\right] \qquad \ldots \text{(A 5.59)}$$

$$\kappa_2 = \frac{\sqrt{\lambda_1^2 - \left(\lambda_2 \sin\psi\right)'^2}}{r_0 \lambda_1 \lambda_2 \sin\psi} \qquad \ldots \text{(A 5.61)}$$

Non-contact region lambda 1 and 2

The equilibrium equations for membranes of revolution in the meridian tangential and normal directions connect the tensions in the membrane to the local shape. Assuming that there are no forces acting tangentially to the membrane they are defined as:

$$\frac{\partial T_1}{\partial \lambda_1}\frac{\partial \lambda_1}{\partial \psi} + \frac{\partial T_1}{\partial \lambda_2}\frac{\partial \lambda_2}{\partial \psi} = \frac{\rho'}{\rho}\left(T_2 - T_1\right) \qquad \ldots \text{(A 5.21)}$$

$$\kappa_1 T_1 + \kappa_2 T_2 = P \qquad \ldots \text{(A 5.22)}$$

Equation 21 can be represented as:

$$f_1\,\lambda_1' + f_2\,\lambda_2' = \frac{\rho'}{\rho}\left(T_2 - T_1\right) \qquad \ldots \text{(A 5.62)}$$

where $f1 = \dfrac{\partial T_1}{\partial \lambda_1}$

$f_2 = \dfrac{\partial T_1}{\partial \lambda 2}$

$f_3 = T_1 - T_2$

where primes represent derivatives with respect to ψ.

Using $\rho = \lambda_2 r_0 \sin\psi$ and $\rho' = r_0 \lambda_2' \sin\psi + r_0 \lambda_2 \cos\psi$ gives:

$$f_1 \lambda_1' + f_2 \lambda_2' = \frac{r_o \lambda_2' \sin\psi + r_o \lambda_2 \cos\psi}{\lambda_2 r_o \sin\psi}(T_2 - T_1) \quad \ldots \text{(A 5.63)}$$

Cancelling r_o gives:

$$f_1 \lambda_1' + f_2 \lambda_2' = \frac{\lambda_2' \sin\psi + \lambda_2 \cos\psi}{\lambda_2 \sin\psi}(T_2 - T_1) \quad \ldots \text{(A 5.64)}$$

To define the meridian stretch ratio for the non-contact region we need to firstly express the circumferential stretch ratio derived with respect to ψ.

$$\rho = r_o \lambda_2 \sin\psi$$

Rearranging this gives:

$$\lambda_2{}' = \left(\frac{\rho}{r_o \sin\psi}\right)'$$

Applying the quotient rule leads to:

$$= \frac{1}{r_o}\left(\frac{(r_o \lambda_2' \sin\psi + r_o \lambda_2 \cos\psi)\sin\psi - r_o \lambda_2 \sin\psi \cos\psi}{\sin^2\psi}\right)$$

Cancelling r_o leads to:

$$= \left(\frac{(\lambda_2' \sin\psi + \lambda_2 \cos\psi)\sin\psi - \lambda_2 \sin\psi \cos\psi}{\sin^2\psi}\right) \quad \ldots \text{(A 5.65)}$$

Equation A 5.65 can be modified further by using the following simplifications.

$$\delta = \lambda_2 \sin\psi \qquad \ldots \text{(A 5.66)}$$

$$\omega = \delta' = \lambda_2' \sin\psi + \lambda_2 \cos\psi \qquad \ldots \text{(A 5.67)}$$

Therefore λ_2' in the non contact region is defined by:

$$\lambda_2{}' = \left(\frac{\omega \sin\psi - \delta \cos\psi}{\sin^2 \psi} \right) \qquad \ldots \text{(A 5.68)}$$

It is now possible to derive the meridian stretch ratio in the non-contact region. Substituting equations A 5.66, A 5.67 and A 5.68 into equation A 5.64 and rearranging gives:

$$\begin{aligned} \mathrm{f}_1 \lambda_1' + \mathrm{f}_2 \left(\frac{\omega \sin\psi - \delta \cos\psi}{\sin^2 \psi} \right) &= \frac{\omega}{\delta}(T_2 - T_1) \\ \mathrm{f}_1 \lambda_1' &= \frac{\omega}{\delta}(T_2 - T_1) - \mathrm{f}_2 \left(\frac{\omega \sin\psi - \delta \cos\psi}{\sin^2 \psi} \right) \end{aligned} \qquad \ldots \text{(A 5.69)}$$

Defining $f_3 = (T_1 - T_2)$ and rearranging gives λ_1' as:

$$\lambda_1' = \left(\frac{\delta \cos\psi - \omega \sin\psi}{\sin^2 \psi} \right) \left(\frac{f_2}{f_1} \right) - \left(\frac{\omega}{\delta} \right) \cdot \left(\frac{f_3}{f_1} \right) \qquad \ldots \text{(A 5.70)}$$

As well as this it is also possible to derive a relationship between the turgor pressure of the cell (P) and ω. This will allow the deformation to be linked to force on the cell through the pressure

P. In order to do this it is necessary to substitute equations A 5.59 and A 5.61 into A 5.22 using equation A 5.67 to express the expressions more simply.

$$\kappa_1 T_1 + \kappa_2 T_2 = P \qquad \ldots \text{(A 5.22)}$$

$$\kappa_1 = \frac{1}{r_0\sqrt{\lambda_1^2 - \omega^2}}\left[\frac{\lambda_1'\omega}{\lambda_1^2} - \frac{\omega'}{\lambda_1}\right] \qquad \ldots \text{(A 5.59)}$$

$$\kappa_2 = \frac{\sqrt{\lambda_1^2 - \omega^2}}{r_0\lambda_1\delta} \qquad \ldots \text{(A 5.61)}$$

$$\left(\frac{1}{r_0\sqrt{\lambda_1^2 - \omega^2}}\left[\frac{\lambda_1'\omega}{\lambda_1^2} - \frac{\omega'}{\lambda_1}\right]\right)T_1 + \left(\frac{\sqrt{\lambda_1^2 - \omega^2}}{r_0\lambda_1\delta}\right)T_2 = P \qquad \ldots \text{(A 5.71)}$$

$$\left(\frac{1}{r_0\sqrt{\lambda_1^2 - \omega^2}}\left[\frac{\lambda_1'\omega}{\lambda_1^2} - \frac{\omega'}{\lambda_1}\right]\right)T_1 = P - \left(\frac{\sqrt{\lambda_1^2 - \omega^2}}{r_0\lambda_1\delta}\right)T_2 \qquad \ldots \text{(A 5.72)}$$

Multiply both sides by $r_o\left(\lambda_1^2 - \omega^2\right)^{1/2}$ gives:

$$\left(\frac{\lambda_1'\omega}{\lambda_1^2} - \frac{\omega'}{\lambda_1}\right)T_1 = Pr_o\left(\lambda_1^2 - \omega^2\right)^{1/2} - \left(\frac{\lambda_1^2 - \omega^2}{\lambda_1\delta}\right)T_2 \qquad \ldots \text{(A 5.73)}$$

Divide both sides by T_1 and rearranging:

$$-\frac{\omega'}{\lambda_1} = \frac{Pr_o\left(\lambda_1^2 - \omega^2\right)^{1/2}}{T_1} - \left(\frac{\lambda_1^2 - \omega^2}{\lambda_1\delta}\right)\left(\frac{T_2}{T_1}\right) - \frac{\lambda_1'\omega}{\lambda_1^2} \qquad \ldots \text{(A 5.74)}$$

Multiply through by -λ_1:

$$\omega' = \frac{\lambda_1'\omega}{\lambda_1} + \frac{\left(\lambda_1{}^2 - \omega^2\right)}{\delta}\left(\frac{T_2}{T_1}\right) - \frac{\lambda_1\left(\lambda_1{}^2 - \omega^2\right)^{1/2} Pr_0}{T_1} \qquad \ldots \text{(A 5.75)}$$

Contact region lambda 1 and 2

The governing equations for the contact region are defined below, provided that there is no friction between the plate and the membrane.

$$f_1\,\lambda_1' + f_2\,\lambda_2' = \frac{\lambda_2'\sin\psi + \lambda_2\cos\psi}{\lambda_2\sin\psi}\left(T_2 - T_1\right) \qquad \ldots \text{(A 5.64)}$$

$$\kappa_1 T_1 + \kappa_2 T_2 = P \qquad \ldots \text{(A 5.22)}$$

The second of these equations is automatically resolved as there is no load on the membrane so $\kappa_1=\kappa_2=0$. Also since the contact surface is perpendicular to the η axis the derivative of η with respect to ψ is zero.

Therefore:

$$\lambda_1 = \frac{\rho'}{r_0} \qquad \lambda_2 = \frac{\rho}{r_0\sin\psi} \qquad \ldots \text{(A 5.76)}$$

It is necessary to firstly derive a relationship for λ_2' before λ_1' can be defined.

$$\lambda_2' = \left(\frac{\rho}{r_0 \sin\psi}\right)' = \frac{1}{r_0}\left(\frac{\rho' \sin\psi - \rho\cos\psi}{\sin^2\psi}\right)$$
$$= \frac{1}{r_0}\left(\frac{\lambda_1 r_0 \sin\psi - \lambda_2 r_0 \sin\psi\cos\psi}{\sin^2\psi}\right) = \left(\frac{\lambda_1 - \lambda_2\cos\psi}{\sin\psi}\right) \quad \ldots \text{(A 5.77)}$$

Note, this equation is different to that shown in Lardner and Pujura (1980) but the same as that shown in Feng and Yang (1973).

Having derived a relationship for λ_2' in the contact region it is now possible to find λ_1'.

$$f_1\lambda_1' + f_2\lambda_2' = \frac{\lambda_2' \sin\psi + \lambda_2\cos\psi}{\lambda_2 \sin\psi}(T_2 - T_1) \quad \ldots \text{(A 5.78)}$$

Substituting in $\lambda_2' = \left(\frac{\lambda_1 - \lambda_2\cos\psi}{\sin\psi}\right)$

$$f_1\lambda_1' + f_2\left(\frac{\lambda_1 - \lambda_2\cos\psi}{\sin\psi}\right) = \frac{\left(\frac{\lambda_1 - \lambda_2\cos\psi}{\sin\psi}\right)\sin\psi + \lambda_2\cos\psi}{\lambda_2 \sin\psi}(T_2 - T_1) \quad \ldots \text{(A 5.79)}$$

$$f_1\lambda_1' + f_2\left(\frac{\lambda_1 - \lambda_2\cos\psi}{\sin\psi}\right) = \frac{\lambda_1}{\lambda_2 \sin\psi}(T_2 - T_1) \quad \ldots \text{(A 5.80)}$$

Rearranging and dividing through by f_1:

$$\lambda_1' = \frac{\lambda_1}{\lambda_2 \sin\psi}\frac{(T_2 - T_1)}{f_1} - \left(\frac{f_2}{f_1}\right)\left(\frac{\lambda_1 - \lambda_2\cos\psi}{\sin\psi}\right) \quad \ldots \text{(A 5.81)}$$

$$\lambda_1' = -\frac{\lambda_1}{\lambda_2 \sin\psi}\left(\frac{f_3}{f_1}\right) - \left(\frac{\lambda_1 - \lambda_2 \cos\psi}{\sin\psi}\right)\left(\frac{f_2}{f_1}\right) \qquad \ldots \text{(A 5.82)}$$

Summary of geometric equations derived

Non-contact region:

$$\lambda_1' = \left(\frac{\delta\cos\psi - \omega\sin\psi}{\sin^2\psi}\right)\left(\frac{f_2}{f_1}\right) - \left(\frac{\omega}{\delta}\right)\cdot\left(\frac{f_3}{f_1}\right)$$

$$\omega' = \frac{\lambda_1'\omega}{\lambda_1} + \frac{\left(\lambda_1^{\,2} - \omega^2\right)}{\delta}\left(\frac{T_2}{T_1}\right) - \frac{\lambda_1\left(\lambda_1^{\,2} - \omega^2\right)^{1/2}\mathrm{Pr}_0}{T_1}$$

$$\lambda_2{}' = \left(\frac{\omega\sin\psi - \delta\cos\psi}{\sin^2\psi}\right)$$

$$\delta = \lambda_2 \sin\psi$$

$$\omega = \delta' = \lambda_2' \sin\psi + \lambda_2 \cos\psi$$

Contact region:

$$\lambda_1' = -\frac{\lambda_1}{\lambda_2\sin\psi}\left(\frac{f_3}{f_1}\right) - \left(\frac{\lambda_1 - \lambda_2\cos\psi}{\sin\psi}\right)\left(\frac{f_2}{f_1}\right)$$

$$\lambda_2' = \left(\frac{\lambda_1 - \lambda_2\cos\psi}{\sin\psi}\right)$$

These relationships all agree with those outlined by Wang (2004). Also it should be noted that the reason for the differences seen between Wang (2004) and Feng and Yang (1977) are due to the different definitions of f_3.

Pressure and Volume relationship

The assumptions used by Feng and Yang (1973) and Lardner and Pujara (1980) about the pressure and volume relationships are different.

Feng and Yang assume that the membrane is a gas filled membrane with a constant pressure and volume. However, for systems such as biological cells this assumption is not appropriate. In these systems it would be more appropriate to use the assumption that the sphere is filled with an incompressible fluid and that a constant volume is maintained during compression. This was assumed by Lardner and Pujara (1980).

The initial volume before contact with the probe is given by:

$$V = \frac{4}{3}\pi r_o^3 \lambda_s^3 \qquad \ldots \text{(A 5.83)}$$

At the end of the compression step the volume of the sphere can be calculated using the boundary coordinates (ρ and η) and the following equation:

$$V_s = 2\pi \int_0^{\bar{\eta}} \rho^2 d\eta \qquad \ldots \text{(A 5.84)}$$

So to be able to solve the above equation we need to define the volume calculation in terms of λ, ψ and δ.

As $\rho = r_o \delta$ and $\eta' = -r_o \sqrt{\left(\lambda_1^{\,2} - \left(\lambda_2 \sin\psi \right)^{\prime 2} \right)}$ this gives:

$$V_s = 2\pi \int_0^{\bar{\eta}} \left(r_o \delta \right)^2 d\eta \qquad \ldots \text{(A 5.85)}$$

Noticing that

$$\eta = 0 \text{ when } \psi = \frac{\pi}{2}$$

and

$$\eta = \overline{\eta} \text{ when } \psi = \Gamma$$

Using equation A 5.50 we can modify A 5.85 to:

$$V_s = 2\pi \int_{\Gamma}^{\overline{\eta}} (r_o \delta)^2 \left(- r_o \sqrt{\left(\lambda_1^{\,2} - \omega^2 \right)} \right) d\psi \qquad \ldots \text{(A 5.86)}$$

This leads to:

$$V_s = 2\pi r_o^3 \int_{\Gamma}^{\overline{\eta}} \left(- r_o \sqrt{\left(\lambda_1^{\,2} - \omega^2 \right)} \right) \delta^2 \, d\psi \qquad \ldots \text{(A 5.87)}$$

These equations complete the governing equations required to solve the contact problem of an inflated membrane compressed between two parallel platens.

Boundary Conditions

To solve the previously described differential equations we need to define a number of boundary restraints which must also be fulfilled.

The first boundary condition for the contact region is:

$$\psi = 0, \lambda_1 = \lambda_2 \qquad \ldots \text{(A 5.88)}$$

This means that on the surface of the inflated membrane under no deformation the meridian and circumferential stretch will be the same.

The other boundary conditions apply to the edge of the contact region and the non-contact region as shown by Figure A 5.9. The angle Γ represents the angle between the vertical axis of symmetry and the point where the contact and non-contact surfaces meet.

$$\psi = \Gamma, \lambda_1(contact\ region) = \lambda_1(non-contact\ region) \quad \ldots \text{(A 5.89)}$$

$$\psi = \Gamma, \lambda_2(contact\ region) = \lambda_2(non-contact\ region) \quad \ldots \text{(A 5.90)}$$

$$\psi = \Gamma, \eta = \overline{\eta} \quad \ldots \text{(A 5.91)}$$

At the point of transition between the contact and non-contact region:

From equation A 5.50:

$$\eta' = -r_o \sqrt{\left({\lambda_1}^2 - \left(\lambda_2 \sin\psi\right)'^2 \right)} \quad \ldots \text{(A 5.50)}$$

If $\overline{\eta} = 0$ this becomes:

$$0 = \left({\lambda_1}^2 - \left(\lambda_2 \sin\psi\right)'^2 \right) \quad \ldots \text{(A 5.92)}$$

$$\lambda_1 = \left(\lambda_2 \sin\psi\right)' = \delta' = \omega \quad \ldots \text{(A 5.93)}$$

$$\psi = \Gamma, \eta' = 0 \text{ or } \omega = \lambda_1 \qquad \ldots \text{(A 5.94)}$$

This means that there is no change in η with respect to ψ at the point of transition. This means that at the point of transition the slope of the tangent is equal to zero so the total force on the ρ direction is zero.

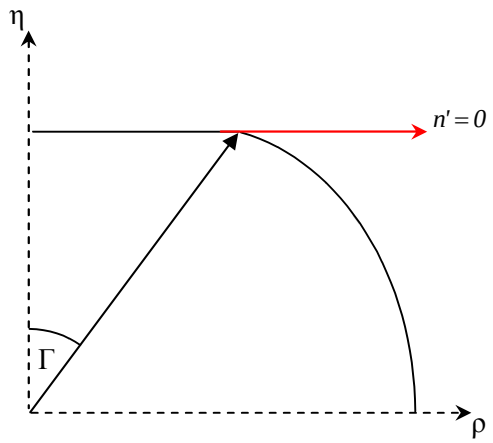

The final condition states that following the deformation of the membrane by increased internal pressure, at the equator of the sphere the tangent to the surface will be vertical.

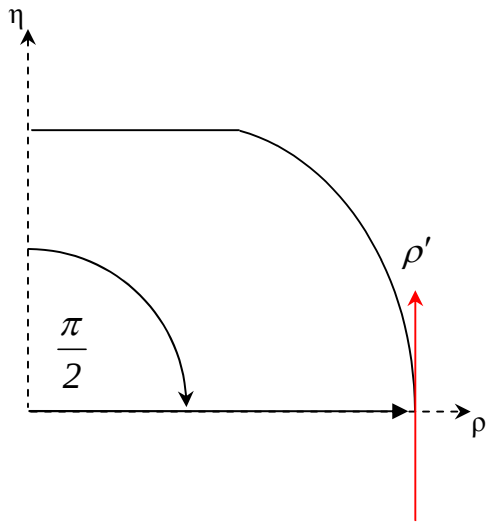

This condition indicates that when the cell has been deformed due to the increased internal pressure the tangent at the point $\frac{\pi}{2}$ in the non-contact region will be vertical.

As:

$$\frac{\rho'}{r_o} = \left(\lambda_2 \sin\psi\right)' \qquad \ldots \text{(A 5.95)}$$

Therefore:

$$\delta' = \left(\lambda_2 \sin\psi\right)' = \omega \qquad \ldots \text{(A 5.96)}$$

Hence:

$$\omega = 0$$

The final boundary condition is:

$$\psi = \frac{\pi}{2}, \omega = 0 \qquad \ldots \text{(A 5.97)}$$

Once all of the boundary conditions have been met the model gives corresponding values of ρ and η for the predefined values of λ_s, E, h_o and ν. From this force (F) and deformation (X) data can be obtained using the following equations:

$$F = PA_c \qquad \ldots \text{(A 5.98)}$$

Where P is the turgor pressure and A_c is the contact area between the probe and the cell. The contact area is calculated using:

$$A_c = \pi\left(r_o \lambda_2 \sin\Gamma\right)^2 \qquad \ldots \text{(A 5.99)}$$

The deformation of the cell is defined using:

$$X = \frac{z}{r_o \lambda_s} = 1 - \frac{\overline{\eta}}{r_o \lambda_s} \qquad \ldots \text{(A 5.100)}$$

where z is half the distance that the cell has been compressed.

The use of chosen values of E, h_o, ν and λ_s produces a force and deformation curve that can be compared to experimental data.

Part b: Derivation of the equations outlined by Feng and Yang (1973).

This section will derive the governing equations given by Feng and Yang (1973). This was done as Feng and Yang (1973) do not define the tension dependent functions f_1, f_2 and f_3 separately so the final governing equations appear different from those used by other workers. The tensions (T_1 and T_2) defined by Feng and Yang (1973) will be used here as this is a check of the equation manipulations. Also it will be assumed that equation 5 given in Feng and Yang (1973) should be corrected to:

$$\kappa_1 = \frac{-\eta''\rho' + \eta'\rho''}{\left(\rho'^2 + \eta'^2\right)^{3/2}} \qquad \ldots \text{(A 5.1b)}$$

The start point for this analysis is the principal curvatures and the tension relationships.

$$\kappa_1 = \frac{1}{r_0\sqrt{\lambda_1^2 - (\lambda_2 \sin\psi)'^2}}\left[\frac{\lambda_1'(\lambda_2 \sin\psi)'}{\lambda_1^2} - \frac{(\lambda_2 \sin\psi)''}{\lambda_1}\right] \quad \ldots \text{(A 5.2b)}$$

$$\kappa_2 = \frac{\sqrt{\lambda_1^2 - (\lambda_2 \sin\psi)'^2}}{r_0 \lambda_1 \lambda_2 \sin\psi} \quad \ldots \text{(A 5.3b)}$$

Tensions T_1 and T_2 are taken from Feng and Yang (1973) equation 11:

$$T_1 = 2hC_1\left(\frac{\lambda_1}{\lambda_2} - \frac{1}{\lambda_1^3 \lambda_2^3}\right)\left(1 + \alpha\lambda_2^2\right) \quad \ldots \text{(A 5.4b)}$$

$$T_2 = 2hC_1\left(\frac{\lambda_2}{\lambda_1} - \frac{1}{\lambda_1^3 \lambda_2^3}\right)\left(1 + \alpha\lambda_1^2\right) \quad \ldots \text{(A 5.5b)}$$

To be able to derive the governing equations it is also necessary to define the equilibrium equations. These are the same as previously described.

$$\frac{\partial T_1}{\partial \lambda_1}\frac{\partial \lambda_1}{\partial \psi} + \frac{\partial T_1}{\partial \lambda_2}\frac{\partial \lambda_2}{\partial \psi} = \frac{\rho'}{\rho}(T_2 - T_1) \quad \ldots \text{(A 5.6b)}$$

$$\kappa_1 T_1 + \kappa_2 T_2 = P \quad \ldots \text{(A 5.7b)}$$

Using equation A 5.4b and A 5.5b it is possible to define the following:

$$\frac{\partial T_1}{\partial \lambda_1} = 2hC_1\left(\frac{1}{\lambda_2} + \frac{3}{\lambda_1^4 \lambda_2^3}\right)\left(1 + \alpha\lambda_2^2\right) \quad \ldots \text{(A 5.8b)}$$

$$\frac{\partial T_1}{\partial \lambda_2} = 2hC_1\left(-\frac{\lambda_1}{\lambda_2^2}+\frac{3}{\lambda_1^3\lambda_2^4}\right)\left(1+\alpha\lambda_2^2\right)+\left(\frac{\lambda_1}{\lambda_2}-\frac{1}{\lambda_1^3\lambda_2^3}\right)\left(2\alpha\lambda_2\right) \quad \ldots \text{(A 5.9b)}$$

$$T_2 - T_1 = 2hC_1\left[\frac{\lambda_2}{\lambda_1}-\frac{\lambda_1}{\lambda_2}+\alpha\left(\frac{1}{\lambda_1^3\lambda_2}-\frac{1}{\lambda_1\lambda_2^3}\right)\right] \quad \ldots \text{(A 5.10b)}$$

Note: The definition of equation A 5.10b is different to that used by Lardner and Pujara (1980) and in the previous section where instead T_1-T_2 was used.

Non-contact region

Using the equations defined previously:

$$\frac{\partial T_1}{\partial \lambda_1}\frac{\partial \lambda_1}{\partial \psi}+\frac{\partial T_1}{\partial \lambda_2}\frac{\partial \lambda_2}{\partial \psi}=\left(\frac{\omega \sin\psi - \delta\cos\psi}{\sin^2\psi}\right)\left(T_2 - T_1\right) \quad \ldots \text{(A 5.11b)}$$

As previously defined in the derivation of Lardner and Pujara:

$$\delta = \lambda_2 \sin\psi$$
$$\omega = \delta' = \lambda_2' \sin\psi + \lambda_2 \cos\psi$$

$$\lambda_2{}' = \left(\frac{\rho}{r_o \sin\psi}\right)'$$

$$\lambda_2{}' = \left(\frac{\omega \sin\psi - \delta\cos\psi}{\sin^2\psi}\right) \quad \ldots \text{(A 5.12b)}$$

Input A 5.8b, A 5.9b, A 5.10b and A 5.12b into equation A 5.11b:

$$\left\{2hC_1\left(\frac{1}{\lambda_2}+\frac{3}{\lambda_1^4\lambda_2^3}\right)\left(1+\alpha\lambda_2^2\right)\right\}\lambda_1' + \left\{2hC_1\left[\left(-\frac{\lambda_1}{\lambda_2^2}+\frac{3}{\lambda_1^3\lambda_2^4}\right)\left(1+\alpha\lambda_2^2\right)+\left(\frac{\lambda_1}{\lambda_2}-\frac{1}{\lambda_1^3\lambda_2^3}\right)\left(2\alpha\lambda_2\right)\right]\right\}$$
$$\left(\frac{\omega\sin\psi-\delta\cos\psi}{\sin^2\psi}\right)=\left(\frac{\omega\sin\psi-\delta\cos\psi}{\sin^2\psi}\right)\left\{2hC_1\left[\frac{\lambda_2}{\lambda_1}-\frac{\lambda_1}{\lambda_2}+\alpha\left(\frac{1}{\lambda_1^3\lambda_2}-\frac{1}{\lambda_1\lambda_2^3}\right)\right]\right\}$$

. . .(A 5.13b)

Dividing through by $2hC_1$ and using the simplification δ and ω:

$$\left\{\left(\frac{\sin\psi}{\delta}+\frac{3\sin^3\psi}{\lambda_1^4\delta^3}\right)\left(1+\frac{\alpha\delta^2}{\sin^2\psi}\right)\right\}\lambda_1' + \ldots$$
$$\left\{\left[\left(-\frac{\lambda_1\sin^2\psi}{\delta^2}+\frac{3\sin^4\psi}{\lambda_1^3\delta^4}\right)\left(1+\frac{\alpha\delta^2}{\sin^2\psi}\right)+\left(\frac{\lambda_1\sin\psi}{\delta}-\frac{\sin^3\psi}{\lambda_1^3\delta^3}\right)\left(\frac{2\alpha\delta}{\sin\psi}\right)\right]\right\}\ldots$$
$$\left(\frac{\omega\sin\psi-\delta\cos\psi}{\sin^2\psi}\right)=\frac{\omega}{\delta}\left(\frac{\delta}{\lambda_1\sin\psi}-\frac{\lambda_1\sin\psi}{\delta}\right)+\frac{\omega\alpha}{\delta}\left(\frac{\sin\psi}{\lambda_1^3\delta}-\frac{\sin^3\psi}{\lambda_1\delta^3}\right)$$

. . .(A 5.14b)

Dividing through by $\left(1+\frac{\alpha\delta^2}{\sin^2\psi}\right)$

$$\left(\frac{\sin\psi}{\delta}+\frac{3\sin^3\psi}{\lambda_1^4\delta^3}\right)\lambda_1' + \ldots$$
$$\left(\frac{\omega\sin\psi-\delta\cos\psi}{\sin^2\psi}\right)\left(-\frac{\lambda_1\sin^2\psi}{\delta^2}+\frac{3\sin^4\psi}{\lambda_1^3\delta^4}\right)+\frac{1}{\left(1+\alpha\delta^2/\sin^2\psi\right)}\left(\frac{\lambda_1\sin\psi}{\delta}-\frac{\sin^3\psi}{\lambda_1^3\delta^3}\right)\left(\frac{2\alpha\delta}{\sin\psi}\right)\ldots$$
$$\left(\frac{\omega\sin\psi-\delta\cos\psi}{\sin^2\psi}\right)=\frac{1}{\left(1+\alpha\delta^2/\sin^2\psi\right)}\frac{\omega}{\delta}\left\{\left(\frac{\delta}{\lambda_1\sin\psi}-\frac{\lambda_1\sin\psi}{\delta}\right)+\alpha\left(\frac{\sin\psi}{\lambda_1^3\delta}-\frac{\sin^3\psi}{\lambda_1\delta^3}\right)\right\}$$

. . .(A 5.15b)

Rearranging and simplifying

$$\left(\frac{\left(\lambda_1^4\delta^2+3\sin^2\psi\right)\sin\psi}{\lambda_1^4\delta^3}\right)\lambda_1' = \ldots$$
$$\left(\omega\sin\psi-\delta\cos\psi\right)\left(\frac{\lambda_1}{\delta^2}-\frac{3\sin^2\psi}{\lambda_1^3\delta^4}\right)-\frac{1}{\left(1+\alpha\delta^2/\sin^2\psi\right)}\left(\frac{\lambda_1\sin\psi}{\delta}-\frac{\sin^3\psi}{\lambda_1^3\delta^3}\right)\left(\frac{2\alpha\delta}{\sin\psi}\right)\ldots$$
$$\left(\frac{\omega\sin\psi-\delta\cos\psi}{\sin^2\psi}\right)+\frac{1}{\left(1+\alpha\delta^2/\sin^2\psi\right)}\frac{\omega}{\delta}\left\{\left(\frac{\delta}{\lambda_1\sin\psi}-\frac{\lambda_1\sin\psi}{\delta}\right)+\alpha\left(\frac{\sin\psi}{\lambda_1^3\delta}-\frac{\sin^3\psi}{\lambda_1\delta^3}\right)\right\}$$

. . .(A 5.16b)

Dividing through by $\left(\frac{\left(\lambda_1^4\delta^2+3\sin^2\psi\right)\sin\psi}{\lambda_1^4\delta^3}\right)$ leads to:

$$\lambda_1' = \left(\frac{\lambda_1^4\delta^3}{\left(\lambda_1^4\delta^2+3\sin^2\psi\right)\sin\psi}\right)\left\langle\begin{array}{l}\left(\omega\sin\psi-\delta\cos\psi\right)\left(\frac{\lambda_1}{\delta^2}-\frac{3\sin^2\psi}{\lambda_1^3\delta^4}\right)\ldots \\ -\frac{1}{\left(1+\alpha\delta^2/\sin^2\psi\right)}\left(\frac{\lambda_1\sin\psi}{\delta}-\frac{\sin^3\psi}{\lambda_1^3\delta^3}\right)\left(\frac{2\alpha\delta}{\sin\psi}\right)\ldots \\ \left(\frac{\omega\sin\psi-\delta\cos\psi}{\sin^2\psi}\right)+\frac{1}{\left(1+\alpha\delta^2/\sin^2\psi\right)}\ldots \\ \frac{\omega}{\delta}\left\{\left(\frac{\delta}{\lambda_1\sin\psi}-\frac{\lambda_1\sin\psi}{\delta}\right)+\alpha\left(\frac{\sin\psi}{\lambda_1^3\delta}-\frac{\sin^3\psi}{\lambda_1\delta^3}\right)\right\}\end{array}\right\rangle$$

. . .(A 5.17b)

By simplification with $\frac{1}{\left(1+\alpha\delta^2/\sin^2\psi\right)}$ gives:

$$\lambda_1' = \left(\frac{\lambda_1^4\delta^3}{\left(\lambda_1^4\delta^2+3\sin^2\psi\right)\sin\psi}\right)\left\langle \begin{array}{l} \left(\omega\sin\psi-\delta\cos\psi\right)\left(\frac{\lambda_1}{\delta^2}-\frac{3\sin^2\psi}{\lambda_1^3\delta^4}\right)-\frac{1}{\left(1+\alpha\delta^2/\sin^2\psi\right)} \\ \left\{\left(\frac{2\alpha\delta}{\sin\psi}\right)\left(\frac{\lambda_1}{\delta}-\frac{\sin^2\psi}{\lambda_1^3\delta^3}\right)\left(\omega-\frac{\delta\cos\psi}{\sin\psi}\right)\ldots\right. \\ \left.-\left[\frac{\omega}{\delta}\left\{\left(\frac{\sin\psi}{\lambda_1^3\delta}-\frac{\sin^3\psi}{\lambda_1\delta^3}\right)\alpha+\left(\frac{\delta}{\lambda_1\sin\psi}-\frac{\lambda_1\sin\psi}{\delta}\right)\right\}\right]\right\} \end{array}\right\rangle$$

. . .(A 5.18b)

Equation A 5.18b is the same as equation 17 shown in Feng and Yang (1973).

Putting equations A 5.2b, A 5.3b, A 5.4b and A 5.5b into equation A 5.7b.

$$\kappa_1 T_1 + \kappa_2 T_2 = P \qquad \ldots \text{(A 5.7b)}$$

$$\frac{1}{r_0\sqrt{\lambda_1^2-\left(\lambda_2\sin\psi\right)'^2}}\left[\frac{\lambda_1'\left(\lambda_2\sin\psi\right)'}{\lambda_1^2}-\frac{\left(\lambda_2\sin\psi\right)''}{\lambda_1}\right]T_1+\left(\frac{\sqrt{\lambda_1^2-\left(\lambda_2\sin\psi\right)'^2}}{r_o\lambda_1\lambda_2\sin\psi}\right)T_2 = P \qquad \ldots \text{(A 5.19b)}$$

Multiplying all terms by $r_0\sqrt{\lambda_1^2-\left(\lambda_2\sin\psi\right)'^2}$

$$\left(\frac{\lambda_1'\left(\lambda_2\sin\psi\right)'}{\lambda_1^2}-\frac{\left(\lambda_2\sin\psi\right)''}{\lambda_1}\right)T_1+\left(\frac{\lambda_1^2-\left(\lambda_2\sin\psi\right)'^2}{\lambda_1\lambda_2\sin\psi}\right)T_2 = P\left(r_0\sqrt{\lambda_1^2-\left(\lambda_2\sin\psi\right)'^2}\right) \qquad \ldots \text{(A 5.20b)}$$

Simplify A 5.20b using the following assumptions:

$$\delta = \lambda_2 \sin\psi$$
$$\omega = \delta' = \left(\lambda_2 \sin\psi\right)'$$
$$\omega' = \left(\lambda_2 \sin\psi\right)''$$

$$\left(\frac{\lambda_1'\omega}{\lambda_1^2} - \frac{\omega'}{\lambda_1}\right)T_1 + \left(\frac{\lambda_1^2 - \omega^2}{\lambda_1\delta}\right)T_2 = P\left(r_0\sqrt{\lambda_1^2 - \omega^2}\right) \quad \ldots \text{(A 5.21b)}$$

Subtracting $\left(\frac{\lambda_1^2 - \omega^2}{\lambda_1\delta}\right)T_2$ and dividing through by T_1:

$$\frac{\lambda_1'\omega}{\lambda_1^2} - \frac{\omega'}{\lambda_1} = \frac{P\left(r_0\sqrt{\lambda_1^2 - \omega^2}\right)}{T_1} - \left(\frac{\lambda_1^2 - \omega^2}{\lambda_1\delta}\right)\left(\frac{T_2}{T_1}\right) \quad \ldots \text{(A 5.22b)}$$

Multiplying by $-\lambda_1$ and rearranging leads to:

$$\omega' = -\frac{P\lambda_1\left(r_0\sqrt{\lambda_1^2 - \omega^2}\right)}{T_1} + \left(\frac{\lambda_1^2 - \omega^2}{\delta}\right)\left(\frac{T_2}{T_1}\right) + \frac{\lambda_1'\omega}{\lambda_1} \quad \ldots \text{(A 5.23b)}$$

Equation A 5.23b is the same as equation A 5.75 derived previously.

Substituting in tension equations A 5.4b and A 5.5b.

$$\omega' = -\frac{P\lambda_1\left(r_0\sqrt{\lambda_1^2 - \omega^2}\right)}{2hC_1\left(\frac{\lambda_1}{\lambda_2} - \frac{1}{\lambda_1^3\lambda_2^3}\right)\left(1 + \alpha\lambda_2^2\right)} + \left(\frac{\lambda_1^2 - \omega^2}{\delta}\right)\left(\frac{2hC_1\left(\frac{\lambda_2}{\lambda_1} - \frac{1}{\lambda_1^3\lambda_2^3}\right)\left(1 + \alpha\lambda_1^2\right)}{2hC_1\left(\frac{\lambda_1}{\lambda_2} - \frac{1}{\lambda_1^3\lambda_2^3}\right)\left(1 + \alpha\lambda_2^2\right)}\right) + \frac{\lambda_1'\omega}{\lambda_1}$$

. . . (A 5.24b)

Substituting into A 5.24b the following simplifications and rearrange T_1:

$$\delta = \lambda_2 \sin\psi$$

$$\beta = \frac{h}{r_o}$$

$$p = \frac{P}{C_1}$$

$$\omega' = -\frac{p\lambda_1\left(\sqrt{\lambda_1^2-\omega^2}\right)}{2\beta\left(\frac{\lambda_1\sin\psi}{\delta}-\frac{\sin^3\psi}{\lambda_1^3\delta^3}\right)\left(1+\frac{\alpha\delta^2}{\sin^2\psi}\right)}\ldots$$
$$+\left(\frac{\lambda_1^2-\omega^2}{\delta}\right)\left(\frac{\left(\frac{\delta}{\lambda_1\sin\psi}-\frac{\sin^3\psi}{\lambda_1^3\delta^3}\right)\left(1+\alpha\lambda_1^2\right)}{\left(\frac{\lambda_1\sin\psi}{\delta}-\frac{\sin^3\psi}{\lambda_1^3\delta^3}\right)\left(1+\frac{\alpha\delta^2}{\sin^2\psi}\right)}\right)+\frac{\lambda_1'\omega}{\lambda_1} \quad \ldots \text{(A 5.25b)}$$

Expanding T_1:

$$\omega' = -\frac{p}{2\beta}\frac{\lambda_1\left(\sqrt{\lambda_1^2-\omega^2}\right)}{\left(\frac{\lambda_1\sin\psi}{\delta}+\frac{\lambda_1\alpha\delta}{\sin\psi}-\frac{\sin^3\psi}{\lambda_1^3\delta^3}-\frac{\alpha\sin\psi}{\lambda_1^3\delta}\right)}\ldots$$
$$+\left(\frac{\lambda_1^2-\omega^2}{\delta}\right)\left(\frac{\left(\frac{\delta}{\lambda_1\sin\psi}-\frac{\sin^3\psi}{\lambda_1^3\delta^3}\right)\left(1+\alpha\lambda_1^2\right)}{\left(\frac{\lambda_1\sin\psi}{\delta}+\frac{\lambda_1\alpha\delta}{\sin\psi}-\frac{\sin^3\psi}{\lambda_1^3\delta^3}-\frac{\alpha\sin\psi}{\lambda_1^3\delta}\right)}\right)+\frac{\lambda_1'\omega}{\lambda_1} \quad \ldots \text{(A 5.26b)}$$

Rearranging:

$$\omega' = \frac{\lambda_1'\omega}{\lambda_1}-\frac{p}{2\beta}\left(\frac{\lambda_1\delta}{\lambda_1\sin\psi}+\frac{\lambda_1\sin\psi}{\lambda_1\alpha\delta}-\frac{\lambda_1^4\delta^3}{\sin^3\psi}-\frac{\lambda_1^4\delta}{\alpha\sin\psi}\right)\left(\sqrt{\lambda_1^2-\omega^2}\right)\ldots$$
$$+\left(\frac{\lambda_1^2-\omega^2}{\delta}\right)\left(\frac{\delta}{\lambda_1\sin\psi}+\frac{\sin\psi}{\lambda_1\alpha\delta}-\frac{\lambda_1^3\delta^3}{\sin^3\psi}-\frac{\lambda_1^3\delta}{\alpha\sin\psi}\right)\left(\frac{\delta}{\lambda_1\sin\psi}-\frac{\sin^3\psi}{\lambda_1^3\delta^3}\right)\left(1+\alpha\lambda_1^2\right) \quad \ldots \text{(A 5.27b)}$$

$$\omega' = \frac{\lambda_1'\omega}{\lambda_1} - \frac{p}{2\beta}\left(\frac{\lambda_1^4\delta^3\left(\sqrt{\lambda_1^2-\omega^2}\right)}{\left(\lambda_1^4\delta^2-\sin^2\psi\right)\left(\sin\psi+\frac{\alpha\delta^2}{\sin\psi}\right)}\right)\ldots$$
$$+\left(\frac{\lambda_1^2-\omega^2}{\lambda_1\delta}\right)\left(\frac{\lambda_1^4\delta^3}{\left(\lambda_1^4\delta^2-\sin^2\psi\right)\left(\sin\psi+\frac{\alpha\delta^2}{\sin\psi}\right)}\right)\left(\frac{\delta}{\lambda_1\sin\psi}-\frac{\sin^3\psi}{\lambda_1^3\delta^3}\right)\left(1+\alpha\lambda_1^2\right) \quad \ldots \text{(A 5.28b)}$$

Take out T_1 and rearrange:

$$\omega' = \frac{\lambda_1'\omega}{\lambda_1} + \left(\frac{\lambda_1^4\delta^3\left(\sqrt{\lambda_1^2-\omega^2}\right)}{\left(\lambda_1^4\delta^2-\sin^2\psi\right)\left(\sin\psi+\frac{\alpha\delta^2}{\sin\psi}\right)}\right)\ldots$$
$$\left\{\left(\frac{\sqrt{\lambda_1^2-\omega^2}}{\lambda_1\delta}\right)\left(\left(\frac{\delta}{\lambda_1\sin\psi}-\frac{\sin^3\psi}{\lambda_1^3\delta^3}\right)\left(1+\alpha\lambda_1^2\right)\right)-\frac{p}{2\beta}\right\} \quad \ldots \text{(A 5.29b)}$$

This equation is exactly the same as the relationship outlined in Feng and Yang (1973). Also equation A 5.23b shown here is exactly the same as equation A 5.75 shown for the derivation of the equation used by Wang *et al.* (2004).

Contact region

All of the geometry assumptions made previously still apply for the contact region so:

$$\eta' = 0$$

From this the principle stretch ratios can be defined as:

$$\lambda_1 = \frac{\rho'}{r_o}$$

$$\lambda_2 = \frac{\rho}{r_o \sin\psi}$$

From this $\lambda_2' = \left(\frac{\lambda_1 - \lambda_2 \cos\psi}{\sin\psi} \right)$ . . . (A 5.30b)

Equation A 5.7b is automatically resolved as there is no load on the membrane so $\kappa_1=\kappa_2=0$. Also since the contact surface is perpendicular to the η axis the derivative of η with respect to ψ is zero. Equation A 5.6b can be represented as:

$$\frac{\partial T_1}{\partial \lambda_1}\frac{\partial \lambda_1}{\partial \psi} + \frac{\partial T_1}{\partial \lambda_2}\frac{\partial \lambda_2}{\partial \psi} = \frac{\lambda_2' \sin\psi + \lambda_2 \cos\psi}{\lambda_2 \sin\psi}\left(T_2 - T_1\right) \quad \text{. . . (A 5.31b)}$$

By substituting in equations A 5.8b, A 5.9b, A 5.10b and A 5.30b:

$$\left[2hC_1\left(\frac{1}{\lambda_2}+\frac{3}{\lambda_1^4\lambda_2^3}\right)\left(1+\alpha\lambda_2^2\right)\right]\lambda_1'+\left[2hC_1\left(-\frac{\lambda_1}{\lambda_2^2}+\frac{3}{\lambda_1^3\lambda_2^4}\right)\left(1+\alpha\lambda_2^2\right)+\left(\frac{\lambda_1}{\lambda_2}-\frac{1}{\lambda_1^3\lambda_2^3}\right)\left(2\alpha\lambda_2\right)\right]...$$

$$\left(\frac{\lambda_1-\lambda_2\cos\psi}{\sin\psi}\right)=\frac{\left(\frac{\lambda_1-\lambda_2\cos\psi}{\sin\psi}\right)\sin\psi+\lambda_2\cos\psi}{\lambda_2\sin\psi}\left\{2hC_1\left[\frac{\lambda_2}{\lambda_1}-\frac{\lambda_1}{\lambda_2}+\alpha\left(\frac{1}{\lambda_1^3\lambda_2}-\frac{1}{\lambda_1\lambda_2^3}\right)\right]\right\}$$

. . . (A 5.32b)

Moving $\frac{\partial T_1}{\partial\lambda_2}\frac{\partial\lambda_2}{\partial\psi}$ across and dividing through by $2hC_1$:

$$\left[\left(\frac{1}{\lambda_2}+\frac{3}{\lambda_1^4\lambda_2^3}\right)\left(1+\alpha\lambda_2^2\right)\right]\lambda_1'=\frac{\lambda_1}{\lambda_2\sin\psi}\left[\frac{\lambda_2}{\lambda_1}-\frac{\lambda_1}{\lambda_2}+\alpha\left(\frac{1}{\lambda_1^3\lambda_2}-\frac{1}{\lambda_1\lambda_2^3}\right)\right]...$$

$$-\left[\left(-\frac{\lambda_1}{\lambda_2^2}+\frac{3}{\lambda_1^3\lambda_2^4}\right)\left(1+\alpha\lambda_2^2\right)+\left(\frac{\lambda_1}{\lambda_2}-\frac{1}{\lambda_1^3\lambda_2^3}\right)\left(2\alpha\lambda_2\right)\right]\left(\frac{\lambda_1-\lambda_2\cos\psi}{\sin\psi}\right)$$

. . . (A 5.33b)

Dividing through by $\frac{\partial T_1}{\partial\lambda_1}$ and rearranging:

$$\lambda_1'=\frac{1}{\left[\left(\frac{1}{\lambda_2}+\frac{3}{\lambda_1^4\lambda_2^3}\right)\left(1+\alpha\lambda_2^2\right)\right]}\left\langle\begin{array}{l}\left(\frac{\lambda_1-\lambda_2\cos\psi}{\sin\psi}\right)\left[\left(\frac{\lambda_1}{\lambda_2^2}-\frac{3}{\lambda_1^3\lambda_2^4}\right)\left(1+\alpha\lambda_2^2\right)-\left(\frac{\lambda_1}{\lambda_2}-\frac{1}{\lambda_1^3\lambda_2^3}\right)\left(2\alpha\lambda_2\right)\right]...\\ +\frac{\lambda_1}{\lambda_2\sin\psi}\left[\left(\frac{\lambda_2}{\lambda_1}-\frac{\lambda_1}{\lambda_2}\right)+\alpha\left(\frac{1}{\lambda_1^3\lambda_2}-\frac{1}{\lambda_1\lambda_2^3}\right)\right]\end{array}\right\rangle$$

. . . (A 5.34b)

This equation is consistent with that given in Feng and Yang (1973) though there is a mistake with $\left(\frac{\lambda_1}{\lambda_2}-\frac{1}{\lambda_1^3\lambda_2^3}\right)$ being missing. This also agrees with the correction shown in Liu thesis (1996).

Part c: Additional errors given in the literature

There are a number of errors in the equations given in both Liu's thesis (1995) and by Liu *et al.* (1996).

Given that $f_3=T_1-T_2$ equation 9 should read:

$$\lambda_1' = -\frac{\lambda_1}{\lambda_2 \sin\psi}\left(\frac{f_3}{f_1}\right) - \left(\frac{\lambda_1 - \lambda_2\cos\psi}{\sin\psi}\right)\left(\frac{f_2}{f_1}\right)$$

Sign missing in Liu *et al.* (1996)

. . . (A 5.1c)

Equation 13 should read:

$$\omega' = \frac{\lambda_1'\omega}{\lambda_1} + \frac{\left(\lambda_1^{\,2} - \omega^2\right)}{\delta}\left(\frac{T_2}{T_1}\right) - \frac{\lambda_1\left(\lambda_1^{\,2} - \omega^2\right)^{1/2} Pr_0}{T_1}$$

Power missing in Liu *et al.* (1996)

. . . (A 5.2c)

And equation 16 should read:

$$f_3 = T_1 - T_2 = 2hC_1\left[\frac{\lambda_1}{\lambda_2} - \frac{\lambda_2}{\lambda_1} - \beta\left(\frac{1}{\lambda_1^3\lambda_2} - \frac{1}{\lambda_1\lambda_2^3}\right)\right]$$

Additional cubic power in Liu *et al.* (1996)

. . . (A 5.3c)

Equation 2.2 in Lardner and Pujara (1980) should read:

$$\lambda_2' = -\left(\frac{\lambda_1 - \lambda_2 \cos\psi}{\sin\psi}\right)$$

Additional negative sign in Lardner and Pujara (1980)

. . . (A 5.4c)

Appendix 11: Matlab program code for the developed Hencky strain mathematical model

Given below is the Matlab program code (The MathWorks Inc., Cambridge, UK) used to solve the Hencky strain mathematical model derived in Appendix 10 and Chapter 5.

XXXXX indicates a new m file followed by the file name.

XXXXX = LP.m

```
%m-file originally written by C Wang April 2002 and modified for use with Hencky
%Strain model by J Stenson Janurary 2008
%adjustment of FengYang.m
clear
close all
%assign global constant9
global mu r0 h E P Kz Lamda0

Lamda0=1.03935;
mu=0.5;
r0 =0.25*10^-5; h = 0.925*10^-7;
beta = h/r0;
E = 100;
Kz = 0.0;
%assign value of Lamdas and find P
lamdas=1.04;
V0=findVo(lamdas,r0);

%solve for contact region guess Lamda0

gamma=2.0;
tspanC=[eps;gamma/180*pi];
y_contact0=[Lamda0;Lamda0];
[t_contact,y_contact] = contact(gamma,tspanC,y_contact0);

%solve for non-contact region
tspanNC=[gamma*pi/180;pi/2];
P=0.516565874021663;
yC1=y_contact(length(y_contact),1);
yC2=y_contact(length(y_contact),2);
ansNC = noncontact(yC1,yC2,gamma,tspanNC,V0,lamdas);
t_noncontact=ansNC{1}(:,1);
y_noncontact=ansNC{1}(:,2:end);
V1=ansNC{3};
Vloss1=ansNC{4};
```

```
t_overall = [t_contact ; t_noncontact];
disp((V1-V0)/V0)
disp((y_noncontact(end,3)))
disp((y_noncontact(end,5)))
y_overall = [y_contact ; y_noncontact(:,1:2)];
%figure; plot(V0-V1'-Vloss1'); title('how close is V'); grid on;
%figure; plot(180*t_overall/pi,y_overall(:,1)); title('Lamda1')
%figure; plot(180*t_overall/pi,y_overall(:,2)); title('Lamda2')
%figure; plot(180*t_overall/pi,y_overall); title('Lamda')
%figure; plot(180*t_noncontact/pi,y_noncontact(:,3)); title('omega')
%figure; plot(180*t_noncontact/pi,y_noncontact(:,4)); title('Delta')
%figure; plot(180*t_noncontact/pi,y_noncontact(:,5)); title('eta')
save 'psi.xls' t_overall -ascii -tabs
save 'lamda.xls' y_overall -ascii -tabs
save 'psi1.xls' t_contact -ascii -tabs
save 'all.xls' y_noncontact -ascii -tabs
```

XXXXX = contact.m

```
function [t_contact,y_contact] = contact(gamma,tspan,yC0)

options=odeset('Maxstep', 0.0017453);
[t_contact,y_contact] = ode45(@f_contact,tspan,yC0);
```

XXXXX = f-contact.m

```
function dydt = f_contact(t_contact,y_contact)
global mu r0 h E Kz Lamda0

b_contact(1) = ((2*E*h)/(3*y_contact(1)*y_contact(2)))*(log(y_contact(1)^2*y_contact(2)));
b_contact(2) = ((2*E*h)/(3*y_contact(1)*y_contact(2)))*(log(y_contact(1)*y_contact(2)^2));

a_contact(1) = ((2*E*h)/(3*y_contact(1)^2*y_contact(2)))*(2 -
log(y_contact(1)^2*y_contact(2)));
a_contact(2) = ((2*E*h)/(3*y_contact(1)*y_contact(2)^2))*(1-
(log(y_contact(1)^2*y_contact(2))));
a_contact(3) = b_contact(1) - b_contact(2);

dydt = [-y_contact(1)/(y_contact(2)*sin(t_contact))*(a_contact(3)/a_contact(1))-((y_contact(1)-
y_contact(2)*cos(t_contact))/sin(t_contact))*(a_contact(2)/a_contact(1))
      (y_contact(1)-y_contact(2)*cos(t_contact))/sin(t_contact)];
```

XXXXX = noncontact.m

```
%This function definition modified to set up initial conditions
function y = noncontact(y_contact_1,y_contact_2,gamma,tspanNC,V0,Ls,Lamda0)
global mu r0 h E P Kz Lamda0

tspan_noncontact=tspanNC;

%set up initial conditions using y_contact_1,y_contact_2


y_noncontact0 = [y_contact_1; y_contact_2; y_contact_1*0.99999;
y_contact_2*sin(gamma*pi/180);0.996912645*Ls*r0];

%SET UP AN ARRAY TO STORE THE OUTPUT (EMPTY)
stored_y_noncontact = [];

%USING A FOR LOOP, STEP THROUGH DIFFERENT VALUES OF P.
P1=zeros(length(P),1);
options=odeset('Maxstep', 0.0017453);
for j=1:length(P)
   [t_noncontact,y_noncontact] =
ode45(@f_noncontact,tspan_noncontact,y_noncontact0,options,j);
   %APPEND EACH OF THE Y(41,3) RESULTS TO THE ARRAY
   stored_y_noncontact = [stored_y_noncontact y_noncontact(length(y_noncontact),3)];

   %check V with V0
   yNC1=y_noncontact(:,1);
   yNC2=y_noncontact(:,2);
   yNC3=y_noncontact(:,3);
   delta=yNC2.*sin(t_noncontact);
   demV=sqrt(yNC1.^2-yNC3.^2).*delta.^2;
   demX=Kz*(0.5-P(j))*sqrt(yNC1.^2-yNC3.^2);
   demA=sqrt(yNC1.^2-yNC3.^2).*delta;
   Lp=length(demV);
   demV1=zeros(Lp-1,1);
   demX1=zeros(Lp-1,1);
   demA1=zeros(Lp-1,1);
   Dt=diff(t_noncontact);
   DV1=diff(demV);
   DX1=diff(demX);
   DA1=diff(demA);
   for i=1:Lp-1
      demV1(i)=Dt(i)*(demV(i)+0.5*DV1(i));
      demX1(i)=Dt(i)*(demX(i)+0.5*DX1(i));
      demA1(i)=Dt(i)*(demA(i)+0.5*DA1(i));
```

```
      demVloss1(i)=demX1(i).*demA1(i);
   end
   demV2=sum(demV1);
   demVloss=sum(demVloss1);
   V1(j)=2*pi*r0^3*demV2;
   Vloss1(j)=4*pi*r0^3*demVloss;
end

y=cell(1,4);
y{1}=[t_noncontact, y_noncontact];
y{2}=stored_y_noncontact;
y{3}=V1;
y{4}=Vloss1;
%print out the results to screen (or you could plot them)
%disp('Values of y_noncontact for each value of P tried:')
%stored_y_noncontact
%figure; plot(stored_y_noncontact)
```

XXXXX = f-noncontact.m

```
function dydt = f_noncontact(t_noncontact,y_noncontact,j)
global mu r0 h E P Kz Lamda0

b_noncontact(1) =
((2*E*h)/(3*y_noncontact(1)*y_noncontact(2)))*(log(y_noncontact(1)^2*y_noncontact(2)));
b_noncontact(2) =
((2*E*h)/(3*y_noncontact(1)*y_noncontact(2)))*(log(y_noncontact(1)*y_noncontact(2)^2));

a_noncontact(1) = ((2*E*h)/(3*y_noncontact(1)^2*y_noncontact(2)))*(2 -
log(y_noncontact(1)^2*y_noncontact(2)));
a_noncontact(2) = ((2*E*h)/(3*y_noncontact(1)*y_noncontact(2)^2))*(1-
(log(y_noncontact(1)^2*y_noncontact(2))));
a_noncontact(3) = b_noncontact(1) - b_noncontact(2);

dydt = [(y_noncontact(2)*sin(t_noncontact).*cos(t_noncontact)-
y_noncontact(3)*sin(t_noncontact))./sin(t_noncontact).^2*a_noncontact(2)/a_noncontact(1)-
y_noncontact(3)./(y_noncontact(2)*sin(t_noncontact))*a_noncontact(3)/a_noncontact(1)
(y_noncontact(3)-y_noncontact(2)*cos(t_noncontact))./sin(t_noncontact)
((y_noncontact(2)*sin(t_noncontact).*cos(t_noncontact)-
y_noncontact(3)*sin(t_noncontact))./sin(t_noncontact).^2*a_noncontact(2)/a_noncontact(1)-
y_noncontact(3)./(y_noncontact(2)*sin(t_noncontact))*a_noncontact(3)/a_noncontact(1)) *
y_noncontact(3)/y_noncontact(1) + (y_noncontact(1)^2-
y_noncontact(3)^2)./(y_noncontact(2)*sin(t_noncontact)) * b_noncontact(2)/b_noncontact(1) -
y_noncontact(1).*sqrt(y_noncontact(1)^2-y_noncontact(3)^2)*P(j)*r0/b_noncontact(1)
y_noncontact(3)
-r0*sqrt(y_noncontact(1)^2-y_noncontact(3)^2)];
```

XXXXX = findVo.m

```
function y=findVo(Ls,r0)
y=4/3*pi*r0^3*Ls^3;
```

Appendix 12: Bulk elastic modulus

The primary use of the volumetric elastic modulus is to describe water transport in plant cells under non-steady conditions. This parameter is often confused with the bulk elastic modulus, which (in solid mechanics) relates the fractional volumetric change of a solid to some external pressure change. However, in studies of plant water relations, the mass of the cell is not conserved, and this definition of the bulk elastic modulus is invalid. The instantaneous volumetric (bulk) modulus of elasticity, ε_{Bulk}, is defined in Wang *et al.* (2004) by equation (A 7.1).

$$\varepsilon_{Bulk} = \frac{dP}{dV}V \qquad \ldots \text{(A 7.1)}$$

After inflation the cell size increases from r_o to $r_o\lambda_s$. At the equilibrium point the relationship with internal pressure (P) and the membrane stress (σ) is found by a force balance to be:

$$P\pi\lambda_s^2 r_o^2 = 2\pi\lambda_s r_o h_o \sigma \qquad \ldots \text{(A 7.2)}$$

$$\sigma = 2E\left(\lambda_s - 1\right) \qquad \ldots \text{(A 7.3)}$$

Combining equations (A 7.2) and (A 7.3) leads to:

$$P = \frac{4Eh_o\left(\lambda_s - 1\right)}{\lambda_s r_o} \qquad \ldots \text{(A 7.4)}$$

$$V = \frac{4}{3}\pi\left(r_o \lambda_s\right)^3 \qquad \ldots \text{(A 7.5)}$$

Then $\lambda_s = \frac{1}{r_o}\left(\frac{3V}{4\pi}\right)^{\frac{1}{3}}$ $\ldots$ (A 7.6)

Combining equations (A 7.4) and (A 7.6), we have:

$$P = \frac{4Eh_o}{r_o}\left(1 - \frac{1}{\lambda_s}\right) \qquad \ldots \text{(A 7.7)}$$

$$P = \frac{4Eh_o}{r_o}\left[1 - r_o\left(\frac{4\pi}{3V}\right)^{\frac{1}{3}}\right] \qquad \ldots \text{(A 7.8)}$$

$$\frac{dP}{dV} = -4Eh_o\left(\frac{4\pi}{3}\right)^{\frac{1}{3}}\frac{d}{dV}\left(V\right)^{-\frac{1}{3}} \qquad \ldots \text{(A 7.9)}$$

$$\frac{dP}{dV} = \frac{4}{3}Eh_o\left(\frac{4\pi}{3}\right)^{\frac{1}{3}}V^{-\frac{4}{3}} \qquad \ldots \text{(A 7.10)}$$

Therefore

$$\varepsilon_{Bulk} = \frac{4}{3}\left(\frac{4\pi}{3}\right)^{\frac{1}{3}}Eh_o V^{-\frac{1}{3}} \qquad \ldots \text{(A 7.11)}$$

Appendix 13: Relationships between the cell size and the von Mises failure criteria.

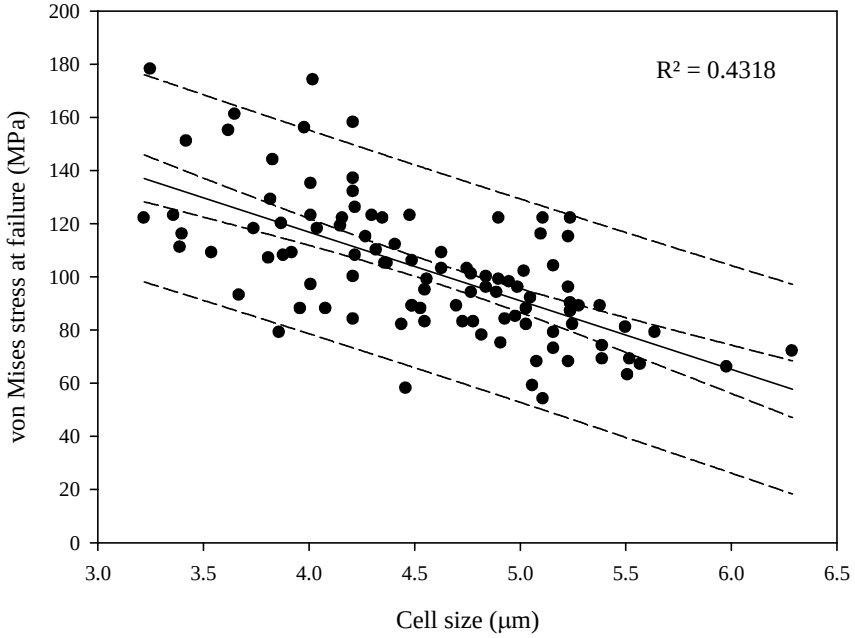

Figure A 32: Trend between the von Mises stress at failure and the cell diameter. Dashed lines represent the 95 % confidence limits for the mean and the individual measurements.

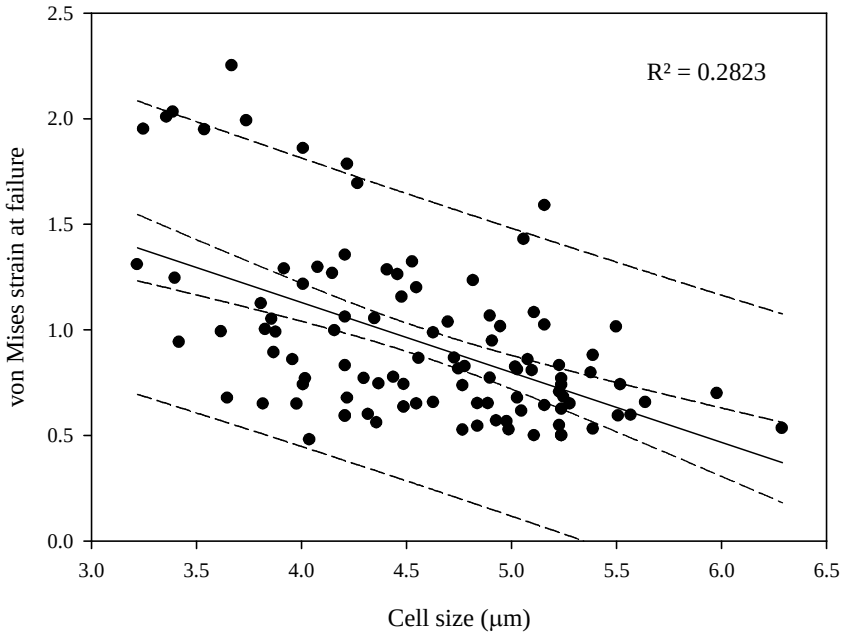

Figure A 33: Trend between the von Mises stress at failure and the cell diameter. Dashed lines represent the 95 % confidence limits for the mean and the individual measurements.

Appendix 14: Effect of the initial stretch ratio on the elastic modulus

Figure A 34 shows the asymmetrical effect of the initial stretch ratio on the elastic modulus produced from the fitting process. This relationship was produced using the same experimental data and fitting procedure as that in Section 6.1.3.

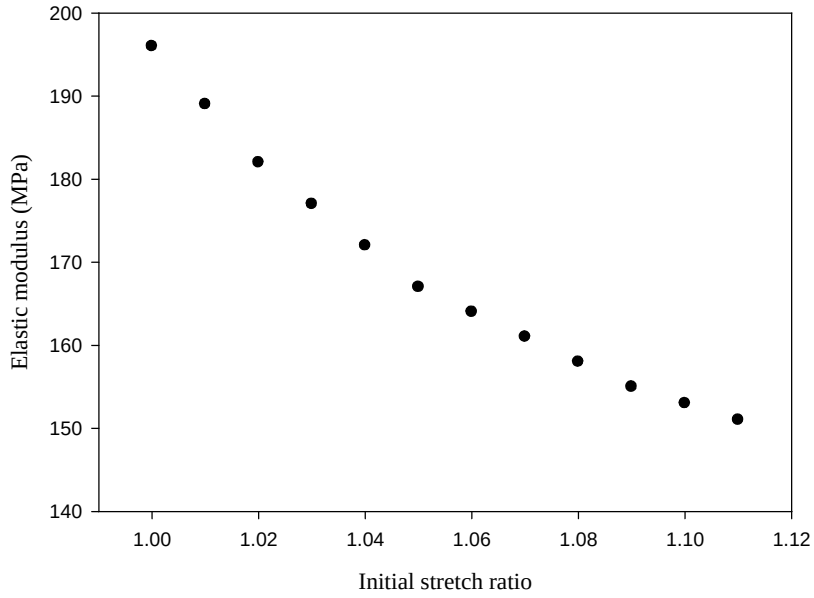

Figure A 34: Asymmetrical effect of the initial stretch ratio on the elastic modulus.

Appendix 15: Boyle van't Hoff relationship

In order to prove that the there is linear relationship between the reciprocal of the external osmotic pressure and the cell volume at high osmotic pressures the Boyle van't Hoff relationship was derived.

This derivation was performed by Professor C.R. Thomas.

Hydrostatic-osmotic pressure balance is given by:

$$\Delta P = P = \Pi_i - \Pi_e \qquad \ldots \text{(A 7.12)}$$

where ΔP is the hydrostatic pressure difference, P is the turgor pressure, Π_i is the internal osmotic pressure, and Π_e is the external osmotic pressure.

Pressure-wall stress balance:

Assuming biaxial plane stress of an incompressible cell wall

$$P\pi r^2 = 2\pi rh\sigma = 4\pi rhE(\lambda - 1) \qquad \ldots \text{(A 7.13)}$$

where r is the cell radius, h is the cell wall thickness, σ is the stress in the wall, E is Young's modulus pressure, and λ is the stretch ratio.

From equation (A 7.13)

$$P = \frac{4hE}{r}(\lambda - 1)$$

and from equation (A 7.12)

$$\frac{4hE}{r}(\lambda - 1) = \Pi_i - \Pi_e \qquad \ldots \text{(A 7.14)}$$

Osmolyte balance:

$$\Pi_i (V - b) = \Pi_0 (V_0 - b) \qquad \ldots \text{(A 7.15)}$$

where V is the volume of the cell, b is the non-osmotic volume, Π_0 is the internal osmotic pressure , and V_0 is the volume of the cell in that condition.

From equations (A 7.14) and (A 7.15)

$$\frac{4hE}{r}(\lambda - 1) = \Pi_0 \left(\frac{V_0 - b}{V - b} \right) - \Pi_e \qquad \ldots \text{(A 7.16)}$$

Constant wall volume assumption:

$$h = h_0 \left(\frac{r_0}{r} \right)^2 = \frac{h_0}{\lambda^2} \text{ as } r = \lambda r_0 \qquad \ldots \text{(A 7.17)}$$

where r_0 and h_0 are the cell radius and wall thickness, respectively, when the turgor pressure is zero. Substituting equation (A 7.17) into equation (A 7.16) gives

$$\frac{4h_0E}{\lambda^3 r_0}(\lambda-1) = \Pi_0\left(\frac{V_0-b}{V-b}\right) - \Pi_e \qquad \ldots \text{(A 7.18)}$$

Stretch ratio-cell volume relationship:

$$\lambda = \left(\frac{V}{V_0}\right)^{\frac{1}{3}} \text{ or } V = \lambda^3 V_0 \qquad \ldots \text{(A 7.19)}$$

Substituting for V in equation (A 7.18) gives

$$\frac{4h_0E}{\lambda^3 r_0}(\lambda-1) = \Pi_0\left(\frac{V_0-b}{\lambda^3 V_0-b}\right) - \Pi_e \qquad \ldots \text{(A 7.20)}$$

$$\text{Also } V_0 = \frac{4\pi}{3} r_0^3 \text{ or } r_0 = \left(\frac{3V_0}{4\pi}\right)^{\frac{1}{3}} \qquad \ldots \text{(A 7.21)}$$

so that

$$4\left(\frac{4\pi}{3}\right)^{\frac{1}{3}} \frac{h_0E}{V_0^{\frac{1}{3}}} \frac{(\lambda-1)}{\lambda^3} = \Pi_0\left(\frac{V_0-b}{\lambda^3 V_0-b}\right) - \Pi_e \qquad \ldots \text{(A 7.22)}$$

Rearranging equation (A 7.22)

$$\Pi_e = \Pi_0\left(\frac{V_0 - b}{\lambda^3 V_0 - b}\right) - 4\left(\frac{4\pi}{3}\right)^{\frac{1}{3}} \frac{h_0 E}{V_0^{\frac{1}{3}}} \frac{(\lambda - 1)}{\lambda^3}$$

$$= \frac{1}{\lambda^3}\left\{\Pi_0\left(\frac{1 - \frac{b}{V_0}}{1 - \frac{b}{\lambda^3 V_0}}\right) - 4\left(\frac{4\pi}{3}\right)^{\frac{1}{3}} \frac{h_0 E}{V_0^{\frac{1}{3}}}(\lambda - 1)\right\} \quad \ldots \text{(A 7.23)}$$

It should be noted that as $V = \lambda^3 V_0 \rightarrow b$, the right hand-side of this equation goes to ∞, which is reasonable as (in theory) it would require an infinite Π_e to reach this condition. On the other hand, if $\lambda = 1$, $\Pi_e = \Pi_0$ as required by the definition of Π_0.

It is worthwhile considering some typical values for the parameters. In the case of yeast:

$\Pi_0 \approx 1.0\ MPa = 1.0 \times 10^6\ Pa$ *- Approximate value determined by Malvern Mastersizer.*

$\frac{b}{V_0} \approx 0.5$ *- Approximate non – osmotic volume of the cell from Malvern mastersizer and visualisation chamber experiments.*

$r_0 \approx 2.5 \times 10^{-6}\,\text{m}$ *- Approximate cell radius value obtained by compression testing, TEM and image analysis*

$$V_0 = \frac{4\pi}{3} r_0^3 \approx \frac{4\pi}{3}\left(2.5 \times 10^{-6}\right)^3\ \text{m}^3 \approx 6.55 \times 10^{-17}\ \text{m}^3$$

$h_0 \approx 100\,\text{nm} = 10^{-7}\,\text{m}$ - *Approximate cell wall thickness value from TEM data (Section 3.5).*

$E \approx 200\,\text{MPa} = 2 \times 10^{8}\,\text{Pa}$ - *Approximate elastic modulus value produced by modelling compression testing data.*

Substituting these values in equation (A 7.23) gives

$$\Pi_e = \frac{1}{\lambda^3}\left\{1.0 \times 10^{6}\left(\frac{0.5}{1-\frac{0.5}{\lambda^3}}\right) - 3.2 \times 10^{7}(\lambda - 1)\right\} \quad \ldots \text{(A 7.24)}$$

In theory, the smallest possible value of λ is $\sqrt[3]{0.5} \approx 0.8$, when the volume of the cell has been reduced to the non-osmotic volume. Consider the function on the right hand side of equation (A 7.24) for $0.8 \leq \lambda \leq 1$, which is equivalent to $0.51V_0 \leq V \leq V_0$. See the (MATLAB) figure below.

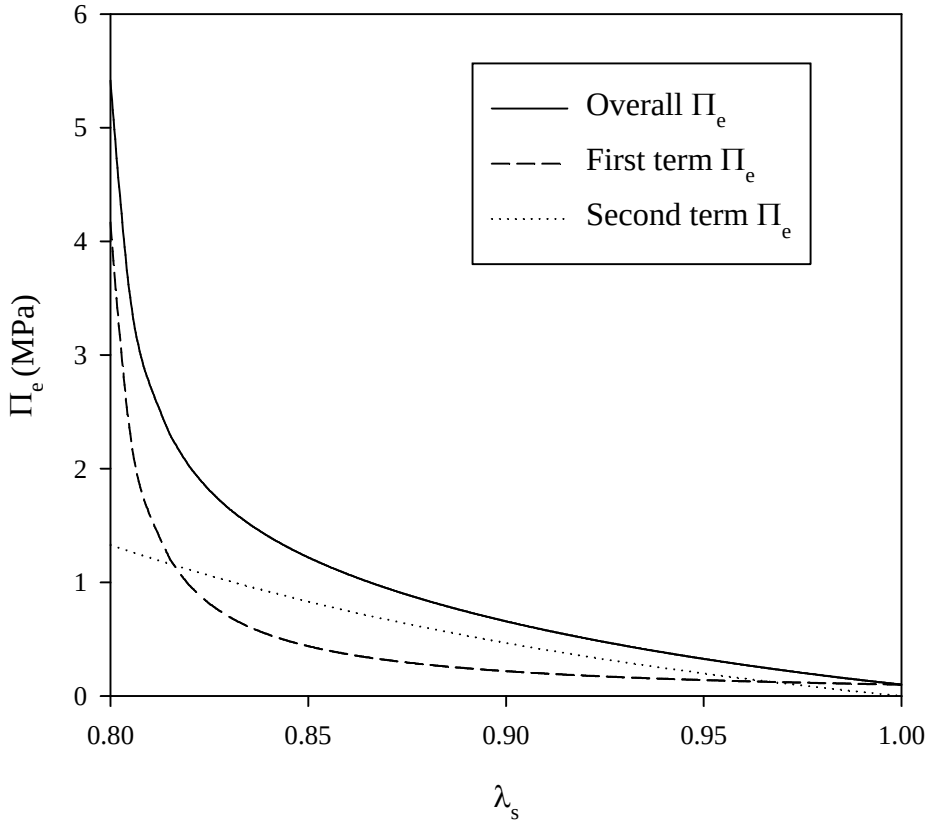

Figure A 35: Plot of comparing the effect of the terms of equation A 7.24 on the overall Π_e.

It would appear that the second term of the function on the right hand side of equation (A 7.24) could be accepted as a reasonable approximation to the whole, at least for $0.9 \leq \lambda \leq 1$, which is equivalent to $0.73V_0 \leq V \leq V_0$. Hence, for parameters near those used in equation (A 7.24), one can rewrite equation (A 7.16) as

$$\Pi_e \sim \Pi_0\left(\frac{V_0 - b}{\lambda^3 V_0 - b}\right) = \Pi_0\left(\frac{V_0 - b}{V - b}\right) \qquad \ldots \text{(A 7.25)}$$

In the conventional plot, V is plotted against $\frac{1}{\Pi_e}$. From equation (A 7.25)

$$V \sim \Pi_0 (V_0 - b) \frac{1}{\Pi_e} + b \qquad \ldots \text{(A 7.26)}$$

which implies for these values of λ, *V* should be an affine function of $\frac{1}{\Pi_e}$. The intercept on the *V* axis of a *V* - $\frac{1}{\Pi_e}$ plot should be *b*, the non-osmotic volume.

From the slope of the plot, one can get $\Pi_0 (V_0 - b)$, and knowing $V_0 = \frac{4\pi}{3} r_0^3$, and *b*, it should be possible to find Π_0.

Appendix 16: Whole cell results produced from compression testing of DTT treated cells.

Appendix 16 shows the effect of the order of compression on the cell size, force and deformation at failure with DTT treated cells. In addition to this the relationships between the cell size and the force and deformation at failure are also shown.

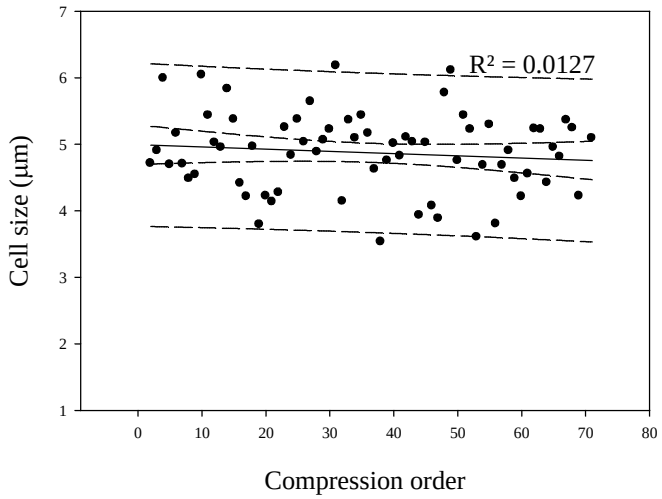

Figure A 36: Effect of order of compression on the cell size of DTT treated cells.

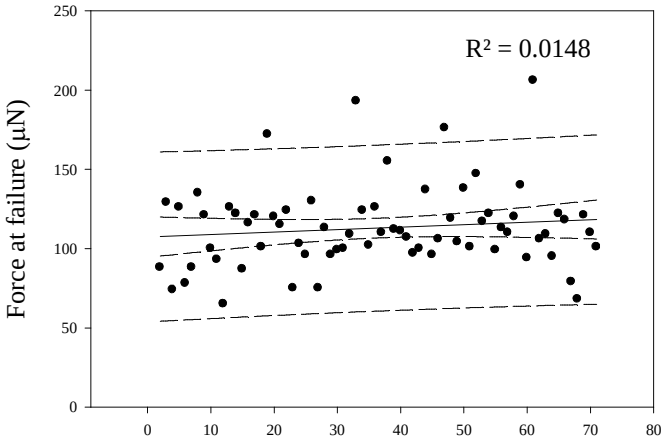

Figure A 37: Effect of order of compression on the force at failure of DTT treated cells.

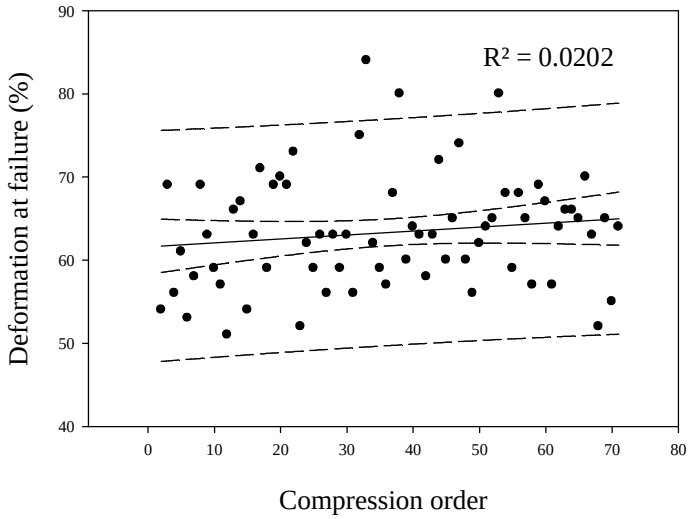

Figure A 38: Effect of order of compression on the deformation at failure of DTT treated cells.

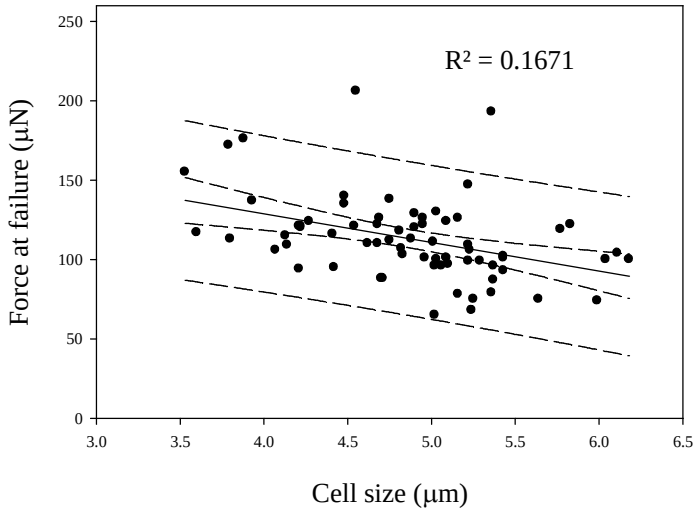

Figure A 39: Effect of cell size on the force at failure of DTT treated cells.

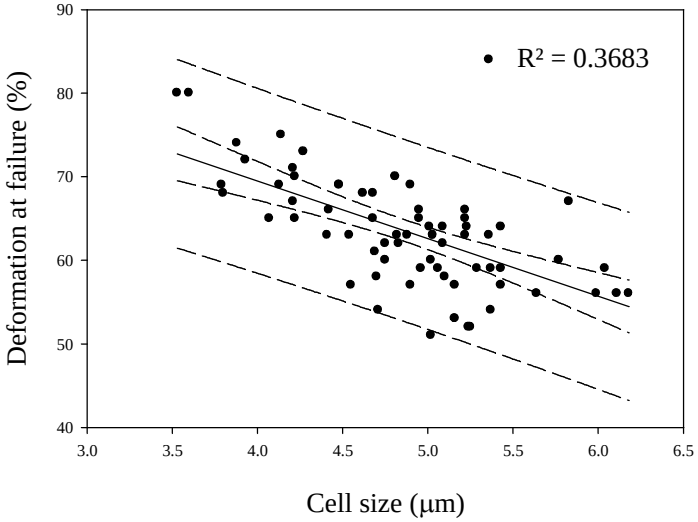

Figure A 40: Effect of cell size on the deformation at failure of DTT treated cells.

Appendix 17: Parameters produced from compression testing of cells sonicated for 5 minutes.

Appendix 17 shows the effect of the order of compression on the cell size, force and deformation at failure with cells sonicated for 5 minutes. In addition to this the relationships between the cell size and the force and deformation at failure are also shown.

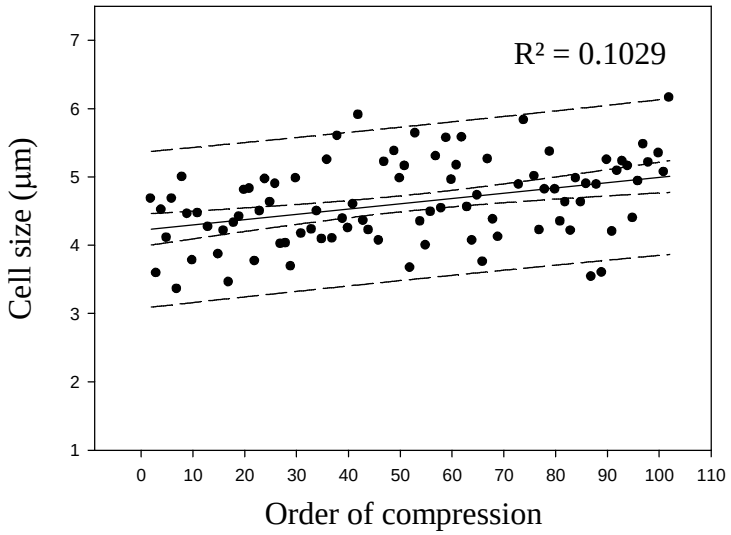

Figure A 41: Effect of order of compression on the cell size for cells sonicated for 5 minutes.

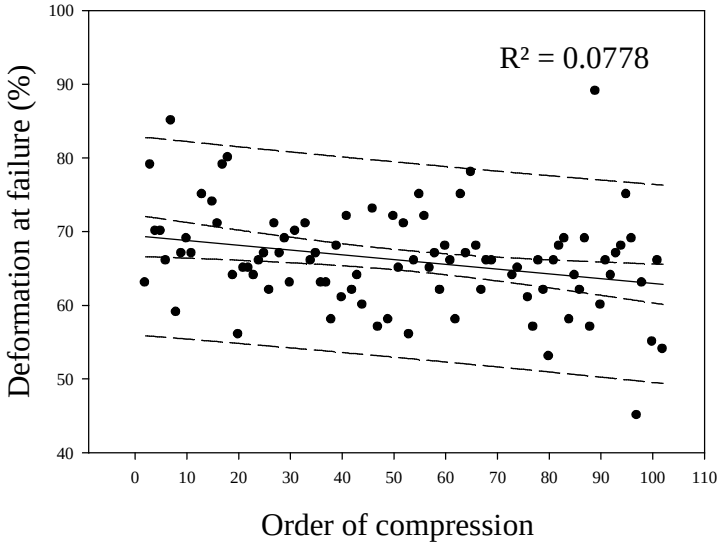

Figure A 42: Effect of order of compression on the deformation at failure for cells sonicated for 5 minutes.

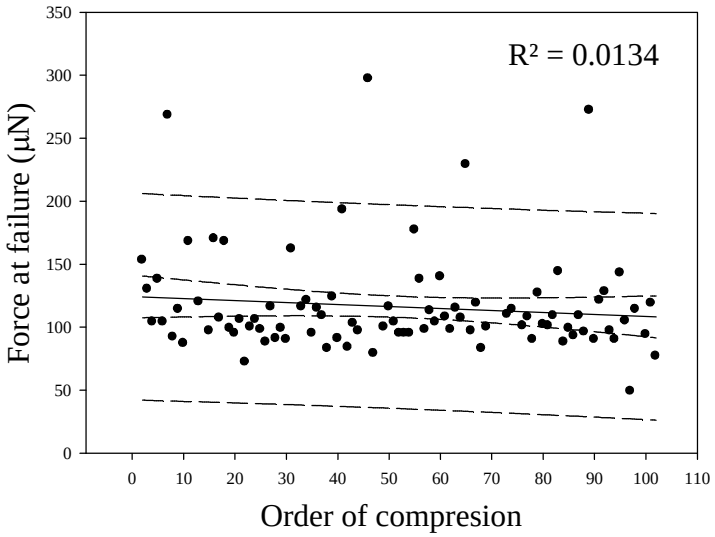

Figure A 43: Effect of order of compression on the force at failure for cells sonicated for 5 minutes.

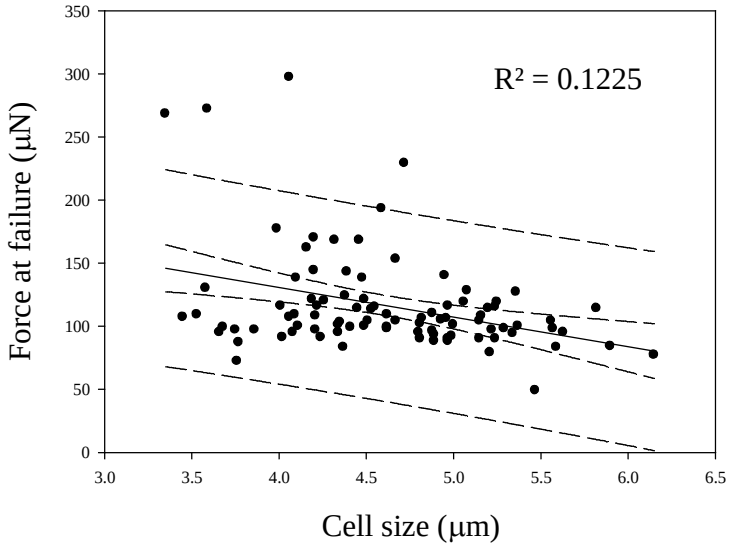

Figure A 44: Effect of cell size on the force at failure for cells sonicated for 5 minutes.

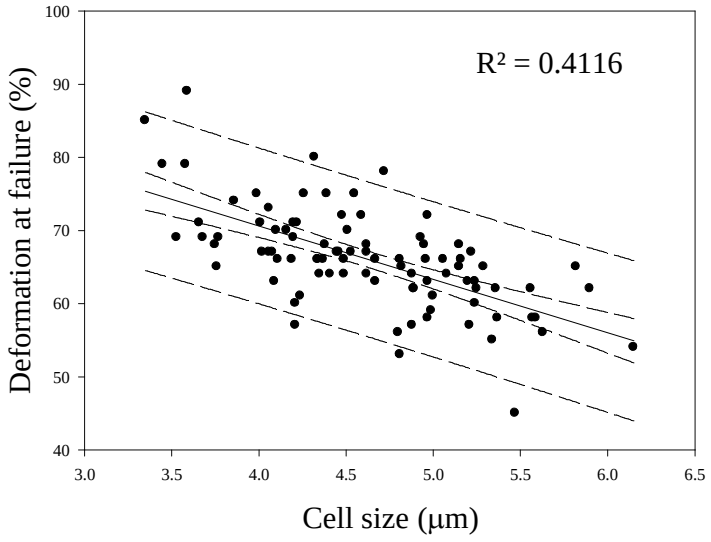

Figure A 45: Effect of cell size on the deformation at failure for cells sonicated for 5 minutes.

Appendix 18: Parameters produced from compression testing of cells sonicated for 10 minutes.

Appendix 18 shows the effect of the order of compression on the cell size, force and deformation at failure with cells sonicated for 10 minutes. In addition to this the relationships between the cell size and the force and deformation at failure are also shown.

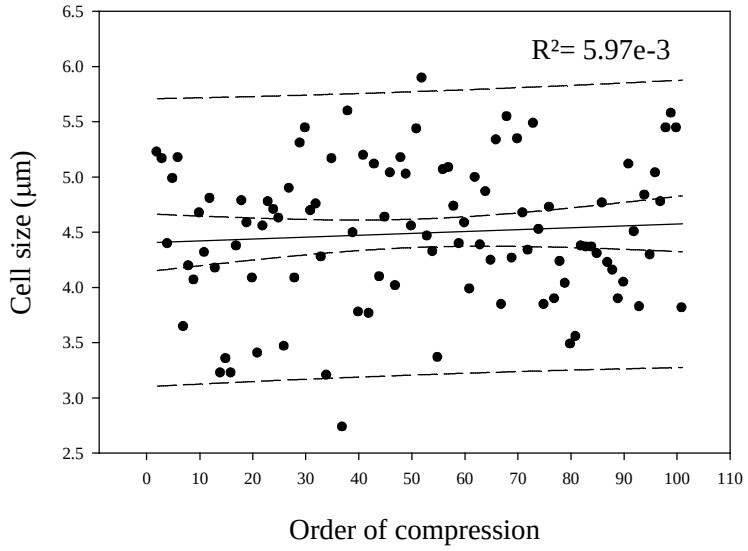

Figure A 46: Effect of order of compression on the cell size for cells sonicated for 10 minutes.

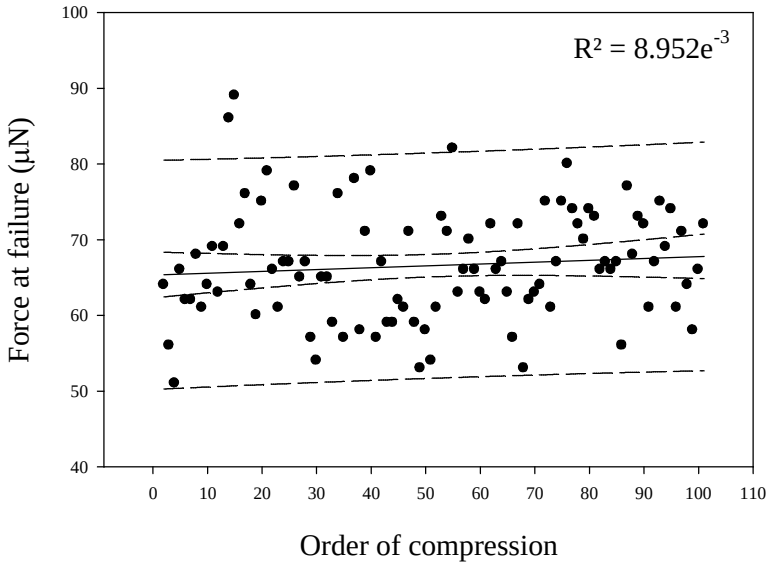

Figure A 47: Effect of order of compression on the deformation at failure for cells sonicated for 10 minutes.

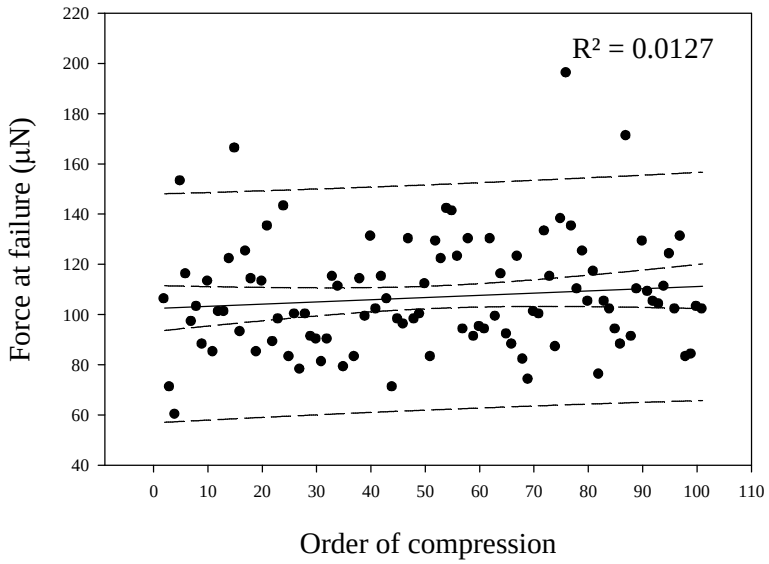

Figure A 48: Effect of order of compression on the force at failure for cells sonicated for 10 minutes.

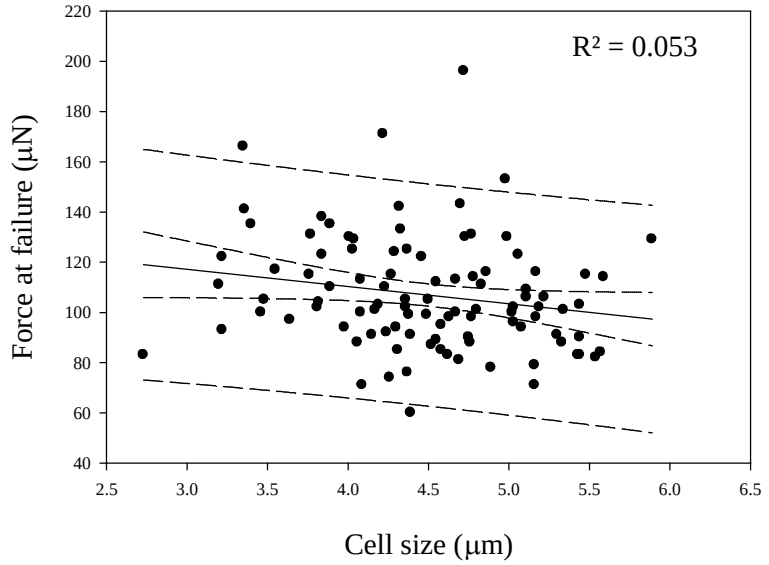

Figure A 49: Effect of cell size on the force at failure for cells sonicated for 10 minutes.

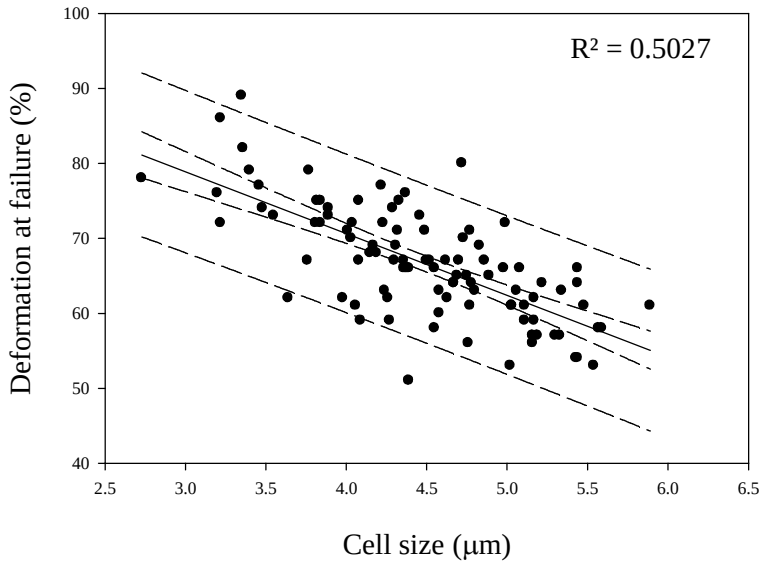

Figure A 50: Effect of cell size on the deformation at failure for cells sonicated for 10 minutes.

Appendix 19: Sketch showing the structure of the yeast cell wall

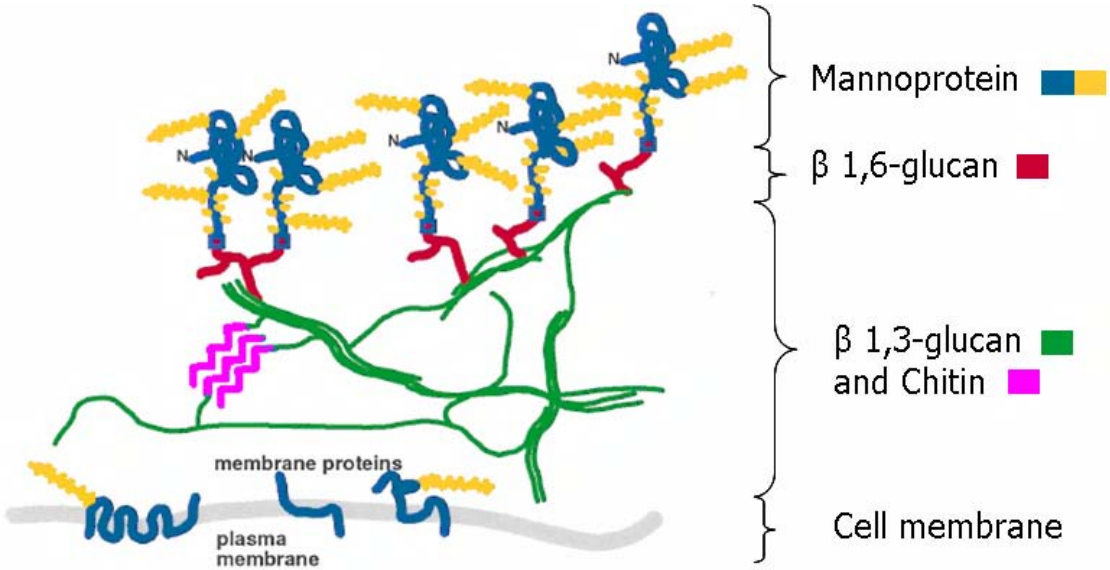

Sketch of the yeast cell wall taken from:

"Lipke PN and Qvalle R *1998. Cell Wall Architecture in Yeast: New structure and new challenges. J of Bacteriology* ***180:****15 3735-3740"*